

University of Windsor

Scholarship at UWindor

Electronic Theses and Dissertations

Theses, Dissertations, and Major Papers

1-1-2003

Development of a new durable aluminum-silicon alloy for the next generation of engine block casting.

Robert Ian Mackay
University of Windsor

Follow this and additional works at: <https://scholar.uwindsor.ca/etd>

Recommended Citation

Mackay, Robert Ian, "Development of a new durable aluminum-silicon alloy for the next generation of engine block casting." (2003). *Electronic Theses and Dissertations*. 7202.
<https://scholar.uwindsor.ca/etd/7202>

This online database contains the full-text of PhD dissertations and Masters' theses of University of Windsor students from 1954 forward. These documents are made available for personal study and research purposes only, in accordance with the Canadian Copyright Act and the Creative Commons license—CC BY-NC-ND (Attribution, Non-Commercial, No Derivative Works). Under this license, works must always be attributed to the copyright holder (original author), cannot be used for any commercial purposes, and may not be altered. Any other use would require the permission of the copyright holder. Students may inquire about withdrawing their dissertation and/or thesis from this database. For additional inquiries, please contact the repository administrator via email (scholarship@uwindsor.ca) or by telephone at 519-253-3000ext. 3208.

Development of a New Durable Al-Si Alloy for the Next Generation of Engine Block Casting

By Robert Ian Mackay

A Dissertation Submitted to the Faculty of Graduate Studies and Research through the
Engineering Materials Program of the Faculty of Engineering in Partial Fulfillment of the
Requirements for the Degree of Doctor of Philosophy at the University of Windsor

Windsor, Ontario, Canada, 2003

©R. Mackay, 2003



Library and
Archives Canada

Bibliothèque et
Archives Canada

Published Heritage
Branch

Direction du
Patrimoine de l'édition

395 Wellington Street
Ottawa ON K1A 0N4
Canada

395, rue Wellington
Ottawa ON K1A 0N4
Canada

Your file Votre référence

ISBN: 978-0-494-35075-1

Our file Notre référence

ISBN: 978-0-494-35075-1

NOTICE:

The author has granted a non-exclusive license allowing Library and Archives Canada to reproduce, publish, archive, preserve, conserve, communicate to the public by telecommunication or on the Internet, loan, distribute and sell theses worldwide, for commercial or non-commercial purposes, in microform, paper, electronic and/or any other formats.

The author retains copyright ownership and moral rights in this thesis. Neither the thesis nor substantial extracts from it may be printed or otherwise reproduced without the author's permission.

AVIS:

L'auteur a accordé une licence non exclusive permettant à la Bibliothèque et Archives Canada de reproduire, publier, archiver, sauvegarder, conserver, transmettre au public par télécommunication ou par l'Internet, prêter, distribuer et vendre des thèses partout dans le monde, à des fins commerciales ou autres, sur support microforme, papier, électronique et/ou autres formats.

L'auteur conserve la propriété du droit d'auteur et des droits moraux qui protègent cette thèse. Ni la thèse ni des extraits substantiels de celle-ci ne doivent être imprimés ou autrement reproduits sans son autorisation.

In compliance with the Canadian Privacy Act some supporting forms may have been removed from this thesis.

Conformément à la loi canadienne sur la protection de la vie privée, quelques formulaires secondaires ont été enlevés de cette thèse.

While these forms may be included in the document page count, their removal does not represent any loss of content from the thesis.

Bien que ces formulaires aient inclus dans la pagination, il n'y aura aucun contenu manquant.


Canada

Abstract

This dissertation is a metallurgical investigation of the Al-9wt.%Si-1wt.%Cu alloys (known herein as the WA328 (Fe ~ 0.4 wt.%) and WB328 (Fe ~ 0.8 wt.%) alloy). The WA328 and WB328 alloys will also be investigated for their capacity to replace the W319 alloy (Al-7wt.%Si-3wt.%Cu alloy) as an engine block cast material.

The main aim of the metallurgical investigation was to understand the role Cu and Si have on the development of shrinkage porosity in the cast structure, which in turn controls high cycle fatigue (HCF) properties. In order to achieve this objective a novel approach using thermal analysis techniques was developed to assess mushy zone kinetics, the state between the liquidus and solidus where a solid skeletal α -Al phase and an Al-Si eutectic phase grow at the expense of an interdendritic liquid. Specifically, the cooling curve and calculated fraction solid curve were partitioned into segments, which reflect different stages of feeding through the entire solidification event of the alloy. Each partitioned segment corresponds to a stage of feeding, which in turn signifies a relative degree of pore growth susceptibility.

The dissertation investigates the viability of the WA328 alloy as a suitable replacement alloy for engine block applications, namely the V8 engine block cast at the Nemak Windsor Aluminum Plant (WAP). A total of forty-three (43) V8 engine blocks along with thermal analysis test samples were produced and extensively evaluated using the aforementioned interpretative techniques of the cooling and fraction solid curves. Microstructure, mechanical test properties and hot tearing susceptibility were also

evaluated and found to meet or exceed the Ford Engineering Material Specification WSE-M2A151-A3 requirement. For example, WSE-M2A151-A3 requires that the mean HCF strength of the bulkhead section of the V8 engine block must be at least 65 MPa. However, the production V8 engine block cast using the W319 alloy attains only a mean HCF strength of 53.8 ± 3 MPa which is short of achieving what is specified by WSE-M2A151-A3. V8 engine blocks cast using the WA328 alloy achieve a mean HCF strength of 73 ± 4.5 MPa. The improvement in HCF properties for the WA328 alloy was found to be due to its reduced susceptibility with respect to pore development.

Dedication

I dedicate this dissertation to my family, Alward, Yvonne and David Mackay, all of whom played the largest and most substantial role in allowing it to be completed.

Acknowledgements

I would like to take this opportunity to thank Dr. J. H. Sokolowski for his support and guidance throughout the tenure of this dissertation. Dr. G. Byczynski (Nemak of Canada Limited), Dr. W. Evans and R. Hasenbusch (Ford Motor Company, Dearborn), are thanked for providing technical support during the work done on casting the WA328 alloy and WB328 alloy in the V8 engine block moulds. D. Cusinato (Nemak of Canada Limited) is also thanked for his assistance and guidance during work on the V8 engine blocks made using the W319 alloy, the WA328 alloy and the WB328 alloy. I would also like to thank current and former IRC staff and students for their support, most notably Dr. M. Djurdjevic & Dr. W. Kasprzak. Also thanked for their support and interaction are Dr. W. T. Kierkus, P. Gallo, M. Paluch and E. Moosberger.

The staff of the University of Windsor Technical Support Centre (TSC) are acknowledged for their help during the tenure of this thesis project, particularly during construction of the Enviro-ALTAS and the final polishing of the fatigue test specimens. J. H. Robinson is thanked for assistance with the Scanning Electron Microscope. E. Mares de la O is thanked for development of the Enviro-ALTAS software.

Friendship and support were provided by my girlfriend Karol Witt, by family members Alan and Janice Cécire, Sharon Taylor, Tom Taylor, and my friends Carolina Polo-Christy, Graciela Pelayo-Chagoya, Samir Danvantari, Dan Szablewski, Laurie Barns, Sean Crowe, Narinder Channa Singh and Daryoush Emadi.

Table of Contents

Abstract.....	III
Dedication	V
Acknowledgements.....	VI
List of Figures.....	XI
List of Tables.....	XXI
Chapter One, Introduction to Al-Si Cast Alloys	1-6
1.0 Use of Al-Si Casting Alloys in Industry	1
1.1 The Casting of Aluminium Engine Blocks	3
1. 1 Focus of this Study.....	6
Chapter Two, Literature Review on Cast Solidification	9-42
2.0 Quiescent Methods of Liquid Metal Filling During the Casting Operation	9
2.0.1 The Cosworth Precision Sand Process.....	9
2.0.1.1 Sand Type Used for the CPSP.....	10
2.0.1.2 Melt Treatment at WAP.....	10
2.0.1.3 Casting of a Engine Block via CPSP	11
2.1 Chemical Composition of the AA319 & W319 Alloys	14
2.1.1 Iron	15
2.1.2 Manganese.....	15
2.1.3 Zinc.....	16
2.1.4 Bismuth	17
2.1.5 Nickel	17
2.1.5 Strontium.....	18
2.1.6 Antimony.....	18
2.1.7 Sodium	19
2.1.8 Lead & Tin	19
2.1.9 Titanium & Boron	20
2.1.10 Zirconium.....	21
2.1.11 Scandium.....	21
2.2 Hydrogen Uptake in Al-Si Alloy	22
2.2.1 Hydrogen Levels at WAP	25
2.3 Source of Hydrogen & Inclusions in Foundry Al-Si Melts	27
2.3.1 Methods of Hydrogen Absorption.....	27

2.4 Oxides & Inclusions in Al-Si Alloys.....	30
2.4.1 Oxide Types in Al-Si Melts	30
2.4.2 Titanium Boride Inclusions.....	31
2.4.3 Strontium Based Inclusions.....	32
2.5 Gas-Shrinkage Pore Nucleation and Growth Mechanisms	32
2.6 Mechanism for Feeding During Mushy Zone Solidification	37
2.6.1 Contraction of Al α -dendrites and the Al-Si Eutectic During Solidification	37
2.6.2 Modes of Liquid Metal Feeding During Solidification of Al-Si Hypoeutectic Alloys	39
Chapter Three, Literature Review of Fatigue Resistance of Al-Si Alloys	43-61
3.0 Introduction	43
3.1 Fundamental of Fatigue Failure	44
3.1.0 Stress Conditions with Fatigue.....	44
3.1.1 Stages of Fatigue Failure.....	46
3.1.2 Methods of Crack Propagation Measurement.....	48
3.1.3 Axial Configurations for Fatigue Analysis	51
3.1.4 Generation of the S-N Curve.....	52
3.1.5 Staircase Testing	54
3.2 Metallurgical/Structural Factors Affecting Fatigue Crack Growth in Al-Si Alloys	56
3.3 Effect of Cooling Rate on the Fatigue Crack Growth in Al-Si Alloys	61
Chapter Four, Experimental Methodology	70-101
4.0 Introduction to Experimental Methodology.....	70
4.1 Production Test Alloy Chemistry Specification.....	71
4.2 Casting of the V8 Engine Block.....	73
4.3 Heat Treatment of the V8 Engine Block.....	74
4.4 Description of Test Samples Excised From the V8 Engine Block	75
4.4.1 Metallographic Test Samples Analysis	82
4.4.1.1 Phase Identification	83
4.4.1.2 Porosity Measurements	84
4.4.1.3 Secondary Dendrite Arm Spacing (SDAS) Measurements & Dendrite Cell Size (DCSz) Measurements.....	84
4.4.1.4 Quantification of the Area Fraction of Sectioned Primary α -Al Dendrites (AFSP(α -Al)).....	85
4.4.1.5 Vickers Microhardness & Brinell Hardness Measurements	86
4.5 Calibration of K-Type Thermocouples	87
4.6 Thermal Analysis Method using the UMSA.....	90

4.7 UMSA Test Sample Quench Methodology	92
4.8 Development of an Enviro-ALTAS:	94
4.9 Fatigue Testing Procedure.....	96
4.9.1 Fatigue Test Sample Soak Time.....	99
4.10 Monotonic Testing Procedure	101
Chapter Five, Metallurgy of the AW328 & WB328 Alloys	102-181
5.0 Chemical Composition of Test Alloys	102
5.1 The Scanning Electron Microscopy (SEM) and Light Optical Microscopy (LOM) Results of the WA328 & WB328 Alloy Structure	103
5.2 Thermal Analysis of the WA328 and WB328 Alloys.....	112
5.2.1 Characteristic Temperature Measurements	117
5.2.2 Partitioned Cooling Curve & Fraction Solid Parameters	121
5.2.3 Heating Behavior of the W319, WA328 & WB328 Alloys.....	126
5.3 Mushy Zone Evolution during the Solidification of the WA328, WB328 and W319 Alloys.....	128
5.3.1 Results of Quenched WA328, WB328 and W319 Alloys	132
5.3.2 Summary of Phase Nucleation and Solidification Sequence in the WA328 and WB328 Alloys	141
5.3.3 Origins of Polyhedral Si in a Quenched Hypoeutectic Al-Si Alloy.....	144
5.4 α -Al Dendrite Coarsening During the Solidification Process.....	147
5.5 Dendrite Ripening in the W319, WA328 & the WB328 Alloys.....	154
5.6 Volume Fraction of Dendrites in the WA328 and the W319 Alloys	160
5.7 Thermal Analysis for Assessing Shrinkage Pore Growth Mechanisms.....	169
5.8 The Contribution of Cu to Pore Development in Al-Si-Cu Based Casting Alloys	173
5.8.1 The Role of Cu in Porosity Development in the As-Cast Wedges.....	173
5.9 The Effect of Chemistry and Cooling Rate on Mushy Zone Evolution as Determined via Partitioned Thermal Analysis & Fraction Solid Parameters	177
Chapter Six, Integrity of the V8 Engine Block Cast in the WA328 & WB328 Alloys	182-222
6.0 Preliminary Discussion	182
6.1 Assessment of Porosity of the V8 Engine Block Bulkhead Sections	182
6.1.1 Radiographic Examination of the WA328 & WB328 Alloys used to cast in the V8 Engine Block	183
6.1.2 Results of Porosity Analysis of the V8 Engine Block	185
6.1.3 The Effect of Distribution of Bulkhead Porosity on Fatigue Performance....	193
6.2 The Value of λ_2 found in the V8 Engine Block	195

6.3 Results of Monotonic Mechanical Testing of the W319 and WA328 Alloy	197
6.4 High Cycle Fatigue Results	201
6.4.1 Summary of the Staircase Results	201
6.4.2 Analysis of the Fatigue Fracture Surfaces	203
6.4.3 Relationship between Thermal Analysis & HCF Performance of the V8 Engine Block	215
6.5 Hot Tearing Susceptibility of the WA328 Alloy	222
Chapter Seven, Conclusions & Future Work	227-234
7.0 Concluding Remarks	227
7.0.1 Metallurgical Conclusions	227
7.0.2 Casting Performance using the WA328 & WB328 Alloys	232
7.1 Future Work	235
References	237
Appendix A, Interpretative Thermal Analysis Methods	253
Appendix B, Fraction Solid Calculation	265
Appendix C, Experimental Method of the Insitu Thermal Analysis	273
Appendix D, Summary of Compositions	279
Appendix E, Porosity Results	280
Appendix F, Enviro-ALTAS & UMSA Results	282
Appendix G, V8 Engine Block & UMSA Mechanical Test Data	284
Appendix H, Summary of Riser Sink Evaluation	286
VITA AUCTORIS	287

List of Figures

Figure 1.0: Summary of the HCF results of the six alloy compositions investigated by the IRC [20], along with HCF data of wedges from Boileau et. al. [18].	5
Figure 2.0a: Schematic depicting the basic functionality of the liquid processing of the W319. Schematic provided by Byczynski [24].	13
Figure 2.0b: Schematic depicting the zircon sand mould and mould cavity reflecting the engine block casting (3.0L V6). The configuration of the electromagnetic pump orifice and the antenna system which monitors filling rate is shown. Schematic provided by G. Byczynski [24].	13
Figure 2.1: This graph illustrates the variation between the final percent porosity and the final pore density during cooling with a given solid fraction. Since there is a change in pore density at the H threshold, it is assumed that the nucleation of the pores is partly dependent on the H content (<i>Reproduced from [53]</i>).	24
Figure 2.2a: The effect of dissolved hydrogen and the increase of porosity in the bulkheads 2 and 3 of the 3.0L V-6 engine block [2].	26
Figure 2.2b: The 3.0L engine block and the location of Bulkheads 2 and 3.	26
Figure 2.3a: The formations of the oxide layer on the dross and the reaction the supplies hydrogen to the melt. Reproduced from [55].	29
Figure 2.3b: The solubility of hydrogen in pure aluminum and the 319 alloy (<i>Reproduced from [2]</i>).	29
Figure 2.4a: The Gas-Shrinkage Map, which illustrates the combination of shrinkage stress, and internal gas pressure that can be relieved by heterogeneous nucleation from particles present within inter-dendritic region of the mushy zone [14].	34
Figure 2.4b: Crevice reducing critical radii (r^*) of a pore (<i>Reproduced from [16]</i>).	36
Figure 2.4c: Schematic of inclusion in interdendritic regions (<i>Reproduced from [15]</i>).	36
Figure 2.5a: Solidification Contraction of a pure metal. (<i>Reproduced from Campbell [14]</i>).	38
Figure 2.5b: Schematic of the liquid feeding stage, mass feeding stage, interdendritic feeding stage, solid feeding and complete solidification of a cast cross-section [66].	42
Figure 3.0: Fatigue test schematics showing the stress nomenclature for a) tension and compression fatigue test, where $R = -1$, and b) is a tension and tension fatigue test, where $R > 0$ (<i>Reproduced from Callister [79]</i>).	45

Figure 3.1: A plot of $\log (da/dN)$ versus $\log \Delta K$ having the sigmodal shape. In region one the crack growth rate decreases with decreasing ΔK until the threshold region ΔK_{th} . Region two is the power law region, or sometimes referred to as the Paris regime. Region three is a region of accelerated crack growth until K_c . The stage three regime is unstable.....	49
Figure 3.2: The schematic representation of the effective stress intensity ΔK_{eff} . In order to fully open a crack a stress K_{op} must occur above K_{min} during the load cycle [80].	50
Figure 3.3: Example of the S-N curve for an FCC metal (Aluminum) and a BCC metal (Iron) (Example scanned from Boileau [81]).	53
Figure 3.4: Example of the S-N curve for the W319 alloy (Example scanned from Boileau [81]).	53
Figure 3.5: Three fatigue test samples at the beginning of a staircase test. The sequence would continue until the desired number of tests have been completed.	55
Figure 3.6a: The SEM fracture surface of the axial fatigue sample in Table 3.0 having a life of 331, 629 cycles [21].	57
Figure 3.6b: Region 1 at 5,000X.....	58
Figure 3.6c: Region 1 at 10,000X.....	58
Figure 3.6d: Region 2 at 10,000X.....	58
Figure 3.6e: Region 2 at 15,000X.....	58
Figure 3.6f: Region 3 at 5,000X.....	58
Figure 3.6g: Region 3 at 10,000X.....	58
Figure 3.7: A schematic of the wedge casting with chill, riser, down spure and ingate. This wedge was used by Boileau et. al [21] for A356-T6, Boileau et. al [78] for W319-T6,T7, Canton et. al [22] for W319-T6, and Ren [19] for -(7-9% wt.)Si-(1-4% wt.)Cu synthetic alloys.....	62
Figure 3.8: Dimensions of the axial fatigue specimen with 28 mm radius polished notched surfaces [22].	66
Figure 3.9a: SEM micrograph of an actate replica showing formation of slip bands prior to crack growth near the chilled region of the W319 alloy wedge casting [22].	67
Figure 3.9b: SEM micrograph of an actate replica of the same sample in figure 3.3c. The crack departs afterwards perpendicular to the loading direction [22].	67
Figure 3.9c: SEM micrograph of a crack nucleated from a $Al_{15}(Mn,Fe)_3Si_2$ script phase in the W319 alloy sample extracted near the risered end of the wedge sample [22].	67

Figure 3.9d: SEM micrograph of a nucleated crack from a $\text{Al}_{15}(\text{Mn,Fe})_3\text{Si}_2$ from another W319 wedge sample extracted from the risered end of the wedge casting [22].	67
Figure 4.0: The pictograph of the 4.6L engine block and the identification of the bulkhead sections and the sections that were radiographed	77
Figure 4.1: Bulkhead A of the 4.6L engine block with the outline of where metallographic samples were extricated and the overlay of the location where UMSA samples were extricated.	78
Figure 4.2: a) Pictograph of the UMSA test sample, b) schematic of the UMSA test sample with dimensions.	78
Figure 4.3a: The orientation of the fatigue test samples excised from the bulkhead section of the 4.6L Engine Block (Bulkhead A as example here)	79
Figure 4.3b: The orientation of the tensile test samples excised from the bulkhead section of the 4.6L Engine Block (Bulkhead A as example here)	79
Figure 4.4a: Description of the fatigue test sample as outlined by ASTM 466-96.	80
Figure 4.4b: Description of the tensile test sample as outlined by ASTM E-8.	80
Figure 4.5: a) The view of the riser in relation to the bulkhead and cylinder cavities, b) a zoom up view of the riser and the sink cavity, c) The riser (from riser D, casting A6) along with graduated cylinder filled with water, d) water deposited within riser open sink until filled to the top of riser. Once riser filled the remaining water is measured and subtracted from the initial amount prior to pouring.	81
Figure 4.6: Calibration Line for the 0.062" Acrolab & 0.042" Low Mass Thermocouple (LMT).	88
Figure 4.7: Picture of the Universal Metallurgical & Analyzer (UMSA) apparatus (Patent number: PCT/CA 02/01903 [91]).	91
Figure 4.8a: Illustration of the quenching setup and a cooling curve showing the effect on solidification at the point labeled as 1.	93
Figure 4.8b: Picture of the UMSA apparatus (Patent number: PCT/CA 02/01903) with suspension apparatus for quenching. Below the UMSA test sample is the salt water quench.	93
Figure 4.9: Cad-Key drawing of the Enviro-AITAS. 1.) Bottom plate, 2.) Lower insulator/TA sample cup holder, 3.) Lower chamber wall, 4.) Lower chamber shroud, 5.) Compressed air flow vent, 6.) Thin walled steel cup, 7.) Upper insulator, 8.) Pressurizing chamber 9.) Back plate attached to pneumatic pump.	95
Figure 4.10: a) Mounted fatigue test sample inside environmental test chamber, b) Close up of mounted fatigue test sample in high temperature 35 KN capacity grips, c) view of the mounted fatigue test sample inside the	

environmental test chamber and temperature controller, d) entire test frame and environmental test chamber in view, e) Load frame, environmental test chamber, Fluke Data logger for strain gauge test sample and Man-Machine-Interface (MMI) and PC for load and strain rate control, f) Mounted strain gauge test sample.	98
Figure 4.11: Rate of heating for the test fatigue sample and the environmental test chamber.....	100
Figure 4.12: a) View of the load frame with mounted tensile test sample with extensometer, and b) Zoom up of the extensometer mounting on the tensile test sample prior to the start of a test.....	101
Figure 5.1(a-f): SEM/BSE micrographs and LOM micrographs for the WA328 alloy (a, c, e) and the WB328 alloy (b, d, f) at low magnification.....	108
Figure 5.1(g-l): SEM/BSE micrographs of the as-cast and heat treated WA328 and WB328 alloys.	109
Figure 5.1m: EDX spectra for the $\text{Al}_{15}(\text{Fe}, \text{Mn}, \text{Cr})_3\text{Si}_2$ script phase seen in Figure 5.1a.....	110
Figure 5.1n: EDX spectra for the Al-Ni-Cu phase seen in Figure 5.1g.....	110
Figure 5.1o: EDX spectra for the Al-Ni-Fe phase seen in Figure 5.1g.....	110
Figure 5.1p: EDX spectra for the Al_2Cu phase seen in Figure 5.1g.	110
Figure 5.1q: EDX spectra for the Mg_2Si script phase seen in Figure 5.1g.	110
Figure 5.1r: EDX spectra for the Al-Ni-Cu phase seen in Figure 5.1l.	110
Figure 5.1 (s-x): LOM micrographs of the as-cast and heat treated WA328 and WB328 alloys.	111
Figure 5.2a: Temperature vs. Time curve obtained by using the UMSA system during heating and cooling cycles for the WA328 Alloy. The main metallurgical reactions during heating and cooling.	113
Figure 5.2b: First Derivative vs. Temperature curves obtained using the UMSA system during heating and cooling cycles for the WA328 alloy. The main metallurgical reactions during heating and cooling.	114
Figure 5.2c: The Enviro-AITAS test sample of the WA328 alloy cast at NEC. The test sample cooling rate was $0.15^\circ\text{C}/\text{sec}$. Identified is #4- α -Al primary dendritic, #5-DCP, #6-Al-Si eutectic plateau, #7-Al-Fe-Mg-Si-Cu reactions & #8-Solidus.....	115
Figure 5.2d: The cooling curve of the WA328 alloy along with the calculated fraction solid curve.....	115
Figure 5.2e: The UMSA cooling curve and first derivative (for the WA328 alloy) of the characteristic temperature values $T_{\text{Al-Fe-Mg-Si-Cu(one)}}^{\text{Al-Fe-Mg-Si-Cu(two)}}$, $T_{\text{E,NUC}}$, $T_{\text{Al-Fe-Mg-Si-Cu(two)}}$ and T_{SOL}	116

Figure 5.2f: The Enviro-ALTAS cooling curve and first derivative (for the WA328 alloy) of the characteristic temperature values $T_{E,NUC}^{Al-Fe-Mg-Si-Cu(one)}$, $T_{E,NUC}^{Al-Fe-Mg-Si-Cu(two)}$ and T_{SOL} .	116
Figure 5.2.1a: The Summary of characteristic temperatures found for WA328 alloy and WB328 alloy using both the UMSA and Enviro-ALTAS platforms.	120
Figure 5.2.1b: The $T_{NUC}^{\alpha DEN}$ and $T_{E,NUC}^{Al-Si}$ seen on a the binary Al-Si are taken from Enviro-ALTAS test samples which were cast along with an OES disk (See <i>Appendix D</i>). The dashed lines represent the compositional limits of Si content defined for the WA328 and WB328 alloys as shown in Table 4.1.	120
Figure 5.2.2a: The results of the partitioned duration (time) range for the WA328 alloy, the WB328 alloy and the W319 alloy, 1) $\Delta t_{SRAN}^{\alpha DEN}$, 2) $\Delta t_{Si SRAN}^{Al-Si}$ & 3) $\Delta t_{SRAN}^{Al-Fe-Mg-Si-Cu}$.	124
Figure 5.2.2b: The results of the partitioned temperature range for the WA328 alloy, the WB328 alloy and the W319 alloy, 1) $\Delta T_{SRAN}^{\alpha DEN}$, 2) $\Delta T_{Si SRAN}^{Al-Si}$ & 3) $\Delta T_{SRAN}^{Al-Fe-Mg-Si-Cu}$.	124
Figure 5.2.2c: The results of the partitioned fraction solid for the WA328 alloy, the WB328 alloy and the W319 alloy, 1) $af_s^{\alpha DEN}$, 2) af_s^{Al-Si} & 3) $af_s^{Al-Fe-Mg-Si-Cu}$.	125
Figure 5.2.2d: Summary of the partitioned cooling rates of the α -Al primary dendritic growth stage, the Al-Si eutectic stage and the Al-Fe-Mg-Si-Cu eutectic stage for the WA328 alloy, the WB328 alloy and the W319 alloy. Also included is the total cooling rate for all three alloys.	125
Figure 5.3a: The four overlays of the UMSA cooling curves of the WA328 alloy. The cooling rate of the quenched event is 60.0°C/sec.	129
Figure 5.3b: The four overlays of the UMSA cooling curves of the WB328 alloy. The cooling rate of the quenched event is 60.0°C/sec.	130
Figure 5.3c: The three overlays of the UMSA cooling curves of the W319 alloy. The cooling rate of the quenched event is 60.0°C/sec.	131
Figure 5.3.1a: WA328 Alloy (100X)	135
Figure 5.3.1b: WB328 Alloy (500X)	135
Figure 5.3.1c: WB328 Alloy (200X)	136
Figure 5.3.1d: WA328 Alloy (500X)	136
Figure 5.3.1e: W319 Alloy (200X)	137
Figure 5.3.1f: W319 Alloy (500X)	137
Figure 5.3.1g: WA328 Alloy (100X)	138
Figure 5.3.2h: WB328 Alloy (500X)	138
Figure 5.3.1i: W319 Alloy (100X)	139
Figure 5.3.2j: W319 Alloy (200X)	139

Figure 5.3.2k: WA328 Alloy (500X).....	140
Figure 5.3.2l: WA328 Alloy (500X).....	140
Figure 5.3.3a: The solidification path that permits the nucleation of polyhedrals of Si. Directly below the equilibrium Al-Si eutectic point (Arrow 1) reflects the path in which polyhedrals nucleate and grow. However the liquid adjacent to the polyhedral will become depleted in Si (Arrow 2). The halo forms around the polyhedral until the composition reaches the skewed couple zone and then stable Al-Si eutectic forms (Arrows 3 & 4).	146
Figure 5.3.3: b) The structure of the WA328 alloy quenched at 575°C seen at. The arrows mark to location of polyhedral Si. The dashed box is the zoomed up to 500X in c) polyhedrals seen in the above micrograph encapsulate both the polyhedral Si crystal and the aluminum α -Al halo.	146
Figure 5.4a: The plot of mean λ_2 ($\pm 8.5 \mu\text{m}$), DCSz ($\pm 9.5 \mu\text{m}$) and Vickers Microhardness (standard deviation listed) of the coarse α -Al dendrites in the as-cast quenched state of the WA328 alloy and the W319 alloy.	149
Figure 5.4b: The change of DAS (λ_2), referenced from various sources listed in Table Six, are displayed in the above graph over large solidification ranges (40 seconds up to 2750 seconds) for the W319 alloy, 356 alloy and WA328 alloy. The best-fitted power equation is identified for each profile.	153
Figure 5.4c: The change of DAS (λ_2), referenced from various sources listed in Table Six, are displayed in the above graph over large cooling rates (0.04°C/sec up to 2.5°C/sec) for the W319 alloy 356 alloy and WA328 alloys. The best-fitted power equation is identified for each profile.	153
Figure 5.5a: At the first quenched stage the dendrite size distribution results a dendrites with a radii of curvature of their tips. In the above case $R_a > R_b$. This drives the diffusion paths of solute elements (Si, Cu and Fe) along the diffusion paths indicated, while solvent element (Al) diffuses along the reverse direction.	157
Figure 5.5b: Near then end of solidification for the WA328 alloy dendrites which were free to ripen for most of the solidification time yield the above case where the thinner dendrite has dissolved at the expense of the larger dendrites. The cells are now larger yielding a radius of curvature of R_c , which is larger than R_a and R_b seen in Figure 5.5a.	157
Figure 5.5c: Total solute content of the W319, the WA328, and the WB328 alloys.	158
Figure 5.5d: The change of λ_2 due to increasing content of a binary alloy of Al with either Si or Cu. The above graph is reproduced from Shivkumar et. al [107]. The best fitted curve along with goodness of fit was not included in the referenced work.	159

Figure 5.6a: The level rule is a basic method to quantify the relative amounts of primary α -Al phase and the Al-Si eutectic phase if the initial alloy composition is known The value are shown in Figure 5.6b.....	161
Figure 5.6b: Summary of the four types of measurements or calculations used to assess the fractional amount of primary α -Al dendrites.	163
Figure 5.6c: The quenched structure at $T_{E, NUC}^{Al-Si}$ for the WA328 alloy.	163
Figure 5.6d: The quenched structure at $T_{E, NUC}^{Al-Si}$ for the W319 alloy.	163
Figure 5.6e: Schematic of dendrites which must experience volumetric contraction on cooling. The smaller the volume of the dendrites, as with the WA328 alloy, the lower the hydrostatic stress is exerted on the liquid and consequently a lowering of the driving force for pore nucleation.	166
Figure 5.6f: The Gas-Shrinkage Map, which illustrates the combination of shrinkage stress, and internal gas pressure that can be relived by heterogeneous nucleation of pores. If the WA328 has a smaller fraction of primary dendrites than the W319 alloy then the contribution of hydrostatic stress towards pore growth will be less.....	167
Figure 5.6g: Microstructure of the W319 alloy (quenched at 555°C) at 50X magnification.....	168
Figure 5.6h: Microstructure of the W319 alloy (quenched at 555°C) at 100X magnification.....	168
Figure 5.7a: The temperature solidification range between the DCP and the nucleation of the Al-Si eutectic, and between the Al-Si nucleation and the Al-Si-Cu eutectic nucleation point, for the Al-7 wt. % Si alloys and the Al-9 wt. % Si alloys having 1, 2 and 4 wt. % Cu. The standard deviation of each mean characteristic temperature point in no higher than ± 3.7 °C.....	171
Figure 5.7b: The apparent fraction solid of the primary dendritic structure, $af_s^{\alpha DEN}$, and the apparent fraction solid of the Al-Si eutectic, af_{sAl-Si} , for the Al-7 wt. % Si alloys and the Al-9 wt. % Si alloys having 1, 2 and 4 wt. % Cu. The standard deviation of each mean characteristic fraction solid point is no more than ± 2.3 %.	172
Figure 5.8.1a: Cooling curves of the Al-9wt.%Si-1wt.%Cu alloy and the Al-9wt.%Si-4wt.%Cu alloy [19, 20]	175
Figure 5.8.1b: Cooling curves of the Al-7wt.%Si-1wt.%Cu alloy and the Al-7wt.%Si-4wt.%Cu alloy [19, 20]	175
Figure 5.8.1c: Relationship between Cu based phase(s) area fraction and SDAS for plates with 7wt%Si in the as-cast condition [19, 20].	176
Figure 5.8.1d: Relationship between Cu based phase(s) area fraction and SDAS for plates with 9wt%Si in the as-cast condition [19, 20].	176
Figure 5.9a: Labelling of partitioned thermal analysis parameters along a temperature gradient.....	180

Figure 5.9b: The cross-section of a simple cast section where one side is the Al-9wt.%Si-1wt.%Cu alloy (WA328) and the other side is the Al-7wt.%Si-4wt.%Cu alloy (W319).	181
Figure 6.1.2a: Bulkhead E with adjoining riser. Note the asymmetry of the riser sink towards the right side of the bulkhead. This implies that the right side of the bulkhead drew more liquid feed than the left side. The dash line delineates the boundaries between left and right bulkhead and riser.	189
Figure 6.1.2b: The level of mean porosity found on both the right and left side of each bulkhead of the 4.6L engine block cast in the listed conditions.	189
Figure 6.1.2c: Summary of the Mean Pore Diameter found in Bulkhead A through to E of the 4.6L engine block.	190
Figure 6.1.2d: Summary of the Maximum Pore Diameter Found in Bulkheads A through E of the V8 engine block. The dashed line with an arrow on the right side represents the maximum pore diameter allowable under the WSE-M2A151-A3 specification.	190
Figure 6.1.2e: The section risers of both the W319 alloy and the WA328 alloy, both in the non-grain refined condition. The asymmetry of the riser volume sink, seen in risers B, C, D, E, is present irrespective of alloy chemistry.	191
Figure 6.1.2f: The summary of volume of riser sink data for both the WA328 and the W319 alloys.	191
Figure 6.1.2g: A schematic vertical cross-section (<i>as shown in the picture of Figure 6.1.2a</i>) showing the configuration between the riser and bulkheads B, C and D. Bulkhead B is the critical bulkhead requiring maximum soundness for the running engine operation. Risers B, C, D, and E contain the asymmetrical nature of the sink. The arrows represent the feed paths that would occur around the crankshaft passage way.	192
Figure 6.1.2h: The difference in mean area fraction percent porosity found on the left side versus the right side of each bulkhead section for the five alloy conditions investigated.	192
Figure 6.2a: The total cooling rate ($\approx (T^{\alpha\text{DEN}}_{\text{NUC}} - T_{\text{SOL}})/(t^{\alpha\text{DEN}}_{\text{NUC}} - t_{\text{SOL}})$) as recorded by each thermocouple as a function of distance from the riser thermocouple. Repeated four times.	196
Figure 6.2b: The layout of the In-situ thermal analysis method used for the 4.6L engine block (Bulkhead E) and the locations from which λ_2 was measured.	196
Figure 6.4.1a: The fatigue staircase results of the bulkhead sections taken from the W319 alloy [18, 114] and the WA328 alloy all cast from the V8 engine block. The arrow signifies the mean HCF stress required for the WSE-M2A151-A3 specification.	202

Figure 6.4.2a: Sample # 3 failed at a stress of 75.8 MPa & having a life of 2,108,933 cycles.....	206
Figure 6.4.2b: Sample # 8 failed at a stress of 75.8 MPa & having a life of 4,933,391 cycles.....	206
Figure 6.4.2c: Sample # 13 failed at a stress of 79.2 MPa & having a life of 385,668 cycles.....	206
Figure 6.4.2d: Sample # 11 failed at a stress of 75.8 MPa & having a life of 6,996,681 cycles.....	206
Figure 6.4.2e: Sample # 22 failed at a stress of 79.1 MPa & having a life of 4,391,998 cycles.....	206
Figure 6.4.2f: Sample # 24 failed at a stress of 75.8 MPa & having a life of 789,774 cycles.....	206
Figure 6.4.2g: (SEM/SE) micrograph taken from the fatigue test sample fracture surface. The stress was at 79.2 MPa with a life of 385,668 cycles. The dash boxes are shown in high magnification in Figures 6.4.2h and 6.4.2i.	207
Figure 6.4.2h: (SEM/SE) micrograph showing subsurface pores located within the fractured region. The dashed region is shown in Figure 6.4.2j.....	207
Figure 6.4.2i: (SEM/SE) micrograph showing striations and a possible oxide within the fatigue fractured region.....	208
Figure 6.4.2j: (SEM/SE) micrograph showing the fast fracture (tensile overload) region just adjacent to the transition line seen in Figure 6.4.2g.	208
Figure 6.4.2k: (SEM/SE) micrograph taken from the fatigue test sample fracture surface. The stress was at 75.8 MPa & having a life of 4,933,391 cycles. The dash boxes are shown in high magnification in Figures 6.4.2l, 6.4.2n and 6.4.2p.....	209
Figure 6.4.2l: (SEM/SE) micrograph showing subsurface pores located within the fatigue fractured region.....	209
Figure 6.4.2m: (SEM/SE) micrograph showing subsurface pores located within the fractured region. The dashed region is shown in Figure 6.4.1o.....	210
Figure 6.4.2n: (SEM/SE) micrograph showing shrinkage pore located within the fatigue fractured region approximately 1mm from the surface and is possibly connected to the surface pore seen in Figure 6.4.1l & 6.4.1m.....	210
Figure 6.4.2o: (SEM/SE) micrograph showing striations (~ 5 μ m spacing) within the fatigue fractured region.....	211
Figure 6.4.2p: (SEM/SE) micrograph showing the fast fracture (Tensile overload) region just adjacent to the transition line.	211
Figure 6.4.2q: (SEM/SE) micrograph taken from the fatigue test sample fracture surface. The stress was at 79.2 MPa with a life of 385,668 cycles. The dash boxes are shown in high magnification in Figures 6.4.2r and 6.4.2u.	212

Figure 6.4.2r: (SEM/SE) micrograph showing subsurface pores located within the fatigue fractured region.	212
Figure 6.4.2s: (SEM/SE) micrograph showing striations (~ 3-5 μm spacing) within the fatigue fractured region.	213
Figure 6.4.2t: (SEM/SE) micrograph showing Si platelets within the fatigue fractured region. Also seen in the micrograph are striations measuring about 5 μm	213
Figure 6.4.2u: (SEM/SE) micrograph showing the fast fracture (Tensile overload) region just adjacent to the transition line seen in Figure 6.4.2q.	214
Figure 6.4.3a: The Mean Area Fraction Porosity of the five bulkhead sections plotted against the mean HCF for the three conditions shown in Figure 6.4.1a.	218
Figure 6.4.3b: The Maximum Pore Diameter of the five bulkhead sections plotted against the mean HCF for the three conditions shown in Figure 6.4.1a.	218
Figure 6.4.3c: Summary of the relationship between HCF and the value of the temperature partitioned parameters. 1) $\Delta T^{\alpha_{\text{DEN}}}_{\text{SRAN}}$, 2) $\Delta T^{\text{Al-Si}}_{\text{SRAN}}$ & 3) $\Delta T^{\text{Al-Fe-Mg-Si-Cu}}_{\text{SRAN}}$	219
Figure 6.4.3d: Summary of the relationship between HCF and the value of the partitioned fraction solid parameters. 1) $a_f^{\alpha_{\text{DEN}}}$, 2) $a_f^{\text{Al-Si}}$ & 3) $a_f^{\text{Al-Fe-Mg-Si-Cu}}$	219
Figure 6.4.3e: The Gas-Shrinkage Map, modified from Figure 5.7f shows the effect of adding a master alloy addition which in turn adds more Sr-based inclusions suitable to nucleate pores during solidification.	220
Figure 6.4.3f: The Gas-Shrinkage Map, modified from Figure 5.7f shows the effect of adding a master alloy addition which in turn adds more Ti and/or B based inclusions suitable to nucleate pores during solidification.	221
Figure 6.5a: The side view of risers B, C and D of the 4.6L engine block castings in the Al-9wt.%Si-1wt.%Cu alloy and the production W319 alloy. The hot tears were only evident in the W319 alloy and are indicated by arrows in the above picture.	224
Figure 6.5b: Picture of a angle view and side view of riser B from a W319 4.6L engine block illustrating the rim, flanging, arch and riser sink.	225

List of Tables

Table 1.0: The Ford Engineering Material Specification WSE-M2A151-A3. * indicates the portion of the specification used in this dissertation to evaluate the compliance of WA328 and WB328 V8 engine blocks to WSE-M2A151-A3.	5
Table 2.0: AA grades of the 319 alloy [30] and the W319 alloy (Ford Engineering Material Specification WSD-M2A151-A3, [17]). Chemical levels are in wt.%.	14
Table 3.0: Principle discontinuities that nucleate cracks in A356 alloy with Sr modification. The axial fatigue samples were tested at constant amplitude 133 MPa ($R = 0.1$) by Gall et. al. [21]. Si modification level not specified but the Sr addition to the 356 alloy melt was 100 ppm.	57
Table 4.0: Comparison between the AA version and the hybrid version of the 319 and 328 alloys. Wabash Alloys supplied the incoming WA328 and the WB328 alloy ingot as pre the limit specification listed in this table.	72
Table 4.1: Cost differential of the alloy per 50 million pounds. The cost of 50 million pounds of W319 alloy is \$35,000,000.00.	72
Table 4.2: The summary of the heat treatment scheme used for the WA328 alloy, WB328 alloy and the W319 alloy.	74
Table 4.3: The identification of the 4.6L engine blocks used for the study along with the test sample type excised from the bulkhead sections.	77
Table 4.4: Summary of the total volume of all risers of the 4.6L engine block.	81
Table 4.5: Summary of the depth of penetration with an incident beam energy of 20 KeV.	83
Table 4.6: Values of the linear fitted lines and the respective goodness of fit parameter.	88
Table 5.0: Average cast chemistry from OES, wt.%.	102
Table 5.2.1a: The results of the Silicon Equivalent (Si_{EQ}) Calculation (using the compositions measured by OES from the disk test samples) and measured characteristic temperature values from the Enviro-ALTAS and the UMSA test. The results are based on 6 repeats.	119
Table 5.2.3: Summary of the characteristic temperature points from analysis of the heating portion of the UMSA thermal curve.. The heating rate for all three alloys was 0.50°C/sec. The results are based on 6 repeats	127
Table 5.3: The temperature of the quenched test alloy samples.	128
Table 5.3.1: Solidification Sequence Summary of the WA328 alloys cast in 4.6L engine block mould. The same solidification sequence exists for the	

WB328 alloy except for the slight change in characteristic temperatures (see Appendix F).....	143
Table 5.4a: Coefficients associated with the λ_2 at a quenched stage of solidification and full solidification time. Its important to point out that the power equation that has been reported within literature is valid even for partially solidified structures.....	149
Table 5.4b: Summary of Fully Solidified Test Sample Conditions used in this work and in the referenced work. The data was used to help compile the results seen in Figures 5.4c and 5.4d.....	152
Table 5.5: The calculated equilibrium partition coefficient, k, The slope of the liquidus line for Si, Cu, Fe, Mg and Mn.	158
Table 5.6: Hydrogen Solubility as calculated by the AISCAN approximation and assuming a melt temperature of 760°C.	167
Table 6.0: The radiographic results for the 4.6L engine block casting cast in a WA328 alloy and the WB328 alloy. The casting x-ray is identified and the date on which radiographic examination was preformed is also indicated. Refer to Figure 4.0, Chapter Four, for the layout of where radiographic section are taken on the 4.6L engine block.	184
Table 6.1: Summary of monotonic test results from the 4.6L engine block cast in the W319 and WA328 alloy after heat treatment.....	200
Table 6.2: Vickers Microhardness from the left Side of the Bulkhead for the W319 alloy, the WA328 alloy and the WB328 alloy. The results contained herein result from an average of 6 indentations.	200
Table 6.3: Brinell Hardness measured on fatigue test bars excised from the left side of Bulkhead C of the 4.6L engine block after heat treatment.	200
Table 6.4: Summary of the mean HCF stress found for the investigated conditions along with Ford Materials Engineering Specification [29].	202

Chapter One

Introduction to Al-Si Cast Alloys

1.0 Use of Al-Si Casting Alloys in Industry

Al-Si cast alloys have numerous applications in the automotive and aerospace industries. The use of aluminum cast alloys is expected to increase in these industries in the near future. The reason for this is that these alloys have many desirable qualities such as a high strength-to-weight ratio, good castability, excellent corrosion resistance, cosmetic surface quality, resistance to hot tearing, relatively good thermal conductivity, relatively lower melting temperatures, good machinability and good weldability. Another important consideration, other than being lightweight, is that aluminum alloys are comparatively easy to recycle, which is becoming more important in this era of recyclability and environmental awareness [1, 2, 3].

The Al-Si family of alloys are extremely important in the aluminum casting industry since they make up 85% or more of the total aluminum cast parts produced [2]. These alloys usually contain between 5.5 and 12% silicon, and the most common alloying elements are copper and magnesium [2, 3].

Alterations to the microstructure of an Al-Si alloy, usually composed of an α -Al dendritic aluminum matrix with the subsequent formation of the Al-Si eutectic structure located in the remaining spaces, can be achieved mainly via a change in cooling rate, or by the addition of

certain master alloys to the alloy melt prior to casting. Boron and titanium boride compounds in the aluminium melt can increase the number of heterogeneous nucleation sites and refine the grain size [2, 3, 4]. The addition of sodium or strontium to the melt can modify the silicon of the eutectic structure from an acicular to a fibrous morphology [5-12]. Additions of strontium reduce solution heat treatment times [9, 12]. An increase in cooling rate can result in similar alterations to the microstructure. This variability of microstructure for the same alloy type via cooling rate or master alloy additions allows aluminium-silicon alloys to achieve a myriad of physical properties, giving them a wide range of uses in the automotive, aerospace, and other industry sectors.

The most deleterious microstructural constituent in Al-Si cast alloys is the presence of voids known as porosity. Porosity usually occurs in Al-Si alloys through the evolution of segregated hydrogen gas and/or liquid feeding difficulties in the mushy zone during solidification. Another factor that can control cast structure is the relative shape of Si phases (part of the main Al-Si eutectic), the size and shape of Fe, Cu, and Mg phases, the condition of the dendritic matrix, and finally the relative cleanliness of the melt [2, 5, 10-14].

The aerospace industry, which uses primary stock cast materials, has driven a large part of this new knowledge on achieving lower porosity in cast parts. Research in aluminium cast aerospace parts has been ongoing since the Second World War. For the automotive industry, the increase in cast aluminium use has occurred in the last two decades, and secondary stock aluminium is used to cast these parts.

It should be pointed out that secondary stock materials have technical issues that do not face primary casting materials such as the effect of residual impurities on the role of pore development during solidification [1, 3, 6, 11, 14-16].

Currently the methods of assessing the propensity for stable pore nucleation and growth, as-cast soundness, and the effect porosity has on cast durability represents the most active area of research within the automotive casting industry. This dissertation is a contribution to this intensely studied area of Al-Si casting research.

1.1 The Casting of Aluminum Engine Blocks

The V8 engine block cast at the NemaK Windsor Aluminum Plant (WAP) has to meet or exceed the Ford Engineering Material Specification WSE-M2A151-A3 [17] in order to be deemed acceptable as a powertrain component. Table 1 shows the outline of the WSE-M2A151-A3 Specification. The current mean High Cycle Fatigue (HCF) stress sustainable in the V8 engine block casting made using the Ford/Cosworth process is 53.8 MPa [18] which is lower than specified by WSE-M2A151-A3. The HCF properties of engine blocks have been found to be controlled by the level of the porosity contained within the bulkhead section [19-23].

Currently most Light Trucks and Sport Utility Vehicles use cast iron engine blocks which in turn add weight to the powertrain and thus reduce fuel efficiency. However, the maximum HCF stress that can be sustained by cast iron engine blocks is superior to what can be achieved using current W319 alloy engine blocks.

The NSERC/Nemak-Ford/University of Windsor Industrial Research Chair (IRC) in Light Metals Casting Technology has undertaken the task of improving engine block properties including durability. The primary focus of this dissertation is to understand the role of both Si and Cu in the nucleation and growth of pores during solidification. Reducing the severity of porosity improves HCF properties.

Six alloy compositions, 7 and 9 wt. % Si alloys each having 1, 2 and 4 wt. % Cu, were prepared and cast into sand wedges at the Nemak Engineering Centre (NEC). The overall level of porosity, in terms of pore diameter and area fraction was measured via Image Analysis (IA) methods for the six alloy compositions [19]. The Al-9wt.%Si-1wt.%Cu alloy was found to contain the lowest overall level of porosity [19, 20]. HCF analysis of the wedge castings, at a full reversed cyclic stress ($R = -1$) of 103 MPa, is shown in Figure 1.0, confirmed that the Al-9wt.%Si-1wt.%Cu alloy has a higher durability [20].

This dissertation will be an extension of the aforementioned work on wedge castings, where analysis will be made of the performance of the Al-9wt.%Si-1wt.%Cu alloy in terms of its castability and HCF performance in a shape casting (V8 engine block). Also, because this alloy is unreported within the literature and is not used as a production cast alloy, many of the metallurgical features that are well known for the type 319 and 356 alloys are unknown for the Al-9wt.%Si-1wt.%Cu alloy.

Table 1: The Ford Engineering Material Specification WSE-M2A151-A3. * indicates the portion of the specification used in this dissertation to evaluate the compliance of WA328 and WB328 V8 engine blocks to WSE-M2A151-A3.

<i>Property</i>	<i>ASTM Standard</i>	<i>Value of Specified property</i>
*SDAS (λ_2)	ASTM E 155	Average value of $\lambda_2 \sim 50 \mu\text{m}$ (10 measurements at 100X) No value of $\lambda_2 > 60 \mu\text{m}$
*Porosity	ASTM E 3	No larger than 1% (from a field at 100X) No pore size $> 750 \mu\text{m}$
*Ultimate Tensile Strength	ASTM B 557	225 MPa
*Yield Stress (0.2% proof)	ASTM B 557	200 MPa
*Total Elongation	ASTM B 557	1.0%
Compressive Yield Strength	ASTM E 9	200 MPa
Shear Stress	ASTM B 769	180 MPa
*Hardness HBS 10/500	ASTM E 10	85-115 HBS500
*Fatigue Limit at 10^7	ASTM E 466	65 MPa
*Modulus of Elasticity	ASTM B 557	70 GPa
Coefficient of Linear Expansion	ASTM E 228	$23.1 \times 10^{-6}/\text{K}$ (20-250°C)
Density	ASTM B 311	2.760 g/cm^3

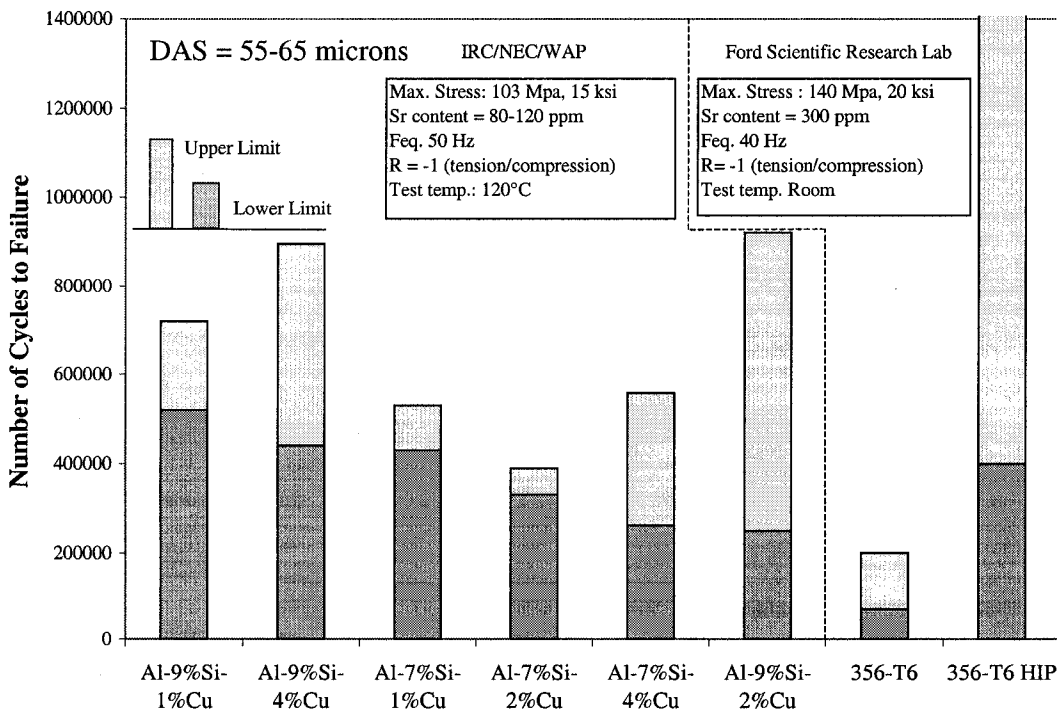


Figure 1.0: Summary of the HCF results of the six alloy compositions investigated by the IRC [20], along with HCF data of 356 alloy wedges from Boileau et al. [21].

1. 1 Focus of this Study

This dissertation will investigate the Al-9wt.%Si-1wt.%Cu alloy's castability, structural integrity as an engine block compliant with the Ford Engineering Material Specification WSE-M2A151-A3 [17], and aspects of its fundamental metallurgy. No published information pertaining to the in-depth analysis of the Al-9wt.%Si-1wt.%Cu alloy exists other than what has been published in this dissertation or by the IRC [19, 20]. Throughout this dissertation the Al-9wt.%Si-1wt.%Cu alloy is known by two Fe based variants: the WA328 alloy (0.40wt.% Fe) and the WB328 alloy (0.80wt.% Fe). The objectives of this dissertation are:

- 1) To provide a comprehensive and concise literature review on the solidification characteristics of Al-Si alloys (*Chapter Two*) and on the fatigue characteristics of Al-Si alloys (*Chapter Three*).
- 2) To outline the use of existing technical platforms and the new and novel technology platforms and interpretive methods developed by the IRC to analyze the fundamental aspects of the metallurgy of the WA328 and WB328 alloys. This analysis will be presented in *Chapter Four*. Details of the interpretive methods of cooling curves and fraction solid curves are shown in Appendix A and the fraction solid calculation is shown in Appendix B.

- 3) To establish a list of the observable phases in the WA328 and WB328 alloys using the methods of Light Optical Microscopy (LOM) and Scanning Electron Microscopy (SEM). This analysis will be presented in *Chapter Five*.
- 4) To use two thermal analysis platforms (Universal Metallurgical Simulator & Analyzer (UMSA) and the Environmental Thermal Analysis System (Enviro-ALTAS)) and the Silicon Equivalent (Si_{EQ}) Method to establish the characteristic temperatures for the WA328 and WB328 alloys. This analysis will be presented in *Chapter Five*.
- 5) To use the UMSA to assess the solidification sequence and fraction solid of the WA328 alloy and the WB328 alloy. This can be done by quenching the UMSA Test Sample at strategic solidification stages between the liquidus and solidus. This analysis will be presented in *Chapter Five*.
- 6) To develop interpretive methods of cooling curves and calculated fraction solid curves, which can indicate the volume fraction of α -Al primary dendrites, the Al-Si eutectic and the complex eutectics involving Al_2Cu , Mg_2Si , Al_5FeSi , etc., in the investigated alloys. This analysis will be presented in *Chapter Five*.
- 7) To use the interpretive methods outlined in *Objective #4* to develop a construct of the evolving mushy zone for several Al-based casting alloys investigated in this dissertation. From the development of the mushy zone through the use of interpretive

thermal analysis and fraction solid partitioning techniques a plausible kinetic driving force for the role of Si and Cu on pore development in cast structures will be identified. This analysis will be presented in *Chapter Five*.

- 8) To study the role of α -Al dendritic growth and coarsening kinetics towards the porosity formation and the mechanical performance in the W319 alloy, the WA328 alloy and the WB328 alloy. This analysis will be presented in *Chapter Five*.
- 9) To cast the WA328 alloy and the WB328 alloy into V8 engine block moulds, heat treat at B & W Heat Treat Limited, and then evaluate these V8 engine blocks in compliance with Ford Engineering Material Specification WSE-M2A151-A3 and additional metallurgical characteristics deemed necessary to fully explore the WA328 and WB328 alloys castability as an engine block. This analysis will be presented in *Chapter Six*.
- 10) To assess the High Cycle Fatigue (HCF) for the WA328 alloy and compare it to the W319 alloy, which is in three conditions: with in-furnace Sr; no grain refiner; and with in-mould grain refiner. This analysis will be presented in *Chapter Six*.
- 11) To correlate HCF characteristics to the level of porosity in the bulkhead section of the V8 engine block and in turn correlate the porosity and HCF characteristics to the partitioned thermal analysis and partitioned fraction solid parameters. This analysis will be presented in *Chapter Six*.

Chapter Two

Literature Review on Cast Solidification

2.0 Quiescent Methods of Liquid Metal Filling during the Casting Operation

There are several variations of quiescent liquid metal filling processes utilized by several cast houses worldwide. Quiescent mould filling methods are the main driving force for the Tilt Pouring Permanent Mould (TPPM) casting process, Reduced Pressure Permanent Mould (RPPM) casting process, Reduced Pressure Sand (RPS) casting process, and Counter Gravity (CG) casting process. The last two processes are mainly devoted to the production of complex aerospace A356, A357, D357 aluminum sand castings [24-28] requiring improved fatigue performance. However for 319 type alloys the TPPM or the RPPM casting process is used since they are better automated for high production. The final quiescent cast mould fill method is the Cosworth Precision Sand Process (CPSP) used mainly for sand automotive castings in Nemak and Ford aluminum casting plants [29].

2.0.1 The Cosworth Precision Sand Process (CPSP)

The CPSP, used at Nemak's Windsor Aluminum Plant (WAP), at the Nemak Engineering Centre (NEC) and at the Ford Motor Company's Cleveland Aluminum Casting Plant (CACP) is an automated method of quiescent metal filling into the sand mould. The

CPSP was developed in the 1970s as a casting process used to make highly specialized Formula One engine blocks. The virtues of the CPSP over other non-quiescent mould filling casting techniques is that the yields are typically 85% or better and that the weight of the castings is up to 10 to 15% lighter [29]. Continuous improvements of the CPSP method is ongoing; leading towards even higher casting yields and reduced cast weight.

2.0.1.1 Sand Type Used for the CPSP

Zircon sand is used at WAP and NEC while silica sand is used at CACP to make engine block sand packages. Zircon sand is considerably more expensive than silica sand, however the cost of using zircon sand is off-set by the fact that its reclamation is near 99.8%, where the remaining 0.2% is lost as fines. In many cases silica sand is difficult to reclaim. The high reclamation rate allows WAP to minimize its waste substantially when compared to other automotive sand foundries. Zircon sand has a much lower thermal expansion which provides exceptional accuracy and minimal core distortion (less than 0.05%), and its heat capacity provides faster alloy cooling than silica sand.

2.0.1.2 Melt Treatment at WAP

The type of metal used at WAP which produces the 2.5L, 3.0L, 3.9L and the 4.6L engine blocks is a non-grain refined and non-Sr modified W319 alloy (Chemistry shown in Section 2.1). The W319 is brought into the foundry in ingot form and is charged into the reverb furnace. The W319 alloy is not grain refined due to the contribution of Ti to the residual buildup that clogs the pump orifice. Under advisement by the IRC Sr is no longer

added due to the fact that Sr leads to an increased propensity for shrink porosity in the finished casting. Finally chlorine was used as a degassing process for the removal of hydrogen from the melt. However this also contributed to the pump clogging occurrence and has since been replaced with argon degassing [30]. An illustration of this process is shown in Figure 2.0a [24].

The assembled sand mould is then delivered to a 4 station index rollover system. The 4 station index rollover system has 4 fixtures which hold the sand package, and it advances the package to the pump nozzle connecting it to the main side sprue. The metal is drawn from a holding well via an electromagnetic pump which is submerged at the middle of the pump well (see Figure 2.0b [24]). This ensures that the cleanest metal is drawn into the mould.

2.0.1.3 Casting of an Engine Block via CPSP

The electromagnetic pump programmable logic control (PLC) system controls the fill rate of the molten metal delivered into the mould with the use of a feedback system. The fill rate and duration at which liquid metal is delivered into the mould is cast part dependent. For example the 4.6L engine block requires a fill time ranging from 20 to 22 seconds. The fill rate is monitored by a parallel plate capacitor setup where one side of the capacitor acts as a stationary antenna and the other is the liquid aluminum within the mould. As the mould fills the distance between the plate and the aluminum in the mould changes, thus changing the capacitance. If the fill rate is too fast (i.e. possible turbulent

flow) or too slow (i.e. cold shuts) the computer control console will adjust the voltage to the pump accordingly to achieve the predetermined fill rate [24].

The sand package containing the solidified castings is then transported to the Thermal Sand Removal (TSR) furnace where the zircon sand is reclaimed. After the sand is reclaimed and partial solutionizing occurs the casting is air quenched. The air quench is preferred over a water quench since air quench induces less distortion in the casting, preserves the integrity of the cast iron liners and deters the formation of Zr based sludge from returning to the remelt. The risers are then removed from the casting and it is then shot blast to remove the remaining sand.

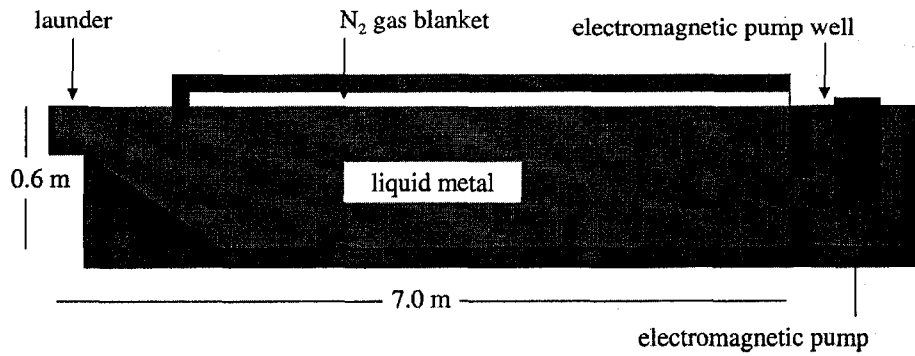


Figure 2.0a: Schematic depicting the basic functions of the liquid processing of the W319 alloy. Schematic provided by G. Byczynski [24].

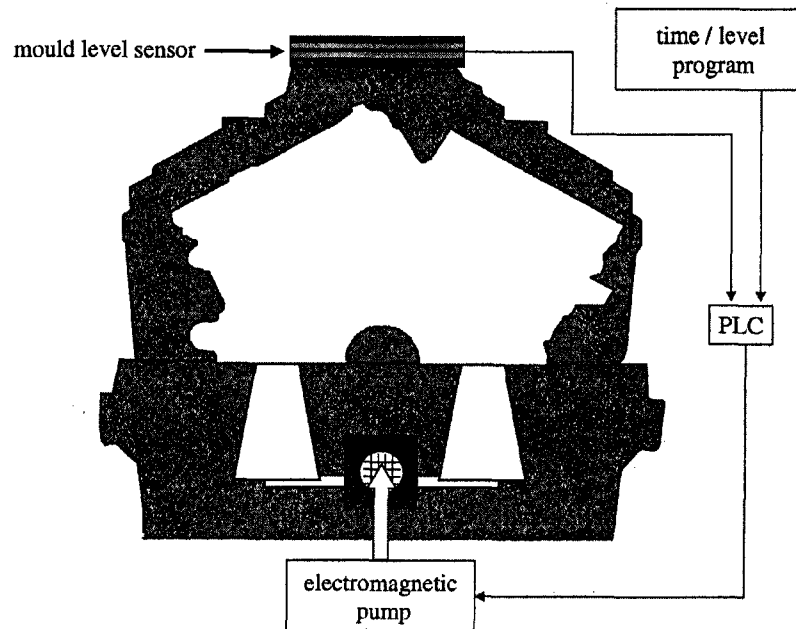


Figure 2.0b: Schematic depicting the zircon sand mould and mould cavity reflecting the engine block casting (3.0L V6). The configuration of the electromagnetic pump orifice and the antenna system which monitors filling rate is shown. Schematic provided by G. Byczynski [24].

2.1 Chemical Composition of the AA319 & W319 Alloys

As stated previously the alloy currently being used to cast aluminum engine blocks at WAP is the W319 alloy. The W319 alloy is a high Si hybrid version of the AA (*Aluminum Association*) designation 319 alloy [31]. Other differences in the W319 alloy when compared to the various AA 319 grades is the lower Fe content (0.40 wt % max) and the lower Mg content (0.05 – 0.50 wt. %). Table 2.0 lists the overall chemistry of the W319 (as listed in the Ford Engineering Material Specification WSD-M2A151-A3 [17]) and the AA grades of the 319 alloy. It is perceived that the combination of higher Si and lower Fe provides better castability and mechanical properties in sand cast automotive parts produced using the CPSP.

Table 2: AA grades of the 319 alloy [31] and the W319 alloy (Ford Engineering Material Specification WSD-M2A151-A3, [17]). Chemical levels are in wt.%.

<i>Alloy</i>	<i>Si</i>	<i>Fe</i>	<i>Cu</i>	<i>Mn</i>	<i>Mg</i>	<i>Ni</i>	<i>Zn</i>	<i>Ti</i>
319.0	5.5-6.5	1.0	3.0-4.0	0.5	0.1	-	1.0	0.25
319.1	5.5-6.5	0.8	3.0-4.0	0.5	0.1	-	1.0	0.25
319.2	5.5-6.5	0.6	3.0-4.0	0.1	0.1	-	0.10	0.25
A319.0	5.5-6.5	1.0	3.0-4.0	0.5	0.1	-	3.0	0.25
A319.1	5.5-6.5	0.8	3.0-4.0	0.5	>0.1	0.35	3.0	0.25
B319.1	5.5-6.5	1.2	3.0-4.0	0.8	>0.1	0.35	1.0	0.25
B319.2	5.5-6.5	0.9	3.0-4.0	0.8	>0.1	0.35	1.0	0.25
W319	6.5-8.0	0.4	2.2-3.8	0.2-0.3	0.05-0.50	0.30	1.0	0.25

2.1.1 Iron

One of the principal impurity elements in many secondary Al-Si alloys is Fe. Fe results in the formation of brittle intermetallic compounds. The occurrence of Fe based intermetallics is less in primary Al-Si alloys since Fe levels are kept below 0.20 wt %. In secondary stock Al-Si alloys the Fe levels range from 0.20 wt % to 1.0 wt % [31].

Depending on the cooling rate, Fe levels can lead to deleterious secondary phase constituents within the cast structure at about 0.70 wt. % [31-36]. In Al-Si casting alloys, Fe reacts with Al and Si to form a thermodynamically stable phase having the stoichiometry of Al_5FeSi , also known as the β -phase [31-38]. The morphology of this phase is in platelet form, but seen as needle-like in a two-dimensional metallographic cross-section [31]. As a consequence, one of the major difficulties with Al-Si alloys is that Fe, if present in large enough quantities, can lead to this particular intermetallic having deleterious effects on the mechanical properties of the cast part [31, 33, 37, 38]. In addition, these compounds are very hard with the result that machining cast parts with relatively high Fe content can be difficult, resulting in high casting finishing costs [31].

2.1.2 Manganese

Manganese has very little solubility in Al and as a consequence Mn in the remaining liquid will combine with Fe, Si and Al to produce a different Fe-bearing intermetallic having the stoichiometry $\text{Al}_{15}(\text{Mn,Cr,Fe})_3\text{Si}_2$, also known as the α -phase [33, 36, 37, 39]. The morphology is script shape, but the phase has been shown to have other morphologies such as blocky and dendritic [33]. The commonly accepted ratio of Mn to Fe to adequately

convert β -phase to α -phase is 1 to 2 [36, 39]. Overall the α -phase is much more compact and less detrimental to the mechanical properties and slightly improves feeding into interdendritic channels.

2.1.3 Zinc

15 years ago, Resch et al. [40] performed a study on the mechanical properties of 319, 332 and 333 alloy samples having elevated Zn levels. The result was that incremental adjustments of Zn from acceptable Aluminum Association limits (less than ~1.0 wt. % [31]) up to 4.1 wt. % actually slightly improved tensile properties, while ductility was largely unaffected in the T5 and T6 conditions. The final result was that the lower limit of Zn in these secondary alloys had no real basis in mechanical property deterioration. It was suggested that since cast houses would find little supporting evidence of the deleterious effects of elevated Zn on mechanical properties, that a re-evaluation of a realistic upper limit of Zn in 3xx.x alloys needed to be determined.

Mackay et al. [41] investigated the role of Zn in a base 356 alloy with residual levels up to 15wt.% Zn. This research was conducted to better understand the basic metallurgy and solidification kinetics of Al-Si-Zn-Mg alloys. The work was spurred by the previous, but scanty reports, of superior mechanical properties attained by Al-Si alloys containing unusually high levels of Zn. Thermal Analysis (TA) was used by the authors to better understand the solidification kinetics of an Al-7wt.% Si-0.30wt.% Mg alloy having incremental Zn levels between approximately 0 wt.% and 15 wt.%. The findings of this work indicated that the behaviour of Al-Si-Zn alloys is similar to that of 3xx.x alloys.

That is, they solidify as primary dendritic structures with Al-Si eutectic phases. Other secondary phase reactions are script and needle phases. These phases grow more numerous after the Al-Si eutectic reaction when Zn levels increase.

2.1.4 Bismuth

Recently Bi levels have been detected in increasing levels in secondary stock materials. Bi most likely originates from the recycling of Bi containing wrought Al alloys [42, 43]. With improved recycling a wider variety of wrought and cast alloys are used as raw materials to make specific secondary alloy grades. AA319, W319 and 356 have been reported to have excessive Bi that can nullify Sr's ability to modify Si particles during solidification. Thus it has been recommended that Bi levels be reduced so the Si modification is not affected. One report found that Ca additions to Al-Si-Cu melts could reduce Bi levels by forming a Bi-Ca compound that would settle to the bottom of the melt and thereby remove Bi from the mid to upper portions of the melt that are used for casting [43].

2.1.5 Nickel

Ni is commonly added to some aluminum casting alloys to increase tensile strength, yield strength and reduces elongation at room temperature [3, 31, 44]. The Al_3Ni compound forms within the cast structure improving elevated temperature strength for high temperature applications ranging between 250°C and 375°C [31]. Another study was conducted where between 0.2wt.% and 0.5 wt.% Ni was added to a Al-7wt.%Si alloy. The Al-7wt.%Si alloy containing up to 0.2 to 0.3 wt.% Ni resulted in an increase in room temperature yield and

tensile properties by 50 MPa over the base Al-7wt.%Si alloy [44]. However beyond 0.3 wt.% a negligible improvement in properties was obtained. The most detrimental factor for wider use of Ni in Al-Si alloys is the cost.

2.1.5 Strontium

In recent years Sr has grown as a Si modifier. Sr is usually introduced as a master alloy to the alloy melt prior to producing the cast product. Sr modifies Si through the twin plane poisoning technique leading to a fibrous Si structure [1-6, 9-12, 34, 35, 45]. Sr however has a fairly deleterious effect on mechanical properties. As Sr content increases the level of porosity increases [2, 4, 5, 6, 45]. This has resulted aluminum castings made for aerospace applications without Sr in order to achieve the highest possible cast mechanical properties [2, 45].

The main purpose of using Sr has been to take advantage of the fact that fibrous Si leads to a reduced solution duration (to achieve Si spherodization) and to reduce machining costs [1-3, 5, 6, 35].

2.1.6 Antimony

Unlike Sr, Sb refines the size of Si particles as opposed to modifying Si particle structure [1, 2, 5, 6, 10, 31, 45]. Sb is very popular in Japan and is used to refine the Si structure of aluminum engine blocks and cylinder heads. As these cars are recycled in North America the Sb levels in some secondary batches produced in secondary smelters may be higher than usual. Once a melt containing excess Sb is Sr modified a Sr-Sb based compound will form.

The only one that has been identified is the $\text{Mg}_2\text{Sb}_2\text{Sr}$ intermetallic, which has a density of 4.2 gm/cm^3 and sinks to the bottom of the melt upon formation [2, 12]. Thus Sr becomes depleted from the melt and modification becomes very difficult to achieve. The only way to get a desired modification from these melts is to add a sufficient level of Sr to react with most of the Sb, so the remainder can modify the Si particles.

2.1.7 Sodium

Na has been used in the past as a Si particle modifier. Na is used less today due to its relatively rapid fading in comparison to Sr [2, 3, 10, 12, 30, 45]. Secondary stock materials can have elevated levels of Na in melts. Limited research into Sr-Na reactions found that no compounds containing both modifying elements exists in cast Al-Si melts. In fact it has been found that a background level of Na can enhance the added level of Sr addition to the melt since both Na and Sr induce twin planes in Si crystals [45].

2.1.8 Lead & Tin

The literature is rather limited on the study of Pb and Sn in Al-Si alloys. However the IRC has embarked on several studies of the levels of Pb and Sn and their effects on thermal analysis cast structures [42, 46, 47]. Typically it was found that Pb and Sn are found in Cu rich eutectics due to their highly segregating nature during dendrite and Al-Si eutectic solidification. It is believed that the Pb and Sn may affect the solidification kinetics of the Al-Si-Cu eutectic reactions but further work is necessary to establish these relationships.

At WAP a study was conducted where thermal analysis test samples and 3.0L V-6 aluminum cast blocks were produced at the same time [47]. It was found that the slight variation in both Sn and Pb had an effect on various solidification events (namely dendrite coherency and Al-Si eutectic growth temperatures) as measured by thermal analysis. However, the tensile and elongation properties of the 3.0L V-6 castings made at the same time (i.e. same chemistry) were unaffected by Pb and Sn. Instead the slight increase in hydrogen content of the melt directly caused a slight increase in the cast porosity of the 3.0L V-6 casting bulkhead structure.

2.1.9 Titanium & Boron

Due to the growing popularity of grain refining many re-melted cast materials have higher Ti and B levels. Master alloys containing Ti and B will introduce particles such as Al_3Ti and AlB_2 which are believed to act as heterogeneous nuclei [2-6, 16, 31, 44, 47-49]. The effect of elevated Ti in the ingot material has been found to affect the grain refining potency of grain refiners [3, 5, 11, 30, 47]. The initial Ti level has recently been referred to as “background Ti”. Many publications have indicated that Ti levels need to be as low as possible so the full grain refining effect can be met with added grain refiners [47, 48, 49]. Recent work however has challenged this concept and has indicated that a high background Ti level in the cast melt can reduce the level of added grain refiner that needs to be added to get a desired grain size [47].

2.1.10 Zirconium

As with the case of Bi, Zr originates from wrought stock materials used in the secondary smelting process. However Zr has not been shown to be deleterious to cast properties [2, 31, 50]. Recently Zr has been investigated as a grain refiner and shown to be effective at grain refining at levels of Zr between 0.37 wt. % to 0.69 wt. % [50] in the 356 alloy.

2.1.11 Scandium

Sc has not been investigated other than its grain refining potential. Typically Sc is not analyzed on chemistry checks (such as OES) due to its relatively low occurrence in secondary stock materials. Sc is very expensive but has a highly beneficial effect on wrought Al mechanical properties. Preliminary work done on its grain refining potential (in the 356 alloy) shows only a beneficial effect of Sc on mechanical properties at levels between 0.39 wt. % and 0.75 wt. % [50]. Also, due to the high cost of Sc its use in aluminium castings is essentially non-existent.

2.2 Hydrogen Uptake in an Al-Si Alloy

An elemental constituent which is not desired in aluminum is hydrogen (H). The level of hydrogen cannot be determined by the common on-line chemical methods used in foundries (i.e. OES) except through the use of an AISCAN unit or the Telegas unit, both of which are especially designed for this purpose. A new on-line method for hydrogen detection is to use the thermal analysis technique as been reported by Djurdjevic et al. [51, 52]. In this work it was found that the nucleation of Cu-rich phases, as determined from the cooling curve analysis, was lowered as hydrogen levels increased.

For any given alloy and specific solidification conditions there is a “threshold hydrogen content” below which no observable gas porosity is formed [53, 54]. If the area fraction of porosity is independent of the hydrogen level this would indicate that only shrinkage plays a primary role in pore growth. Above the threshold, however, the area fraction of porosity increases linearly with respect to hydrogen content, indicating that the growth in pores is directly related to gas evolution.

Sand castings typically cool slowly and the threshold level of hydrogen that may contribute to gas porosity is lower than for permanent mould castings and die-castings. This makes sense since in order for gas based pores to grow, diffusion of hydrogen is necessary and that diffusion is a time dependent process.

For castings that solidify at low cooling rates the accepted threshold level is approximately 0.10cc/100g Al [2, 3, 12, 16, 34, 44, 47]. However recent work by Anson

et al. [53] has indicated that this threshold is actually slightly higher, at about 0.18cc/100g Al (*sample cooling rate approximately 0.30 °C/sec*). Below this level of hydrogen in the melt the resulting porosity was invariant and negligible (*% porosity ≥ 0.005*).

Hydrogen content, when above the threshold level, also affects the fraction solid at which new pores begin to grow in the solidifying alloy. In the 356 alloy quenched sample experiments performed by Anson et al. [53, 54], it was found that a baseline number of pores existed within the solidifying structure that originated either by turbulent filling or from gas bubbles being in suspension in the melt. The number of overall baseline pores did not change during solidification until about 50-60% f_s , where the nucleation of new pores occurred (*nucleation mechanisms of pores discussed in section 2.5*). The expansion of the baseline pores occurred because hydrogen diffuses into the pores and thus achieves the threshold pressure required for pore expansion. Figure 2.1 illustrates the above observations by Anson et al. [53].

It should be noted that a morphological difference exists between baseline pores and new pores that nucleate after solidification has begun. Baseline pores are typically spherical since expansion has occurred during low fraction solid. Conversely pores which nucleated at a higher fraction solid are forced to have the outline of the interdendritic structure. This has some consequences on fatigue properties since interdendritically shaped pores have a stress concentration effect while spherically shaped pores tend to blunt the propagation of cracks.

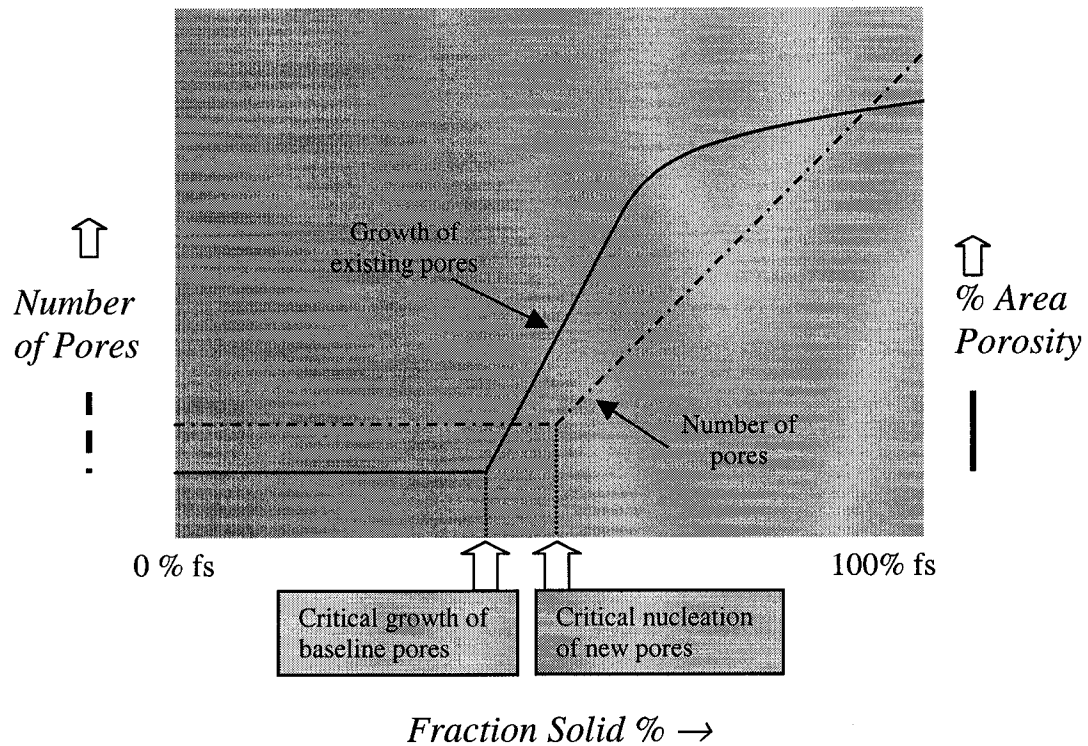


Figure 2.1: This graph illustrates the variation between the final percent porosity and the final pore density with a given solid fraction. Since there is a change in pore density at the H threshold, it is assumed that the nucleation of the pores is partly dependent on the H content (*Reproduced from [53]*).

2.2.1 Hydrogen Levels at WAP

During a period 1999-2000, the hydrogen levels of the W319 alloy melt were measured at WAP using the Alscan system. The typical levels of dissolved hydrogen in W319 melts processed at WAP were found to range between 0.13 up to 0.17 cc/100 grams Al during the June-July 1999 period, and between 0.10 up to 0.15 cc/100 grams Al during the Feb-May 2000 period [47]. The increased hydrogen content during the summer months may be due to the higher humidity.

The threshold at which dissolved hydrogen levels contribute to pore growth is about 0.18 cc/100 grams Al for 356 alloys [53]. Research has not been conducted to establish what threshold of hydrogen would contribute to pore nucleation and growth for the W319 alloy used at WAP.

Despite the small range of hydrogen found in WAP melts, the porosity in bulkhead 2 of the 3.0L V-6 increased from 0.1% up to 0.3% which could be due to the increase of measured hydrogen from 0.10 to 0.15 cc/100 grams Al. This is shown in Figure 2.2a. The location of the bulkhead sections in the 3.0L V6 engine block is shown in Figure 2.2b.

The results in Figure 2.2a indicate that the threshold of hydrogen for the W319 alloy is clearly lower than the 0.18cc/100g Al found for the 356 alloy investigated by Anson et al. [53]. This may be due to the fact that the cooling rate of the 3.0L engine block is slower than 0.30°C/sec (*cooling rate of Anson et al. [53] test samples*) and/or the threshold of the solubility of Hydrogen in the W319 alloy is considerably lower.

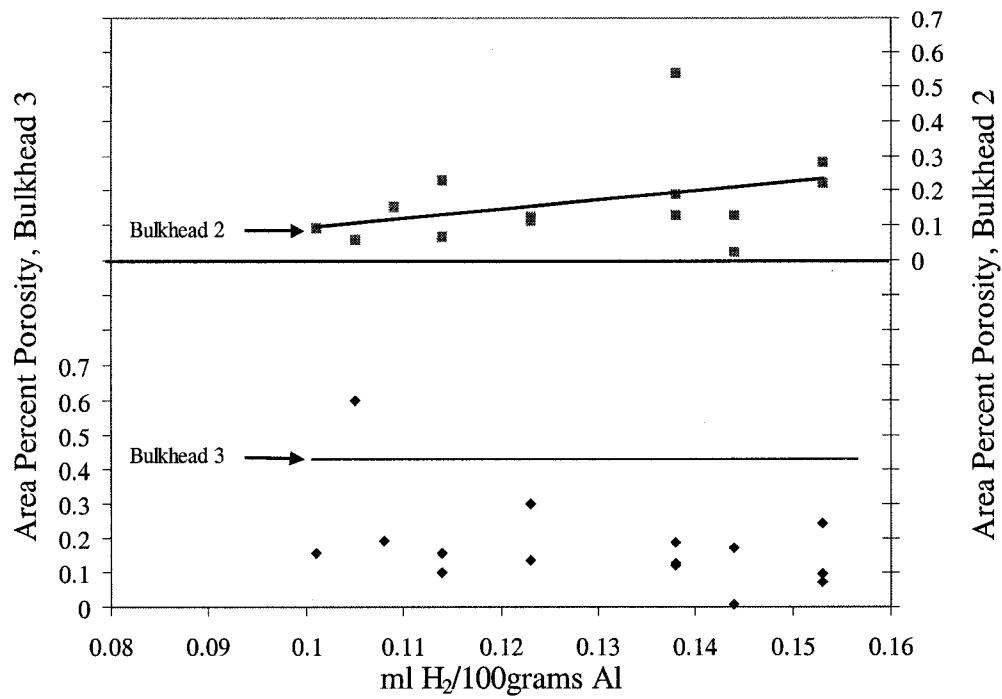


Figure 2.2a: The effect of dissolved hydrogen and the increase of porosity in bulkheads 2 and 3 of the 3.0L V-6 engine block [47].

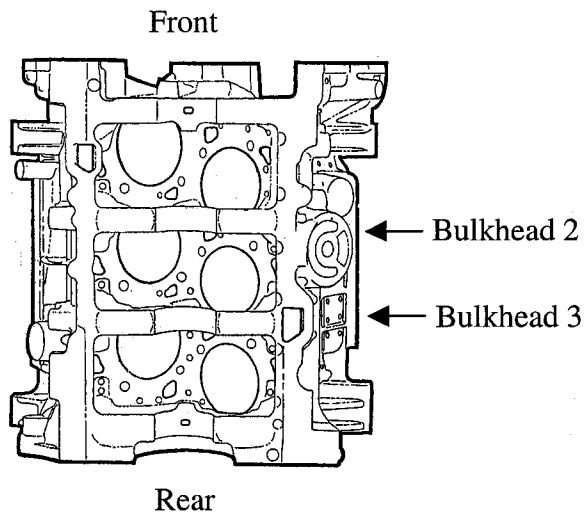


Figure 2.2b: The 3.0L engine block and the location of Bulkheads 2 and 3.

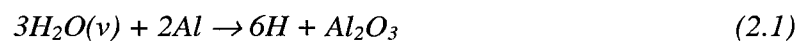
2.3 Sources of Hydrogen & Inclusions in Foundry Al-Si Melts

Both hydrogen and insoluble inclusions are necessary for stable nucleation and development of pores in cast structures. In this section both the methods of hydrogen absorption and inclusion generation that occur in foundry Al-Si melts will be reviewed.

2.3.1 Methods of Hydrogen Absorption

Hydrogen is the only gas that is soluble in aluminum and its alloys [2, 3, 5-16, 44, 48-52]. Gases such as oxygen and nitrogen may form stable compounds with aluminum or other elements, which are usually considered as insoluble impurities, and they have almost no gaseous solubility in liquid aluminum.

Water vapour is mainly responsible for the presence of hydrogen in the aluminum melt. It may originate from the atmosphere or in any form of contamination of tools, flux tubes, grain refiners and other master alloys [2, 31]. Upon exposure to the molten metal, the water vapour ($H_2O(v)$) reacts to form magnesium oxide (Equation 2.0) and aluminum oxide (Equation 2.1) and gaseous hydrogen [3, 55-57]:



These reactions are considered irreversible in the sense that a large negative free energy change would be required. It should be noted that the initially formed oxide films are

amorphous for milliseconds and then crystallize [57]. During the short amorphous stage the oxide layer sitting on the melt surface hydrogen absorption does not readily take place. However, the crystallized oxide loses its protectiveness against hydrogen absorption due to the fact that diffusion of Al^{3+} cations from the liquid side to the O_2 rich side of the oxide can now occur. Once Al^{3+} cations react with H_2O to form Al_2O_3 (called dross in the foundry) the dissociated H^+ cations (protons in this case) diffuse in the reverse direction through the oxide into the melt. This is illustrated in Figure 2.3a.

Previously it was believed that O_2 anions diffuse from the surface of the oxide into the melt. However the concept of the Al^{3+} species diffusion through the oxide as opposed to O_2 anions is supported by the size of the diffusing species [57]. Al^{3+} cations are 0.51 Å while O_2 is 1.32 Å. The smaller the cation size the easier it is for that species to diffuse through the crystallized Al_2O_3 .

The H^+ cations that are generated at the oxide surface diffuse through to the melt quite readily. The rate at which this occurs is governed by the solubility of hydrogen in the melt and the thickness of the oxide layer. As far as solubility is concerned various alloys have different hydrogen absorption tendencies. For example, under the same conditions (i.e. melt temperature) soluble hydrogen content in the 356 alloy is 18% higher than in the 319 alloy, but 22% lower than in pure Al. The hydrogen uptake can be higher at higher melt temperatures. For example the soluble hydrogen content at 750°C is 38% higher than that at 700°C [2] for pure Al (see Figure 2.3b).

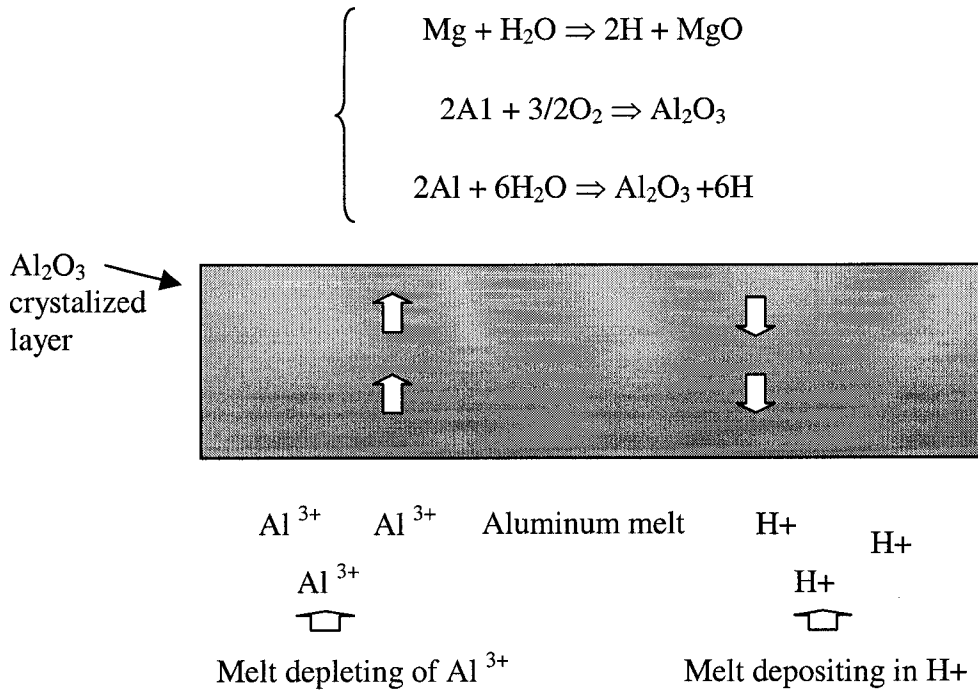


Figure 2.3a: The formation of the oxide layer on the dross and the reaction that supplies hydrogen to the melt (*Reproduced from [57]*).

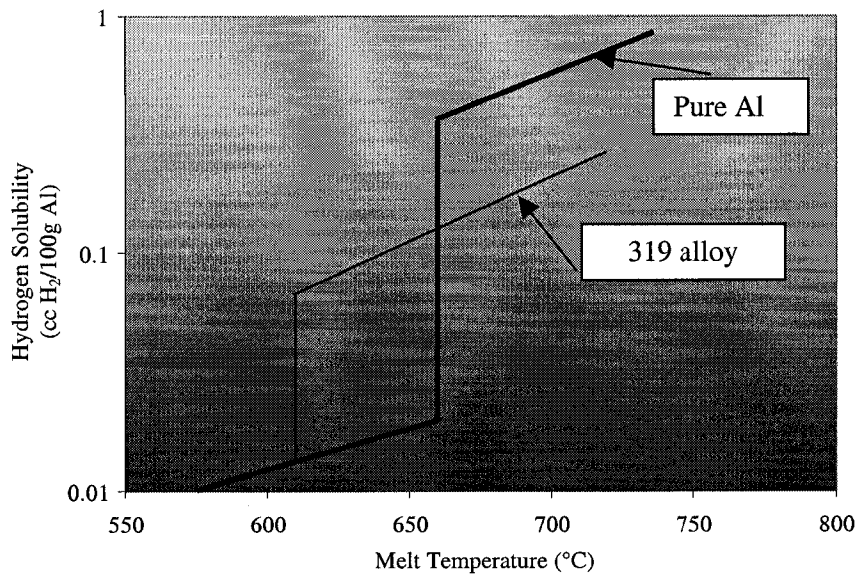


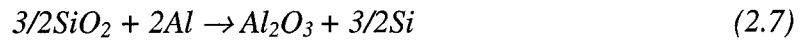
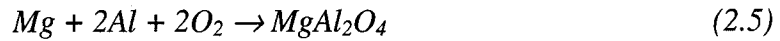
Figure 2.3b: The solubility of hydrogen in pure aluminum and the 319 alloy (*Reproduced from [2]*).

As time passes the oxide layer thickens and the diffusion distances for H^+ become greater. The consequence of the greater diffusion distances is that the supply of Al^{3+} cations becomes less and the oxide thickening rate slows down.

2.4 Oxides & Inclusions in Al-Si Alloys

2.4.1 Oxide Types in Al-Si Melts

The most deleterious oxides observed in aluminum alloy castings are Al_2O_3 (alumina) and $MgAl_2O_4$ (spinel) [2, 16]. Other slightly less deleterious compounds found in Al melts are MgO and Si-C particles. The general reactions by which these oxides form are shown as follows [2, 3, 16, 55]:



However Al_2O_3 is the predominant oxide. The general classification is normally based on the types of alumina present, as follows [2, 13, 16, 25, 55]:

- Amorphous alumina film inclusions (“new oxide films”) is the product of direct oxidation of aluminum melts which have no time to crystallize. New oxide films are a

byproduct of turbulent pouring, bubble trails or confluent fronts. Their formation usually takes only between 10 and 60 seconds [16, 24, 57]. It has a continuous aspect, low thickness, and exhibits a wrinkled appearance. Thickness ranges from 0.05 μm up to 10 μm [57].

- Gamma alumina film inclusions (“old oxide films”) is the product of crystallization of amorphous alumina, its formation requires a certain incubation; therefore, these types of inclusions are associated with turbulent operations before mould pouring. The formation usually requires several minutes to several hours. The thickness can be much larger than new oxides, ranging from 100 μm to 1000 μm [2, 24, 57].
- Alpha alumina inclusions (“hard spots”): alpha alumina is the product of recrystallization of $\gamma\text{-Al}_2\text{O}_3$ after long exposure to high temperatures. As the incubation conditions are severe, $\alpha\text{-Al}_2\text{O}_3$ is normally formed due to adherence and accumulation of $\gamma\text{-Al}_2\text{O}_3$ films at the crucible walls, mainly in a holding furnace that contains “dirty metal” (high content of $\gamma\text{-Al}_2\text{O}_3$ films). Its main characteristics are the inclusion size, typically more than 1 mm, the black colour and the high hardness (corundum) [2, 24].

2.4.2 Titanium Boride (TiB_2) Inclusions

In a study by Mohanty et al. [16] TiB_2 particles were capable of nucleating pores. However TiB_2 becomes active at pore nucleation if the excess Ti in the melt is kept below 0.001 wt.% of what is needed to achieve TiB_2 particles for $\alpha\text{-Al}$ phase nucleation. The basic reason why background Ti in the Al melt is beneficial towards reducing

porosity is due to the observation that TiB_2 particles are engulfed by the solidifying interface while low Ti containing melts (below the excess 0.001 wt.% needed) the TiB_2 crystals were pushed out in front of the solid liquid interface and into the interdendritic regions.

2.4.3 Strontium Based Inclusions

Additions of Sr are common in foundry melts and as a consequence Sr based inclusions are found in some cast structures. However, SrO and Sr(OH)_2 inclusions reduce in the melt to form complex compounds ($\text{Sr}(\sim 15\%)\text{-Al}(\sim 40\%)\text{-Si}(\sim 40\%)$) that become engulfed by the advancing $\alpha\text{-Al}$ dendritic solid liquid interface. Thus, it was proposed that Sr based compounds do not contribute to the nucleation of pores within the solidifying melt [58]. However there is a growing number of recent publications which indicate, that due to the significant increase in porosity when Sr is added to melts, that Sr based compounds are not engulfed and actively contribute to pore nucleation [2, 4, 15, 16, 44, 47-49, 55, 58].

2.5 Gas-Shrinkage Pore Nucleation and Growth Mechanisms

In order for a pore to grow, its internal pressure (caused by H_2 gas) must be sufficient to overcome all the external forces, which would normally act to make the pore collapse. The stability of pores is affected by three factors: the atmospheric pressure (P_{atm}), the metallostatic head (P_{H}) and the surface tension (γ). Of these factors, surface tension has the

largest retarding effect and must be overcome before a pore can have stable growth [2, 14, 56, 58].

The factors that assist pore growth in the liquid are two fold: the internal gas pressure of the pore (P_G) which results from hydrogen rejected into the solid-liquid interface, and the hydrostatic stress or shrinkage pressure (P_S) which can be viewed as the tensile stress on the liquid pockets in interdendritic regions caused by solidification shrinkage. This last factor can be intensified if adequate feeding into such regions is not allowed. The equation that ties all the factors that hinder and assist pore growth is expressed in Equation 2.8 as follows [2, 3, 14, 56, 58]:

$$P_G + P_S \geq P_{atm} + P_H + \gamma \left(\frac{1}{r_1} + \frac{1}{r_2} \right) \quad (2.8)$$

where r_1 and r_2 are the principal radii of curvature of the pore.

The relationship expressed in Equation 2.8 and its description is an over simplification for the conditions of stable pore growth. Usually $P_G + P_S$ is insufficient to cause pore nucleation and it is well known that for heterogeneous nucleation to occur, a foreign particle (*Oxide or Inclusion, see Section 2.4*) is required. This is due to the fact that a small gas pore of only several atomic diameters would be required to obtain an internal pressure of 30,000 atm [14].

Thus Campbell has introduced a concept of the Gas-Shrinkage Map to show the relationship between internal gas pressure and the hydrostatic stress on the liquid. The Gas-Shrinkage Map shown in Figure 2.4a illustrates the conditions by which the interdendritic liquid may be forced to nucleate a pore through heterogeneous nucleant 1 if the hydrostatic stress and the internal gas pressure are high enough. However, if feeding becomes retarded the level of hydrostatic stress on the interdendritic liquid should be higher and thus activate more heterogeneous nucleants, such as nucleants 1 (highest potency), 2 (medium potency) and possibly 3 (lowest potency).

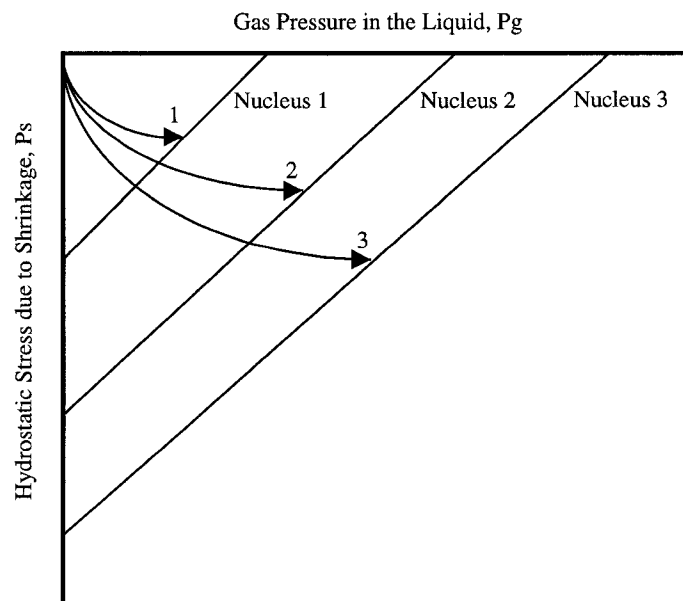


Figure 2.4a: The Gas-Shrinkage Map, which illustrates the combination of shrinkage stress, and internal gas pressure that can be relieved by heterogeneous nucleation from particles present within interdendritic regions of the mushy zone [14].

Experiments have conclusively shown that oxide and other inclusion particles facilitate heterogeneous pore nucleation [2, 14-16, 25, 55, 57]. Moreover, Rooy [15] has argued that oxide and inclusions having a sharp groove imperfection can reduce the critical radius for stable pore growth substantially. This is illustrated in Figure 2.4b. This is a realistic hypothesis since most inclusions found in Al foundry melts do have pores and cracks ranging from 5-40 μm [55, 57]. Mohanty et al. [16] has added that an obstructionist method in addition to the surface imperfection of an oxide or inclusion can reduce further the critical radius for stable pore growth. This is shown in Figure 2.4c. The inclusion in this case would reduce fluid flow into an interdendritic region and reduce the pressure required to nucleate a pore. Then the energy barriers to $P_G + P_S$ become less and a gas-shrink pore may form.

Experimental observations have been made that Al-Si alloy melts containing inclusions typically make more porous cast structures than clean metal [2, 16, 28, 32, 46, 56-58]. The Reduced Pressure Test (RPT) has been used to confirm these observations [2, 56]. In light of the numerical value required to homogeneously nucleate a gas pore (*posed by Campbell [13, 14]*) and the apparent relationship between inclusion content and pores in the cast structure it would be fair to assume that inclusions in addition to hydrogen content play a role in stable nucleation of a gas pore.

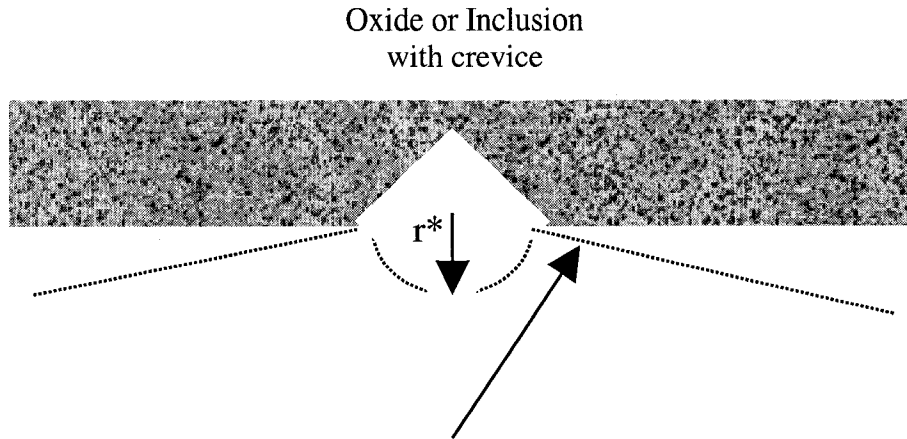


Figure 2.4b: Crevice reducing critical radii (r^*) of a pore (*Reproduced from [16]*).

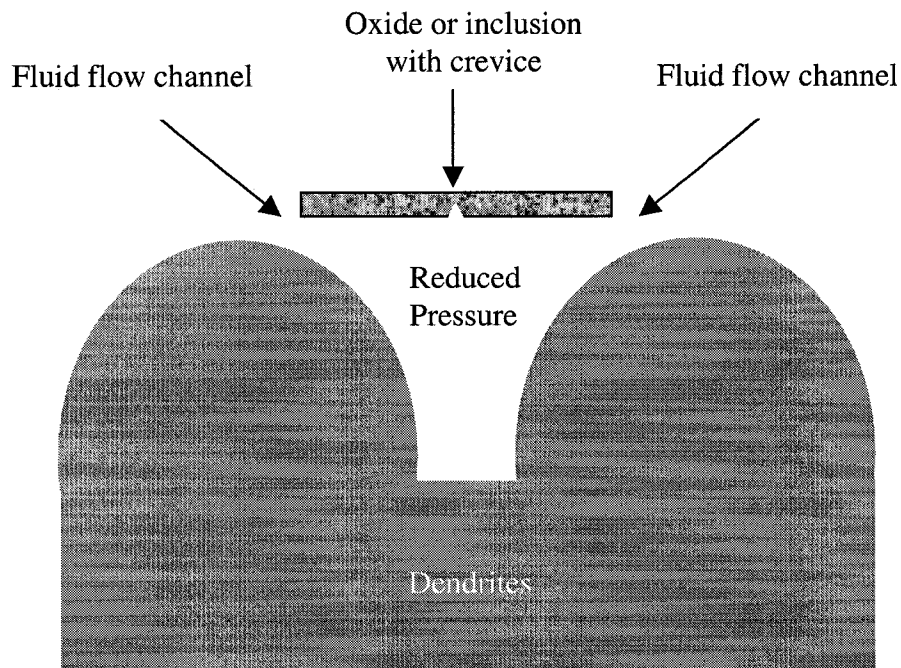


Figure 2.4c: Schematic of inclusion in interdendritic regions (*Reproduced from [15]*).

2.6 Mechanism for Feeding During Mushy Zone Solidification

The degree at which fluid flows within a partially solidified metal mesh (*or mushy zone*) in hypoeutectic alloys can be subjected to the chemical composition of the alloy (macroalloying) and the level of deliberate additions (microalloying), and to the thermal conditions in which solidification occurs (risering and chilling in the sand mould). Several conditions, which will be outlined, may occur in which fluid flow becomes more retarded, giving rise to small voids within the interdendritic structure.

2.6.1 Contraction of α -Al dendrites and the Al-Si Eutectic during Solidification

Figure 2.5a shows the schematic of volumetric contraction undergone by most metals as the temperature decreases through liquid cooling, partial solidification, and then solid state cooling [14]. The α -Al dendrites solidify and experience a volumetric contraction due to the transition from liquid to solid ($\sim 8.14\%$ for pure Al [14, 59]) and thus will need to draw upon the liquid metal alloy from an adjacent source to compensate.

The contraction of the Al-Si eutectic is less than for the α -Al dendrites due to the fact that Si actually expands during solidification ($\sim -2.9\%$ for pure Si [14, 59]). It has been reported that for an Al-7%Si sample cooled quickly (i.e. little internal microporosity) the overall volumetric shrinkage is 4.5% [2, 59]. The volumetric contraction value reduces to 3.8% if the Si content increases to 12% [15].

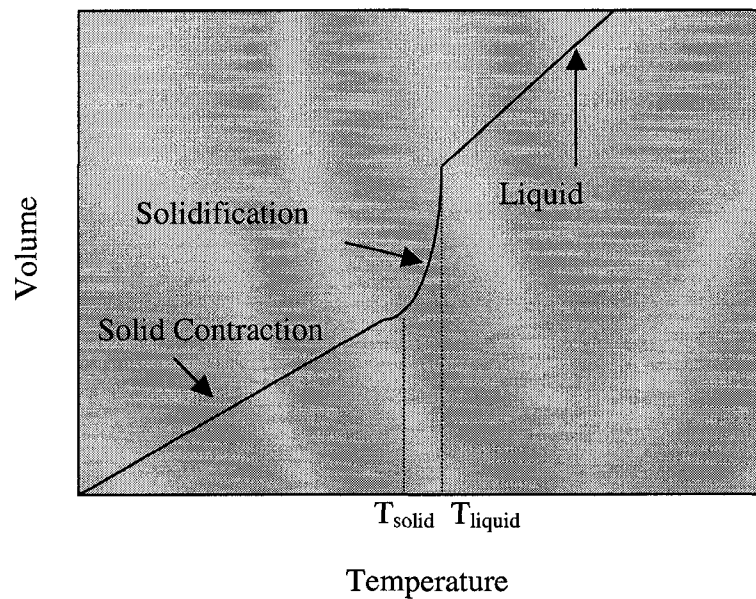


Figure 2.5a: Solidification Contraction of a pure metal (*Reproduced from Campbell [14]*).

Adding Cu to Al alloys may increase the amount of volumetric shrinkage which will occur in the final cast structure. When considering an Al-Cu binary alloy of eutectic composition, the volumetric contraction will be 8.4% [59, 60]. This will have an important consequence on the internal volumetric contraction of Cu rich pockets of liquid during the cast solidification of the 319 alloy. Typically these pockets are isolated from a feed source due to the fact they will solidified after most of the Al-Si eutectic has formed.

2.6.2 Modes of Liquid Metal Feeding During Solidification of Al-Si Hypoeutectic Alloys

Prior to the onset of primary α -Al dendritic nucleation, feeding can occur via **Liquid Feeding**. This is a process where the liquid metal alloy feeding occurs to compensate for solidification shrinkage of an adjacent region that has solidified, or partially solidified [14, 60-70]. After the primary α -Al dendritic nucleation (at the liquidus), but prior to contact of the α -Al dendritic crystals with neighbouring dendrites (at the dendrite coherency point), compensation for solidification shrinkage occurs via **Mass Feeding** [61-68]. The α -Al dendritic crystals are free to rotate about any axis and are mobile within the cast cross-section.

The point when neighbouring α -Al dendritic crystals come in contact and physically become fixed in space is known as the **Dendrite Coherency Point** (DCP) [61-70]. This marks the transition between mass feeding and interdendritic feeding. This becomes a major transition point during the course of solidification of alloys. The conditions that mainly control the time, temperature and fraction solid where DCP occurs are governed by both constitutional (i.e. chemical) and thermal undercooling (i.e. cooling rate) effects at dendrite tips.

Interdendritic Feeding occurs by the liquid alloy flow within the regions between dendrite stems. It is important to note that chemistry and cooling rate will have a profound effect on the permeability of the dendritic skeleton network after DCP. The temperature decreases and the liquid becomes enriched with Si and Cu and eventually equilibrium eutectic chemistry is

achieved. Within the traditionally accepted definition of interdendritic feeding, feeding during Al-Si eutectic solidification is also included. This view of interdendritic feeding becomes rather confounded since the nucleation of Al-Si crystals may obstruct fluid flow in differently than that of the primary dendrites. In addition, Campbell [14] argued that in purely eutectic alloys the solidification front is generally planar and that feeding of this interface occurs by liquid feeding. The planarity of the Al-Si eutectic interface has been confirmed by Sigworth [71] via quenching of a solidifying 356 alloy.

Further questions on the nature of the solidification of the Al-Si eutectic and its possible role on pore formation on the cast structure has been reported by St. John et al. [72]. It was found through the Electron Backscatter Diffraction (EBSD) Technique on an Scanning Electron Microscope (SEM), that the crystal orientation of the α -Al of the eutectic was similar to that of the α -Al primary dendrites. This indicated that the eutectic grew from the dendrite surfaces. With the presence of Sr the eutectic cells did not nucleate from the dendrite surfaces. It was presumed that the Sr build-up on the solute boundary layer of the dendrite surfaces acted as a poisoning effect and forced less favourable heterogeneous nuclei to start Al-Si nucleation. This consequent change in growth mechanism, due to elevated Sr content of the Al-Si alloy, was that feeding channels became slightly more obstructed and the propensity for stable pore development grew.

Anson et al. [53, 54], Kim et al. [73] and Iwahori et al. [74] have studied feeding and porosity formation in the 356 alloy and have found that stable conditions for pore growth do not really occur until a critical fraction of solid has been achieved. This has been typically

around 50% fraction solid, near or at the time for Al-Si eutectic growth. Although no satisfactory explanation has been given as to why the stability of the pore nucleation process occurs at this stage of solidification, it could be due to the tortuosity (or permeability) of the primary interdendritic regions of the mushy zone. Although Anson et al. [53, 54] indicated that some porosity in samples quenched at a low fraction solid were evident. This porosity could have possibly nucleated from conditions associated with the structure at the DCP, or due to turbulent effects of mould filling.

The question of feeding during the Al-Si-Cu reaction creates some controversy. Typically it has been felt that these isolated pockets of Cu rich liquid are physically surrounded by solid Al-Si eutectic and primary α -Al dendrites and are difficult to feed. Edwards et al. [59] indicated through calculation of hydrogen pressure in the Cu rich liquid pools (due to the reduction of solubility) and the shrinkage of those pools, that the predicted theoretical porosity calculated in Cu containing Al-Si alloys is higher than what is observed in their alloy samples by two fold. It was argued that some feeding is possible to these Cu rich pools even though they are typically considered isolated. It is quite clear that the temperature gradient in the vicinity of the Cu rich liquid pools needs to be high enough to permit liquid metal feeding. Some argue that these regions are not fed other than through ***Solid Feeding***. The condition for solid feeding is that within the encapsulated liquid, hydrostatic stresses reach the point that the surrounding solid yields and is forced to collapse inward [63].

Figure 2.5b illustrates the role of each of the feeding stage discussed.

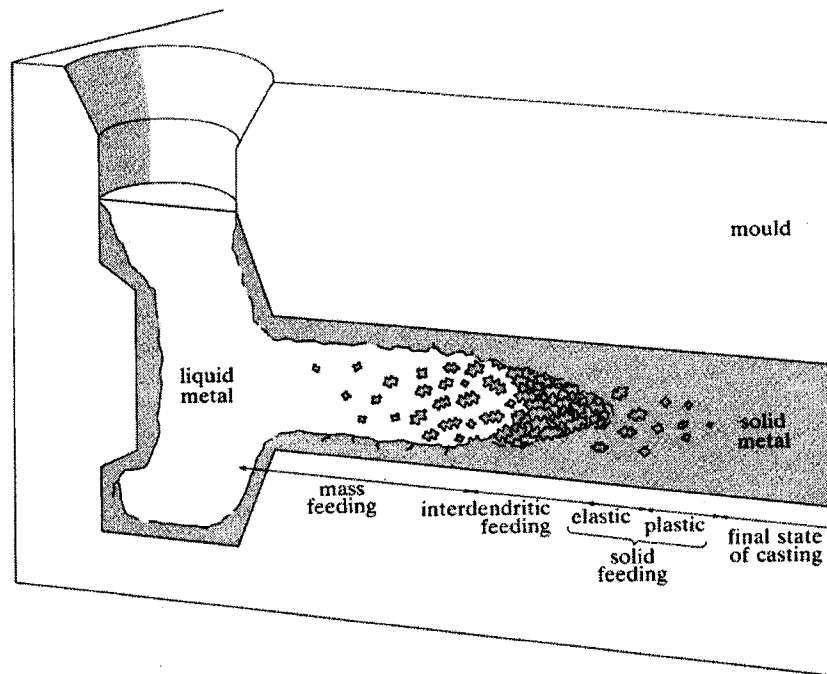


Figure 2.5b: Schematic of the liquid feeding stage, mass feeding stage, interdendritic feeding stage, solid feeding and complete solidification of a cast cross-section [66].

Chapter Three

Literature Review of Fatigue Resistance of Al-Si Alloys

3.0 Introduction

The general growth of aluminum alloys in automotive powertrain systems has warranted the need to further understand the factors that affect their fatigue performance. In general, the small body of research in the fatigue of aluminum castings has historically been mainly, but not exclusively, devoted to the evaluation of aerospace component performance. The United States Council of Automotive Research (USCAR) consortium has compiled a large amount of information pertaining to the effect of porosity distribution in shape castings made from the A356 alloy, the A357 alloy and the AM60 alloys [75]. Other published texts have either summarized or catalogued the fatigue performance of automotive components cast or forged in aluminum or magnesium [76, 77]. Currently very limited work has been performed for Al-Si alloys containing Cu such as the 319 alloy [19-23, 77, 78]. Nonetheless much of the existing work on fatigue performance related to the 356 alloy is valuable and provides a sufficient understanding of the factors controlling fatigue crack growth in Al based alloys.

3.1 Fundamentals of Fatigue Failure

3.1.0 Stress Conditions Pertaining to Fatigue

The range of stress σ_r is defined as the difference between the maximum stress and the minimum stress encountered within a single cycle as shown in Equation 3.0 [79, 80] as:

$$\sigma_r = \sigma_{\max} - \sigma_{\min} \quad (3.0)$$

Alternating stress, σ_a , can be defined in Equation 3.1 [79, 80] as:

$$\sigma_a = \frac{\sigma_r}{2} = \frac{\sigma_{\max} - \sigma_{\min}}{2} \quad (3.1)$$

Mean stress, σ_m , can be defined as the sum of the maximum stress and minimum stress within a single cycle and is expressed in Equation 3.2 [79, 80] as:

$$\sigma_m = \frac{\sigma_{\max} + \sigma_{\min}}{2} \quad (3.2)$$

Finally the stress ratio, R , can be defined in Equation 3.3 [79, 80] as:

$$R = \frac{\sigma_{\min}}{\sigma_{\max}} \quad (3.3)$$

Figure 3.0 shows σ_r , σ_a , σ_m and R schematically. By convention tensile stresses are considered to be positive while compressive stresses are negative. In this dissertation $R = -1$, and this means that a fully reversed stress cycle is employed.

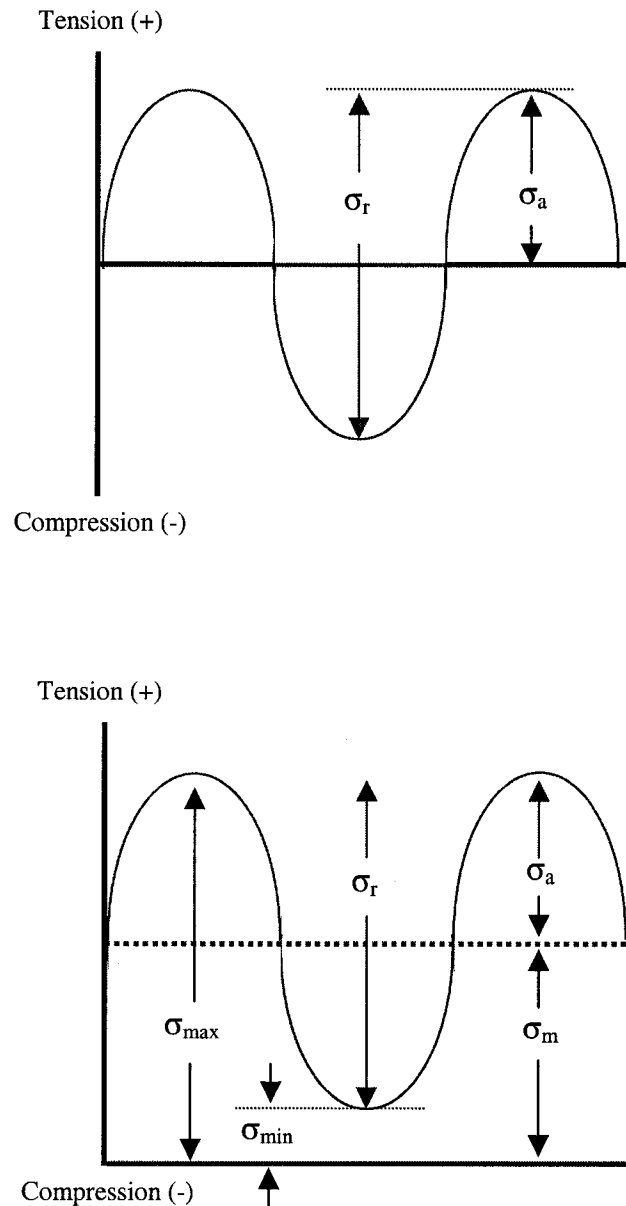


Figure 3.0: Fatigue test schematics showing the stress nomenclature for a) *tension* and *compression* fatigue test, where $R = -1$, and b) is a *tension* and *tension* fatigue test, where $R > 0$ (Reproduced from Callister [79]).

3.1.1 Stages of Fatigue Failure

High Cycle Fatigue (HCF) will be the primary focus within this dissertation. HCF is usually defined as a test sample or a field component (i.e. engine block) which has experienced cyclic plastic deformation at low stress levels many times ($\leq 10^5$) [23, 76, 79].

The life of a crack may be defined as follows in Equation 3.4 [80]:

$$N_{TotalCyclesTilFailure} = N_i + N_p + N_f \quad (3.4)$$

Where:

N_i = the number of cycles required to initiate a crack

N_p = the number of cycles required to propagate the crack

N_f = the number of cycles to failure is usually insignificant since it occurs so rapidly

The initial life spent on initiating cracks (N_i) is usually very small in most 3xx.x castings having a high volume fraction of discontinuities (voids, inclusions, etc.) within the structure. Typically the sites that initiate a crack, be it a pore, an oxide, etc., are usually near the surface of a fatigue test sample. This is due to the fact that the stress is the highest near the casting or fatigue test specimen surface. This is why surface polishing of fatigue test samples is critical so that as-cast surface roughness, or depression artifacts

associated with the sample cutting and preparation, do not initiate cracks instead of the intrinsic condition (*i.e. internal porosity, α -Al matrix/secondary phase constituent interface or oxide inclusion*) of the as-cast structure.

The number of cycles required for propagation (N_p) is usually dominated by the path a crack can grow along the weakest discontinuities. Due to the small number of cycles required to initiate a crack, the understanding of the mechanism for propagation can be critical in determining the over all life of a cast part during service.

N_p is usually determined by two distinct stages in polycrystalline materials having no secondary phase constituents. The first stage can be governed by the growth of cracks along crystallographic planes of high shear stress. These cracks are not orientated perpendicular to the direction of tension and compression during cyclic testing. The second stage of growth can occur more rapidly since the propagation direction is perpendicular to the direction of tension and compression [3, 22, 76, 77].

The continual crack growth size during each cycle can be due to plastic rupture of the metal matrix as in some wrought aluminum alloys, but in aluminum castings the microstructure is very complicated due to the much higher level of alloying that leads to a large volume fraction of secondary phase constituents. Many secondary phase constituents are nonmetallic and have regions of poor matrix/secondary phase cohesion [20, 21, 22, 25, 28, 76, 81].

Finally, porosity plays a factor not only in initiating cracks, but can affect propagation time as well [75, 76, 78]. Porosity can be looked at as a physical reduction in the cross-section of a casting. This leads to the overall distance between the crack initiation site (usually near the surface) to propagate to adjacent pores through the cross-section of the test sample. Crack coalescences (cracks nucleated from other pores) occur rapidly producing a larger crack with a correspondingly high crack driving force. The higher the driving force becomes the lower the overall number of cycles are needed to cause total failure.

3.1.2 Methods of Crack Propagation Measurement

The fatigue life of many structural components may be related to the *rate* of fatigue crack growth. Crack growth rates as a function of the stress intensity range have been obtained for many of the Al Casting Alloys. The rate of crack growth is the incremental growth in the crack length (da) per fatigue cycle. The stress intensity range is a measure of the maximum (K_{\max}) and minimum (K_{\min}) stress intensity associated with cycling tension and tension, or compression. The stress intensity may be defined in Equation 3.5 as [79, 80]:

$$\Delta K = Y\Delta\sigma\sqrt{\pi a} \quad (3.5)$$

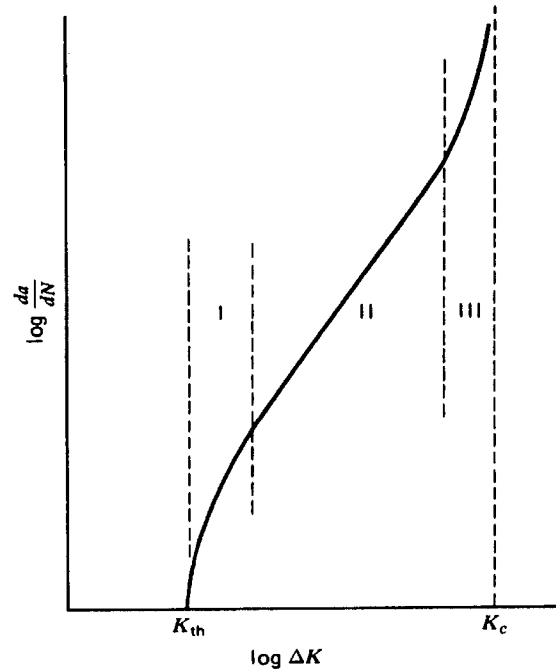
Here $\Delta\sigma = \sigma_r$, and Y is a geometrical function depending on the shape of the crack and the sample. For 4 or 5 decades of data generation the da/dN verses ΔK profile becomes *sigmodal* [79]. This sigmodal profile, as depicted in Figure 3.1, characterizes the stage

one (I), two (II) and three (III) propagation modes. Stage I is where pre-existing cracks or other regions of material weakness will not grow under loading. Stage II is the Paris regime or power law region and is described in Equation 3.6 as:

$$\frac{da}{dN} = C(\Delta K)^m \quad (3.6)$$

Where C and m are constants that can be determined from the plotted data of the $\text{Log}(da/dN)$ versus $\text{Log}(\Delta K)$ which depends on the frequency of the cycle loading and the stress ratio, R . Thus ΔK dependence on crack growth rates is a strong function of the size of the growing crack, the stress ratio, and the applied stress.

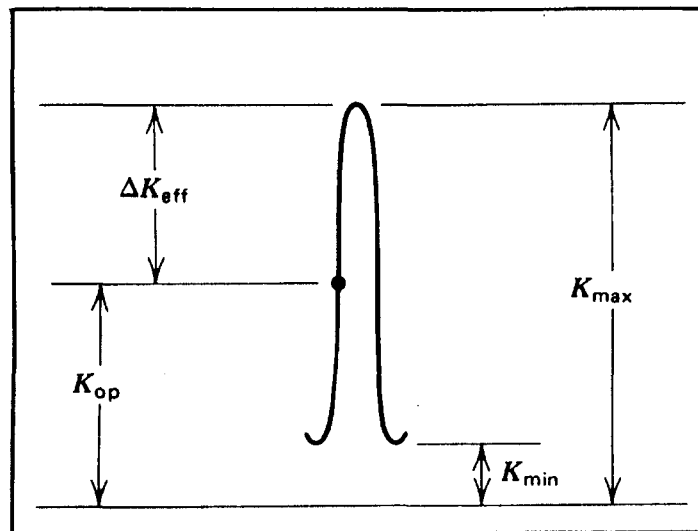
Figure 3.1: A plot of $\log(da/dN)$ versus $\log \Delta K$ having the sigmodal shape. In region one (Stage I) the crack growth rate decreases with decreasing ΔK until the threshold region K_{th} . Region two (Stage II) is the power law region, or sometimes referred to as the Paris regime. Region three (Stage III) is a region of accelerated crack growth until K_c . Stage III is unstable crack propagation [80].



Stage III represents the stage at which, for plastic materials, unstable crack growth occurs. Stage III constitutes a small number of the cycles of the total life of a fatiguing material.

A modified version of the stress intensity range exists which takes into account crack closure effects on crack propagation rates [79, 80]. This is referred to as the effective stress intensity range (ΔK_{eff}). The determination of ΔK_{eff} is achieved by quantifying the reduction of crack surface area associated with crack closure, K_{cl} , where the subscript *cl* denotes closure. Alternatively other sources chose to use K_{op} , where the subscript *op* denotes open. The existence of K_{op} or K_{cl} is due to the presence of asperities that exist along the crack surface as the crack tip advances during fatigue testing. This value of K_{op} is then subtracted from K_{max} , (i.e. $\Delta K_{\text{eff}} = K_{\text{max}} - K_{\text{op}}$) as shown in Figure 3.2. The magnitude of K_{op} can usually be determined by observing the change in compliance of load versus displacement curves [80].

Figure 3.2: The schematic representation of the effective stress intensity ΔK_{eff} . In order to fully open a crack a stress K_{op} must occur above K_{min} during the load cycle [80].



The threshold stress intensity range, K_{th} , is essentially the stage at which fatigue damage of aluminum cast parts is unlikely. It is defined as the stress intensity range below which no measurable crack propagation will occur, measured over many cycles ($da < 1\text{nm}$ or 5 atom diameters). This can be determined from the value of the da/dN profile during Stage I and its intersection with the ΔK axis (see *Figure 3.1*), typically at $da/dN = 10^{-9}$ to 10^{-10} m/cycle.

3.1.3 Axial Configurations for Fatigue Analysis

Axial fatigue test samples have been used in fatigue performance studies of aluminum castings, particularly for aluminum cast engine blocks [19, 20, 21, 22, 23, 76, 77, 82, 83, 84]. This type of fatigue test sample specimen will be used in this dissertation. The number of cycles to failure were measured, and analysis of the fracture surface were conducted using visual observation and the SEM. An example of axial fatigue test specimens is shown in the picture in *Figure 4.3a* with dimensions shown in *Figure 4.4a*, all found in *Chapter Four*.

3.1.4 Generation of the S-N Curve

The generation of the S-N curve allows for the determination of the full stress range and corresponding numbers of cycles to failure. Figure 3.3 shows an example of a schematic of an S-N curve for a FCC (*Face Centered Cubic*) metal (Aluminum) and a BCC (*Body Centered Cubic*) metal (Iron) [76-78, 80]. A true example of an S-N curve for a cast Al alloy is found in the dissertation of Boileau [81] and is shown in Figure 3.4.

The generation of such a plot is done using axial fatigue test samples tested at a given cyclic stress level and then plotting the fatigue lives on the logarithmic abscissa (see Figure 3.4). The testing begins by fatiguing test samples at high stress (a low number of cycles to failure) and then a new (subsequent) fatigue test sample is tested at successive incrementally reduced stresses until no fatigue failures exist. The stress range at which no failures occur is known as the *fatigue limit* [77, 79, 80, 81]. FCC metals however will show a continual downward trend in the S-N curve as seen in Figure 3.4 [80, 81]. Thus, in the case of FCC metals, an arbitrary life of 10^7 or 10^8 cycles is used to define the fatigue limit [80, 81].

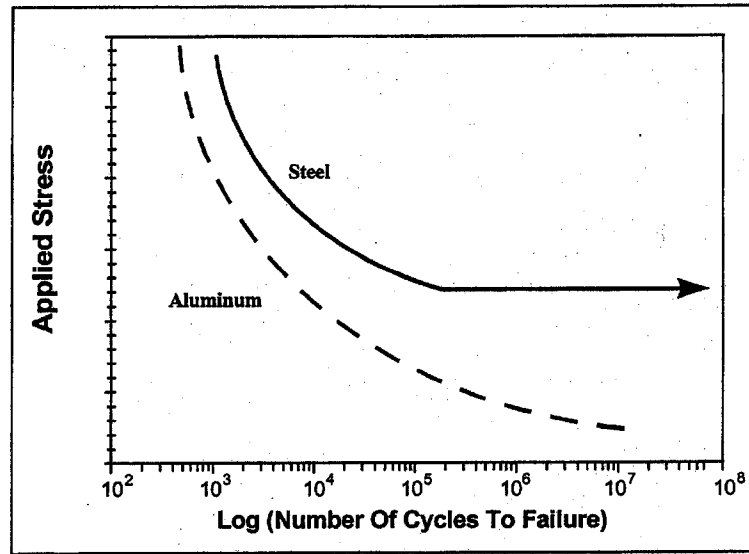


Figure 3.3: Example of the S-N curve for an FCC metal (Aluminum) and a BCC metal (Iron) (Example scanned from Boileau [81]).

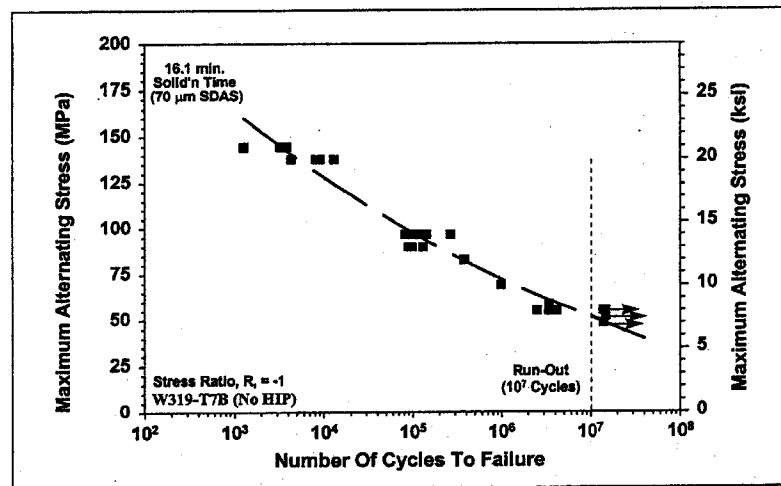


Figure 3.4: Example of the S-N curve for the W319 alloy (Example scanned from Boileau [81]).

3.1.5 Staircase Testing

The staircase method of determining a sustainable stress level is more amenable for product durability evaluation. Also the axial fatigue test sample numbers required to generate a fatigue staircase test are generally lower than for the S-N curve [25]. This is also the method of fatigue analysis outlined by the Ford Engineering Material Specification WSE-M2A151-A3 for the durability assessment of cast aluminum engine blocks [17].

Before commencing a fatigue staircase study a fatigue life cycle goal must be determined for the cast part. Normally this is defined as 10^7 cycles [19, 25, 80]. The first test sample can be tested at a specific stress and should that test sample sustain a total of 10^7 cycles it would be considered a *run out* or a passed test. The stress on a second test sample would then be increased by a set incremental amount $\Delta\sigma$. Should this second test fail to achieve a total of 10^7 cycles it would then be a failed test. A third test sample would be stressed at the same level as the first test sample. Figure 3.5 illustrates the first three test samples of a staircase test.

The mean HCF stress (*from a staircase test*) is then determined for all the stress levels of the test samples which did not fail (run outs) or all the failed test samples, whichever number is smaller [25].

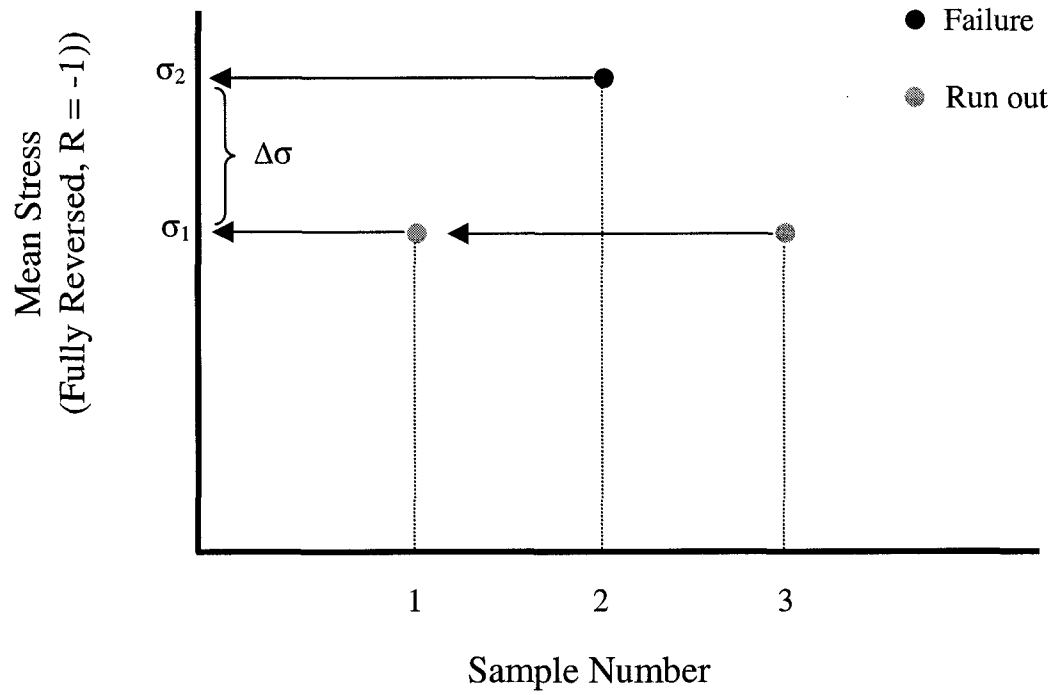


Figure 3.5: Three fatigue test samples at the beginning of a staircase test. The sequence would continue until the desired number of tests have been completed.

3.2 Metallurgical/Structural Factors Affecting Fatigue Crack Growth in Al-Si Alloys

The nucleation of cracks, as found in almost all literature sources, regardless of oxide content or secondary phase morphology, size and distribution, was from one or two shrinkage type pores [14, 20, 21-23, 28, 29, 75, 76, 78, 80, 81]. Table 3 is a survey of the five fractured surfaces of five separate A356 alloy axial fatigue test samples (133 MPa, $R = 0.1$) which was studied by Gall et al.[23].

An SEM fracture surface of one of the samples in Table 3 is shown in Figure 3.6a. As seen in Table 3 the larger the pore found on the fracture surface the shorter the number of cycles till failure. Also, all cast defects which initiated failure were near the test sample surface.

Figures 3.6b and 3.6c show the SEM micrographs at higher magnifications of the fracture surfaces near the crack nucleation site (see Region 1 in Figure 3.2a). As seen in this SEM image the striations are spaced $0.1\ \mu\text{m}$ apart in the α -Al dendrites and in the cavities or depressions of the α -matrix which formally contained Si crystals. These striations were used to indicate that the crack growth rates were less than $1 \times 10^{-7}\ \text{m/cycle}$.

Table 3: Principle discontinuities that nucleate cracks in the A356 alloy with Sr modification. The axial fatigue samples were tested at a constant amplitude of 133 MPa ($R = 0.1$) by Gall et al. [23]. Si modification levels are not specified but the Sr addition to the 356 alloy melt was 100 ppm.

<i>Number of cycles</i>	<i>Crack nucleation site characteristics</i>	<i>Nucleation site area on specimen fracture surface (within the Transition line)</i>
9,369	A single pore with major axis 900 μm .	0.225 mm^2
49,420	Two near surface pores 200 μm from each other.	0.118 mm^2
142,755	Two near surface pores 300 μm from each other.	0.060 mm^2
157,569	Distributed casting porosity (sponge shrink) near the specimen surface.	Total $\sim 0.225 \text{ mm}^2$
331,629	Oxides near the specimen surface.	0.012 mm^2

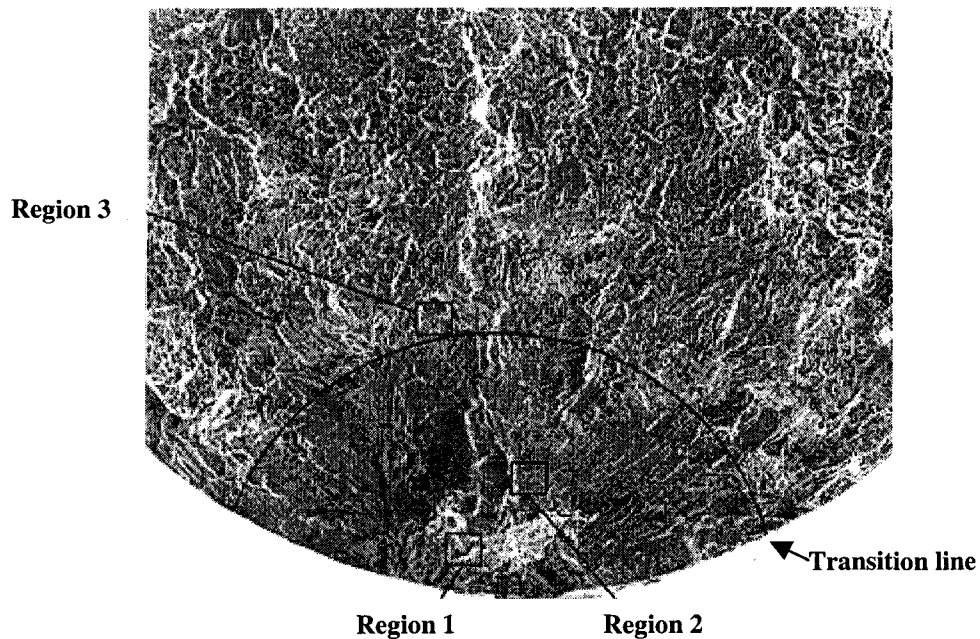


Figure 3.6a: The SEM fracture surface of the axial fatigue sample in Table 3 having a life of 331, 629 cycles [23].

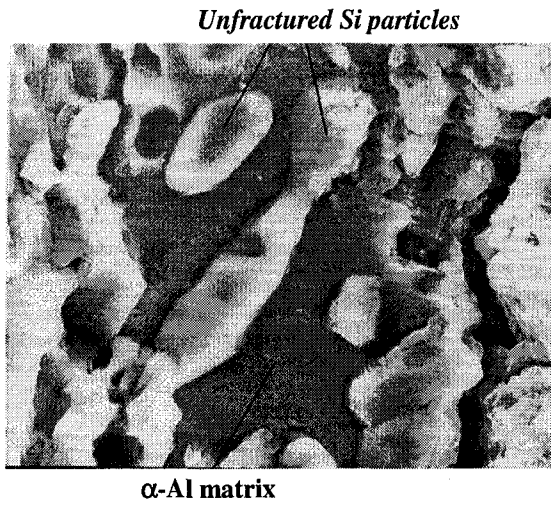


Figure 3.6b: Region 1 at 5,000X mag.

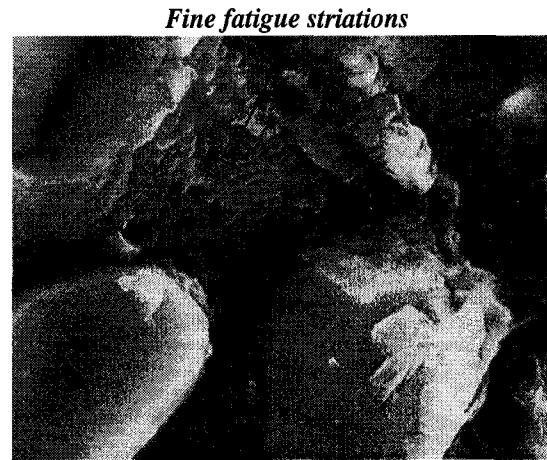


Figure 3.6c: Region 1 at 10,000X mag.

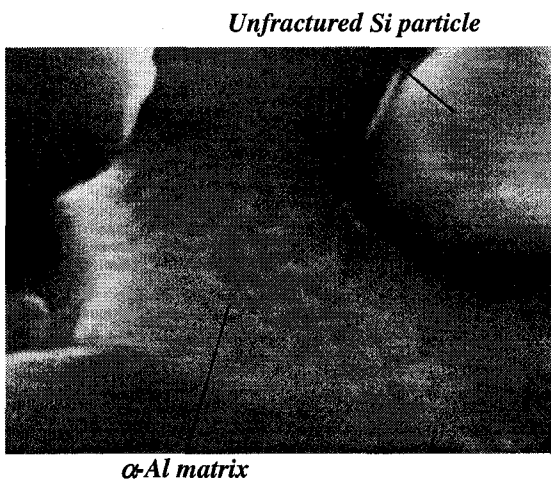


Figure 3.6d: Region 2 at 10,000X mag.

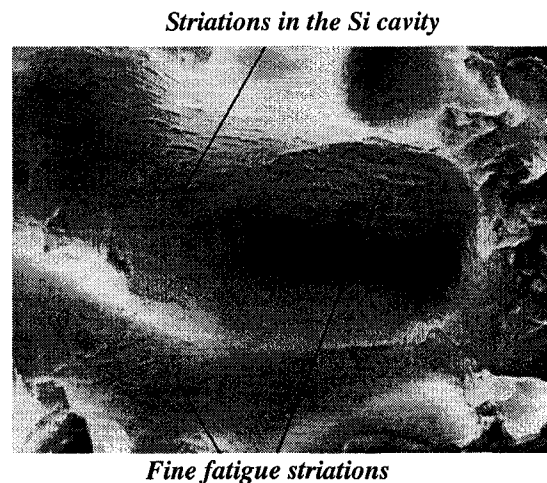


Figure 3.6e: Region 2 at 15,000X mag.

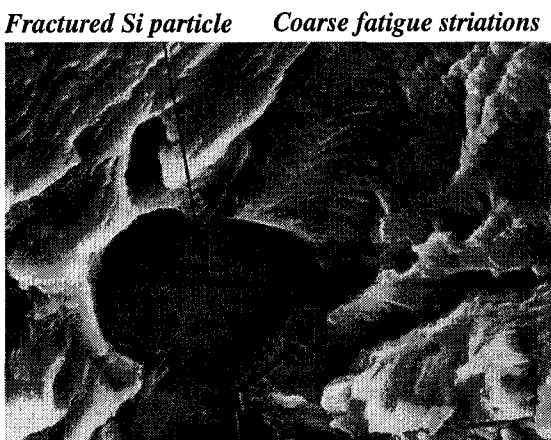


Figure 3.6f: Region 3 at 5,000X mag.

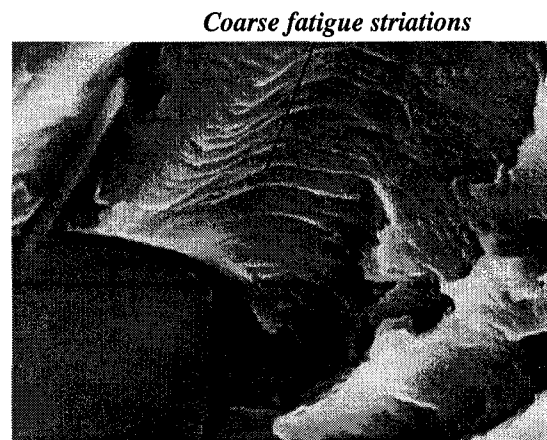


Figure 3.6g: Region 3 at 10,000X mag.

SEM images of the fracture surface close to the transition line are shown in Figures 3.6d and 3.6e (**Region 2**). Generally, the Si particle/ α -Al decohesion mechanism is still prevalent within the structure, except that the striation spacing is larger and a growing number of small Si particles are now becoming fractured, indicative of higher crack driving forces.

Past the transition line of Figure 3.6a, shown at higher SEM magnifications in Figures 3.6f and 3.6g, the striation width increased to $1\mu\text{m}$, corresponding to a crack growth rate of 1×10^{-6} m/cycle. The roughness seen in Figure 3.6a past the transition line is due to the fact that Si particles are fracturing as opposed to decohesing from the Al matrix on the fracture surface.

The difference in fracture behaviour seen before and after the transition line in Figure 3.6a was believed to be due to the size of the plastic zone associated with the crack tip. Before the transition line growth the plastic zone was not large enough to encompass secondary phase constituents. The small plastic zone cannot produce enough elastic energy required to fracture the entire Si platelet, but is large enough to induce local decohesion of the Si platelet from the α -Al matrix. However, the Si platelets orientated parallel to the principle stress directions were generally fractured. The work of Gall et al. [23] could not observe this phenomenon near the crack nucleation site, but Lee et al. [82] observed many cracked Si crystals where the principal axis was perpendicular to the fracture surface.

At higher stress intensities, or when the crack becomes sufficiently large, the plastic zone is now large enough to encompass secondary phases ahead of the crack tip. This results in Si platelets fracturing prior to the arrival of the crack tip, providing a material path of weakness for the crack to propagate. Lee et al. [82], Major et al. [83], Zhang et al. [84] and Gall et al. [28] all proposed that decohesion may also occur between the Si platelet and the α -Al matrix resulting in a nucleated void prior to the arrival of the crack tip in the A356 alloy. Eventually the nucleated void and the advancing crack tip would coalesce. Since the stress intensity is the highest at the crack tip, the voids that result from interfacial decohesion decrease in size at larger distances from the advancing crack tip. This observation was made to explain the presence of non-fractured Si particles found past their transition line in the 413 alloy fatigue samples of Lee et al. [82].

3.3 Effect of Cooling Rate on the Fatigue Crack Growth in Al-Si Alloys

The contributing factors of porosity distribution and secondary phase size on fatigue crack propagation rates will change in their relative proportions when the cooling rate of the alloy increases. In thin sections of sand castings mechanical properties are generally better than in thicker cast cross-sections, or sections adjacent to risers, due to the slower cooling rates.

The wedge cast test sample, as seen in Figure 3.7, was used by metal casting researchers at the Ford Motor Company Scientific Research Laboratory, at the University of Michigan and at the University of Windsor to evaluate the effect of cooling rate on the cast structure and on mechanical properties of automotive grade W319 and 356 alloys [19-22, 78, 81]. The narrow end of the wedge sand casting had a copper chill, while the thicker region of the wedge was next to a riser. This configuration allows for directional solidification from the thin section to the thicker section in order to reduce the formation of a hot spot inducing shrinkage porosity. The solidification time of the chilled end was approximately 40 seconds and near the risered end about 2500 seconds.

This wedge mould design was widely utilized in fatigue studies by Boileau et al. [21] on 356-T6 alloy wedges and in another study on W319-T6,T7 wedges by Boileau et al. [78], Caton et al. [22], and on synthetic Al-Si-Cu compositions by Ren [19]. It was found that in the A356, W319 and synthetic compositions that fatigue properties decreased as cooling rates for alloy solidification decreased.

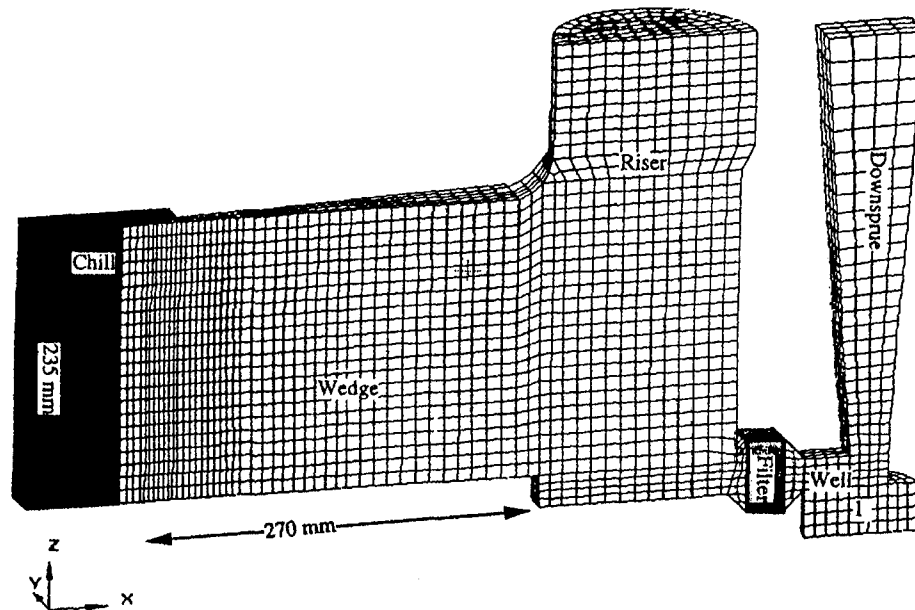


Figure 3.7: A schematic of the wedge casting with chill, riser, down spure and ingate. This wedge was used by Boileau et al. [21] for A356-T6, Boileau et al. [78] for W319-T6,T7, Caton et al. [22] for W319-T6, and Ren [19] for Al-(7-9% wt.)Si-(1-4% wt.)Cu synthetic alloys.

Boileau et al. [21, 78], studied the number of cycles till failure on axial fatigue specimens ($R = -1.0$) along the wedge length both in *Hot Isostatic Pressed* (HIP) and *non-Hot Isostatic Pressed* (non-HIP) conditions. HIP treatments are preformed by placing a casting under hydrostatic pressure at high temperature for a set period of time (Pressure = 105 MPa, Temp. = 480°C, duration = 3 hours [21]). It was found that the decrease in the fatigue life (from the chilled end to the risered end) was considerably more for the HIP W319 alloy (~10x) than for the HIP and non-HIP 356 alloy (~3x) when the applied cyclic stress was 138 MPa. This was due to the fact that segregation of Cu-rich phases in the

W319 alloy resulted in differing matrix hardness and an increase in matrix discontinuities between Al and Al₂Cu. In addition, the overall maximum porosity size in the W319 (10% area fraction in the thick section) is much larger than for the 356 alloy (only 0.50% area fraction in the thick section). The wedges studied by Ren [19] had much lower porosity, where the risered end had only ~ 0.25% for all compositions (*see Figure 1.0, Chapter One*). There are three reasons for this:

- 1) Both alloys (W319 & 356) studied by Boileau et al. [21, 78] were modified with 300 ppm of Sr, which induces much higher levels of porosity in the W319 alloy than in the 356 alloy. Ren [19] added only 100 ppm of Sr.
- 2) Due to the increases in both Si and Cu in the W319 alloy over the 356 alloy, more shrinkage based pores will form in the W319 alloy.
- 3) The riser in the wedge was increased in size (40%) for the wedges of Ren [19] which would have enhanced directional solidification, and minimized feeding problems.

The monotonic mechanical testing done on the wedge cast W319 alloy samples in the T6 condition shows a decrease in tensile and yield strength and an increase in elongation [78]. In the T7 condition the same general trend was found except that elongation was higher and the tensile and yield strengths were lower [78]. The decrease in yield strength was not expected by Boileau et al. [81] since it was believed that the solution treatment was adequate to homogenize the dendrites with Cu and Mg. However, macrosegregation most likely occurred and the Cu content at the risered end of the wedge may not be the same as in the chilled end. Ren [19] quantified the amount of Cu phases along the wedges

for his work and found that the amount (area percent from image analysis) of Cu phases decreased from the chilled end to the risered end and that the size of the Al_2Cu particles were larger at the risered end. The limited amount of monotonic testing along the wedges used by Ren [19] basically showed a similar behaviour as for the wedges by Boileau et al. [78]. Research carried out by Caton et al. [22] also showed the same trend.

Boileau et al. [78] found that for the W319 alloy fatigue samples fatigue lives were generally the same in both the T6 and T7 conditions. Intuitively this would not support the findings of the monotonic testing which shows that the matrix had become softer in the T7 condition and this should have affected crack propagation. However, the high porosity levels presumably dominated fatigue lives in the W319 samples and not the test treatment used (T6 or T7 condition). If porosity was much lower in the wedge casting the effect of the matrix condition may have played a role in fatigue performance.

A point of interest not addressed thus far is what is the size and distribution of pores that ultimately caused failure of the fatigue test samples? To answer this Boileau et al. [21] put some of the 356-T6 alloy wedges in the HIP process. The authors studying the wedge castings used the HIP method to separate the effects of pores and matrix/secondary phase constituent discontinuities on the fatigue behavior in the 356 alloy. It was found that after the HIP process the fatigue life increased 10-fold as compared to the non-HIP wedge. Analysis of the fracture surface of the HIP fatigue specimens revealed no porosity.

However, through SEM analysis crack initiation seems to have occurred from irregular shaped features thought to be the remanence of microvoids that collapsed during the HIP process. In non-HIP processed samples, failures were definitely due to shrinkage pores being located near the subsurface of the fatigue sample. For the W319 fatigue samples studied this was also the case. Unfortunately no distinct relationship between fatigue life and pore size and distribution could be made. It was found that in some cases, where a particular pore size caused failure in one sample, a sample having a shorter fatigue life had even smaller pores within the fracture surface. In addition it was found that the average pore sizes found on a metallographic cross-section were smaller than those found on the fracture surface. Thus Boileau et al. [78] argued that determining pore size via metallographic analysis might result in an underestimate in probable fatigue life.

This observation, that maximum pore size and not pore density is a larger determining factor in crack nucleation and propagation has also been made by Major [83] on Sr-modified and unmodified A356 alloy, Zhang et al. [84] on A356 with different levels of both Sr and H₂, and by Gall et al. [22] on A356 alloy with 100 ppm Sr.

Intuitively if a large shrink pore has larger stress intensity associated with the tip, then it surely would initiate a growing crack over smaller pores. However, the point being made here is that observing the largest pore in the polished cross-section may not yield the actual largest pore that would initiate a fatigue crack. However, if one refers the results as outlined in Table 3, porosity initiated the fatigue cracks, and the fatigue life was considerably shortened as the initiating pore became larger.

Caton et al. [22] showed in a more detailed fatigue study of the W319 alloy wedge castings the crack propagation rates of small cracks on axial fatigue samples ($R = -1.0$, 30Hz). These axial fatigue test samples had 28 mm radius notches ground on two sides (positioned 180° from one another) in order to facilitate crack nucleation on the notched surface and use replication methods (*using cellulose acetate*). This is illustrated in Figure 3.8. Long cracks analysis was also conducted on (Compression-Tension) CT samples ($R = 0.1$, 20 Hz). Both types of fatigue samples were cast in the same wedge mould as shown in Figure 3.7. In this case the authors employed the HIP process in order to better understand the propagation mechanics through matrix material and secondary phase constituents.

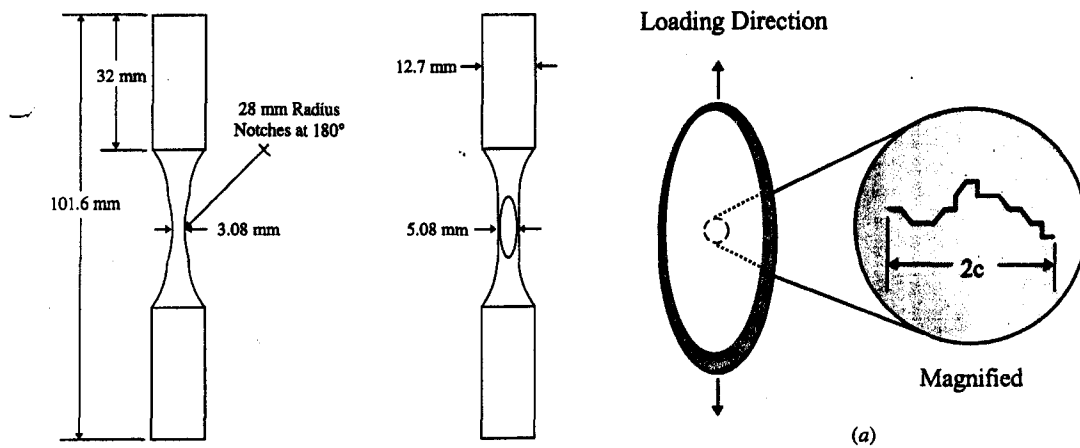


Figure 3.8: Dimensions of the axial fatigue specimen with 28 mm radius polished notched surfaces [22].

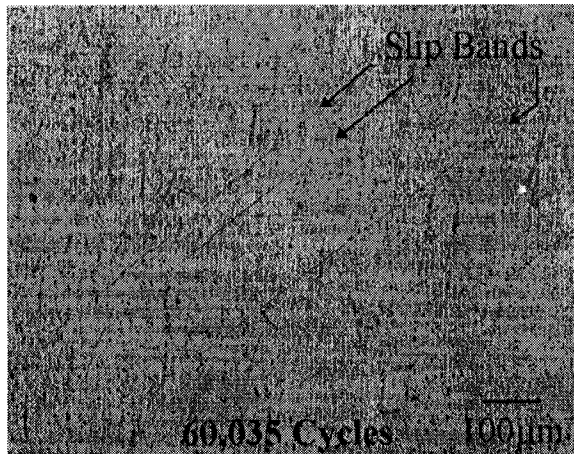


Figure 3.9a: SEM micrograph of an acetate replica showing formation of slip bands prior to crack growth near the chilled region of the W319 alloy wedge casting [22].

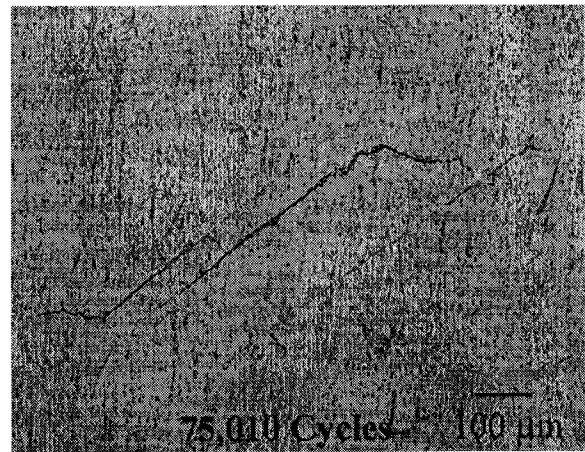


Figure 3.9b: SEM micrograph of an acetate replica of the same sample in Figure 3.3c. The crack departs perpendicular to the loading direction [22].

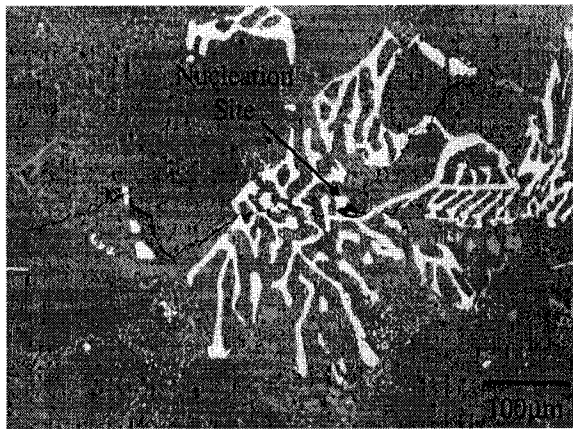


Figure 3.9c: SEM micrograph of a crack nucleated from a $\text{Al}_{15}(\text{Mn,Fe})_3\text{Si}_2$ script phase in the W319 alloy sample extracted near the risered end of the wedge sample [22].

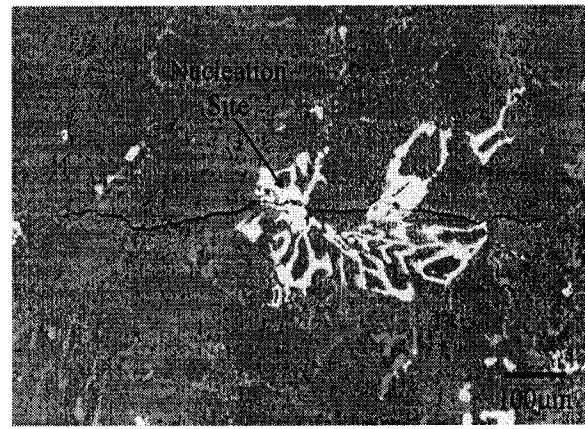


Figure 3.9d: SEM micrograph of a nucleated crack from a $\text{Al}_{15}(\text{Mn,Fe})_3\text{Si}_2$ script phase from another W319 wedge sample extracted from the risered end of the wedge casting [22].

The fatigue testing was interrupted and replication occurred at static holds of 70% σ_{yield} . The replicas were then examined using optical microscopy and SEM analysis where the crack length as a function of cycles was measured.

Caton et al. [22] found that the nucleation of cracks from fatigue test samples excised from the HIP wedge mould were not from pores, as in the case of the non HIP fatigue samples of Cooper et al. [85], and Boileau et al. [21, 81], but from slip bands as seen in Figures 3.9a and 3.9b. Figures 3.9a and 3.9b show the acetate replicas as viewed on the SEM at 60,035 and 70,010 cycles at a 140 MPa amplitude load. Figure 3.9a shows the formation of slip bands and after approximately 10,000 cycles (as shown in Figure 3.9b) the decohesion of these slip bands occurred. One of the decohesed slips facilitated branching along a direction perpendicular to the load direction. The characterization of the precipitation was not done for these samples. They had undergone a T6 treatment with HIP afterwards. Most likely the W319 samples were overaged (i.e. T7) and slipping was easier than for peak hardness conditions (i.e. T6).

Near the risered end of the wedge casting, where the solidification time is approximately 42 minutes and the secondary phases are large, cracks were observed to nucleate from $\text{Al}_{15}(\text{Mn,Fe})_3\text{Si}_2$ phases. Figures 3.9c and 3.9d are two examples of crack nucleation sites. Once a crack has nucleated within the $\text{Al}_{15}(\text{Mn,Fe})_3\text{Si}_2$ the fracture apparently grows along the particle length, and then eventually once the crack migrates into the matrix the crack direction then propagates along a new direction perpendicular to the load direction.

It was found that cracks would originate from the chinese script phase before any cracking of the Si particles.

It is known that the cohesion between the matrix and $\text{Al}_{15}(\text{Mn,Fe})_3\text{Si}_2$ is better than for the Si or Al_5FeSi platelets. In addition, crack propagation occurred more easily through both Fe (*needle and chinese script*) and Cu containing phases along the crack as observed on a polished cross-section.

Chapter Four

Experimental Methodology

4.0 Introduction to Experimental Methodology

This chapter discusses the experimental methodology utilized to yield the results contained in Chapter 5, *Metallurgy of the WA328 & WB328 Alloys*, and Chapter 6, *Castability & Mechanical Integrity of the V8 Engine Block cast from the WA328 & WB328 Alloys*.

In this chapter test alloy composition and test alloy designation are discussed followed by the analytical testing methods used to assess the V8 engine blocks and thermal analysis test samples. These analytical testing methods are metallographic (*Light Optical Microscopy (LOM) with Image Analysis (IA) and Scanning Electron Microscopy (SEM)*) analysis, radiographic analysis, solidification analysis (*Mushy Zone Development assessment via thermal analysis*), and monotonic analysis and fatigue analysis.

Part of the aforementioned metallurgical analysis was carried out using the *Universal Metallurgical Simulator & Analyzer (UMSA)* and the *Environmental Aluminum Thermal Analysis System (Enviro-AITAS)* platforms. Description of the UMSA setup and the Enviro-AITAS setup is given in subsequent sections of this chapter. The *Instron 8801 Universal Mechanical Testing Workstation* was used to yield the monotonic and fatigue data for the new alloys.

4.1 Production Test Alloy Chemistry Specification

The newly developed alloys investigated within this dissertation are a slightly modified version of the *synthetic* Al-9wt.%Si-1wt.%Cu alloy studied by Ren [19]. The synthetic version of the Al-9wt.%Si-1wt.%Cu alloy has a much lower level of impurities and has been treated with in-furnace added Sr (~ 100 ppm).

The ranges of principal alloying elements for the Al-9wt.%Si-1wt.%Cu alloy will be within 1wt.% (i.e. 8.5wt.% to 9.5wt.% of Si, and 0.5 wt.% to 1.5 wt.% of Cu). The composition of the rest of the alloy (i.e. Mg, Ni, etc.) will be set as they are for the W319 alloy. Table 4.0 summarizes the compositional range of the test alloy ingot used to produce the V8 engine blocks. In addition, two different Fe levels (0.40wt.% and 0.80wt.%) of the production (secondary grades) Al-9wt.%Si-1wt.%Cu alloy will be investigated aiming to reduce the alloy cost per pound (see Table 4.1). The test alloys were acquired from Wabash Alloys, Guelph Ontario in ingot form.

The production Al-9wt.%Si-1wt.%Cu test alloy investigated within this dissertation does not have an Aluminum Association (AA) designation. This alloy is in fact a hybrid alloy of another alloy recognized by the AA. The AA 328.1 cast alloy is similar to the test alloys investigated in this dissertation, just as W319 and AA 319 are similar (see Table 4.0). Thus the two test alloys will be denoted the WA328 alloy and the WB328 alloy. The prefixes A and B denote the two Fe variants [3], while the prefix W reflects the fact that this alloy is destined for the CPSP used at the WAP.

Table 4.0: Comparison between the AA version and the hybrid version of the 319 and 328 alloys. Wabash Alloys supplied the incoming WA328 and the WB328 alloy ingots as per the limit specification listed in this Table.

<i>Alloy</i>		<i>Si</i>	<i>Fe</i>	<i>Cu</i>	<i>Mn</i>	<i>Mg</i>	<i>Ni</i>	<i>Zn</i>	<i>Ti</i>
WB328	Max	9.5	0.9	1.5	0.3	0.50	0.30	1.0	0.25
	Min	8.5	-	0.5	0.2	0.05	-	-	-
WA328	Max	9.5	0.4	1.5	0.3	0.50	0.30	1.0	0.25
	Min	8.5	-	0.5	0.2	0.05	-	-	-
Synthetic Al9Si1Cu [19]	Max	8.9	0.12	1.0	0.5	0.31	0.21	0.007	0.09
	Min	-	-	-	-	-	-	-	-
AA 328.0	Max	8.5	1.0	2.0	0.6	0.6	-	1.5	0.25
	Min	7.5	-	1.0	0.2	0.2	-	-	-
AA 328.2	Max	8.5	0.6	2.0	0.6	0.6	-	1.5	0.25
	Min	7.5	-	1.0	0.2	0.2	-	-	-
W319 (WAP) [17]	Max	8.0	0.4	3.8	0.3	0.50	0.30	1.0	0.25
	Min	6.5	-	2.2	0.2	0.05	-	-	-
AA 319.0	Max	6.5	1.0	4.0	0.5	0.1	nl	3.0	0.25
	Min	5.5	-	3.0	-	-	-	-	-
AA 319.1	Max	6.5	0.8	4.0	0.5	> 0.1	0.35	3.0	0.25
	Min	5.5	-	3.0	-	-	-	-	-

Table 4.1: Cost differential of the alloy per 50 million pounds. The cost of 50 million pounds of W319 alloy is \$35,000,000.00.

<i>Alloy Type</i>	<i>Cost Reduction/ 50 million pounds</i>
W319	0
WA328	\$150,000.00
WB328	\$375,000.00

4.2 Casting of the V8 Engine Block

A 4000lb capacity gas fired melting furnace, having the CPSP capability, was used to melt the WA328 and WB328 alloys at the Nemak Engineering Center (NEC). Degassing using argon was done via a perforated lance at the back of the melting furnace to ensure that the hydrogen levels would be kept to a minimum. Only four V8 engine block castings could be cast at a time before the melting furnace would have to be recharged with new ingots.

The Fe content of the alloy was adjusted up to 0.80wt.% Fe by adding a Al-24wt.%Fe master alloy to the melting furnace containing the melt. In order to maintain the proper ratio of Fe to Mn at less than 2:1 [2, 11, 31, 32] so as to nucleate more α -script phase over the β -phase, Mn was added to the melting furnace using a Al-25wt.%Mn master alloy. The chemistry was verified on a daily basis by the use of an Optical Emission Spectrometer (OES), as per the ASTM E1251 specification. The results recorded each day that an OES disk was cast and checked for chemistry are shown in Appendix D.

The total number of V8 engine blocks manufactured for this research was *forty three* (43). *Twenty-one* (21) V8 engine blocks labeled A1 through to A21 were cast in the WA328 alloy and V8 engine blocks labeled A22 through to A43 were cast in the WB328 alloy. The type of test samples that were excised, and from which bulkhead, is discussed in Section 4.4.

4.3 Heat Treatment of the V8 Engine Block

Thermal Sand Removal (TSR) was performed at NEC and carried out at $499 \pm 5^\circ\text{C}$ for 4.5 hours. The castings were then air quenched and shipped to B&W Heat Treat Limited in Kitchener, Ontario, which is the facility that heat treats production V8 engine blocks cast from the W319 alloy. The heat treatment performed at B&W was a T6 (solution, quench and then age) treatment, and was the same one used for the wedge castings made of six synthetic Al-Si-Cu alloy compositions evaluated by the IRC [19, 20]. Table 4.2 illustrates the thermal history used on the V8 engine blocks cast in the WA328 alloy and the WB328 alloy.

Table 4.2: The summary of the heat treatment scheme used for the WA328, WB328 and the W319 alloys.

<i>Alloy cast in the V8 mould</i>	<i>TSR Temperature and Duration</i>	<i>Solution Temperature and Duration</i>	<i>Age Temperature and Duration</i>
WA328 & WB328 Alloys	$499 \pm 5^\circ\text{C}$ 4.5 Hours (Air Quench)	$505 \pm 5^\circ\text{C}$ 5 Hours (Boiling Water Quench)	$230 \pm 5^\circ\text{C}$ 4 Hours
W319 Alloy	$499 \pm 5^\circ\text{C}$ 4.5 Hours (Air Quench)	$495 \pm 5^\circ\text{C}$ 8 Hours (Boiling Water Quench)	$270 \pm 5^\circ\text{C}$ 5.5 Hours

4.4 Description of Test Samples Excised From the V8 Engine Block

The test samples that were cut from the bulkhead section of the V8 engine block are referred to as the UMSA test samples (Figures 4.1, 4.2a & 4.2b), metallographic test samples (Figure 4.1), the fatigue test samples (Figure 4.3a), and the tensile test samples (Figure 4.3b). The engine block that was sectioned is shown in Table 4.3. A picture showing the V8 engine block along with the layout of bulkhead sections A through E is shown in Figure 4.0.

Figure 4.1 shows the layout of the bulkhead (bulkhead E) of the V8 engine block and the location of the UMSA test samples and the orientation of the metallographic test samples. Bulkhead E was used because it was the bulkhead which was assessed using the in-situ thermal analysis method (see Appendix C). The correlation with the bulkhead cooling rate is made with the microstructure observed in the metallographic test samples.

The UMSA test samples, as seen in Figures 4.2a and b, have a cylindrical geometry and are 18mm in height and 14mm in diameter. A 13.5 mm deep hole, which is 1.5 mm in diameter, is drilled to facilitate the placement of a thermocouple (K-type) during thermal analysis testing.

Fatigue and tensile test samples came from bulkheads A through E. Figure 4.3a shows the orientation as of two fatigue test samples within bulkhead section A. This is the same orientation as the samples cut from in bulkheads B through E. The tensile test samples would have the same orientation since the tensile samples had similar dimensions as the fatigue test samples. This is shown in Figure 4.3b. Figures 4.4a and 4.4b show the listed

dimensions and tolerances as prescribed by ASTM standards for the fatigue test sample (ASTM 466-6) and the tensile test sample (ASTM E-8).

The risers were kept for analysis of the volume of riser sink and the orientation of the riser sink. While no in-mould grain refining or Sr modification were used for the WA328 and WB328 alloys, many of the V8 engine block castings made using the W319 alloy were. The condition of the risers made using the W319 alloy, which were cast with in-mould master alloy additions, were used as a comparison to the riser performance of the WA328 alloy being assessed in this dissertation. The sink of a riser refers to the depression left by the drainage of liquid metal down into the mushy regions of the adjoining bulkhead section of the engine block. This is illustrated in Figures 4.5a and 4.5b.

The method of evaluating the riser sink was done by adding water from a graduated cylinder into the sink and recording the volumetric amount of water added. This is illustrated in Figures 4.5c and 4.5d. The risers were sealed with Epoxy Steel[®] (a filler product by Lepage[®]). The sealing of the hot tears was adequate since no leakage of water from the sinks occurred during volumetric measuring and thus accurate volumetric readings were made. The volume of each riser of the V8 engine block is listed in Table 4.4.

Table 4.3: The identification of the V8 engine blocks used for this study along with the test sample type excised from the bulkhead sections.

V8 Engine Block Identification	Alloy	Bulkhead section				
		A	B	C	D	E
A1	WA328	X-Ray Radiography				
A2	WA328					
A3	WA328					
A4	WA328	UMSA				
A7	WA328	Metallographic analysis for Porosity (Percent area, mean pore diameter and largest pore found)				
A9	WA328	Fatigue	Fatigue	Fatigue	Tensile (R)	
A10	WA328	Fatigue	Fatigue	Fatigue	Fatigue	Fatigue
A11	WA328	Fatigue	Fatigue	Tensile (R)	Fatigue	Fatigue
A17	WA328		Tensile (R)	Fatigue	Fatigue	Fatigue
A18	WA328		Fatigue	Fatigue	Fatigue	
A21	WA328		Tensile (R)	Tensile (R)	Tensile (R)	
A35	WB328	Radiography				
A41	WB328	Metallographic analysis for Porosity (Percent area, mean pore diameter and largest pore found)				
A43	WB328	UMSA				

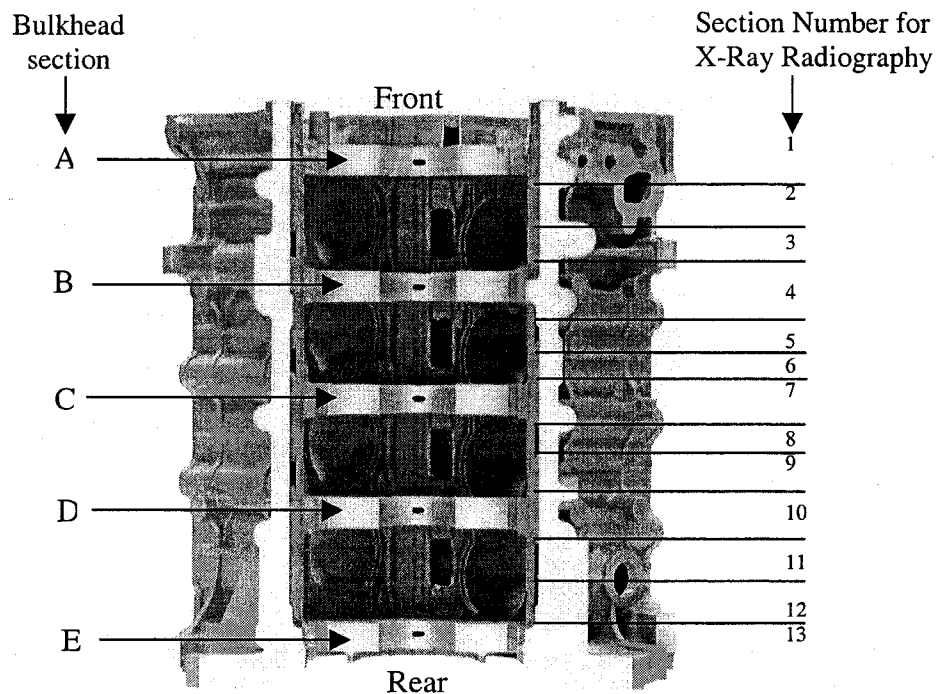


Figure 4.0: The picture of the V8 engine block and the identification of the bulkhead sections and the sections that were radiographed.

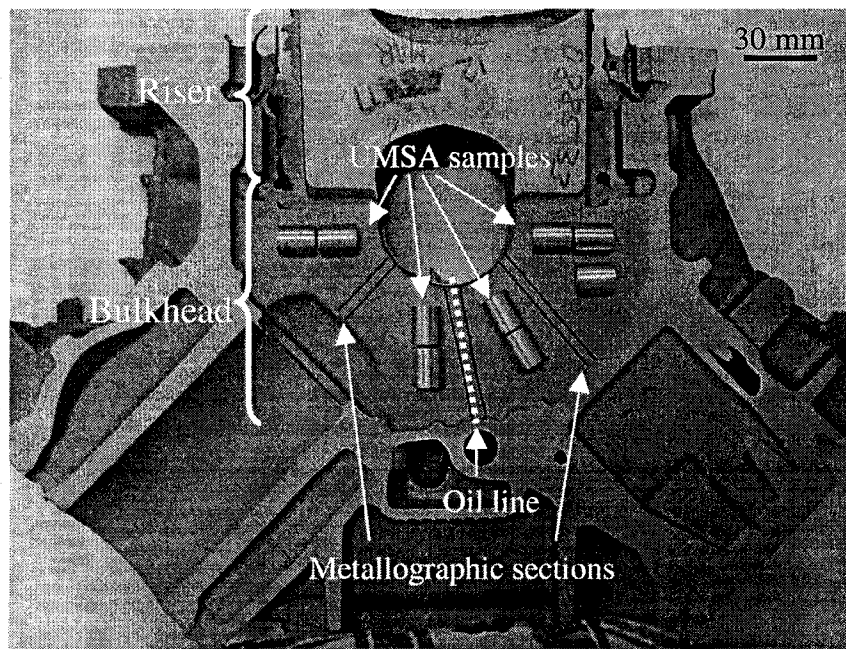


Figure 4.1: Bulkhead A of the V8 engine block with the outline of where metallographic samples were excised and the overlay of the location of UMSA samples.

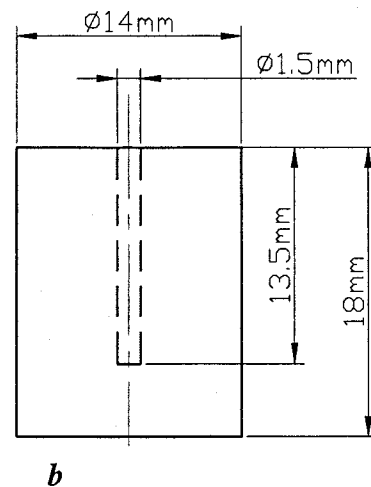
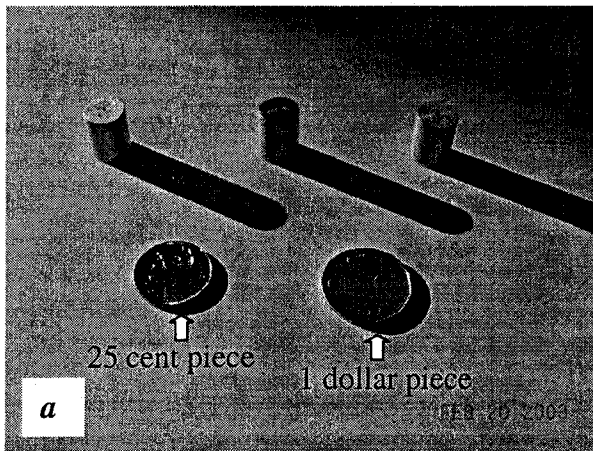


Figure 4.2: a) Picture of the UMSA test sample, b) schematic of the UMSA test sample with dimensions.

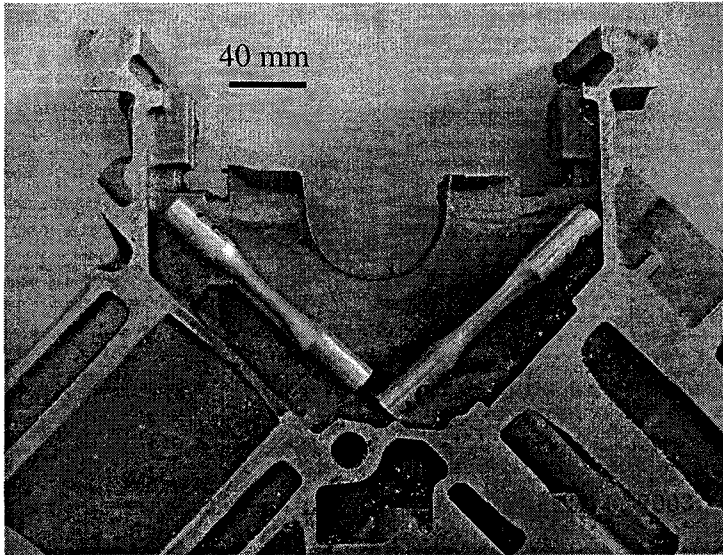


Figure 4.3a: The orientation of the fatigue test samples excised from the bulkhead section of the V8 Engine Block (Bulkhead A as an example here)

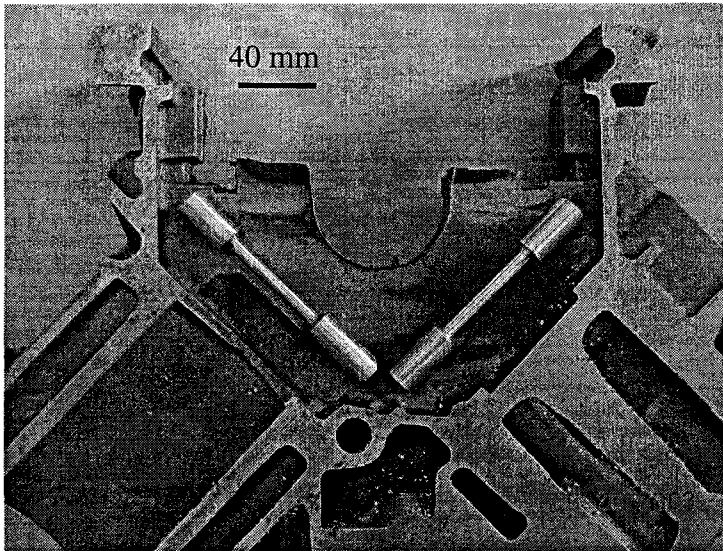
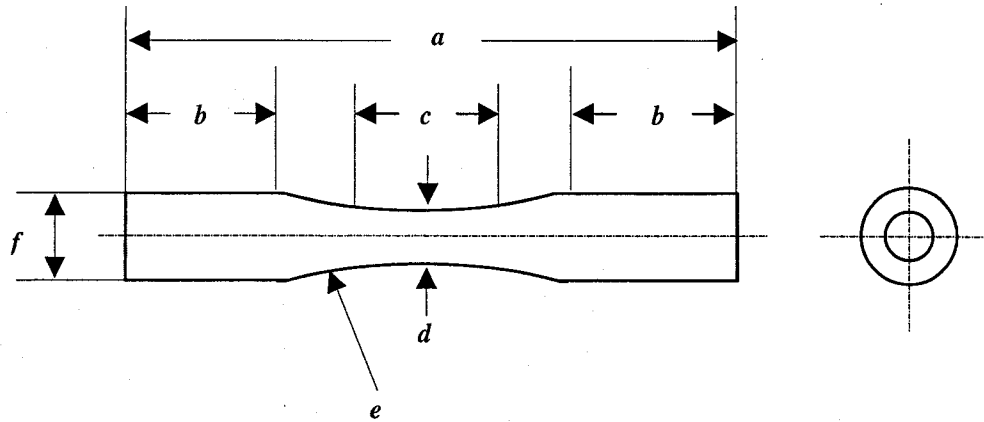
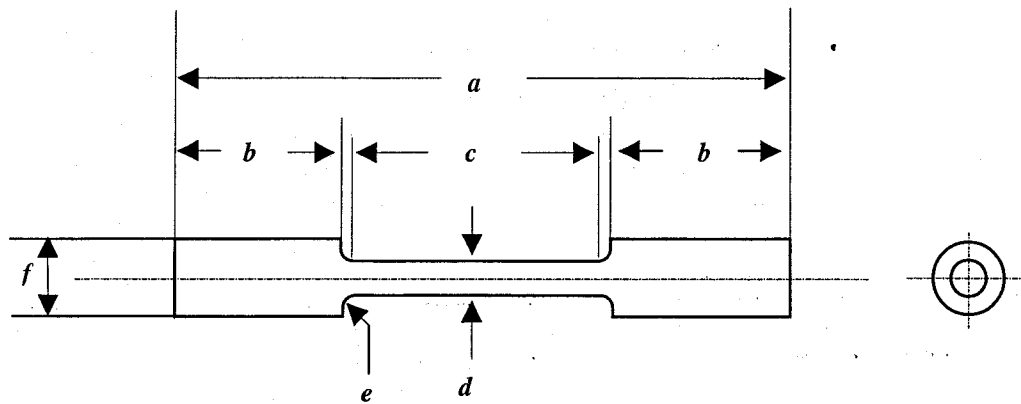


Figure 4.3b: The orientation of the tensile test samples excised from the bulkhead section of the V8 Engine Block (Bulkhead A as an example here)



Fatigue test sample feature	<i>a</i>	<i>b</i>	<i>c</i>	<i>d</i>	<i>e</i>	<i>f</i>
Dimension (mm)	127.0	28.5	16.0	8.0	63.75	15.0

Figure 4.4a: Description of the fatigue test sample as outlined by *ASTM 466-96*.



Tensile test sample feature	<i>a</i>	<i>b</i>	<i>c</i>	<i>d</i>	<i>e</i>	<i>f</i>
Dimension (mm)	110	32.0	47.0	6.0	6.0	13.7

Figure 4.4b: Description of the tensile test sample as outlined by *ASTM E-8*.

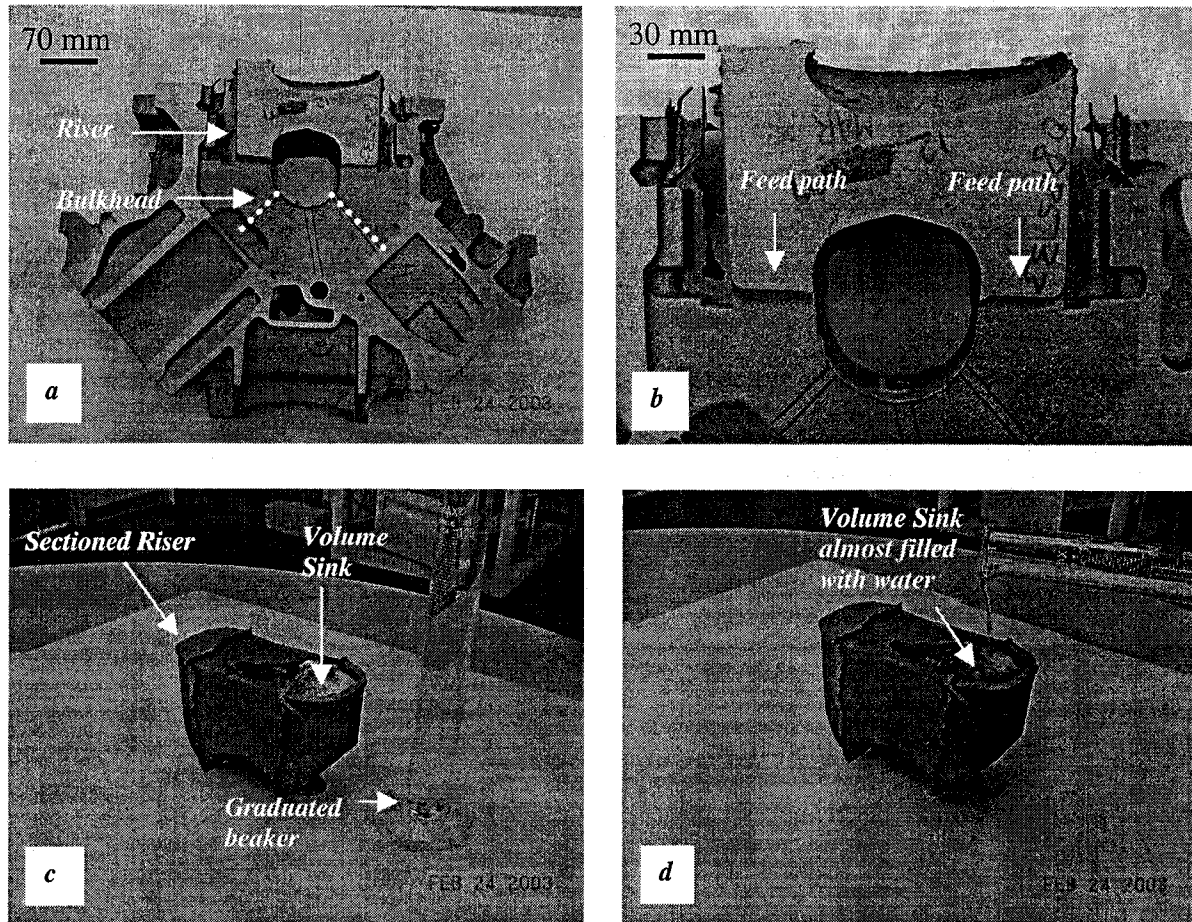


Figure 4.5: a) The view of the riser in relation to the bulkhead and cylinder cavities, b) a zoom up view of the riser and the sink cavity, c) the riser (from riser D, casting A6) along with a graduated cylinder filled with water, d) water deposited within the riser open sink until filled. Once the riser is filled the remaining water is measured and subtracted from the initial amount (in mls) of water prior to pouring.

Table 4.4: Summary of the total volume of all risers of the V8 engine block.

<i>Riser Identification</i>	<i>Volume of riser (cm³)</i>
A	972.1
B	749.4
C	749.4
D	749.4
E	1002.4

4.4.1 Metallographic Test Sample Analysis

Light Optical Microscopy (LOM) was used to assess the morphology of structural characteristics (*Secondary Dendrite Arm Spacing* (λ_2), *Dendrite Cell Size* (DCS_z), and *Area Fraction of Sectioned Primary α -Al Dendrites* (AFSP(α -Al) at $\Delta T_{SRAN}^{\alpha DEN}$)). Phase assessment and quantification was done using the Leica 550 DMR Image Analysis system (at the University of Windsor). The porosity (area fraction, mean pore diameter and maximum pore found in the V8 engine block bulkhead sections) was measured using the Clemex Image Analysis System (JS-2000) at the NEC. Both Image Analysis (IA) systems were calibrated using either Leica or Clemex calibration standards (depending on the IA system used) before any cast structure features were measured.

Scanning Electron Microscope (SEM) analysis of the cast structure and the fracture surfaces of fatigue test samples were conducted using a JEOL JSM 5800 system. Observation of phase constituents was done in the Back Scattered Electron (BSE) mode under magnifications ranging from 100X to 1,500X. Qualitative chemical analysis was determined by using the Energy Dispersive X-Ray (EDX) microanalysis method using the Noran EDX Spectrometer. The observation of the fatigue test sample fracture surface was done in the Secondary Electron (SE) mode under magnifications ranging from 20X to 250X. The accelerating voltage in both BSE and SE modes was 20keV.

The size of this interaction volume is related to the atomic number (Z) of the element which the incident beam has interacted. It is from this interaction volume from which generated X-rays emanate. There are two methods in which the depth of the interaction volume can be

assessed: the *Bethe Range* and the *Kanaya-Okayama Range* [86]. Table 4.5 lists the calculated values of the depth of penetration of the electron from the incident beam of 20 KeV with the assumption of a zero tilt angle [86].

Table 4.5: Summary of the depth of penetration with an incident beam energy of 20 KeV.

<i>Element (Z)</i>	<i>Bethe Range</i>	<i>Kanaya-Okayama Range</i>
Al (13)	6.0 μm	4.2 μm
Fe (26)	2.4 μm	-
Cu (29)	2.3 μm	1.5 μm

Clearly from Table 4.5 the largest depth of interaction volume will be in the α -Al dendrites assuming no phase becomes incorporated within that volume. As higher atomic number elements are found in phases the interaction volume size will decrease. When performing EDX analysis an acquisition time of 2 minutes was used to receive a sufficient number of X-ray counts.

4.4.1.1 Phase Identification

Both heat treated (excised bulkhead sections) and non-heat treated (Enviro-ALIAS sectioned test samples) were analyzed using the SEM with EDX microanalysis techniques. Using light optical microscopy (LOM) methods the phase morphology and colour were compared to that of existing Atlases for the 3xx.x series alloys [2, 11, 87, 88].

4.4.1.2 Porosity Measurements

Due to the orientation of the metallographic test sample seen in Figure 4.1 the porosity data gathered via Image Analysis (IA) methods gave a relative sense of the porosity encountered in the reduced section of a fatigue test sample (see Figure 4.3a) than if the metallographic sectioning was to occur elsewhere in the bulkhead. Table 4.3 lists which bulkheads were sectioned and evaluated for porosity in this fashion.

Metallographically the percent area fraction porosity (with standard deviation), along with the mean pore size (with standard deviation) and the maximum (longest diameter) pore diameter were analyzed for each polished sections via the IA method. The IA was performed using a minimum of 25 fields at 50X magnification which covered an area of 72 mm². The Ford Engineering Material Specification WSE-M2A151-A3 requires that the minimum area for porosity analysis be no less than 25 mm² and that no single pore found will exceed 750 μm along any dimension [17].

4.4.1.3 Secondary Dendrite Arm Spacing (SDAS or λ_2) & Dendrite Cell Size (DCSz) Measurements

λ_2 was measured in the UMSA test samples, Enviro-ALTAS test samples and the V8 engine block casting cast in the WA328, the WB328 and in the W319 alloys. The value of λ_2 was also measured for the UMSA test samples which were quenched before fully achieving solidification. The method used for λ_2 measurements is the same as that outlined in the Ford Engineering Material Specification WSE-M2A151-A3 (also the ASTM E 3). That is, at a

magnification of 100X several lines are drawn which orthogonally intersect secondary dendrites. The WSE-M2A151-A3 specification requires that this is to be done 10 times in total for a single metallographic test sample. However in this dissertation this was performed 50 times along with a calculated standard deviation.

No standard (ASTM or Ford Engineering Material Specification) exists for the measurement of the DCSz. However this measurement was performed for this dissertation. It was decided to measure a total of 200 dendrite cell sizes by determining the length from one side of the dendrite cell surface to the other side. The magnification used in this measurement was at 200X magnification. As with λ_2 measurements DCSz was measured on quenched and fully solidified UMSA test samples.

4.4.1.4 Quantification of the Area Fraction of Sectioned Primary α -Al Dendrites (AFSP(α -Al))

The IA method was used to quantify the area of sectioned α -Al dendrites observed on an micrographic image. Automated methods invoked concerns about accuracy (due to the fact that α -Al dendrites and α -Al eutectic appear similar in the gray scale). Thus the process of manually drawing an outline of a delineated dendrite on an image (at 200X) and then quantifying that area within that outline was carried out. This process was repeated 40 times per UMSA test sample. The result was a mean percentage of the image occupied by section dendrites along with a standard deviation.

4.4.1.5 Vickers Microhardness & Brinell Hardness Measurements

The dendrite α -Al matrix hardness was measured via the Vickers Microhardness tester for the W319, WA328 and WB328 alloys (UMSA test samples (as-cast) and the bulkhead sections (after heat treatment)). Vickers Microhardness was performed as outlined by the ASTM E-384 specification. Measurements were comprised of a mean with standard deviation from a total of 12 random indentations.

The specific condition of the Vickers Microhardness testing was a load of 25 grams for a duration of 15 seconds. The Vickers Microhardness tester was calibrated by performing indentations on a 200 HV25 calibration standard 10 times. Calibration was found to be 197 ± 6 HV25.

Brinell Hardness testing was performed on the grip ends of the W319 alloy and the WA328 alloy fatigue test samples. The Brinell Hardness was performed as outlined by the ASTM E-10 specification. Measurements were comprised of a mean with standard deviation from a total of 12 random indentations.

The specific condition of the Brinell Hardness test is a load of 500 Kg for a duration of 15 seconds. Brinell Hardness testing was calibrated by performing indentations on a 100 BH500 calibration standard 10 times. Calibration was found to be 102 ± 7 HB500.

4.5 Calibration of K-Type Thermocouples

Thermocouple calibration is important to verify a thermocouple's ability to accurately measure temperature. It is important to eliminate any bias in temperature measurement associated with thermocouple error. Calibration is accomplished by comparison of the thermocouples intended for test measurement to a certified Resistance Temperature Detector (RTD) probe. The RTD probe had been calibrated in an International Standards Organization (ISO) certified laboratory (Acrolab) located in Windsor (ISO-10012) [90].

The types of thermocouples used for thermal analysis investigations were the commercial 0.062 inch (*Outer Diameter*) O.D. and a Low Mass Thermocouple (LMT) specially manufactured by the IRC. Both are K-type thermocouples and have a maximum working temperature of 1260°C well above the maximum temperature of 750°C as reported in this research.

The LMT has the advantage of having the minimum amount of ceramic material for temperature to transmit through. The thermocouples were constructed from Omegatite® Tubing, 8 inches in length, and threaded with one wire of Chromel and the other of Alumel. The ends of the Chromel and Alumel wires, exposed from the end of the Omegatite® Tubing, were welded and then covered with high temperature cement film.

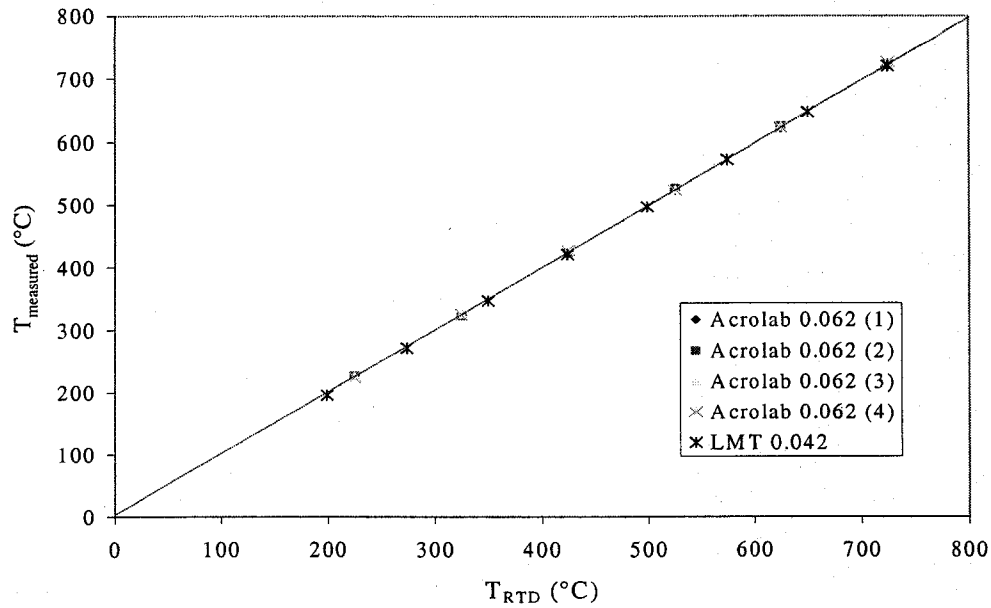


Figure 4.6: Calibration Line for the 0.62'' Acrolab & 0.042'' Low Mass Thermocouple (LMT).

Table 4.6: Values of the linear fitted lines and the respective goodness of fit parameters.

Thermocouple Type (Outer Diameter of Omegatite® Tubing)	Equation $T_{measured} = aT_{RTD} + b$		Goodness of fit (R^2)
	a	b	
Low Mass Thermocouple K-type (0.045in/1.14 mm) Enviro-ALTAS	0.997	-1.7738	0.99997655
Acrolab (1) K-type 0.62in/1.57mm) Enviro-ALTAS	0.999	0.22023	0.99992694
Acrolab (2) K-type 0.62in/1.57mm) Enviro-ALTAS	0.993	3.1214	0.99991254
Acrolab (3) K-type 0.62in/1.57mm) Enviro-ALTAS	0.992	3.5591	0.99991240
Acrolab (4) K-type 0.62in/1.57mm) Enviro-ALTAS	0.995	2.1001	0.99993254

Figure 4.6 shows the plot of the RTD probe versus four Acrolab K-type 0.062" thermocouples and one LMT. As seen in Figure 4.6 the agreement is satisfactory for use and the best fitting linear equation and the goodness of fit (R^2) are shown in Table 4.6. Essentially, the thermocouples that were tested and used to obtain the results in Chapter 5 indicate that reliable temperature measurements were made.

An additional point should be made that the calibration of the Acrolab thermocouples was performed using the temperature readings extracted from the software and data logging systems of the Enviro-ALTAS.

4.6 Thermal Analysis Method using the UMSA

The WA328 and WB328 alloy UMSA test samples were studied for heating and cooling cycles and for the establishment of the characteristic temperature of specific phase nucleation (upon cooling, i.e. $T^{\alpha\text{DEN}}_{\text{NUC}}$, etc., see Appendix A). The heating and cooling cycles were repeated three (3) times on the same sample and with the same LMT to establish repeatability.

During thermal analysis testing the UMSA test sample was placed within an Al_2O_3 based ceramic cup (*UMSA test sample cup*) with dimensions slightly larger (in diameter) than the size of the UMSA test sample so that positioning could be fixed with respect to the coil and thermocouple. A lid made of a similar type of ceramic material as the test sample cup, having a single perforation to facilitate thermocouple insertion within the contained UMSA test sample, was used during heating and cooling testing. The picture of the UMSA is seen in Figure 4.7.

As melting and cooling occurred the cup and lid allowed no molten metal leakage and maintained the dimension of the sample after successive heating and cooling cycles. The temperature and time characteristic points of cooling curves were analyzed as shown in Appendix F.

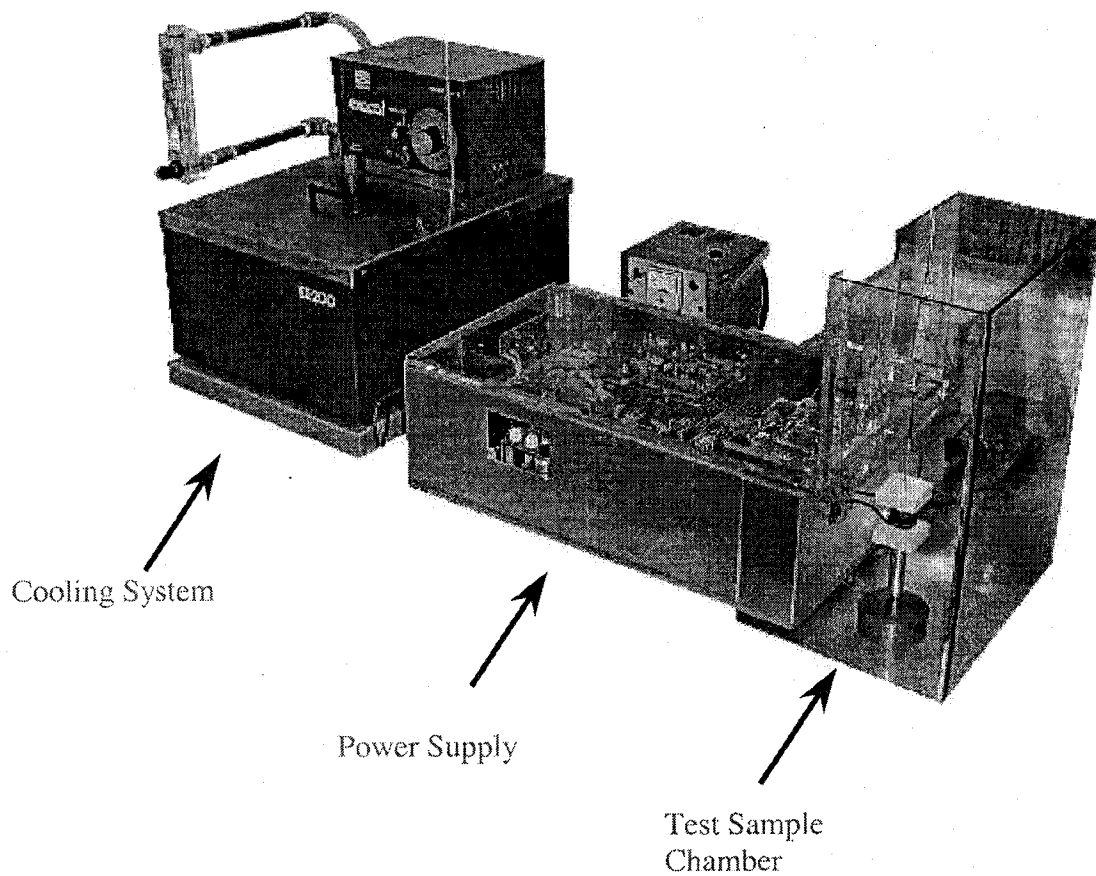


Figure 4.7: Picture of the Universal Metallurgical Simulator & Analyzer (UMSA) apparatus (Patent number: PCT/CA 02/01903).

4.7 UMSA Test Sample Quench Methodology

Quenching of the WA328, the WB328 and the W319 alloys was done from prescribed target temperatures between the liquidus and solidus. These quench points, known as target temperatures, were determined to be a stage of solidification at which either phase nucleation occurs or when a phase is in progress and growing during solidification. The target temperatures used for all alloys investigated were 585°C, 575°C, 555°C while the WA328 and WB328 alloys were also quenched from 527°C. The schematic of the quench setup is illustrated in Figure 4.8a and a picture of the UMSA quench setup is shown in Figure 4.8b. The quenching operation was conducted by holding the test sample stationary within the coil via a holder specially designed for the quenching operation. From the target temperature the sample holder apparatus along with the sample itself was rapidly immersed into 1.150 kilograms of a 15wt.% salt-water solution. The salt-water solution was maintained and monitored at 30°C (room temperature).

The test sample cup made of Al_2O_3 (as discussed in Section 4.6), would not survive the thermal shock of the quenched event. Thus the test sample cup used for the quenching operation was made of stainless steel foil that would survive the rapid change in temperature associated with the quenched event. The 304 stainless steel foil approximately 0.025mm in thickness was cut to the dimension required to fully wrap the circular surface of the UMSA test sample. To deter molten metal leakage, and to deter molten metal reaction during testing the inside of the foil wrap was coated with a boron nitride solution and was allowed to dry at room temperature for 24 hours to eliminate moisture.

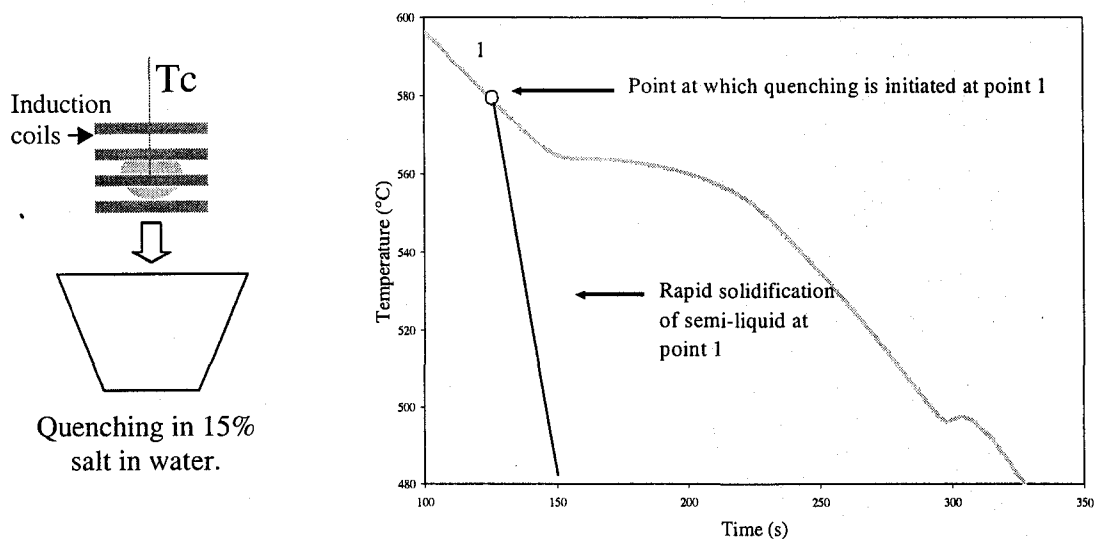


Figure 4.8a: Illustration of the quenching setup and a cooling curve showing the effect on solidification at the point labeled 1.

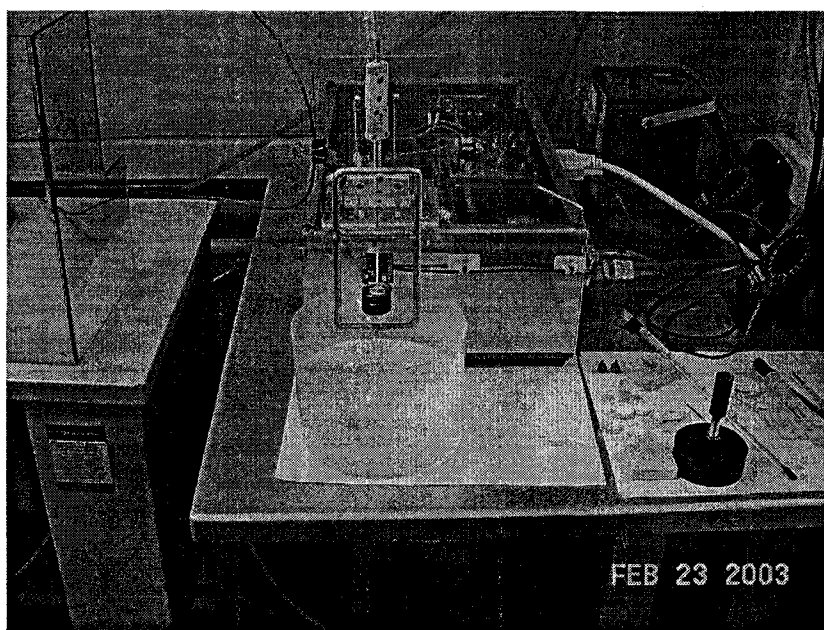


Figure 4.8b: Picture of the UMSA apparatus with suspension apparatus for quenching. In the picture the salt water quench is situated below the UMSA test sample.

4.8 Development of the Enviro-ALTAS:

The IRC has developed a new Environmental Aluminum Thermal Analysis System (Enviro-ALTAS). The Enviro-ALTAS will produce cooling curves and calculated fraction solid curves of thermal analysis test samples. During Enviro-ALTAS test sample solidification elevated pressures of 0 – 15 psi (to simulate metallostatic head) and different cooling rates ranging from 0.1 to 0.45°C/sec can be controlled.

The Enviro-ALTAS stand will be similar to the ALTAS which was situated at the north pump well at WAP, except that the actual TA sample will be in contact with a two component cylindrical chamber. The cross-section of the Enviro-ALTAS is illustrated in Figure 4.9. Pressurization will occur in the upper chamber (driving interdendritic fluid flow) using argon gas. The lower chamber, which is in contact with the sides of the TA test sample cup, is where the cooling rate of the sample will be controlled. The influx of air in the lower chamber will be controlled by a servo valve and monitored by a flow meter which will be connected to the lower chamber. The pressurization in the upper chamber will be monitored by a pressure sensor and the influx of argon will be controlled by an additional servo valve. All servo valves, the pressure sensor, the flow meter, and all thermocouples (in the thermal analysis sample and in the chambers) will interface with the LabVIEW software. Since the environmental conditions (i.e. flow rate, pressure, lower and upper chamber temperature, and gradient temperature) are recorded in addition to the sample cooling curve, this ensures that the highest level of control is attained for every test.

It should be pointed out that the investigation of the pressure or the variable cooling has already been performed and evaluated, however since the US patent is pending these results will not be presented other than cooling curve acquisition.

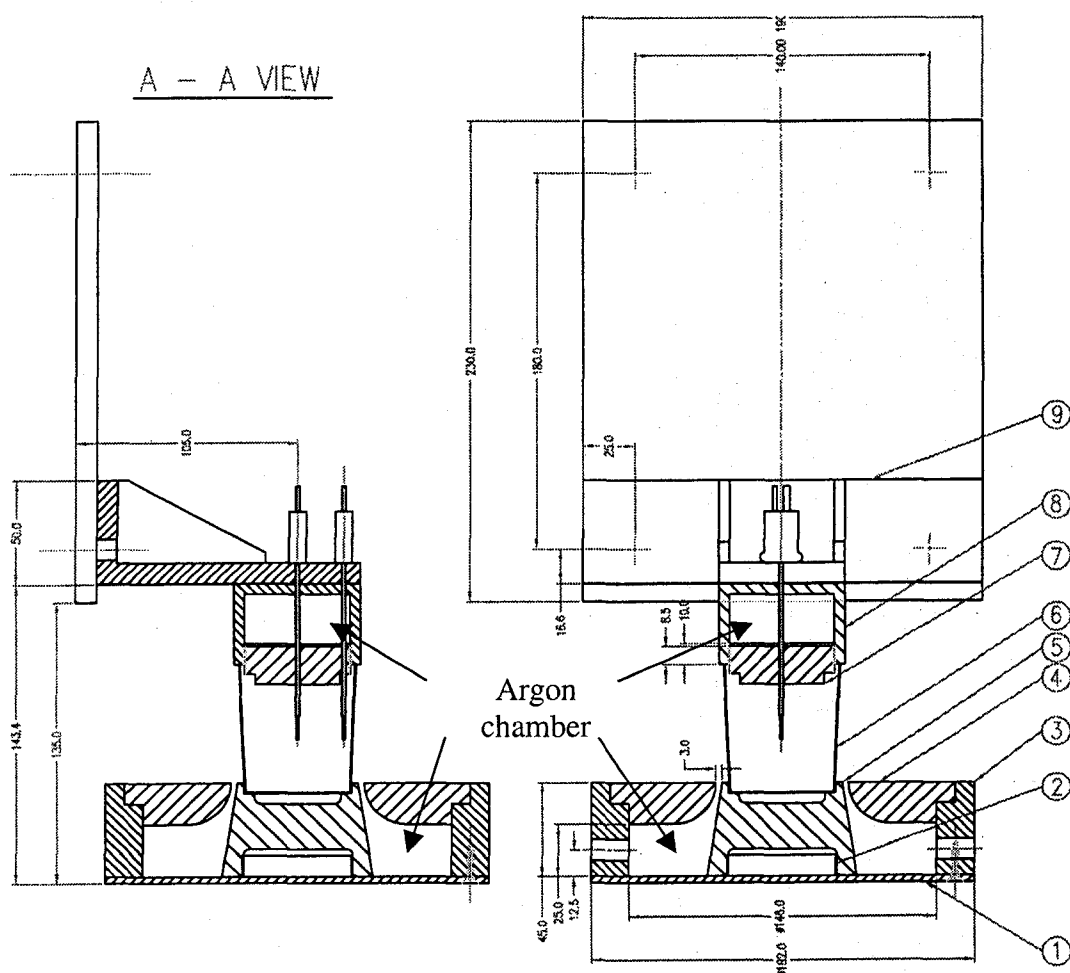


Figure 4.9: Cad-Key drawing of the Enviro-ALTAS. 1.) Bottom plate, 2.) Lower insulator/TA sample cup holder, 3.) Lower chamber wall, 4.) Lower chamber shroud, 5.) Compressed air flow vent, 6.) Thin walled steel cup, 7.) Upper insulator, 8.) Pressurizing chamber, 9.) Back plate attached to pneumatic pump.

4.9 Fatigue Testing Procedure

The Instron 8801 *Axial Servohydraulic Dynamic Two Column Load Frame* with a maximum fatigue capacity of 250 kN was used to perform fatigue testing. This is shown in Figure 4.10. The load applied, whether static or cyclic, is monitored by a Dynamic Load Cell having a maximum load capacity of 100 kN. The Instron trade name is *Dynacell*. The load cell has a 300% overload capacity before failure of the load cell can occur.

Single Axis (SAX)TM fatigue software by Instron was used to monitor the sinusoidal axial fatigue at a frequency of 40Hz. The stress ratio was $R = -1$, (R is defined as $\sigma_{\min}/\sigma_{\max}$). The fatigue test specimens were tested in compliance with the ASTM E 466-96 protocol. The type of fatigue testing used was the staircase method (*a series of test samples which pass or fail within a narrow stress range, see Section 3.1.5*).

The staircase method can be described more specifically as follows: If a life goal of 10^7 cycles without a failure occurred then it is considered a *run out* for a given targeted stress level. A subsequent test would be conducted on a fresh fatigue test sample at an incrementally higher stress level. A sample not achieving the 10^7 cycle life goal is considered a run out, and results in the very next sample being tested at an incrementally lower stress. This process would continue until all 33 fatigue test samples (the total conducted for this dissertation), either passed or failed. The Initial Staircase Stress Level used for testing was 68.3 MPa (max stress) with an incremental stress level of 3.5 MPa.

The mean stress of the staircase study would be determined by taking the average stress of all the fatigue test samples which failed (higher value of stress) or all the fatigue test samples which passed (lower value of stress), whichever is greater in number. This was provided along with a standard deviation of the results.

The results acquired from the aforementioned testing protocol were compared to fatigue staircase studies conducted by Climax Research Services (CRS). The 4.6L engine block cast using the W319 alloy with Sr modification and the W319 alloy with in-mould grain refining were sectioned by CRS and assessed using the staircase method at 120°C. Thus, it became prudent to conduct the staircase study, for this dissertation, at the same temperature. Maintaining a test temperature of 120°C was done using an Environmental Temperature Chamber as seen in Figure 4.10a. Other views of the Mechanical Workstation and Environmental Test Chamber can be seen in Figures 4.10b through 4.10f.

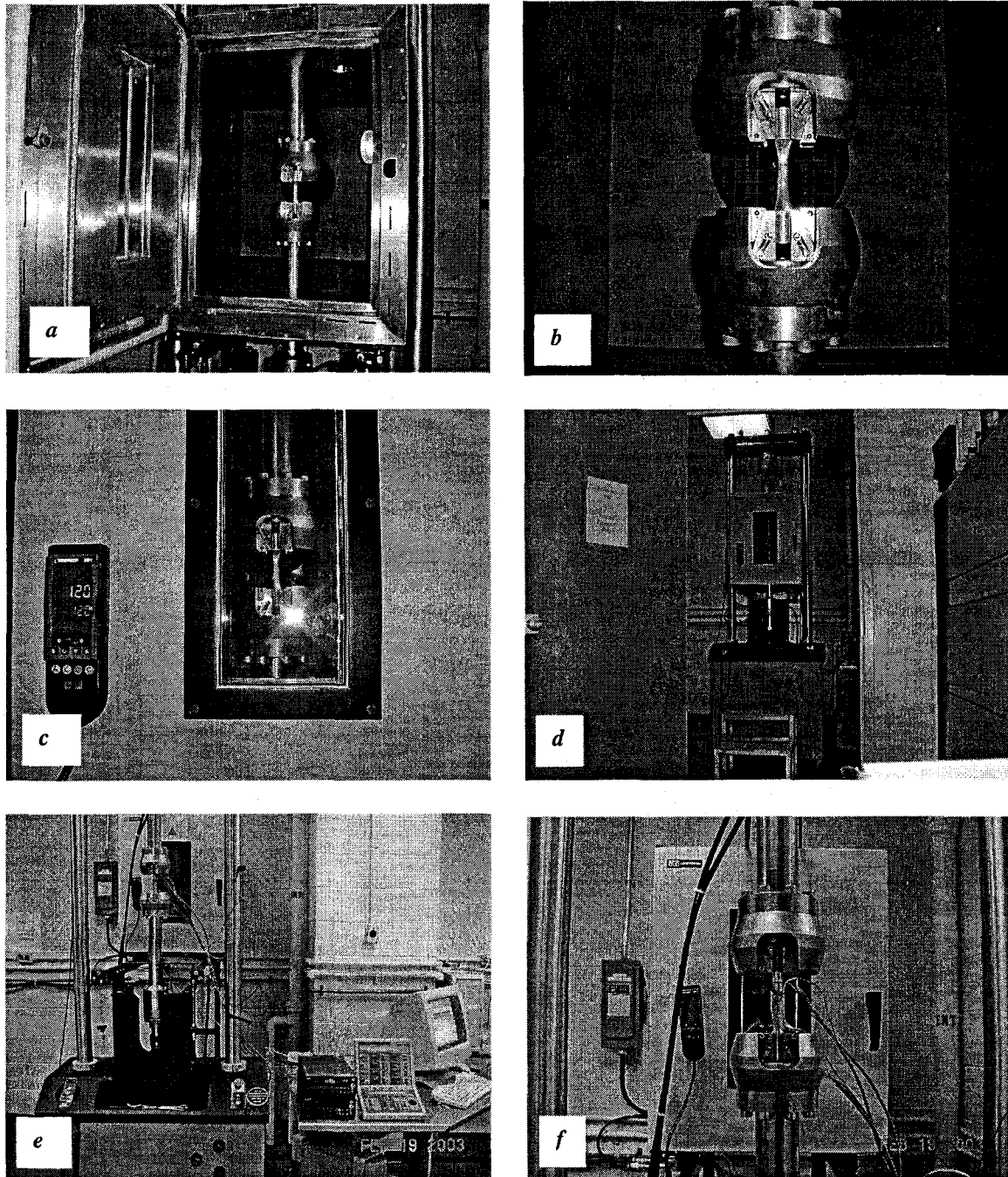


Figure 4.10: a) Mounted fatigue test sample inside an environmental test chamber, b) Close up of the mounted fatigue test sample in high temperature 35 kN capacity grips, c) View of the mounted fatigue test sample inside the environmental test chamber and temperature controller, d) entire test frame and environmental test chamber, e) Load frame and environmental test chamber and f) Mounted strain gauge test sample.

4.9.1 Fatigue Test Sample Soak Time

While the furnace can achieve the target temperature in a short period of time the fatigue test sample requires a sufficient amount of soak time in order to reach a homogenous targeted temperature. A dummy fatigue sample of the W319 alloy, having a hole drilled from the grip end down to the center of the reduced gauge section (*containing a K-type 0.62" thermocouple*) was used to establish the actual soak time.

The sample was mounted within the grips and the Environmental Test Chamber door was closed. The controller to the Environmental Test Chamber was set to have a target temperature of 120°C. Figure 4.11 shows the time required for the Environmental Test Chamber to reach target temperature and the heating rate of the test sample to also achieve this target temperature. The furnace reached 120°C within 5 minutes while the test sample reached the target temperature of 120°C within 60 minutes. Thus, it became clear that the safe soak time for the test sample reduced gauge section to achieve the targeted 120°C is 60 minutes.

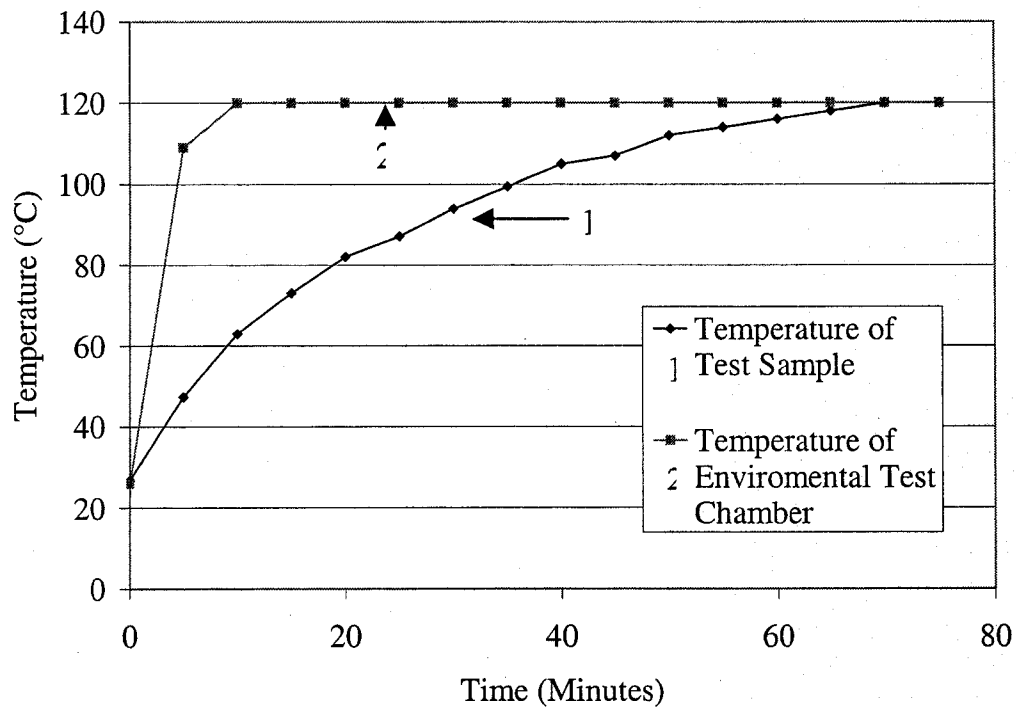


Figure 4.11: Rate of heating for the fatigue test sample and the environmental test chamber.

4.10 Mechanical Monotonic Testing Procedure

Using the same Instron 8801 Servo-Hydraulic System tensile samples were tested at room temperature at a strain rate of 8×10^{-4} (mm/mm)/second. A completed test (at the point of fracture) would take approximately 10 minutes. Data was collected by the Series TM software 4 times per second. A strain gauge extensometer was attached to the tensile test sample for the measurement of elongation (see Figures 4.12a and 4.12b). A total of ten test samples (for each alloy) were evaluated, along with standard deviation, for the WA328 alloy and the W319 alloy. After the test was conducted the Yield Stress (0.2% offset), Tensile Stress, Modulus of Elasticity, Elastic Elongation and Total Elongation were measured as defined in the ASTM B 557 protocol.

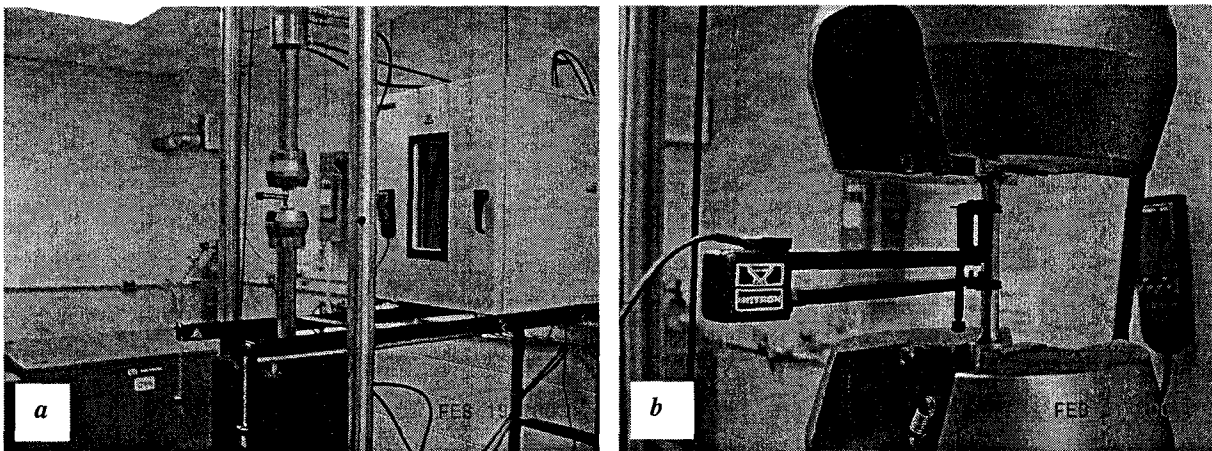


Figure 4.12: a) View of the load frame with mounted tensile test sample with extensometer and b) Close up of the extensometer mounting on the tensile test sample prior to the start of testing.

Chapter Five

Metallurgy of the WA328 & WB328 Alloys

5.0 Chemical Composition of Test Alloys

During the casting of the 4.6L engine blocks at NEC, Optical Emission Spectrometry (OES) test samples were cast and measured on a regular basis. Appendix D lists the full composition measured for each OES disk (mean of three sparks) and the date when each specific test sample was taken. Table 5.0 shows the average composition of the WA328 alloy and the WB328 alloy.

Table 5.0: Average cast chemistry from OES, wt.%.

<i>Alloy</i>	<i>Si</i>	<i>Fe</i>	<i>Cu</i>	<i>Mn</i>	<i>Mg</i>	<i>Ni</i>	<i>Zn</i>	<i>Sr</i>	<i>Ti</i>
WA328	9.17	0.372	1.02	0.159	0.310	0.185	0.145	0.0007	0.076
WB328	8.68	0.833	1.02	0.372	0.300	0.176	0.140	0.0008	0.074

5.1 The Scanning Electron Microscopy (SEM) and Light Optical Microscopy (LOM) Results for the WA328 & WB328 Alloy Structures

Figures 5.1a and 5.1b show the SEM micrographs taken from bulkhead E from castings A4 and A43 respectively, both at 100X magnification. Figures 5.1c and 5.1d show the SEM micrographs taken from the Enviro-ALTAS test samples on the same dates that the engine blocks A4 and A43 were cast. Visually, from Figures 5.1a, 5.1b, 5.1c and 5.1d one can ascertain that the α -phase (see description in Section 2.1.1, Chapter Two) is the third most numerous phase found, after the primary α -Al dendrites and the eutectic Si phase. As the Fe levels increase from 0.40 wt.% for the WA328 alloy up to 0.80wt.% for the WB328 alloy the α -phase increases in prominence. LOM micrographs of the same bulkhead structures as seen in Figures 5.1a and 5.1b are shown in Figures 5.1e and 5.1f respectively, both at 100X magnification.

SEM/BSE micrographs at higher magnifications (500X up to 2500X) reveal phases difficult to observe at 100X magnification and are shown in Figures 5.1g through 5.1l along with EDX spectra for some of the observed phases shown in Figures 5.1m through 5.1r.

The typical EDX spectrum of an α -phase, as seen in Figure 5.1a, shows the Al, Fe, Mn, Cr and Si K_{α} and/or K_{β} peaks (see Figure 5.1m for an example). There are several Fe-based candidate stoichiometries which exhibit script-type morphologies and these are the α - $\text{Al}_8\text{Fe}_2\text{Si}$, α - $\text{Al}_{12}\text{Fe}_3\text{Si}_2$, α - $\text{Al}_{15}(\text{Fe},\text{Cr},\text{Mn})_3\text{Si}_2$, δ - Al_4FeSi_6 , p - $\text{Al}_8\text{Mg}_3\text{FeSi}_6$ and the π - $\text{Al}_5\text{Mg}_8\text{Cu}_2\text{Si}_6$ phases [31, 32, 34-37, 87, 88]. Through the process of elimination the p - $\text{Al}_8\text{Mg}_3\text{FeSi}_6$ and the π - $\text{Al}_5\text{Mg}_8\text{Cu}_2\text{Si}_6$ phases can be ruled out since Cu or Mg K_{α} or K_{β}

peaks were absent on the EDX spectra of the α -phase seen in Figure 5.1a through Figure 5.1d. However the Cr and Mn peaks were present on the EDX spectra thus leaving identification of the α -AlFeSi type phase (α -Al₁₅(Fe,Cr,Mn)₃Si₂) as the probable stoichiometry. Additionally this script phase appears to be unaltered by heat treatment which is a known observation with the α -Al₁₅(Fe,Cr,Mn)₃Si₂ script phase [3, 88]. Many of the identified script phases found in both the WA328 and WB328 Fe alloys taken from bulkhead E were analyzed via EDX spectra and the same Fe, Si, Mn and Cr peaks were predominately observed on EDX spectra.

Figure 5.1g is an SEM micrograph that shows the coexistence of a Al₂Cu blocky phase, Mg₂Si script phase, an unreported Al-Fe-Ni, and an unreported Al-Cu-Ni based phase in an as-cast WA328 alloy at 1,000X magnification. The individual EDX spectra of the phases as seen in Figure 5.1g are presented in Figures 5.1n for the Al-Ni-Cu phase, Figure 5.1o for the Al-Ni-Fe phase Figure 5.1p for the Al₂Cu phase, and Figure 5.1q for the Mg₂Si phase. Due to the small size of all four observed phases and their close proximity to each other, it is believed that this is a reaction that has resulted from a highly segregated liquid pool that solidified after the main Al-Si eutectic reaction. It is also known that Al₂Cu phase and the Mg₂Si phase usually form at the later stages in all known Al-Si-Cu-Mg based casting alloys [8, 9, 35, 42, 43, 87, 88]. The Al-Fe-Ni and Al-Cu-Ni phases have not been previously reported and thus their stoichiometries are unknown.

Figure 5.1h shows, at a magnification of 1,000X, the Pb-based particle, the Al-Cu-Ni phase, the Mg₂Si phase and a small Al₅FeSi platelet phase in the as-cast WB328 alloy. The Pb-

based particle is commonly found in the W319 alloy and is a by-product of the secondary smelting process [42, 43, 92]. Figure 5.1i shows another SEM/BSE micrograph from the same sample, at a magnification of 500X. Observed are the $\text{Al}_{15}(\text{Fe}, \text{Mn}, \text{Cr})_3\text{Si}_2$ script phase, the Mg_2Si phase, and the Al-Cu-Ni phase.

Figure 5.1j shows an example of the structure of the WA328 alloy sample excised from the 4.6 engine block after experiencing TSR and the heat treatment scheme illustrated in *Table 4.2, Chapter 4*. Figure 5.1j shows a Al_5FeSi phase, an undissolved Mg_2Si phase, the Pb-based particle, the $\text{Al}_{15}(\text{Fe}, \text{Mn}, \text{Cr})_3\text{Si}_2$ script phase and most likely a partially dissolved Al-Fe-Ni particle. The partially dissolved Al-Fe-Ni phase requires some explanation. The region of the SEM micrograph identified as a fine Al-Fe-Ni structure appears to be encapsulated within the outline of what was formerly a whole Al-Fe-Ni particle. Such fine Al-Fe-Ni phases are not present within the as-cast structures. The Mg_2Si phase seems to remain undissolved as is found with the W319 alloy after heat treatment. The Mg_2Si phase is known to dissolve at a slightly higher temperatures ($\sim 520^\circ\text{C}$) as used in the 356 alloy [87, 88, 91, 92-95], thus explaining its apparent existence in Figure 5.1j.

The Al-Cu-Ni particles appear to respond in the same way as the Al-Ni-Fe particles under the imposed TSR and Solution & Age heat treatment scheme. Figure 5.1k shows a $\text{Al}_{15}(\text{Fe}, \text{Mn}, \text{Cr})_3\text{Si}_2$ script phase and a Mg_2Si phase mixed in with the suspected partially dissolved Al-Cu-Ni phase. A zoom up of 2500X magnification is shown in the lower right hand corner of Figure 5.1k in the dashed box and is enlarged in Figure 5.1l. The EDX spectra for this phase is shown in Figure 5.1r.

The absence of the Al_2Cu phase from the heat treated structures as seen in Figures 5.1j and 5.1k indicates that this phase must have dissolved. The solution temperature utilized for the 4.6L engine block in this Dissertation (505°C) is known to dissolve most of the Al_2Cu phase in the 319-type alloys [3, 94, 95].

Figure 5.1s shows a LOM micrograph of the as-cast structures of the WA328 alloy at 200X magnification. Figure 5.1t is a LOM micrograph at 500X magnification and is taken from the dashed region in Figure 5.1s. Figure 5.1t shows the phase which looks as if it is either the Al-Cu-Ni phase or the Al-Ni-Fe phase as seen in the SEM images of 5.1g and 5.1h, a Mg_2Si phase, a Al_2Cu phase and a $\text{Al}_{15}(\text{Fe,Mn,Cr})_3\text{Si}_2$ script phase.

Figure 5.1u shows a micrograph of the as-cast structure of the WB328 alloy at 200X magnification. The dashed region in Figure 5.1u is shown at 500X magnification in Figure 5.1v. Found in close proximity to each other are the blocky $\text{Al}_{15}(\text{Fe,Mn,Cr})_3\text{Si}_2$ script, the Mg_2Si phase, Al_2Cu phase and a Al-Ni-Fe or Al-Ni-Cu phase.

Figure 5.1w shows a LOM micrograph of the WA328 alloy at 200X magnification after the TSR and the heat treatment. Figure 5.1w does not appear to reveal any change in response to the thermal treatment. Figure 5.1x is a LOM at 500X magnification and is from the dashed region of Figure 5.1w and reveals a partially dissolved phase which is either the Al-Ni-Cu phase or the Al-Ni-Fe phase, as seen in the SEM micrographs of 5.1j and 5.1k. Interestingly, as with the observed with SEM micrographs the Mg_2Si appears undissolved.

From both SEM and LOM micrographs it appears that the Al_2Cu phase dissolves, the Al-Fe-Ni and the Al-Cu-Ni phases partially dissolve and the Mg_2Si phase remains unaffected. Both the Al-Fe-Ni phase, the Al-Cu-Ni phase and the Mg_2Si phase require either a higher solution temperature, a longer solution duration or a combination of both. To deter incipient melting of the Al_2Cu phases a two step solution treatment would have to be investigated [83, 84, 92].

However, despite the fact that a specially augmented heat treatment procedure could be implemented to further enhance the quantity of phase dissolution, Chapter Six will show that the heat treatment outlined in Table 4.2, Chapter Four, will be sufficient to achieve the elastic mechanical properties which are similar to the W319 alloy.

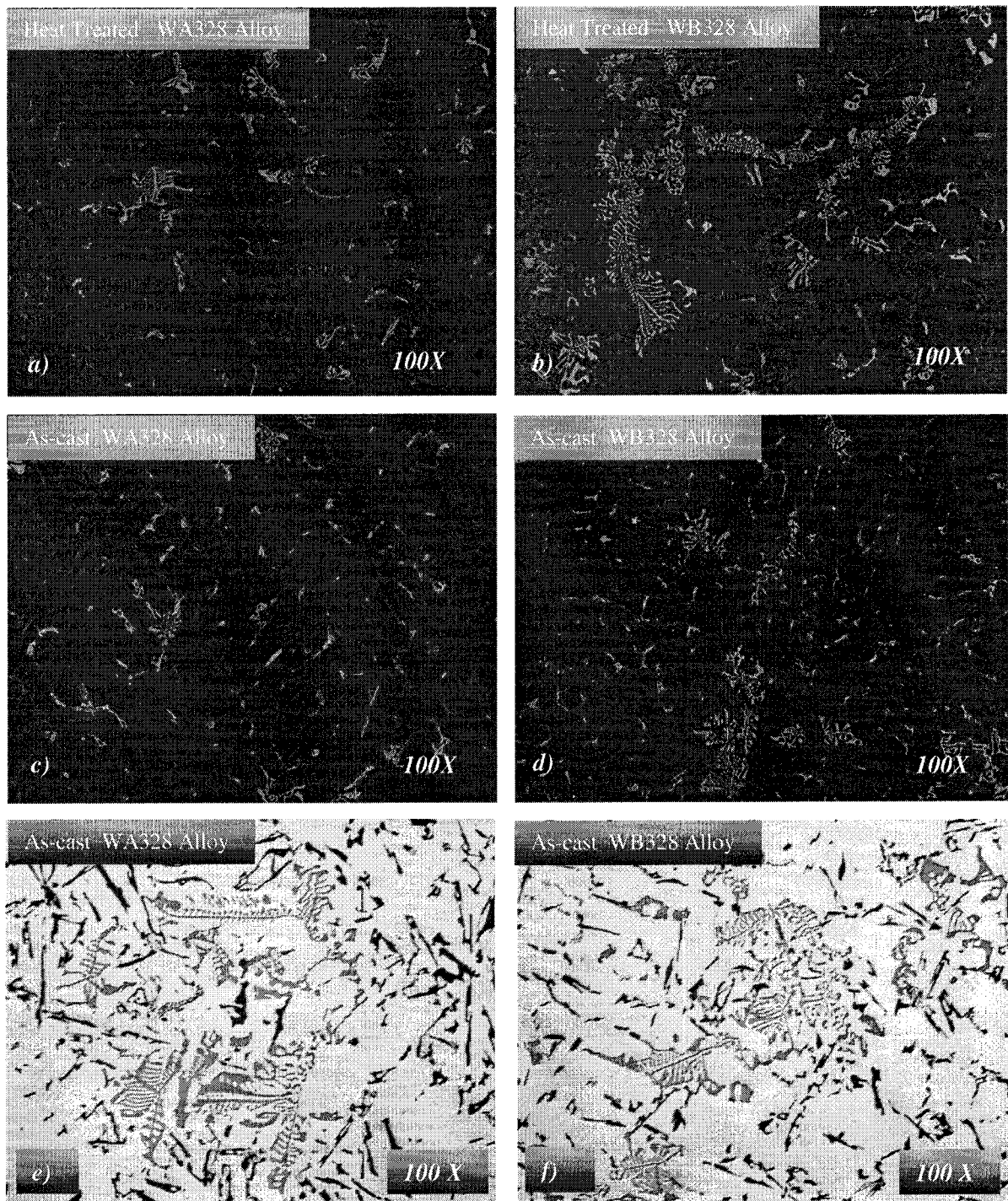


Figure 5.1: SEM/BSE micrographs and LOM micrographs for the WA328 alloy (a, c, e) and for the WB328 alloy (b, d, f), both at low magnification.

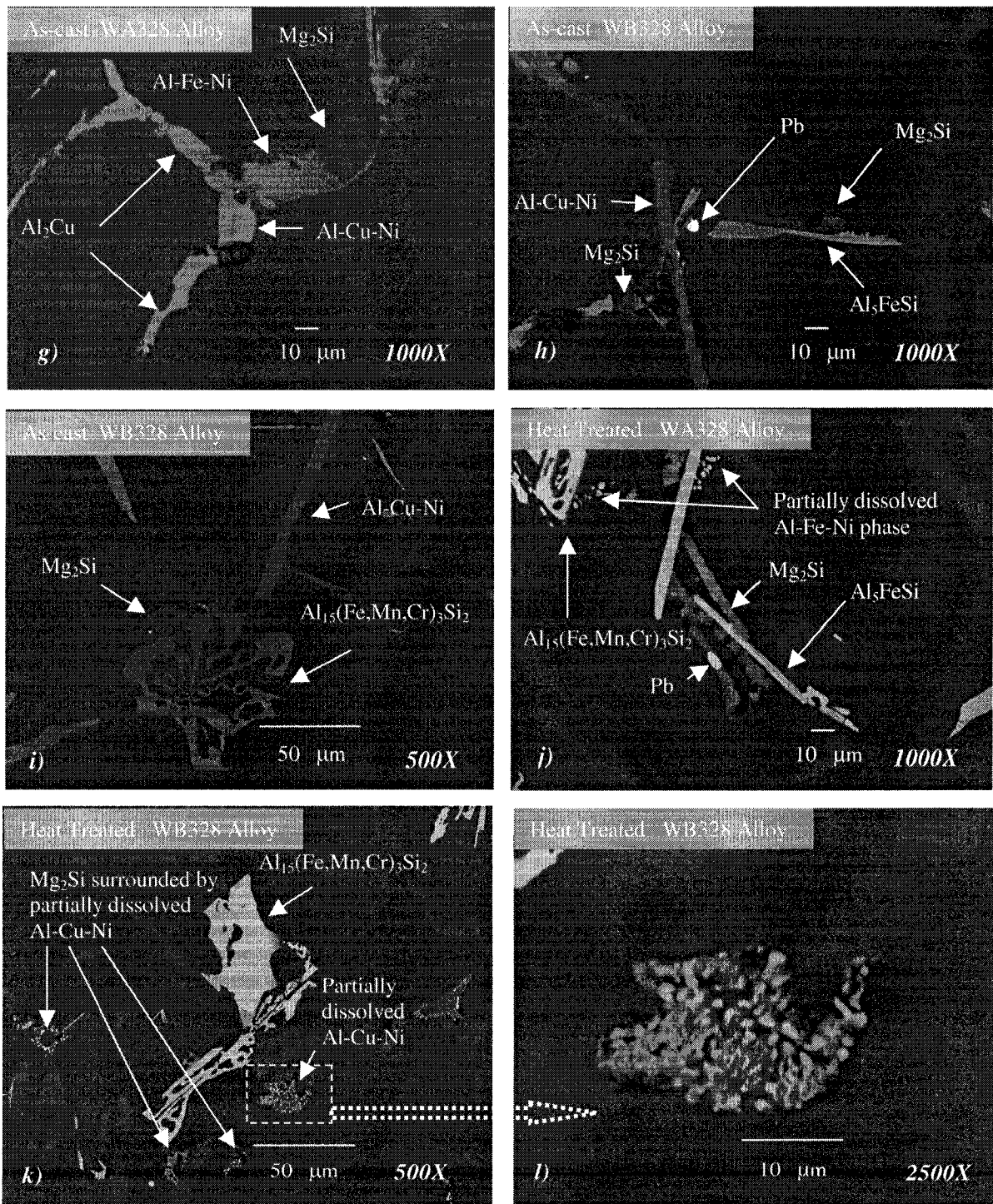


Figure 5.1(g-l): SEM/BSE micrographs of the as-cast and heat treated WA328 and WB328 alloys.

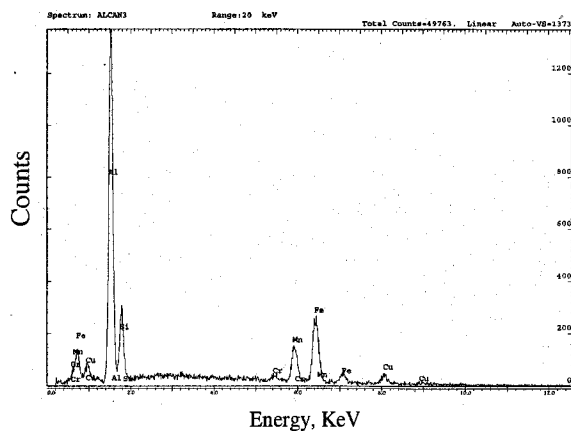


Figure 5.1m: EDX spectra for the $\text{Al}_{15}(\text{Fe},\text{Mn},\text{Cr})_3\text{Si}_2$ script phase seen in Figure 5.1a.

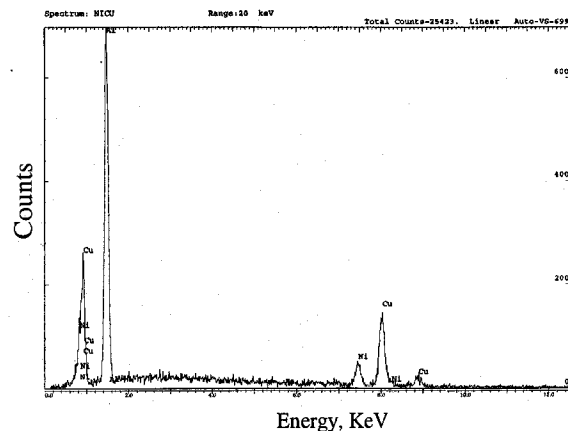


Figure 5.1n: EDX spectra for the Al-Ni-Cu phase seen in Figure 5.1g.

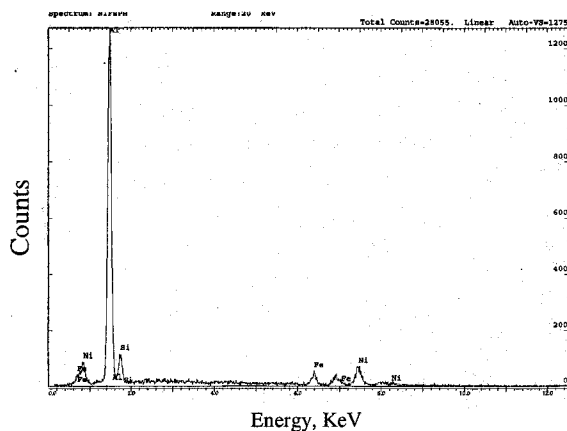


Figure 5.1o: EDX spectra for the Al-Ni-Fe phase seen in Figure 5.1g.

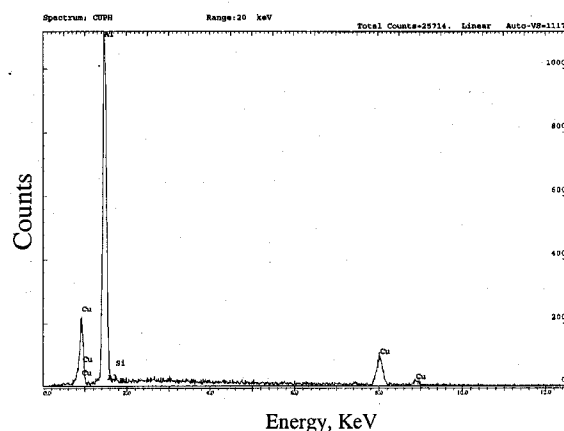


Figure 5.1p: EDX spectra for the Al_2Cu phase seen in Figure 5.1g.

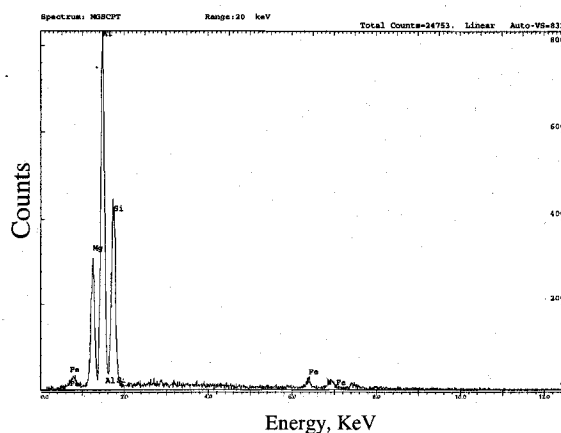


Figure 5.1q: EDX spectra for the Mg_2Si script phase seen in Figure 5.1g.

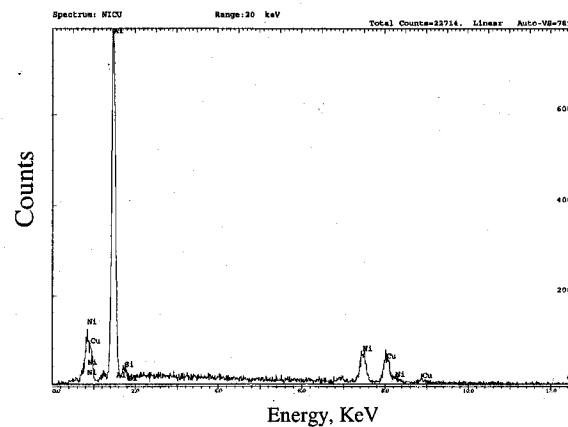


Figure 5.1r: EDX spectra for the Al-Ni-Cu phase seen in Figure 5.1l.

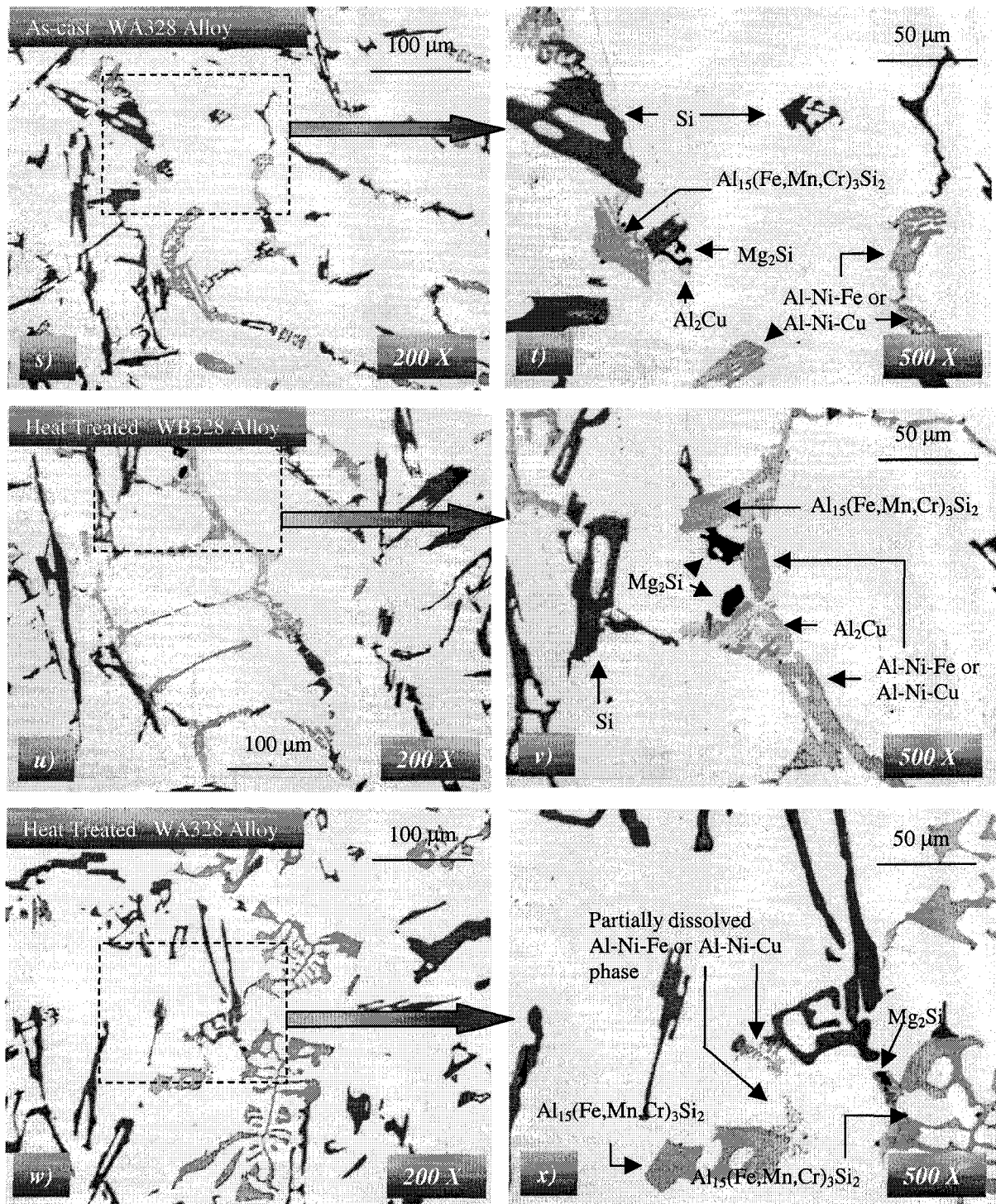


Figure 5.1(s-x): LOM micrographs of the as-cast and heat treated WA328 and WB328 alloys.

5.2 Thermal Analysis of the WA328 and WB328 Alloys

The cooling curve analysis, calculated fraction solid curve analysis, and the cooling rate of the WA328 alloy, WB328 alloy and the W319 alloy were partitioned via the interpretative methods outlined in Appendix A. The Enviro-ALTAS (*total cooling rate* = 0.15°C/sec) was used to acquire the cooling curves and calculated fraction solid curves of all alloys, while the UMSA (*total heating rate* = 0.50°C/sec & *total cooling rate* = 0.55°C/sec) was used to process *heating curves* and *cooling curves* from samples directly excised from bulkhead E of the 4.6L engine blocks cast at NEC (see Figure 4.2). A minimum of four repeats (Enviro-ALTAS and UMSA) were made to establish characteristic temperature values and partitioned values while the scatter in these measured values is reflected by a standard deviation. The results are listed together in Appendix F.

Figure 5.2a shows an example of a WA328 alloy heating and cooling curve and its corresponding derivative curve is shown in Figure 5.2b. Figure 5.2c shows the WA328 alloy cooling curve (and the associated first derivative) acquired using the Enviro-ALTAS. Figure 5.2d shows the same cooling curve as seen in Figure 5.2c except the associated calculated fraction solid curve is shown (the method for calculating the fraction solid is shown in Appendix B). Figures 5.2e and 5.2f show the peaks associated with the final two reactions which occur on the WA328 UMSA and Enviro-ALTAS cooling curves.

To assess the integrity of the measured characteristic temperature values the composition as measured from each OES disk will be used to calculate the characteristic temperatures via the Silicon Equivalent (Si_{EQ}) method [96]. This will be presented in Section 5.2.1.

All thermocouples (both the commercial 1.57mm and LMT 1.14mm) and the Data Acquisition System are calibrated as indicated in Section 4.5. A correction factor for the temperature was determined and applied to the cooling curve results.

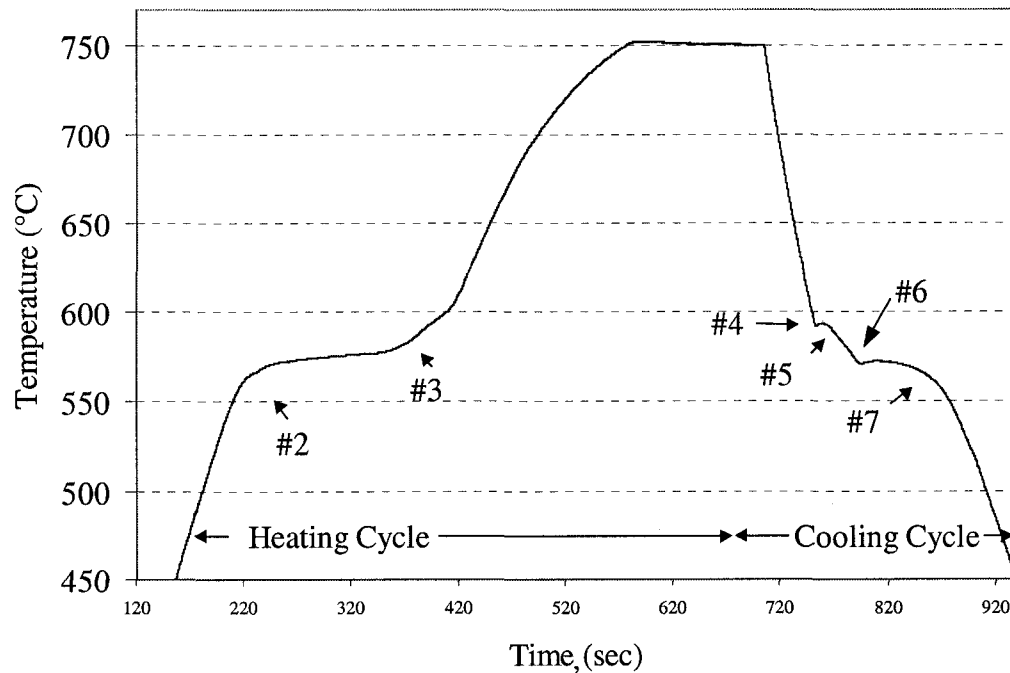


Figure 5.2a: Temperature vs. Time curve obtained by using the UMSA system during heating and cooling cycles for the WA328 Alloy. The main metallurgical reactions during heating and cooling are:

- #2 - Start (beginning) of the alloy melting process.
- #3 - Finish (end) of the alloy melting process.
- #4 - Nucleation of the α Al dendrite network (Liquidus Temperature).
- #5 - Dendrite Coherency Point.
- #6 - Nucleation of the Al-Si eutectic.
- #7 - Nucleation of the Al-Fe-Mg-Si-Cu enriched eutectic(s).

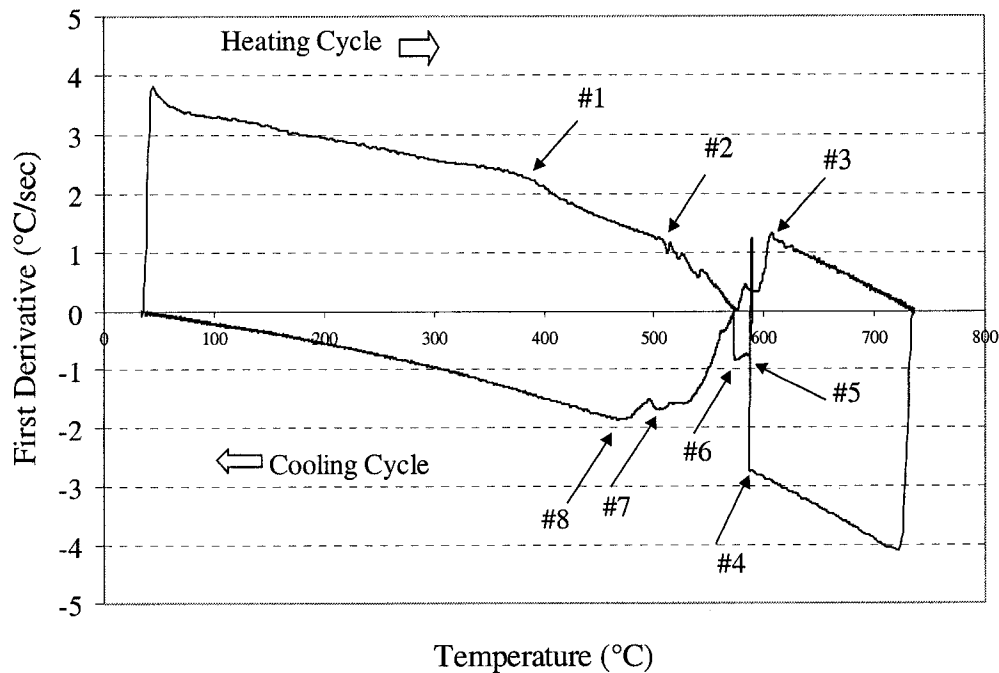


Figure 5.2b: First Derivative vs. Temperature curves obtained using the UMSA system during heating and cooling cycles for the WA328 alloy. The main metallurgical reactions during heating and cooling:

- #1 - Apparent start of dissolution of soluble phases(s) – Minimum TSR Transfer Temperature.
- #2 - Start (beginning) of the alloy melting process.
- #3 - Finish (end) of the alloy melting process.
- #4 - Nucleation of the α Al dendrite network (Liquidus Temperature).
- #5 - Dendrite Coherency Point.
- #6 - Nucleation of the Al-Si eutectic.
- #7 - Nucleation of the Al-Fe-Mg-Si-Cu enriched eutectic(s).
- #8 - End of the alloy solidification (Solidus Temperature).

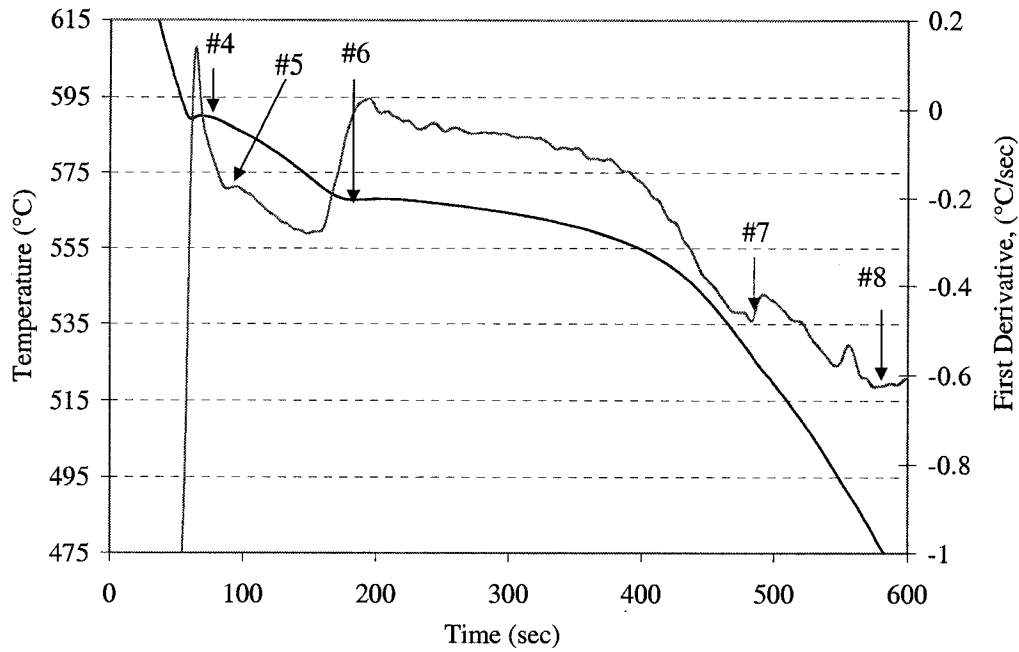


Figure 5.2c: The Enviro-ALTAS test sample of the WA328 alloy cast at NEC. The test sample cooling rate was $0.15^{\circ}\text{C}/\text{sec}$. Identified is #4- α -Al primary dendritic, #5-DCP, #6-Al-Si eutectic plateau, #7-Al-Fe-Mg-Si-Cu reactions & #8-Solidus.

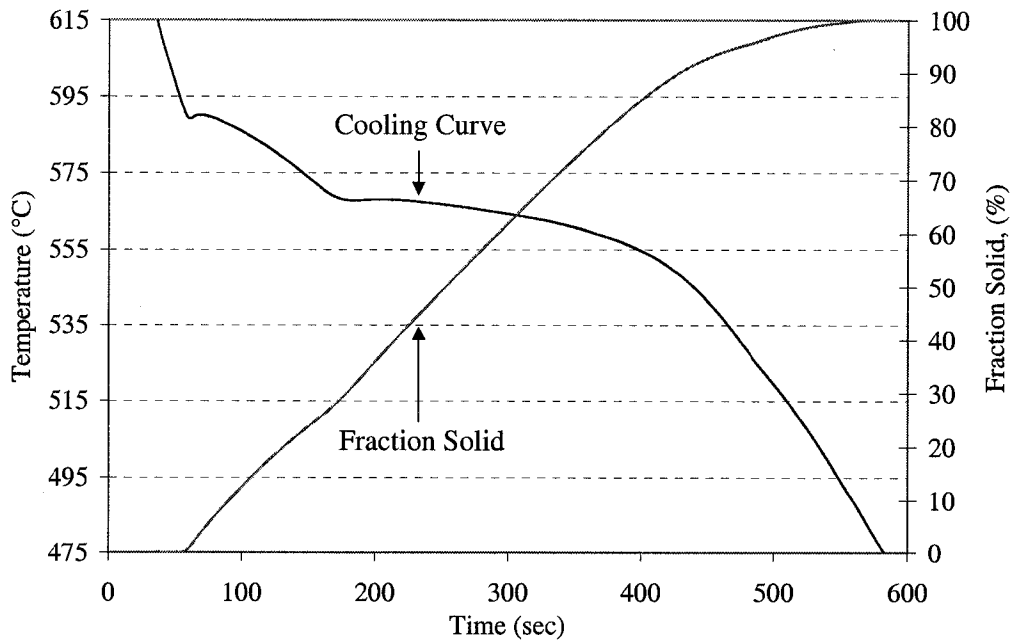


Figure 5.2d: The cooling curve of the WA328 alloy along with the calculated fraction solid curve.

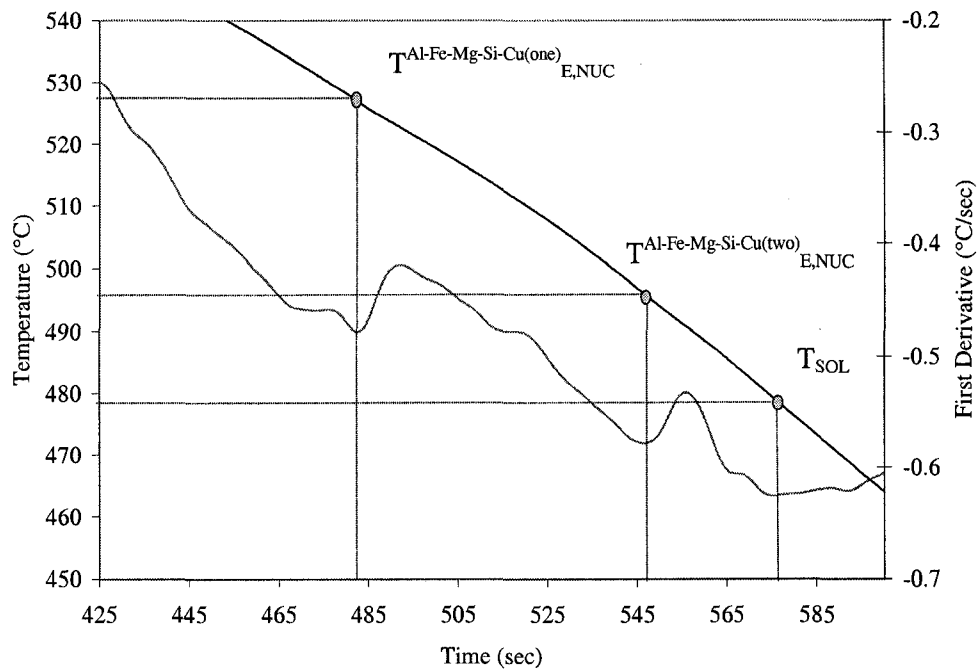


Figure 5.2e: The UMSA cooling curve and first derivative (for the WA328 alloy) of the characteristic temperature values $T_{Al-Fe-Mg-Si-Cu(one)_{E,NUC}}$, $T_{Al-Fe-Mg-Si-Cu(two)_{E,NUC}}$ and T_{SOL} .

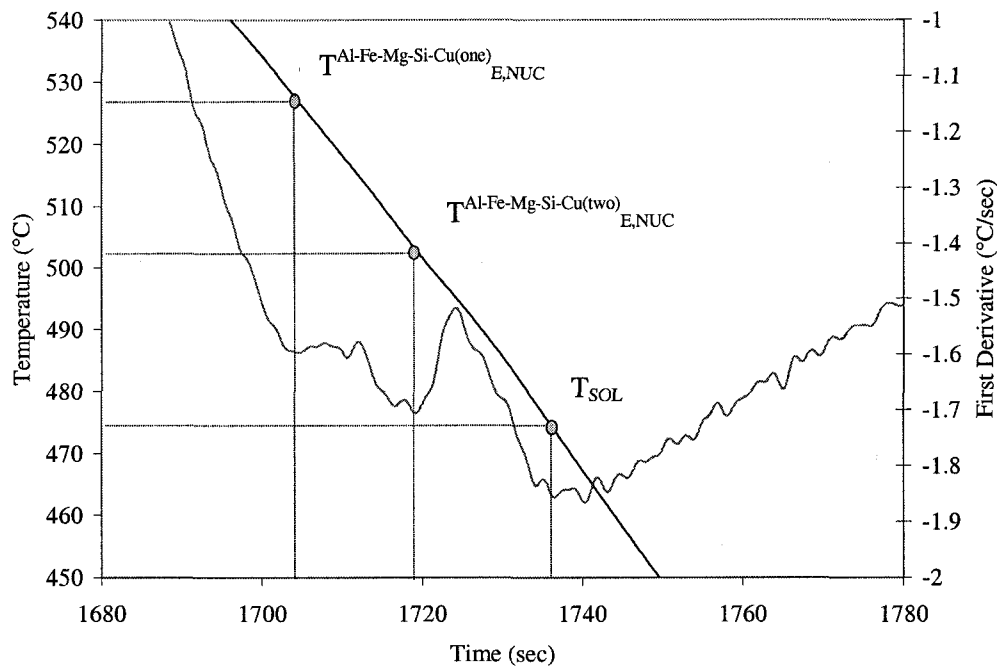


Figure 5.2f: The Enviro-ALTAS cooling curve and first derivative (for the WA328 alloy) of the characteristic temperature values $T_{Al-Fe-Mg-Si-Cu(one)_{E,NUC}}$, $T_{Al-Fe-Mg-Si-Cu(two)_{E,NUC}}$ and T_{SOL} .

5.2.1 Characteristic Temperature Measurements

Figure 5.2.1a shows a summary of the characteristic temperature values determined from the Enviro-ALTAS and the UMSA platforms. In all cases a slight increase in the liquidus temperature ($T^{\alpha\text{DEN}}_{\text{NUC}}$) is determined for the WB328 alloy. This observation is made regardless of the thermal analysis testing system used. Table 5.2.1a summarizes the mean liquidus temperatures from the Enviro-ALTAS and UMSA cooling curves along with $T^{\alpha\text{DEN}}_{\text{NUC}}$ calculated using the Si_{EQ} method. The composition used to calculate the Si_{EQ} method came from the OES disk samples and is found in Table D.2, Appendix D.

The increase in liquidus temperature for the WB328 alloy, as confirmed using the three independent methods in Table 5.2.1a, is most likely due to the depression of the Si content seen in Table 5.0. Figure 5.2.1b shows a binary Al-Si phase diagram with the liquidus data determined from the cooling curves of the Enviro-ALTAS test samples and the Si level as measured from the OES disk cast at the same date. Visually there is good agreement revealing the probable dominant effect of the lower Si content of the WB328 alloy.

Determining if there is a change in $T^{\text{Al-Si}}_{\text{E,NUC}}$ between the WA328 alloy and the WB328 alloy is not straight forward. The work conducted by the author of this dissertation showed that changes in Si and Fe content do not noticeably change $T^{\text{Al-Si}}_{\text{E,NUC}}$ [37]. However it has been shown then when a 0.10 wt.% increase in Fe in the W319 alloy (Pelayo [47]) occurs an increase in $T^{\text{Al-Si}}_{\text{E,NUC}}$ by 3°C occurs. As seen in Figure 5.2.1a and as noted in the results in Table 5.2.1a no noticeable difference (outside of standard deviation) in either the measured

value of $T_{E,NUC}^{Al-Si}$ from the Enviro-ALTAS or UMSA cooling curves, or $T_{E,NUC}^{Al-Si}$ calculated using the Si_{EQ} method, was seen.

The first post Al-Si eutectic reactions measured from the UMSA cooling curves ($T_{E,NUC}^{Al-Fe-Mg-Si-Cu(one)}$) shows an increase of about $3^{\circ}C$, from $527.6 \pm 2.1^{\circ}C$ to $530.3 \pm 0.8^{\circ}C$ in their value for the WB328 alloy compared to the WA328 alloy. The second post Al-Si eutectic reaction from the UMSA cooling curves ($T_{E,NUC}^{Al-Fe-Mg-Si-Cu(two)}$) is $500 \pm 3^{\circ}C$ and $499 \pm 3^{\circ}C$ for both the WA328 and WB328 alloys, respectively. The value determined from the Enviro-ALTAS essentially mirrors what was measured by UMSA. The Si_{EQ} method was not used to generate values for $T_{E,NUC}^{Al-Fe-Mg-Si-Cu(one)}$ and $T_{E,NUC}^{Al-Fe-Mg-Si-Cu(two)}$ since its calculation reflects a change in the liquidus and $T_{E,NUC}^{Al-Si}$ due to the chemistry. Thus, its accuracy at measuring temperatures past $T_{E,NUC}^{Al-Si}$ is low.

The solidus temperature shows a higher temperature using the Enviro-ALTAS ($\sim 480^{\circ}C$) than using the UMSA ($\sim 460^{\circ}C$). Unlike the consistency of the characteristic temperature measurement found for $T_{NUC}^{\alpha NUC}$, T_{NUC}^{Al-Si} , $T_{E,NUC}^{Al-Fe-Mg-Si-Cu(one)}$, and $T_{E,NUC}^{Al-Fe-Mg-Si-Cu(two)}$ both the Enviro-ALTAS and UMSA platforms register their own bias in determining the solidus. The bias arises not from the thermal analysis system but the difference in cooling rates. The dependence of the cooling rate on the solidus is currently under investigation by the developers of the UMSA [92].

Table 5.2.1a: The results of the Silicon Equivalent (Si_{EQ}) Calculation (*using the compositions measured by OES from the disk test samples*) and measured characteristic temperature values from the Enviro-AITAS and the UMSA test samples. The Results are based on 6 repeats.

Alloy	$T_{NUC}^{Al-DEN} (^{\circ}C)$			$T_{NUC}^{Al-Si} (^{\circ}C)$		
	Si_{EQ}	Enviro-AITAS (0.15°C/sec)	UMSA (0.55°C/sec)	Si_{EQ}	Enviro-AITAS (0.15°C/sec)	UMSA (0.55°C/sec)
WA328 Alloy (i.e. 9.2wt.%Si & 0.4wt.%Fe)	592 ± 3.6	590.1 ± 1.6	590.3 ± 0.7	570 ± 2.1	569.2 ± 2.2	571.6 ± 0.5
WB328 Alloy (i.e. 8.8wt.%Si & 0.8wt.%Fe)	593 ± 1.9	596.4 ± 2.0	592.2 ± 1.1	572 ± 3.3	573.5 ± 4.1	571.3 ± 0.4

Alloy	$T_{E,NUC}^{Al-Fe-Mg-Si-Cu(one)} (^{\circ}C)$		$T_{E,NUC}^{Al-Fe-Mg-Si-Cu(two)} (^{\circ}C)$	
	Enviro-AITAS (0.15°C/sec)	UMSA (0.55°C/sec)	Enviro-AITAS (0.15°C/sec)	UMSA (0.55°C/sec)
WA328 Alloy (i.e. 9.2wt.%Si & 0.4wt.%Fe)	525.3 ± 1.1	527.6 ± 2.1	495.5 ± 6.2	499.4 ± 1.9
WB328 Alloy (i.e. 8.8wt.%Si & 0.8wt.%Fe)	533.6 ± 4.4	530.3 ± 0.8	501.9 ± 5.7	498.2 ± 2.6

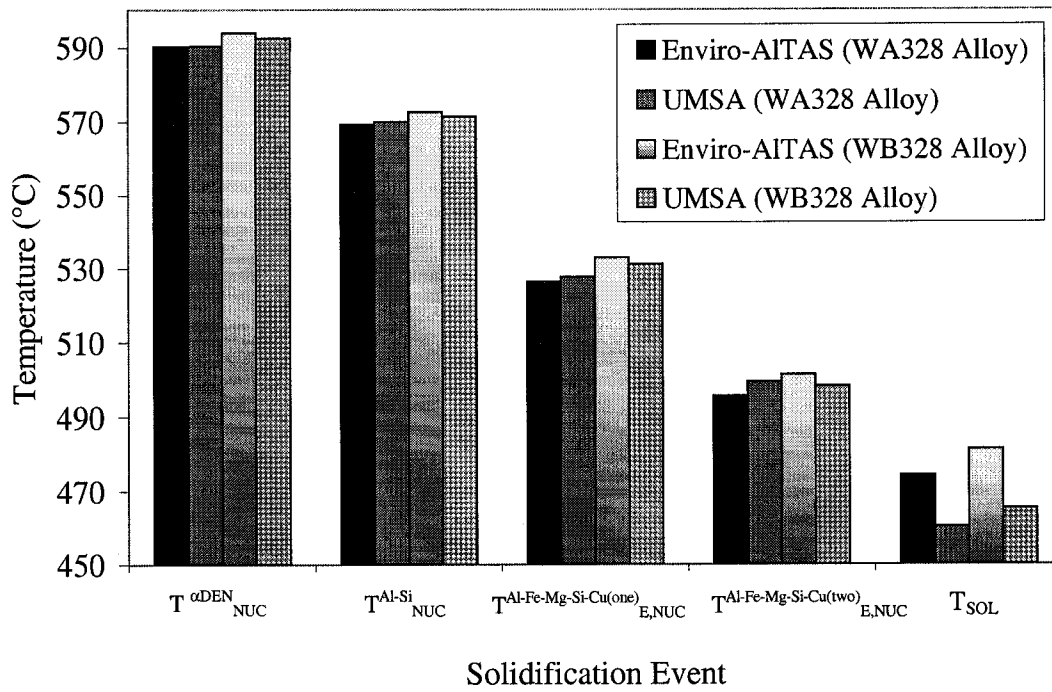


Figure 5.2.1a: The Summary of characteristic temperatures found for WA328 alloy and WB328 alloy using both the UMSA and Enviro-ALTAS platforms.

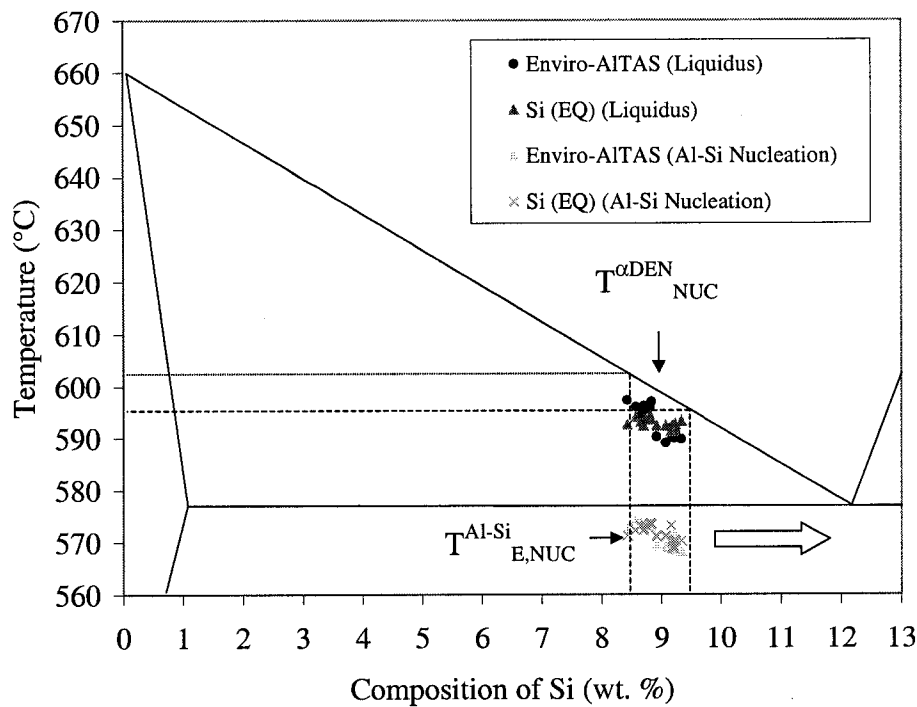


Figure 5.2.1b: The $T^{\alpha\text{DEN}}_{\text{NUC}}$ and $T^{\text{Al-Si}}_{\text{E,NUC}}$ seen on a the binary Al-Si are taken from Enviro-ALTAS test samples which were cast along with an OES disk (See **Appendix D**). The dashed lines represent the compositional limits of Si content defined for the WA328 and WB328 alloys as shown in Table 4.1.

5.2.2 Partitioned Cooling Curve & Fraction Solid Parameters

Once the characteristic temperatures (determined from cooling curves acquired using calibrated thermocouples and a Data Acquisition System, *see Section 4.5*) were acquired (verified through Si_{EQ}, UMSA and Enviro-ALTAS, *see Section 5.2.1*), then the accurate determination of the partitioned thermal analysis and fraction solid parameters could be made.

The partitioned time (UMSA), partitioned temperature (UMSA) and the partitioned fraction solid (Enviro-ALTAS) for each solidification event is shown in Figures 5.2.2a, 5.2.2b and 5.2.2c respectively. The data seen in Figures 5.2.2a and 5.2.2b is calculated from the UMSA, however from Table 5.2.1a one can see that if the bar graphs were generated from the Enviro-ALTAS test samples the partitioned thermal analysis parameters would be the same. The fraction solid calculation in the Enviro-ALTAS software is calculated and is used in Figure 5.2.2c.

Clearly one can see that the W319 alloy has the longest total solidification time and temperature range for complete solidification. This can be reflected in the extended range in time and temperature of the α -Al dendrite formation prior to the advent of the Al-Si nucleation (*i.e.* $\Delta T^{\alpha DEN}_{SRAN}$, & $\Delta t^{\alpha DEN}_{SRAN}$ is greater for the W319 alloy than for the WA328 or WB328 alloy). This of course corresponds to a larger partitioned fraction solid ($af_s^{\alpha DEN}$ from 20% up to 40%) for the α -Al primary dendrites as seen in Figure 5.2.2c. However the partitioned cooling rate ($CR^{\alpha DEN}_{SRAN}$), seen in Figure 5.2.2d, for the α -Al dendrite growth is

the same for all three alloys. This observation is important and will be discussed in Sections 5.4 and 5.5 of this chapter.

The partitioned fraction solid for the Al-Si eutectic reaction (af^{Al-Si}) of the WA328 and WB328 alloys is much larger than for the W319 alloy as seen in Figure 5.2d despite the fact that the temperature range (ΔT^{Al-Si}_{SRAN}) is smaller than for the W319 alloy. This may seem counter intuitive, unlike the behaviour for the α -Al primary dendrites. This is due to the fact that the larger fractional amount of the Al-Si eutectic that forms in the WA328 and WB328 alloys occurs within a narrower temperature range. This is primarily due to the fact that the lower level of Cu (of the WA328 and WB328 alloys) increases the temperature of the first post eutectic reaction ($T^{Al-Fe-Mg-Si-Cu(one)}_{E,NUC}$). As a consequence the partitioned cooling rate for the Al-Si eutectic (CR^{Al-Si}_{SRAN}) is 0.38°C/sec and for the WA328 and the WB328 alloys is 0.40°C/sec while this same partitioned cooling rate jumps up to 0.51°C/sec for the W319 alloy.

The average partitioned cooling rate increases during the solidification of the two post eutectic reactions (i.e. between $T^{Al-Fe-Mg-Si-Cu(one)}_{E,NUC}$ and T_{SOL}). The average values of the cooling rates are 1.67°C/sec, 1.70°C/sec and 1.48°C/sec for the WA328 alloy, the WB328 alloy, and the W319 respectively. This increase in cooling rate after $T^{Al-Fe-Mg-Si-Cu(one)}_{E,NUC}$ is most likely due to the fact that the quantity of latent heat generation is coming from less than 5% liquid fraction, and that the latent heat is removed quickly. In fact Mulazimoglu et al. [88] have indicated that the fineness of the post Al-Si eutectic phases is a result of quenching due to the small size and dispersed distribution. Observation of the fineness of Al_2Cu and Mg_2Si phases in the cast

structure of the 4.6L engine block and the Enviro-ALTAS test samples (*see Figures 5.1a through 5.1x*) confirms that a high cooling rate was present during solidification of these phases.

If one were to look at the total cooling rate during solidification (i.e. between $T^{\text{DEN}}_{\text{NUC}}$ and T_{SOL}), as do the majority of metal casting researchers [2, 8, 9, 11, 42, 46, 53, 62, 67, 87, 88], the values of total cooling rate for the WA328 alloy, the WB328 alloy and the W319 alloy would be 0.68°C/sec, 0.70°C/sec and 0.66°C/sec respectively. One would make the assessment that for the same cup containment and processing conditions in the UMSA system that the cooling rate was fixed regardless of alloy composition. Partitioning of the cooling rates has shown that this is not the case. In fact, since the W319, WA328 and WB328 alloys have differing susceptibilities toward pore nucleation and growth, the effect of the total cooling rate (as seen in Figure 5.2d) could have been totally ruled out as a contributor. It is known that the higher the cooling rate the lower the severity of porosity [2, 21, 22, 28, 59, 62, 74, 78, 81, 83, 85]. It is known from Ren [19] that the susceptibility to pore formation is higher for the Al-7wt.%Si-4wt.%Cu alloy (close to the W319 alloy) than for the Al-9wt.%Si-1wt.%Cu alloy (close to the WA328 alloy).

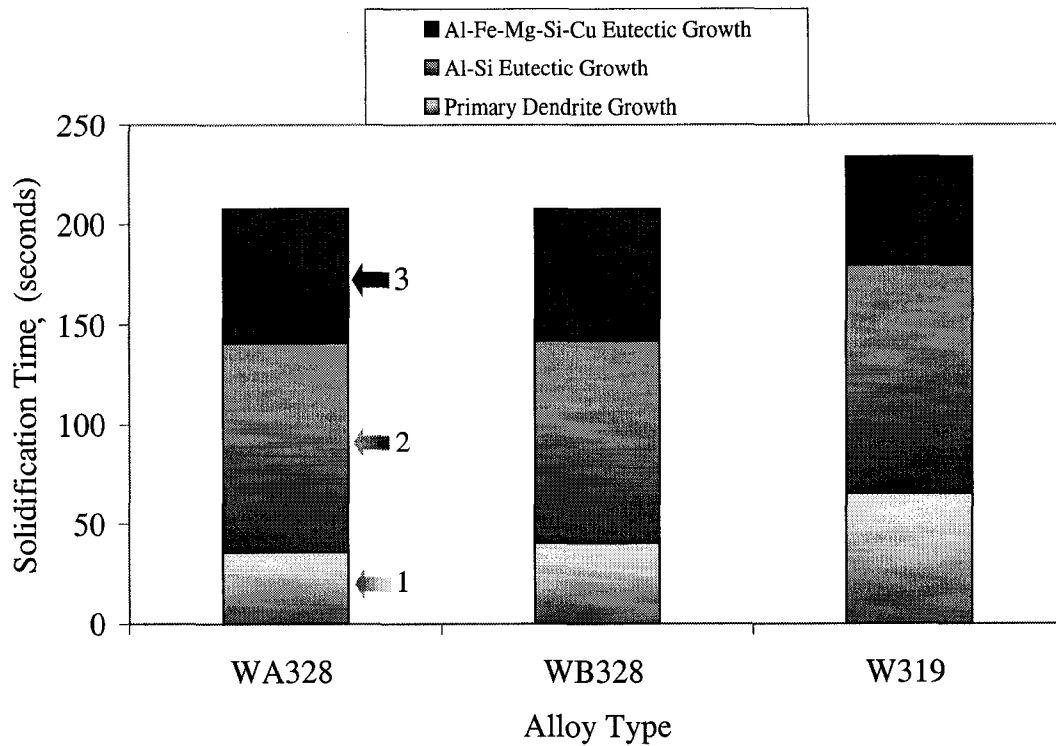


Figure 5.2.2a: The results of the partitioned solidification time for the WA328 alloy, the WB328 alloy and the W319 alloy, 1) $\Delta t^{\alpha_{DEN}}_{SRAN}$, 2) Δt^{Al-Si}_{SRAN} & 3) $\Delta t^{Al-Fe-Mg-Si-Cu}_{SRAN}$. Standard deviation is given in Appendix F.

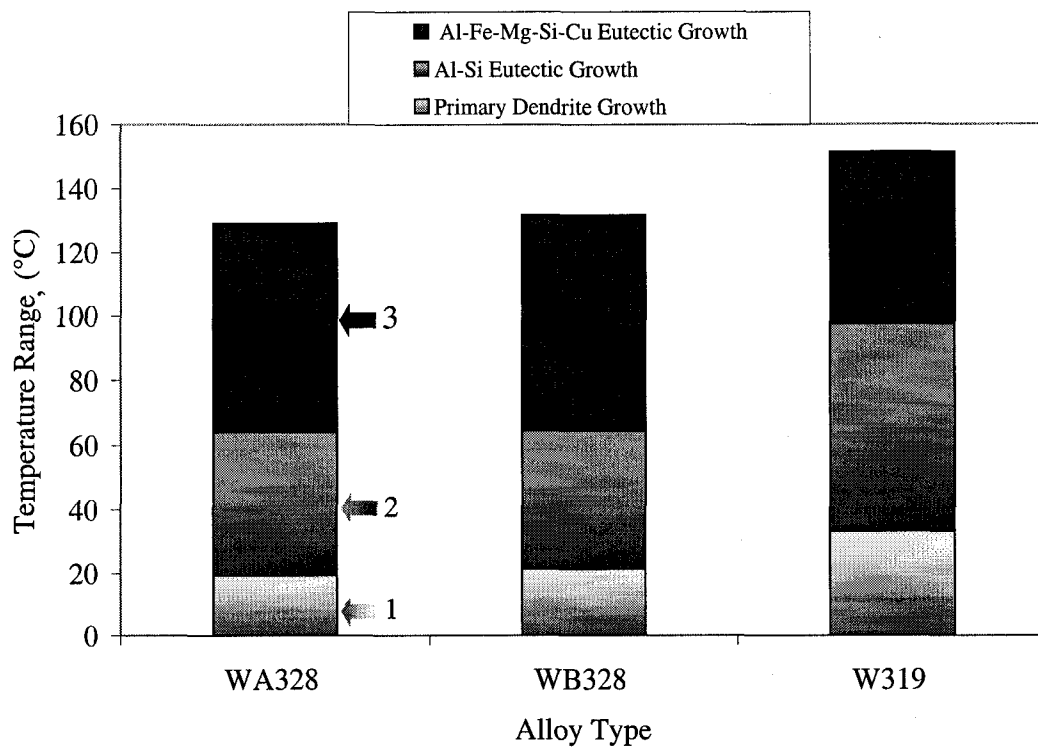


Figure 5.2.2b: The results of the partitioned temperature range for the WA328 alloy, the WB328 alloy and the W319 alloy, 1) $\Delta T^{\alpha_{DEN}}_{SRAN}$, 2) ΔT^{Al-Si}_{SRAN} & 3) $\Delta T^{Al-Fe-Mg-Si-Cu}_{SRAN}$. Standard Deviation is given in Appendix F.

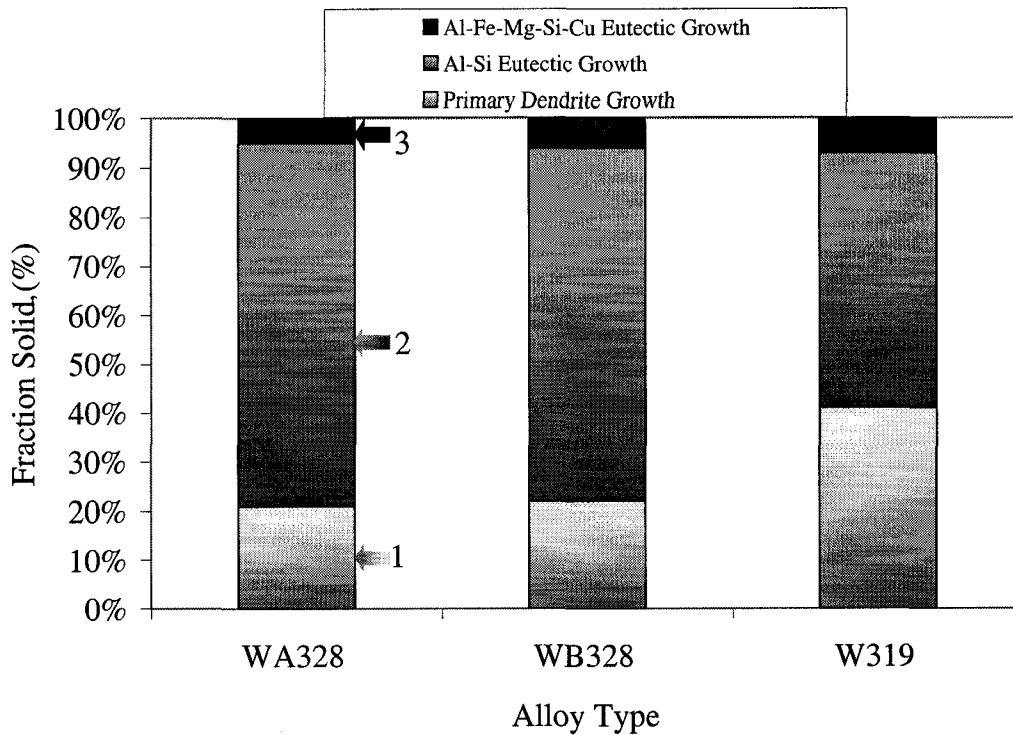


Figure 5.2.2c: The results of the partitioned fraction solid for the WA328 alloy, the WB328 alloy and the W319 alloy, 1) α^{DEN} , 2) $\alpha^{\text{Al-Si}}$ & 3) $\alpha^{\text{Al-Fe-Mg-Si-Cu}}$. Standard deviation given in Appendix F.

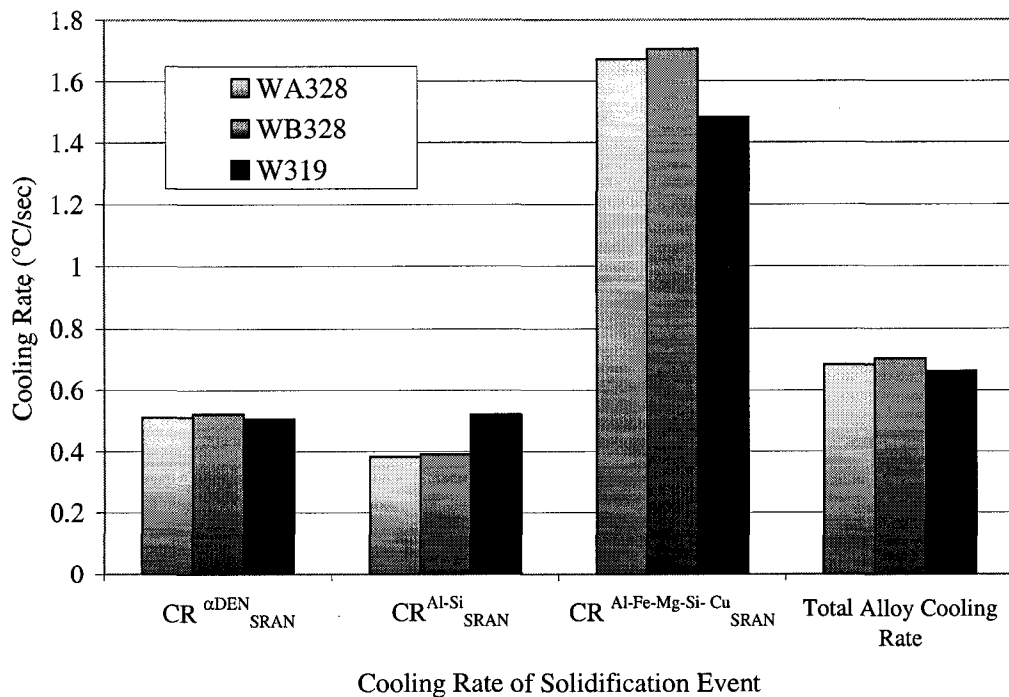


Figure 5.2.2d: Summary of the partitioned cooling rates of the α -Al primary dendritic growth stage, the Al-Si eutectic stage and the Al-Fe-Mg-Si-Cu eutectic stage for the WA328 alloy, the WB328 alloy and the W319 alloy. Also included is the total cooling rate for all three alloys.

5.2.3 Heating Behaviour of the W319, WA328 & WB328 Alloys

Figure 5.2a shows the UMSA heating and cooling curves of the WA328 alloy and Figure 5.2b shows the associated calculated first derivative curve. Labeled in Figures 5.2a and 5.2b are the specific characteristic heating temperatures that are of interest.

Table 5.2.3 summarizes the temperature which is the apparent start of the dissolution of soluble elements within the α -Al matrix (and which corresponds to a Minimum TSR Transfer Temperature) the temperature at which the first melting occurs and the temperature at which the alloy becomes 100% liquid [92].

It was found on the heating portion of the UMSA thermal cycle that the minimum transfer TSR temperature (*the lowest drop in temperature between removal of the engine block casting from the carousel into the TSR furnace*) was approximately 422.8°C for the W319 alloy, 419.2°C for the WA328 alloy and 411.2°C for the WB328 alloy. The temperature at which incipient melting (*Point 2 in Figures 5.2a and 5.2b*) occurs at 505.7°C for the W319 alloy, 511°C for the WA328 alloy and 512°C for the WB328 alloy. The temperature for the incipient melting of the alloy is the safe maximum temperature at which the single step solution temperature (TSR) and the solution treatment process can be achieved.

Table 5.2.3: Summary of the characteristic temperature points from analysis of the heating portion of the UMSA thermal curve. The heating rate for all three alloys was 0.50°C/sec. The results are based on 6 repeats.

<i>Thermal Characteristics</i>	<i>WB328</i>	<i>WA328</i>	<i>W319</i>
	<i>Temperature (°C)</i>	<i>Temperature (°C)</i>	<i>Temperature (°C)</i>
Apparent start of dissolution of soluble phases(s) – Minimum TSR Transfer Temperature (<i>Point 1, Figure 5.2b</i>)	411.2 ± 0.7	419.2 ± 0.7	422.8 ± 0.7
Start (beginning) of the alloy melting process (<i>Point 2, Figure 5.2a & 5.2b</i>)	512 ± 0.7	511 ± 0.7	505.7 ± 0.2
Finish (end) of the alloy melting process (<i>Point 3, Figure 5.2a & 5.2b</i>)	615 ± 0.7	611 ± 0.7	626.9 ± 2.7

5.3 Mushy Zone Evolution during the Solidification of the WA328, the WB328 and the W319 Alloys

Figures 5.3a, 5.3b and 5.3c summarize the targeted temperatures at which quenching occurred in the WA328 alloy, the WB328 Alloy, and the W319 alloy, respectively. The quenched temperatures were chosen for reasons outlined in Table 5.3.

Table 5.3: The temperature of the quenched test alloy samples.

<i>Quenched Temperature</i>	<i>Cast Structure To be measured</i>	<i>Stage of Solidification to be Observed</i>
585°C (all alloys)	λ_2 DCSz HV25g/15sec	Past the Dendrite Coherency Point (DCP), revealing the structure during interdendritic feeding. Alloy still hypereutectic.
575°C (WA328 & WB328) 565°C (W319)	λ_2 DCSz HV25g/15sec AFSP(α -Al)	Corresponds to the nucleation temperature of the Al-Si eutectic ($T_{E,NUC}^{Al-Si}$).
555°C (all alloys)	λ_2 DCSz HV25g/15sec	Al-Si cells will have begun to grow within the interdendritic regions. Some dendrite coarsening may still occur.
527°C (all alloys)	λ_2 DCSz HV25g/15sec	Most of all Al-Si cells have grown and the first post eutectic reaction begins ($T_{E,NUC}^{AlMgFeSi(one)}$).
Solidus (all alloys)	λ_2 DCSz HV25g/15sec	Full solidification (Not quenched)

The dendrite cell itself was usually visibly delineated in quenched structures allowing both *Dendrite Arm Spacing* (λ_2 , (μm)) and *Dendrite Cell Size* (DCSz, (μm)) measurements to be taken from the metallographic sections. In addition Image Analysis (IA) was used to measure the *Area Fraction of Sectioned Primary α -Al dendrites* (AFSP(α -Al), (%)).

Vickers Microhardness (HV25g/15sec) was also measured on the coarse primary α -Al dendritic matrix (*not the quenched primary α -Al dendrite matrix*). The aforementioned measured parameters of the coarse α -Al dendrite condition are listed together with each of the subsequent LOM micrographs of the quenched alloy structures (seen in Figures 5.3.1a to 5.3.1d).

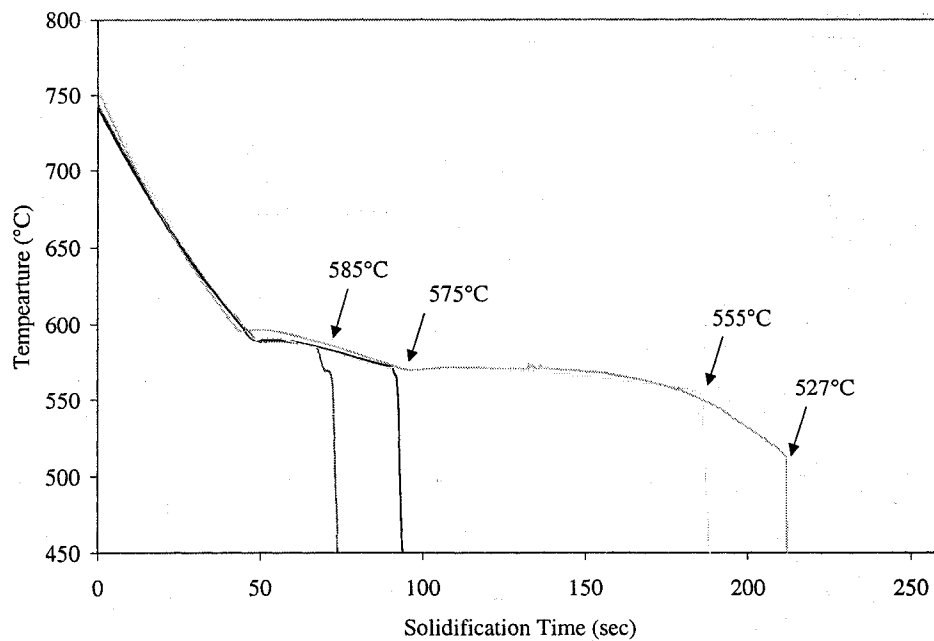


Figure 5.3a: The four overlays of the UMSA cooling curves for the WA328 alloy. The cooling rate of the quenched event is $\sim 60.0^{\circ}\text{C}/\text{sec}$.

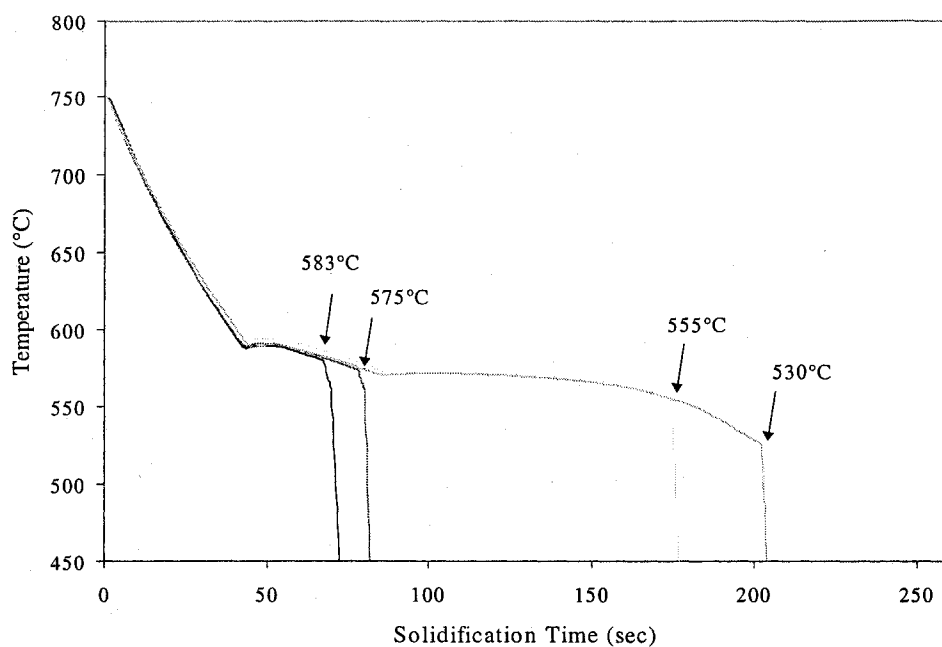


Figure 5.3b: The four overlays of the UMSA cooling curves for the WB328 alloy. The cooling rate of the quenched event is $\sim 60.0^{\circ}\text{C}/\text{sec}$.

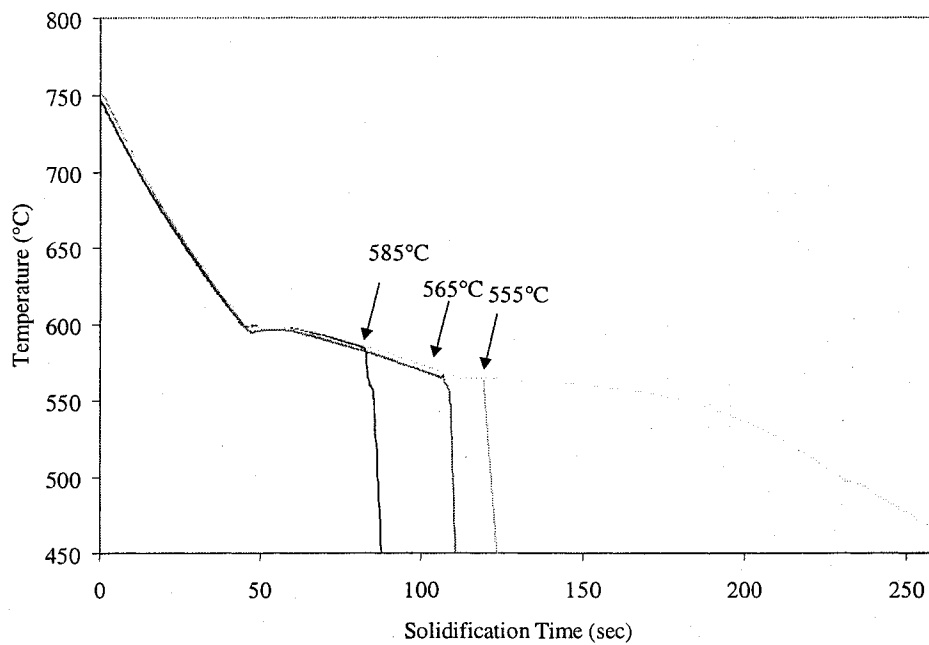


Figure 5.3c: The three overlays of the UMSA cooling curves for the W319 alloy. The cooling rate of the quenched event is $\sim 60.0^{\circ}\text{C}/\text{sec}$.

5.3.1 Results of Quenched WA328 Alloys, WB328 Alloys & W319 Alloys

The LOM micrograph shown in Figure 5.3.1a is from the quenched cast structure at 585°C for the WA328 alloy. Figure 5.3.1a shows several coarse α -Al dendrites which grew between 591°C and 585°C. Located between these coarse dendrites are fine quenched dendrites. The same type of quenched structure for the WB328 alloy is seen in Figure 5.3.1b. The fraction solid as calculated for the Enviro-ALTAS test samples at this stage of solidification is approximately 15% (see Figure 5.2.2c).

These fine dendrites seen in Figures 5.3.1a and 5.3.1b are present mostly on the surfaces of coarse primary α -Al dendrites and in limited cases within the interdendritic quenched regions. This observation is similar to what Neilson et al. [97] found in his quenched Al-Ni alloy structures.

The next temperature for quenching was at 575°C ($T_{E,NUC}^{Al-Si}$). Figure 5.3.1c and Figure 5.3.1d revealed coarse dendrites only for the WA328 alloy and WB328 alloy respectively. The partitioned events Δt_{SRAN}^{AlSi} , ΔT_{SRAN}^{AlSi} and $af_s^{\alpha DEN}$ (whose values are listed on the side inset of each figure) are reflected by the LOM micrographs seen in Figures 5.3.1c and 5.3.1d. The absence of fine dendrites indicates that the liquid has become sufficiently enriched with Si, enough to achieve eutectic composition.

Present in the quenched structure of Figures 5.3.1c and 5.3.1d are polyhedrals of Si amongst very fine Al-Si eutectic structures. These polyhedrals were the result of the eutectic

composed liquid experiencing rapid solidification. The thermodynamic description for polyhedral Si formation will be given in Section 5.3.3.

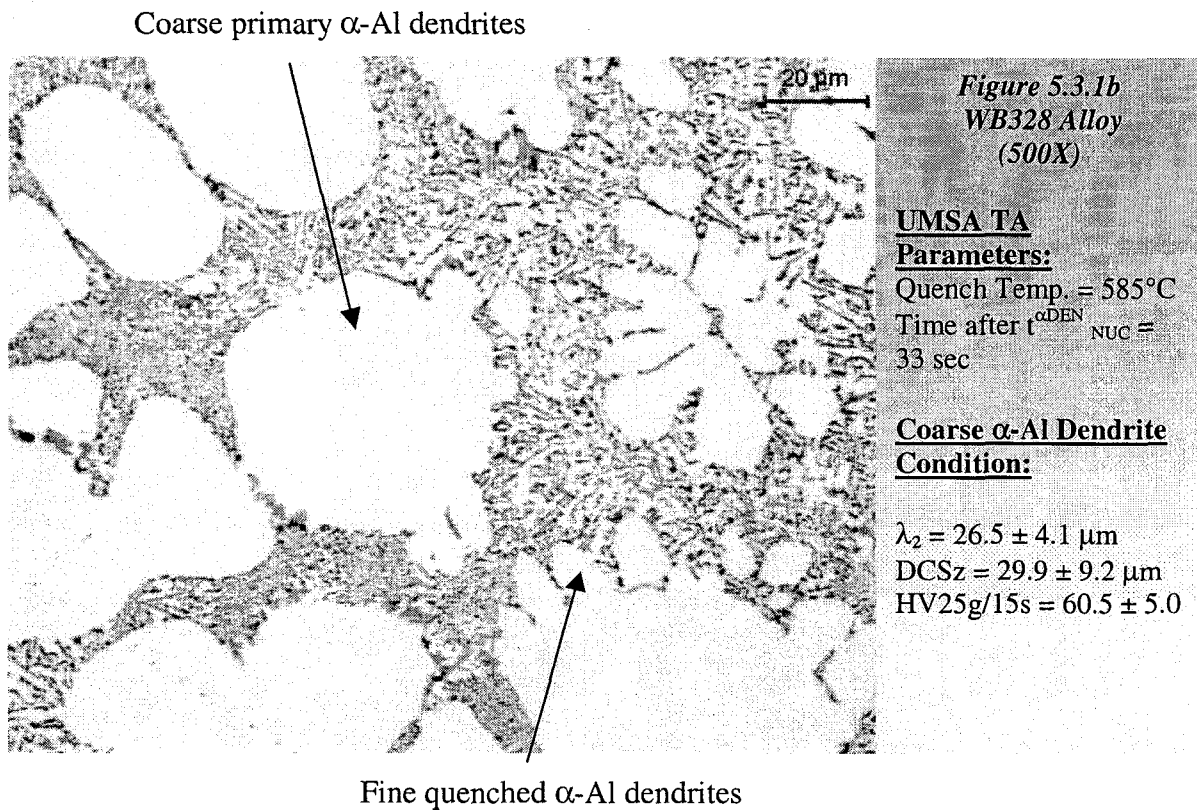
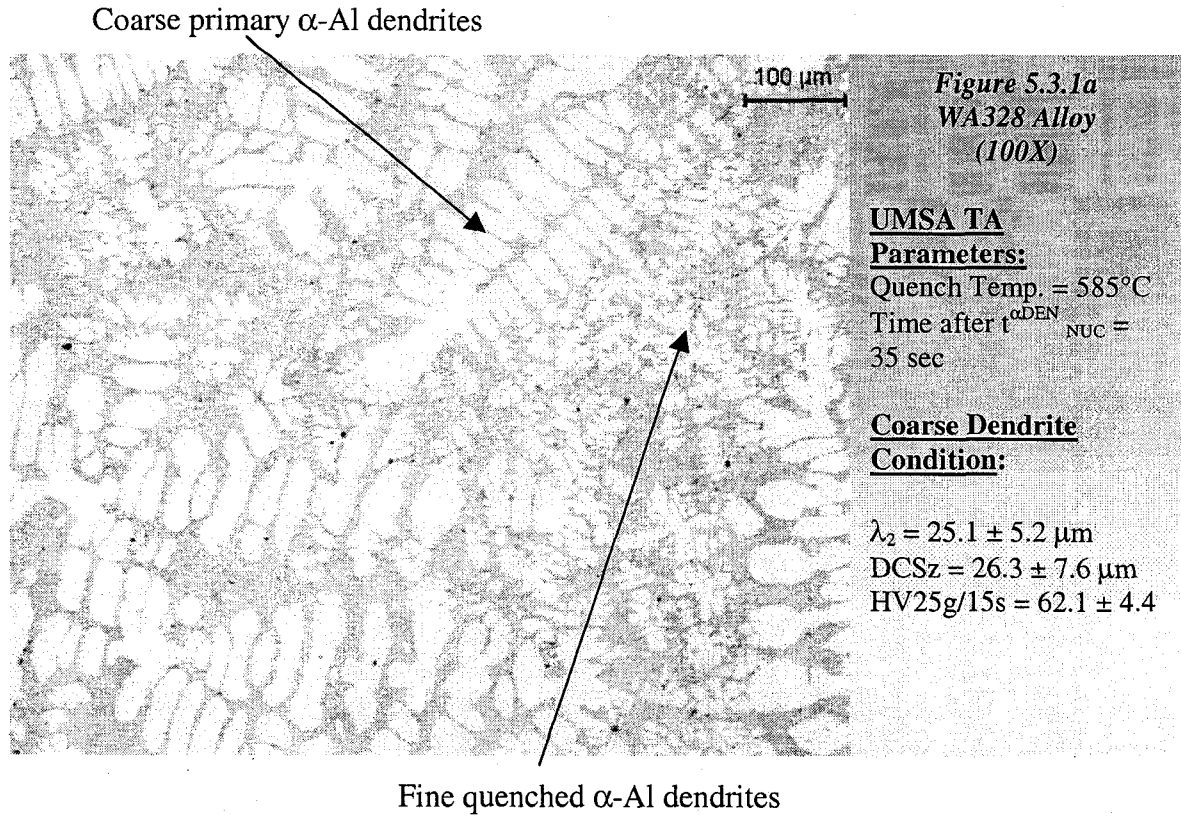
Figure 5.3.1e shows the quenched structure of the W319 alloy at 585°C. Note that the measured value for λ_2 is $32.3 \pm 8.01 \mu\text{m}$, an $\sim 7\mu\text{m}$ larger value than the λ_2 for the WA328 and WB328 alloys. The calculated fraction solid at this point is approximately 24% to 26%. The larger fraction solid and λ_2 found at the target quench temperature 585°C for the W319 alloy compared to the WA328 or the WB328 alloys is due to the fact that the liquidus is higher for the W319 alloy resulting in a longer time for Newtonian cooling of growing dendrites prior to the quench event.

Figure 5.3.1f shows the quenched structure of the W319 alloy at 565°C ($T_{\text{NUC}}^{\text{Al-Si}}$) that reveals the solidified structure that corresponds to the partitioned thermal analysis events $\Delta t_{\text{SRAN}}^{\text{AlSi}}$, $\Delta T_{\text{SRAN}}^{\text{AlSi}}$ and $af_s^{\alpha\text{DEN}}$ (whose values are listed on the side inset of Figure 5.3.1f). Again, as with the WA328 alloy and the WB328 alloy, polyhedrals of Si were seen amongst a fine quenched Al-Si structure.

Figure 5.3.1g shows low magnification regions of the WA328 alloy, indicated by arrows, and the quenched structure at 555°C. Also seen in the LOM micrograph are coarse $\text{Al}_{15}(\text{Fe,Mn,Cr})_3\text{Si}_2$ script phases indicating that these phases grow at some point after $T_{\text{E,NUC}}^{\text{Al-Si}}$. This is not unexpected since Zindel et al. [98] found $\text{Al}_{15}(\text{Fe,Mn,Cr})_3\text{Si}_2$ script phase growth in W319 alloy samples quenched during Al-Si eutectic solidification.

Figure 5.3.1h shows the WA328 alloy structure, seen in Figure 5.3.1h, at 500X magnification revealing a region in which liquid existed at the time of quench at 555°C. The quenched liquid seems to reveal a fine dark phase which is most likely very fine Si and a $\text{Al}_{15}(\text{Fe,Mn,Cr})_3\text{Si}_2$ script phase. It is known that from the fully solidified structures, as seen in Figures 5.1t and 5.1v (Section 5.1), the quenched regions seen in Figure 5.3.1h probably contain Cu, Mg, Fe and Ni to form the Al_2Cu phase, the Mg_2Si script phase, Al_5FeSi platelet phase, Al-Ni-Fe phase and the Al-Ni-Cu phase. The fraction solid calculated from the cooling curves at 555°C is approximately 80-85% for both the WA328 alloy and the WB328 alloy.

Figure 5.3.1i shows the W319 alloy structure at 100X which had been quenched at 555°C and Figure 5.3.1j shows the same structure at 200X. Several $\text{Al}_{15}(\text{Fe,Mn,Cr})_3\text{Si}_2$ script phases are seen and resulting from an $\text{Al} + \text{Al}_{15}(\text{Fe,Mn,Cr})_3\text{Si}_2$ eutectic type reaction (*labeled as Reaction 1 in Figure 5.3.1j*). This reaction is reported to be a tertiary type eutectic that includes Si [2, 67, 88, 105]. Figure 5.3.1j shows the $\text{Al} + \text{Al}_{15}(\text{Fe,Mn,Cr})_3\text{Si}_2$ eutectic type reaction and its coupled growth solidification front more clearly. Also seen in Figures 5.3.1i and 5.3.1j is the solidification front of the Al-Si eutectic cells (*labeled as Reaction 2 in Figure 5.3.1j*). Like the $\text{Al} + \text{Al}_{15}(\text{Fe,Mn,Cr})_3\text{Si}_2$ eutectic type reaction the Al and Si phases form through the coupled growth of both phases. The calculated fraction for the W319 alloy at 555°C is 50%.



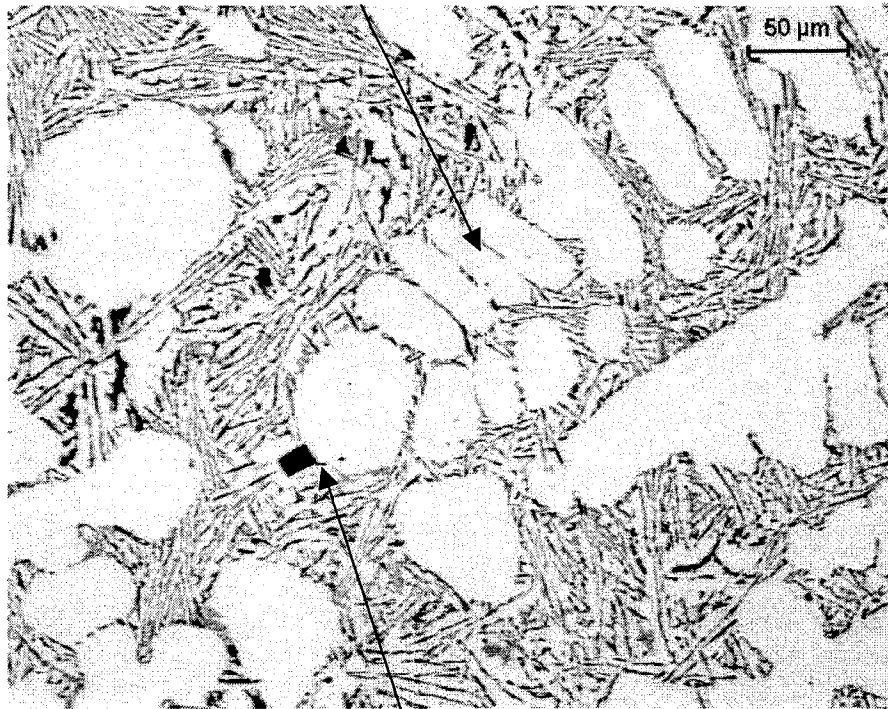
Coarse primary α -Al dendrites

Figure 5.3.1c
WB328 Alloy
(200X)

UMSA TA
Parameters:

Quench Temp. = 575°C
 $\Delta T^{\alpha\text{DEN}}_{\text{SRAN}} = 19^\circ\text{C}$
 Time after $t^{\alpha\text{DEN}}_{\text{NUC}}$ or,
 $\Delta t^{\alpha\text{DEN}}_{\text{SRAN}} = 51 \text{ sec}$

Coarse α -Al Dendrite
Condition:

$\lambda_2 = 34.9 \pm 4.1 \mu\text{m}$
 $\text{DCSz} = 28.7 \pm 9.2 \mu\text{m}$
 $\text{HV}_{25\text{g}/15\text{s}} = 59.1 \pm 2.0$

Polyhedral Si

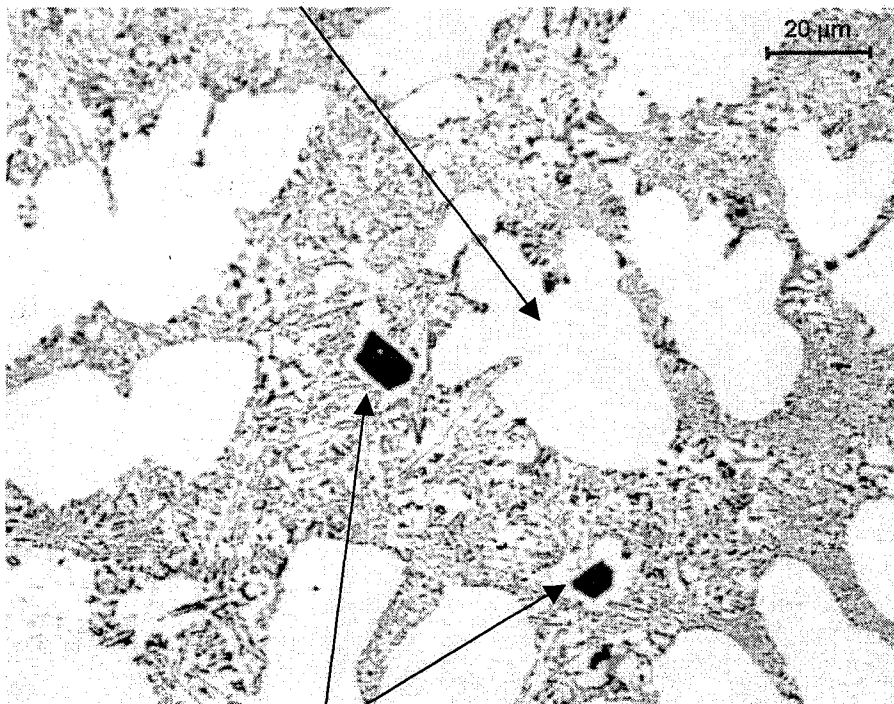
Coarse primary α -Al dendrites

Figure 5.3.1d
WA328 Alloy
(500X)

UMSA TA
Parameters:

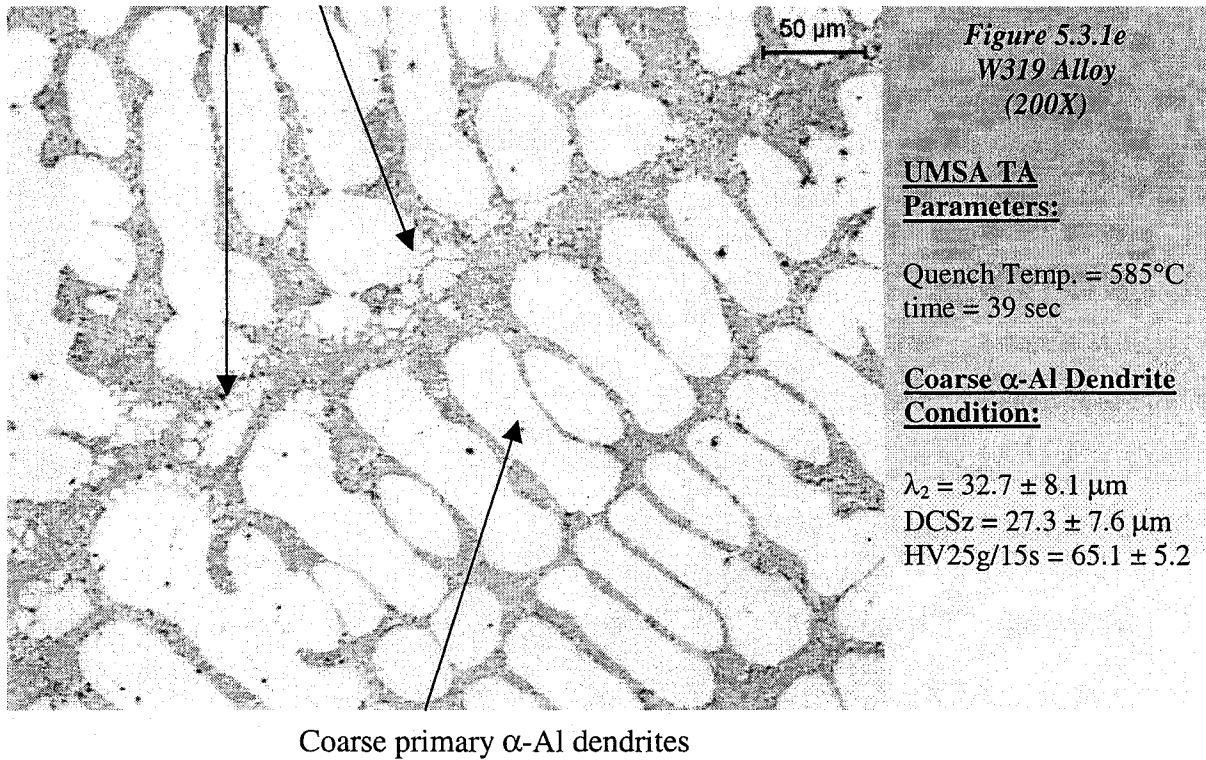
Quench Temp = 575°C
 $\Delta T^{\alpha\text{DEN}}_{\text{SRAN}} = 20^\circ\text{C}$
 Time after $t^{\alpha\text{DEN}}_{\text{NUC}}$ or,
 $\Delta t^{\alpha\text{DEN}}_{\text{SRAN}} = 54 \text{ sec}$

Coarse α -Al Dendrite
Condition:

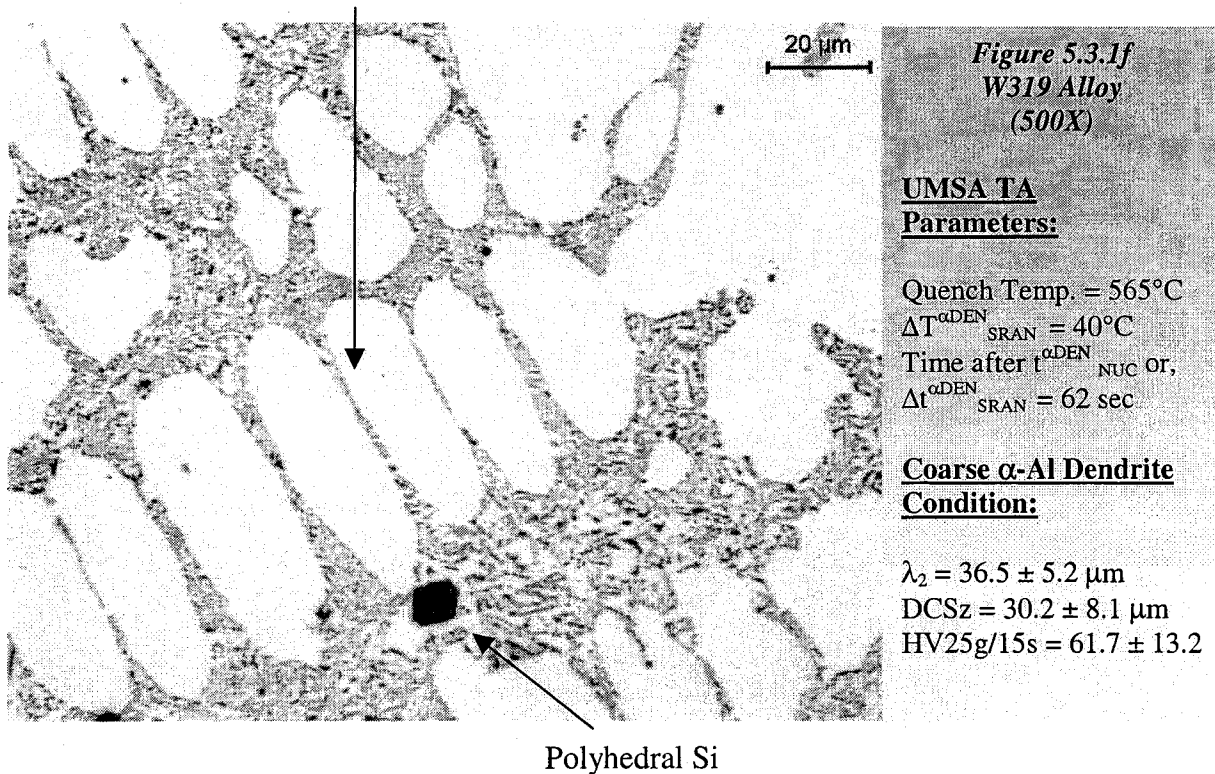
$\lambda_2 = 32.6 \pm 8.25 \mu\text{m}$
 $\text{DCSz} = 29.9 \pm 9.2 \mu\text{m}$
 $\text{HV}_{25\text{g}/15\text{s}} = 62.1 \pm 3.1$

Polyhedral Si

Fine quenched α -Al dendrites



Coarse primary α -Al dendrites



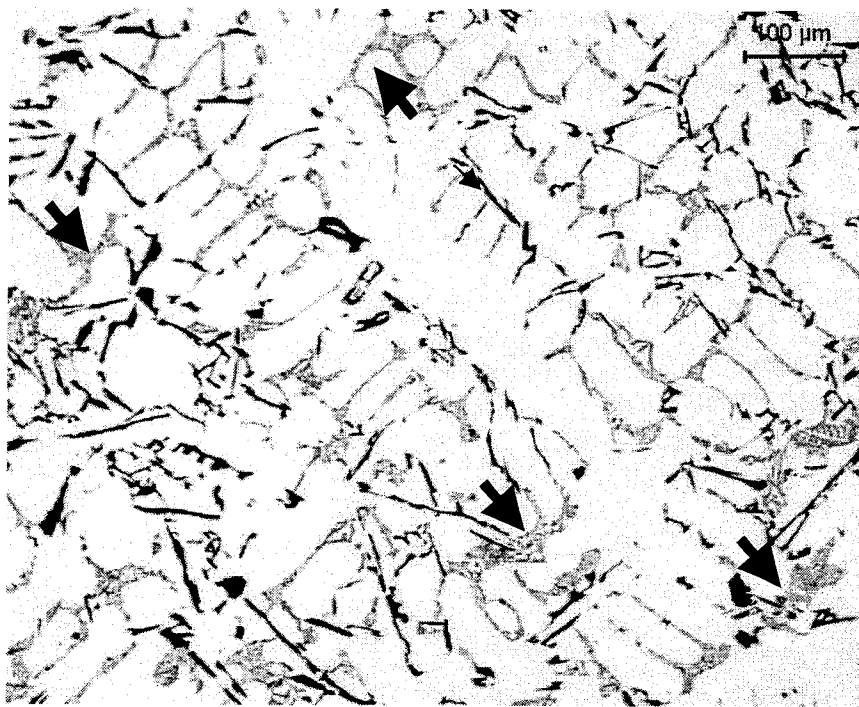


Figure 5.3.1g
WA328 Alloy
(100X)

UMSA TA
Parameters:

Temp. = 555°C
Time after $t^{\alpha\text{DEN}}_{\text{NUC}}$ =
115 sec.
 $f_s = 80\%$

Coarse α -Al Dendrite
Condition:

$\lambda_2 = 44.7 \pm 8.4 \mu\text{m}$
DCSz = $40.8 \pm 10.6 \mu\text{m}$
HV25g/15s = 58.7 ± 2.0

Arrows pointing to quenched regions

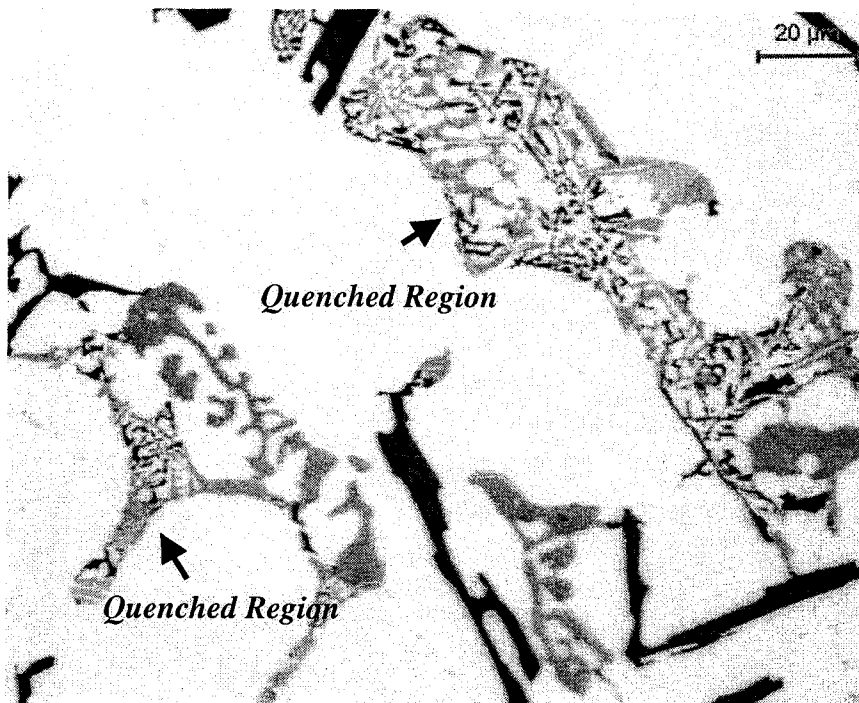


Figure 5.3.1h
WB328 Alloy
(500X)

UMSA TA
Parameters:

Temp. = 555°C
Time after $t^{\alpha\text{DEN}}_{\text{NUC}}$ =
115 sec.
 $f_s = 82\%$

Coarse α -Al Dendrite
Condition:

$\lambda_2 = 44.7 \pm 8.4 \mu\text{m}$
DCSz = $40.8 \pm 10.6 \mu\text{m}$
HV25g/15s = 58.7 ± 2.0

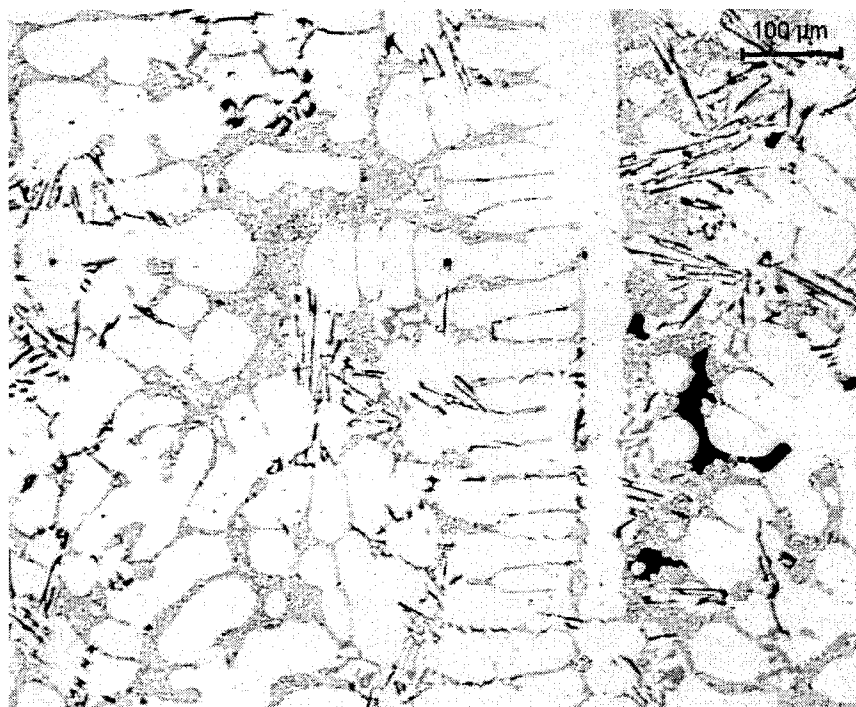


Figure 5.3.1i
W319 Alloy
(100X)

UMSA TA
Parameters:

Temp. = 555°C
Time after $t^{\alpha\text{DEN}}_{\text{NUC}} = 71$
sec.
 $f_s = 50\%$

Coarse α -Al Dendrite
Condition:

$\lambda_2 = 36.6 \pm 8.4 \mu\text{m}$
DCSz = $30.8 \pm 10.6 \mu\text{m}$
HV25g/15s = 63.6 ± 3.7

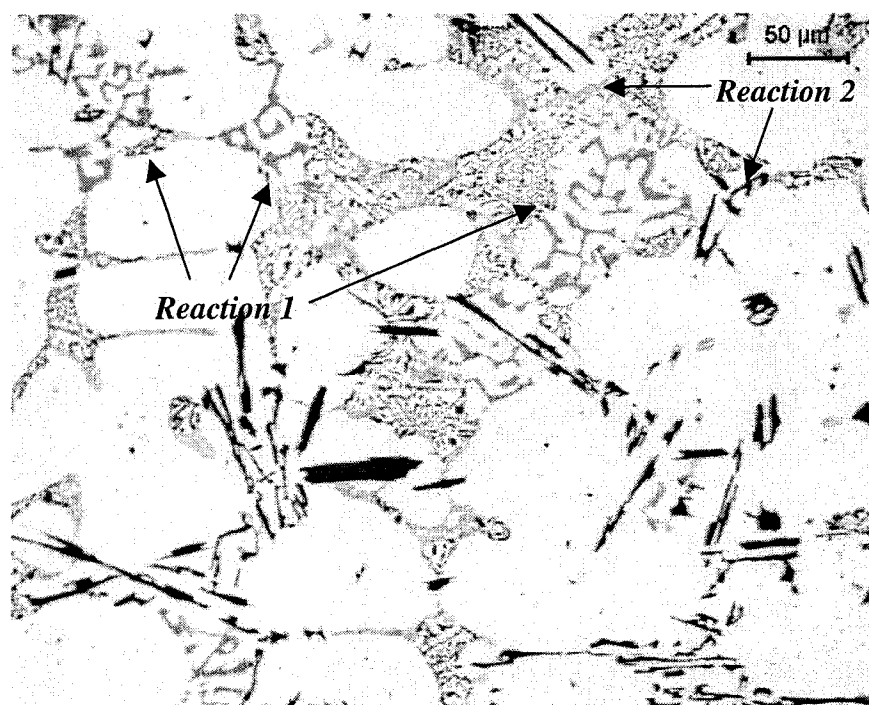


Figure 5.3.1j
W319 Alloy
(200X)

UMSA TA
Parameters:

Temp. = 555°C
Time after $t^{\alpha\text{DEN}}_{\text{NUC}} = 71$
sec.
 $f_s = 50\%$

Coarse α -Al Dendrite
Condition:

$\lambda_2 = 36.6 \pm 8.4 \mu\text{m}$
DCSz = $30.8 \pm 10.6 \mu\text{m}$
HV25g/15s = 63.6 ± 3.7

Observed Reactions:

- 1) $L \Rightarrow \text{Al} + \text{Al}_{15}(\text{Fe}, \text{Mn}, \text{Cr})_3\text{Si}_2$
- 2) $L \Rightarrow \text{Al} + \text{Si}$

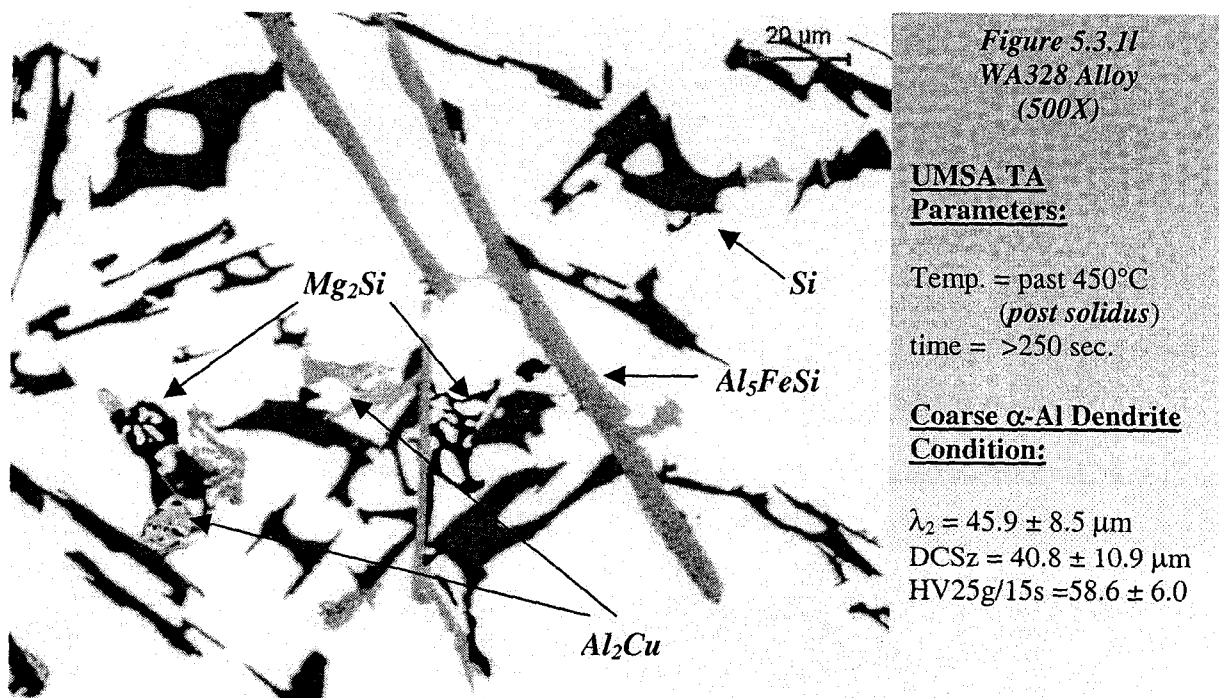
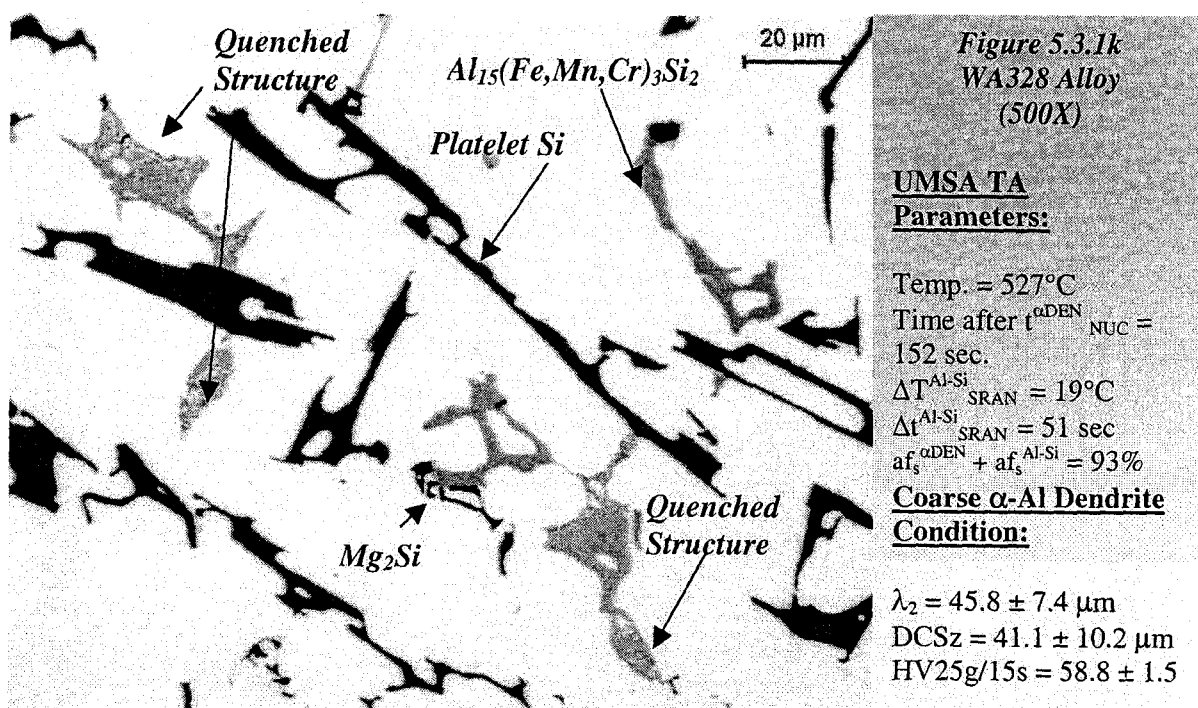


Figure 5.3.1k shows the structure of the WA328 alloy quenched at 527°C, corresponding to the characteristic temperature $T_{E,NUC}^{Al-Fe-Mg-Si-Cu(one)}$. This is the temperature at which the first anomalous change in the cooling curve's cooling rate occurs immediately after the post main Al-Si eutectic reaction has formed completely (see Figure 5.2e, Section 5.2). The calculated fraction solid at this point (i.e. $af_s^{\alpha DEN} + af_s^{Al-Si}$) is 93%. The LOM micrograph of Figure 5.3.1k shows that the Mg_2Si script phase has formed and that discrete pools of liquid (presumably Cu rich) still exist. In Section 5.1 the heat treated WA328 and WB328 alloys had undissolved Mg_2Si while the Al_2Cu phase was absent and was probably dissolved.

Figure 5.3.1l shows the fully solidified WA328 alloy. Present within the structure are the Mg_2Si phase, Al_2Cu phase and Al_5FeSi platelet phases. This structure is similar to that found in the Enviro-ALTAS test sample structure and the 4.6L engine block bulkhead section. Two exceptions are the Al-Ni-Fe and Al-Ni-Cu phases which were difficult to observe in the UMSA test samples at 500X magnification. They were more easily observed in the Enviro-ALTAS test samples and in the bulkhead structures of the 4.6L engine block (*both observed via SEM and LOM micrographs under 500X magnification*) presumably due to the longer solidification times they encountered. In other words sufficient time for diffusion was allotted for the test samples having longer solidification times to crystallize large enough Al-Ni-Fe and Al-Ni-Cu phases.

5.3.2 Summary of Phase Nucleation and Solidification Sequence in the WA328 and WB328 Alloys

Table 5.3.1 shows the summary of the phases observed and the temperatures at which they nucleate and the temperature range in which they grow. Table 5.3.1 contains data which has been generated from the cooling curves/structure of the UMSA test samples and the Enviro-ALTAS test samples, while the quenched structures revealing phase nucleation and growth came from observing the quenched UMSA test sample structure. A series of 5 most probable reactions constitutes the full solidification of the WA328 and WB328 alloys.

Table 5.3.1: Solidification Sequence Summary of the WA328 alloys cast in 4.6L engine block mould. The same solidification sequence exists for the WB328 alloy except for the slight change in characteristic temperatures (see Appendix F).

Summary of Reactions & Corresponding Characteristic Points	Partitioned Temperature Range Parameters	Fraction Solid & Appropriate Partitioned Parameters
(Reaction 1) $L \Rightarrow \alpha\text{-Al dendrites}$ $T_{\text{E,NUC}}^{\alpha\text{-DEN}} = 590^{\circ}\text{C}$ $f_s^{\alpha\text{-DEN}} = 0\%$	$(T_{\text{E,NUC}}^{\alpha\text{-DEN}} - T_{\text{E,NUC}}^{\text{Al-Si}}) = T_{\text{SRAN}}^{\alpha\text{-DEN}}$ $590^{\circ}\text{C} - 570^{\circ}\text{C} = 20^{\circ}\text{C}$ (Enviro-AITAS) $591^{\circ}\text{C} - 571^{\circ}\text{C} = 20^{\circ}\text{C}$ (UMSA)	$(f_s^{\text{Al-Si}} - 0\%) = af_s^{\alpha\text{-DEN}}$ $21\% - 0\% = 21\%$ (Enviro-AITAS)
(Reaction 2) $L \Rightarrow \text{Al} + \text{Si}$ (Eutectic) $T_{\text{E,NUC}}^{\text{Al-Si}} = 571^{\circ}\text{C}$ $f_s^{\text{Al-Si}} = 21\%$	$(T_{\text{E,NUC}}^{\text{Al-Si}} - T_{\text{E,NUC}}^{\text{Al-Fe-Mg-Si-Cu(one)}}) = \Delta T_{\text{SRAN}}^{\text{Al-Si}}$ $573^{\circ}\text{C} - 527^{\circ}\text{C} = 46^{\circ}\text{C}$ (Enviro-AITAS) $571^{\circ}\text{C} - 530^{\circ}\text{C} = 41^{\circ}\text{C}$ (UMSA)	$(f_s^{\text{Al-Fe-Mg-Si-Cu(one)}} - f_s^{\text{Al-Si}}) = af_s^{\text{Al-Si}}$ $95\% - 21\% = 74\%$ (Enviro-AITAS)
(Reaction 3) $L \Rightarrow \text{Al} + \text{Si} + \text{Al}_{15}(\text{Fe,Cr,Mn})_3\text{Si}_2$ $[11, 31, 88].$ Or $L \Rightarrow \text{Al} + \text{Al}_{15}(\text{Fe,Cr,Mn})_3\text{Si}_2$ (observed)	Temperature for the $\text{Al}_{15}(\text{Fe,Cr,Mn})_3\text{Si}_2 =$ Somewhere between 571°C and 555°C . Solidification ends before or at solidus (T_{SOL}).	Between $21\% f_s \text{ \& } 80\% f_s$
(Reaction 4) $L \Rightarrow \text{Al} + \text{Si} + \text{Mg}_2\text{Si} + \text{Al}_3\text{FeSi}$ $T_{\text{E,NUC}}^{\text{Al-Fe-Mg-Si-Cu(one)}} = 527^{\circ}\text{C}$ $f_s^{\text{Al-Fe-Mg-Si-Cu(one)}} = 94\%$	$(T_{\text{E,NUC}}^{\text{Al-Fe-Mg-Si-Cu(two)}} - T_{\text{E,NUC}}^{\text{Al-Fe-Mg-Si-Cu(one)}}) = \Delta T_{\text{SRAN}}^{\text{Al-Fe-Mg-Si-Cu(one)}}$ $527^{\circ}\text{C} - 498^{\circ}\text{C} = 35^{\circ}\text{C}$ (Enviro-AITAS) $530^{\circ}\text{C} - 500^{\circ}\text{C} = 30^{\circ}\text{C}$ (UMSA)	$(f_s^{\text{Al-Fe-Mg-Si-Cu(two)}} - f_s^{\text{Al-Fe-Mg-Si-Cu(one)}}) = af_s^{\text{Al-Fe-Mg-Si-Cu(one)}}$ $98\% - 94\% = 2\%$ (Enviro-AITAS)
(Reaction 5) $L \Rightarrow \text{Al} + \text{Si} + \text{Al}_2\text{Cu} + \text{Al}_3\text{FeSi} + \text{Al-Ni-Cu} + \text{Al-Ni-Fe} + \text{Pb particles}$ $T_{\text{E,NUC}}^{\text{Al-Fe-Mg-Si-Cu(two)}} = 500^{\circ}\text{C}$ $f_s^{\text{Al-Fe-Mg-Si-Cu(two)}} = 98\%$	$(T_{\text{SOL}} - T_{\text{E,NUC}}^{\text{Al-Fe-Mg-Si-Cu(two)}}) = \Delta T_{\text{SRAN}}^{\text{Al-Fe-Mg-Si-Cu(two)}}$ $498^{\circ}\text{C} - 482^{\circ}\text{C} = 16^{\circ}\text{C}$ (Enviro-AITAS) $500^{\circ}\text{C} - 461^{\circ}\text{C} = 39^{\circ}\text{C}$ (UMSA)	$(f_s^{\text{SOL}} - f_s^{\text{Al-Fe-Mg-Si-Cu(two)}}) = af_s^{\text{Al-Fe-Mg-Si-Cu(two)}}$ $100\% - 98\% = 2\%$ (Enviro-AITAS)

Cooling rate of Enviro-AITAS = 0.15°C/sec , & Cooling rate of the UMSA = 0.55°C/sec .

5.3.3 Origins of Polyhedral Si in a Quenched Hypoeutectic Al-Si Alloy

Polyhedrals of Si crystals are found in the cast alloy structures quenched at $T_{E,NUC}^{Al-Si}$. Quenching at a higher or lower temperature than $T_{E,NUC}^{Al-Si}$ will not allow the growth of polyhedral Si. The growth mechanisms of polyhedral Si and platelet Si can be described as follows. The equilibrium phase diagram has non-equilibrium extensions such as the *couple zone* for growth of the Al-Si eutectic [2, 99]. Due to the fact that the Si phase is faceted and the Al phase is not faceted the couple zone for growth is skewed towards the Si-rich end of the phase diagram (shown in Figure 5.3.3a).

Solute is supplied from the α -Al lamellae to feed the growth of the Si platelet. The solidification path from just below the equilibrium Al-Si eutectic temperature (Arrow 1) forms more α -Al dendrites only until the liquid composition of Si becomes further enriched and moves into the couple zone (Arrow 2). Within the couple zone the process of couple diffusion and growth of a lamellae type Al-Si eutectic will occur.

Polyhedral Si does not form through a coupled diffusion growth zone, as with lamellae of Si and Al. Polyhedral Si precipitates from the liquid itself. Due to the high cooling rate (*and thus high undercooling*) polyhedral Si forms (Arrow 1) below the equilibrium Al-Si composition and temperature. The liquid surrounding the polyhedral Si has become so enriched in Al that the α -Al halo forms (Arrow 2). The halo can be seen in Figures 5.3.2b & c. This α -Al envelops the polyhedral depriving it of a supply of Si and thus halts its growth. As the α -Al halo forms the liquid at the solid-liquid interface becomes progressively enriched in Si (Arrows 3 & 4) eventually yielding a liquid composition that falls within the

coupled zone. Once the liquid composition is within the coupled zone the coupled growth yielding eutectic Al-Si lamellae will occur.

It is hypothesized that quenching at $T_{E,NUC}^{Al-Si}$ all eutectic phase growth begin by following the solidification path of polyhedral Si first, followed by the formation of halo α -Al and the lamellae eutectic, or does the inhomogeneous distribution of Si play a role in this solidification path occurring only in discrete regions of the quenched UMSA test sample. The apparent density of polyhedral Si may lend itself to the former. This will be the subject of future work.

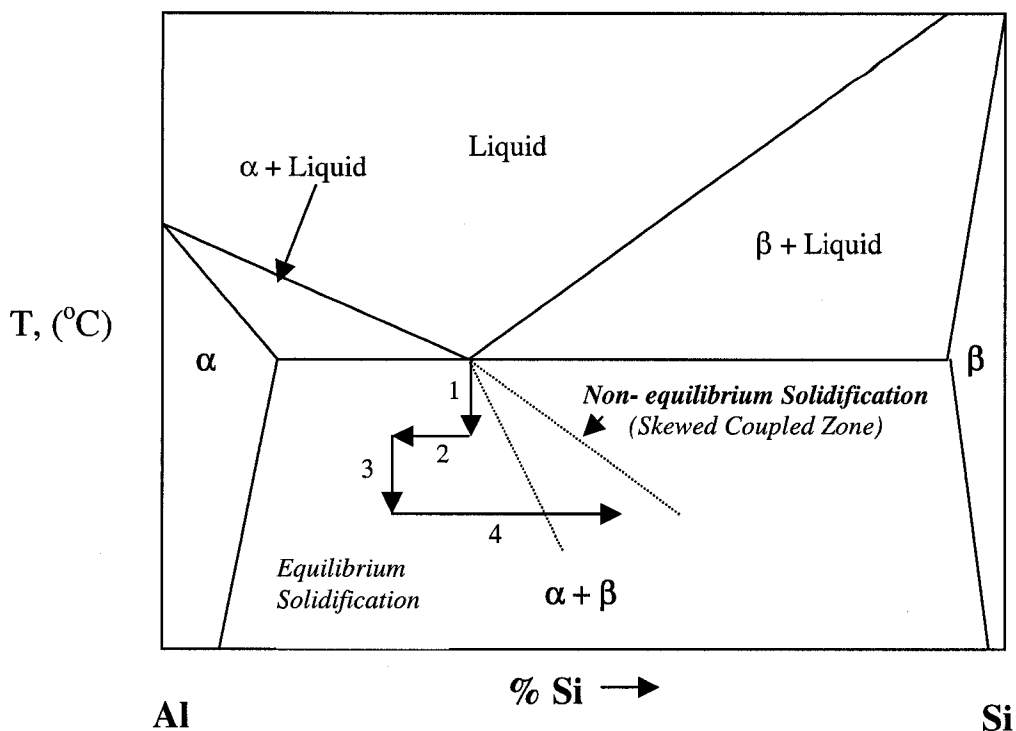


Figure 5.3.3a: The solidification path that permits the nucleation of polyhedral crystals of Si. Directly below the equilibrium Al-Si eutectic point (Arrow 1) is the path in which polyhedrals nucleate and grow. However the liquid adjacent to the polyhedral will become depleted in Si (Arrow 2). The halo forms around the polyhedral until the local composition reaches the skewed coupled zone and then stable Al-Si eutectics form (Arrows 3 & 4).

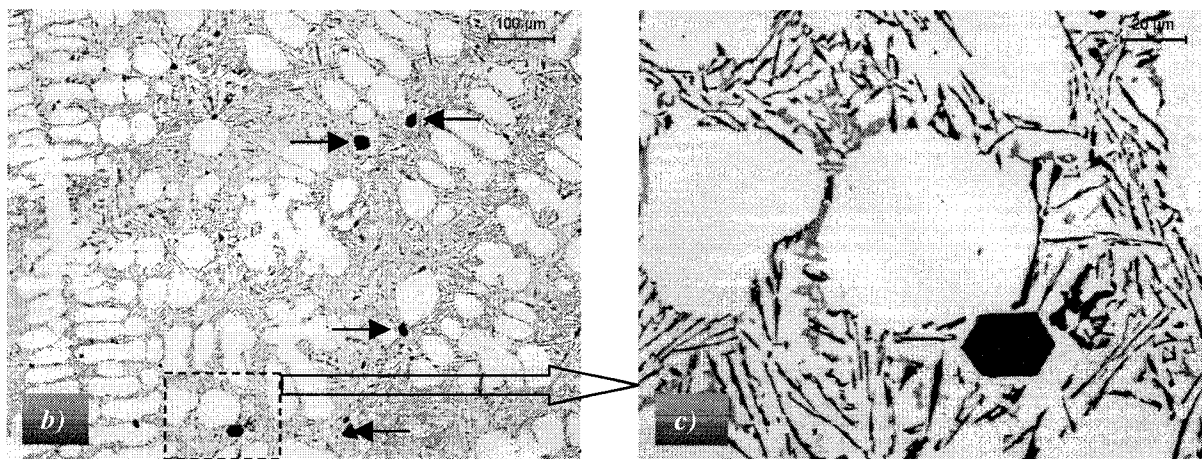


Figure 5.3.3: b) The structure of the WA328 alloy quenched at 575°C (200X). The arrows mark the location of polyhedral Si. The dashed box is zoomed up to 500X c) polyhedrals seen in the above micrograph encapsulate both the polyhedral Si crystal and the aluminum α -Al halo.

5.4 α -Al Dendrite Coarsening During the Solidification Process

Dendrites play a substantial role in the way that the interdendritic regions evolve during solidification. It is in these interdendritic regions that hypoeutectic and/or eutectic fluid flow must occur to compensate for dendrite shrinkage [14-16, 19, 44, 58-70]. Section 5.3 showed metallographically how the alloy structures of the WA328 alloy, the WB328 alloy and the W319 alloy evolve between 585°C and full solidification. However it becomes difficult to assess the evolving dimension and nature of the coarsening dendrites upon viewing LOM micrographs unless additional quantifying Image Analysis and microhardness methods are employed.

Flemings et al. [100], among others [101-104] have introduced an empirical relationship that relates the effect of the *final* solidification time (t_f) on Secondary Dendrite Arm Spacing (λ_2). The mathematical trend that was used to describe the relationship between λ_2 and solidification time is given in Equation 5.0:

$$\lambda_2 = at_f^n \quad (5.0)$$

Where a is a constant, the value which depends on the alloy, n is an exponential value reported to be between 0.3 and 0.4 [100-104]. The validity of this relationship will be determined by using a best fit curve and goodness of fit (R^2). Figure 5.4a shows the change in λ_2 for both the W319 and WA328 alloys. The value a is 9.54 and the exponent n is 0.31, which is essentially similar to the constant a and exponent n when observing the same trend

for the W319, WA328 and WB328 alloys as seen in Table 5.4a. This succinctly shows that the variation of λ_2 for a given time is the same for both the W319 alloy and the WA328 alloy, irrespective of the differing levels of Si and Cu. Included in Table 5.4a are the results of the dendrite coarsening for an Al-4wt.%Cu alloy, reported by Flemings et al. [100], showing similar values for a and n .

Figure 5.4a also shows the change in Dendrite Cell Size (DCSz) as measured from quenched and fully solidified W319 and WA328 UMSA test samples. The variation of DCSz follows the at_f^n trend with the constant value a being 9.88 and the exponential value n being 0.28. The change in DCSz with solidification time is essentially similar to the change of λ_2 with solidification time. This is an unreported observation prior to this dissertation.

Thus, the data shown in Figure 5.4a and Table 5.4a reveals that dendrite coarsening, as indicated by both λ_2 and DCSz measurements, is controlled predominantly by the solidification process, but insignificantly controlled by the alloying elements of the investigated alloys.

Another important observation made from Figure 5.4a is that the Vickers Microhardness of the as-cast quenched dendrites remains invariant throughout solidification and that the value of this mean microhardness is within the same range for both the W319 alloy and the WA328 alloy (*between 60 to 68 HV25*). The interval between the quenching of the UMSA test samples and the subsequent measurement of the Vickers Microhardness was 213 days.

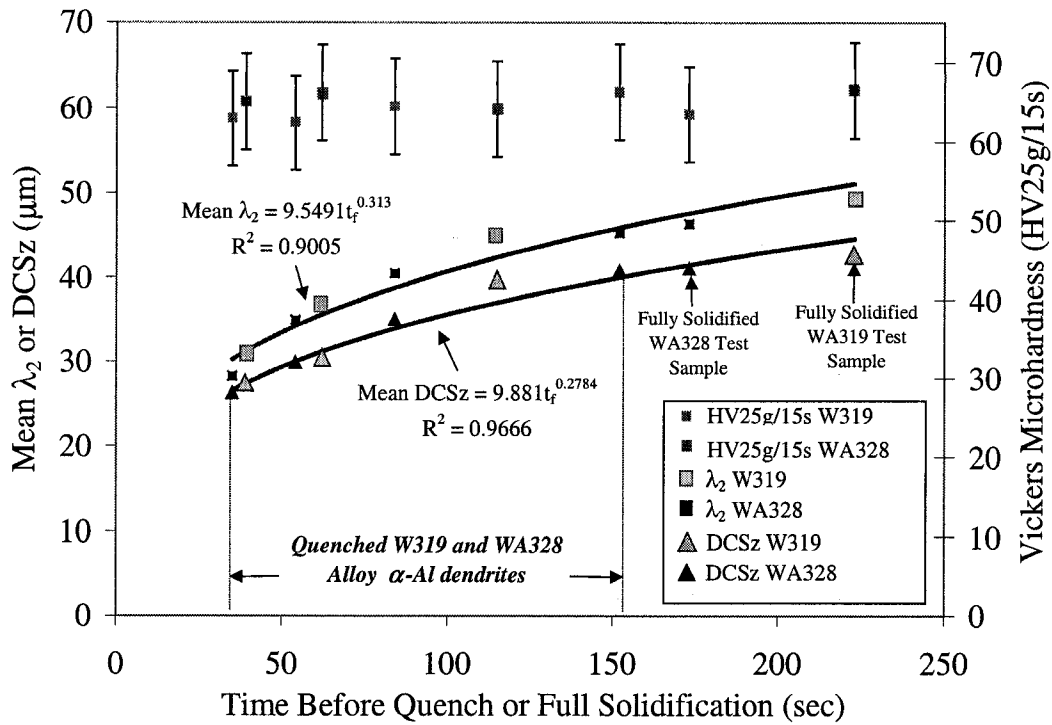


Figure 5.4a: The plot of mean λ_2 ($\pm 8.5 \mu\text{m}$), DCSz ($\pm 9.5 \mu\text{m}$) and Vickers Microhardness (standard deviation listed) of the coarse α -Al dendrites in the as-cast quenched test samples of the WA328 alloy and the W319 alloy.

Table 5.4a: Coefficients associated with the λ_2 at a quenched stage of solidification and full solidification time. It is important to point out that the power equation that has been reported within the literature is found to be valid even for partially solidified structures.

Alloy Type/s	$\lambda_2 = at_f^n$		
	a	n	R^2
Al-4.5%Cu alloy from Flemings et al. [100] (<i>Final solidification</i>)	10	0.33	-
WA328 alloy (<i>Quenched & final solidification of UMSA test samples</i>)	8.17	0.33	0.91
WB328 alloy (<i>Quenched & final solidification of UMSA test samples</i>)	8.85	0.34	0.97
W319 alloy (<i>Quenched & final solidification of UMSA test samples</i>)	10.85	0.30	0.99

Upon further investigation it was found that the trend of coarsening of α -Al dendrites with solidification time can be extended further (*with longer solidification times then used for the UMSA test samples*) through the compilation of numerous published data (t_f vs. λ_2) for the 319 type alloys, the 356 alloy, and the WA328 alloy which are plotted together in Figure 5.4b [19, 21, 43, 78, 98, 105]. The summary of the λ_2 data sources used in Figure 5.4b, such as alloy type, sample mould type, cooling rates & solidification time are listed in Table 5.4b.

The relationship between λ_2 and alloy cooling rate has been reported within the literature for Al-Cu and Al-Si-Cu alloys [100-106]. Within this dissertation the results presented in Figure 5.4b are plotted against the cooling rate in Figure 5.4c. The cooling rate for each referenced case and the analyses in this work are also listed in Table 5.4b. The relationship between λ_2 and alloy cooling rate during solidification is given in Equation 5.1 as [100]:

$$\lambda_2 = b\epsilon^{-n} \quad (5.1)$$

Where b is a constant, the value which depends on the alloy, n is a constant with a value which has been reported to be between 0.35 and 0.40; ϵ is the alloy cooling rate [104].

The constant values of b and n found for Flemings et al. [100] was 0.39 for the Al-4.5wt.%Cu alloy. Figure 5.4d lists the values of b and n for the W319 alloy, the 356 alloy, and the WA328 alloy where the plot of ϵ against solidification time is presented in Figure 5.4c. The cooling rate seen in Figure 5.4c spans between 0.04°C/sec up to 2.5°C/sec.

Thus, the effect of λ_2 coarsening by cooling rate for the W319 alloy, the 356 alloy and the WA328 alloy appears to behave similarly. The values of b and n are also similar to the results of the Al-4.5%wtCu alloy presented by Flemings et al. [100]. Clearly the total solidification time is dominant while the alloy composition appears to be insignificant for λ_2 coarsening.

Table 5.4b: Summary of Fully Solidified Test Sample Conditions used in this work and in the referenced work. The data was used to help compile the results seen in Figures 5.4c and 5.4d.

<i>Alloy Type</i>	<i>Cup Dimensions/ Mould Condition</i>	<i>Test Sample Mass (grams)</i>	<i>Thermocouple Type</i>	<i>Solidification Time (sec)</i>	<i>Sample Cooling Rate (°C/sec)</i>
W319 (Current work)	14mm O.D. 18mm L 0.025mm W.T. (304 steel)	7.3	Low mass K-type	220	0.55
W319 (Zindel et al. [98])	22.2mm O.D. 0.89mm W.T. (Stainless steel tube)	Unspecified	K-type (unspecified)	300	0.33
WA328 alloy (Current work)	14mm O.D. 18mm L 0.025mm W.T. (304 steel)	7.3	Low mass K-type	180	0.37
WB328 alloy (Current work)	14mm O.D. 18mm L 0.025mm W.T. (304 steel)	7.3	Low mass K-type	180	0.38
356 Alloy (Cho et al. [43])	Graphite moulds	Unspecified	Unspecified	50 - 2500	2.0 – 0.04
W319 alloy Mackay et. al [106]	Non-risere graphite cup	280-300	0.62 Omega K-type	52 -262	2.0 – 0.37
4.6L FWD engine block (Bulkhead E) (Appendix C)	Zirconium Sand Mould	-	0.62 Omega K-type	456 – 470	0.19
4.6L RWD engine block (Bulkhead E) (Appendix C)	Zirconium Sand Mould	-	0.62 Omega K-type	472 – 497	0.17
W319 alloy (Current work)	Risere Steel wall cup	550-575	Low mass K-type	1148	0.10
356 alloy (Boileau et al. [21])	Silica Sand Mould (wedge casting)	8,200	Unspecified	40, 360 & 1290	2.5, 0.27 & 0.07
W319 alloy (Caton et al. [22])	Unspecified sand type (wedge casting)	8,200	Unspecified	44 & 2600	
W319 Alloy (Boileau [78])	Silica Sand Mould (wedge casting)	8,200	Unspecified	42, 654, 966 & 2604	2.5, 0.45, 0.10, & 0.04
Al-9wt.%Si-1wt.%Cu alloy (Ren [19])	Zirconium Sand Mould (wedge casting)	8,200	0.62 Omega K-type	41 , 230, 1750 & 2750	2.5, 0.45 0.06 & 0.038
Al-7wt.%Si-4wt.%Cu alloy wedge (Ren [19])	Zirconium Sand Mould (wedge casting)	8,200	0.62 Omega K-type	41 , 230, 1750 & 2750	2.5, 0.45 0.06 & 0.038

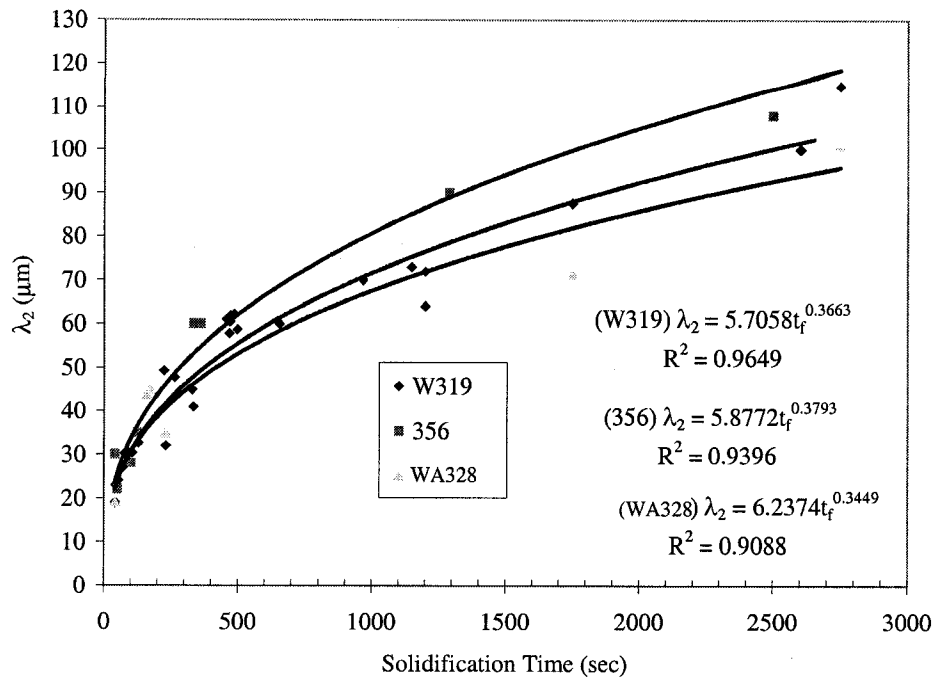


Figure 5.4b: The change of λ_2 , referenced from various sources listed in Table 5.4b, are displayed in the above graph over large solidification ranges (40 seconds up to 2750 seconds) for the W319 alloy, 356 alloy and WA328 alloy. The best-fit power equation is identified for each profile.

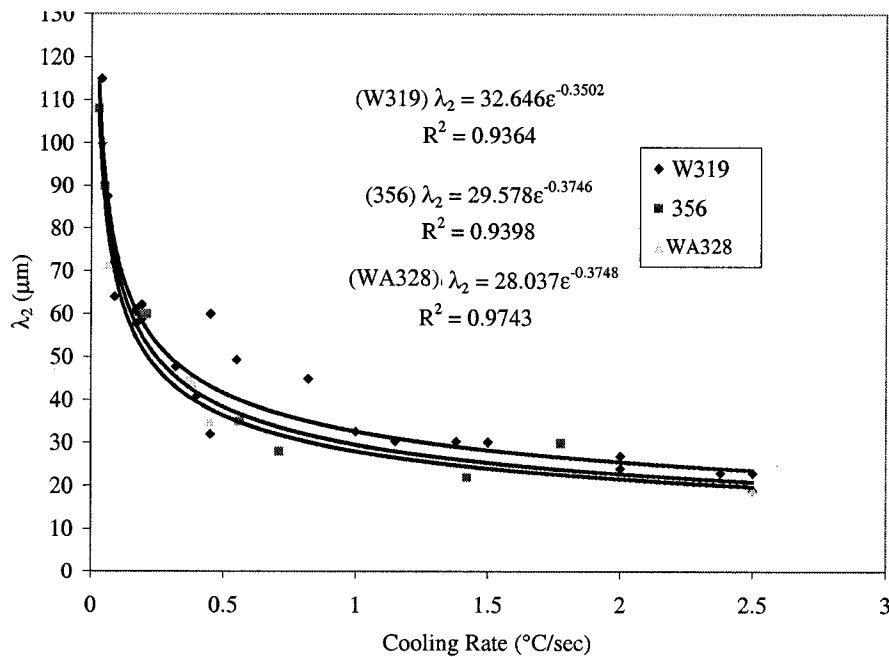


Figure 5.4c: The changes in λ_2 , referenced from various sources listed in Table 5.4b are displayed in the above graph over large cooling rates (0.04°C/sec up to 2.5°C/sec) for the W319 alloy, 356 alloy and WA328 alloy. The best-fit power equation is identified for each profile.

5.5 Dendrite Ripening in the W319, WA328 & WB328 Alloys

As indicated in Section 5.4, the dendrite coarsening of the alloys investigated shows a very pronounced dependence on solidification time (or cooling rate), and a relatively insignificant dependence on alloy chemistry. This section will explain the probable reasons for these observations.

The factors controlling dendrite coarsening stem from several thermodynamic driving forces. There is the effect of free energy associated with the surface of the dendrite (G_s), the bulk volume energy of the dendrite (G_v), and the partitioning of solute (k) [2, 99, 104]. To better visualize the role of each of the thermodynamic factors it helps to consider a dendrite as a separate entity from the adjacent secondary dendrites and from the primary stock dendrite from which it grew. The schematic of dendrite ripening, and the thermodynamic driven diffusion process are shown in Figure 5.5a for the initial stage of solidification, and in Figure 5.5b for the fully solidified UMSA test sample cast structure. The data seen in the upper left hand corner represents actual data acquired from Section 5.3.

The dendrites try to attain a larger portion of their free energy through bulk volume energy (G_v) at the expense of the dendrites surface energy (G_s) [99, 104]. This thermodynamic driving factor exists for any phase such as the α -Al embryos and GPZ (*Guinier-Preston zones*) [2, 14, 86, 95, 104]. In the context of Figure 5.5a this means that dendrite *a* (*thicker dendrite*) is more stable than dendrite *b* (*thinner dendrite*) because $G_{va} > G_{vb}$, $G_{va} > G_{sa}$ and $G_{sb} \geq G_{sa}$ (i.e subscript *va* refers to the volume of dendrite *a*, see Figure 5.5a). Eventually, as solutes (Si and Cu) diffuse from dendrite *a* to dendrite *b* and solvent (Al) diffuses from

dendrite *b* into dendrite *a*, dendrite *b* should eventually, with time, dissolve altogether. For the same given solidification time a change in the alloy composition could change the rate of this dendrite ripening. Presumably a larger quantity of solute present would dissolve thinner dendrites sooner [107]. However, as stated in Section 5.4, the compositional ranges investigated exhibit an inferior role compared to solidification time in controlling dendrite ripening. The solidification phenomena needed to explain the dominance of the solidification time over compositional differences on dendrite ripening can be described as follows:

In Figure 5.4a the Vickers microhardness of the α -Al dendrites was the same for both the W319 alloy and the WA328 alloy throughout solidification. This implies that the amount of solute that can remain in solid solution within α -Al dendrites is limited and that most of the solute has to be rejected into the interdendritic liquid [104]. Solute in the interdendritic liquid is needed for dendrite ripening. Table 5.5 shows the equilibrium partition coefficient, k , for Cu, Si, Fe, Mn, Mg, Zn and Ni. From Table 5.5 it can be seen that Si and Cu have among some of the lowest equilibrium partition coefficients ($k \approx 0.13 - 0.18$) and these two elements are also the largest in content for both the W319 and WA328 alloys.

Figure 5.5c shows a bar graph of the accumulative alloy elements (by weight) for the three alloys investigated. It would appear that the total weight amount of Si and Cu which must be ejected from dendrites during solidification (where $k \approx 0.13 - 0.18$), has a narrow range of approximately 10-11 wt.%. The remaining elements, Mg, Mn and Fe, constitute only 1wt.% of the total weight amount of alloying in the W319 alloy and the WA328 alloy, and approximately 2 wt.% for the WB328 alloy.

Thus, one may conclude that the similarity of dendrite ripening in the W319 and WA328 alloys is due to the fact that Si and Cu partition by the same amount, and that the weight amount of the two elements together, ejected into the liquid to actively contribute to the ripening process of dendrites, is almost the same. In other words if Si replaced Cu (i.e going from W319 to WA328 alloy) the rate of coarsening should not be substantially altered.

This assessment is valid since the behaviour of the size of λ_2 versus the increase of Si and Cu (binaries with Al) shows the same change with increasing alloying content as shown in Figure 5.5d (*graph reproduced from Shivkumar et. al [107]*). Not reported in the work by Shivkumar et al. [107] was the similarity of the best fit equations. The goodness of fit values shows that the two curves (λ_2 vs. wt.% Si or Cu) are in fact similar. Figure 5.5d visually implies that if Si and Cu were interchanged dendrite coarsening kinetics would be unaltered. This fundamentally explains why both λ_2 and DCSz seem relatively insensitive to the proportion of alloying content and are dominated by the solidification time.

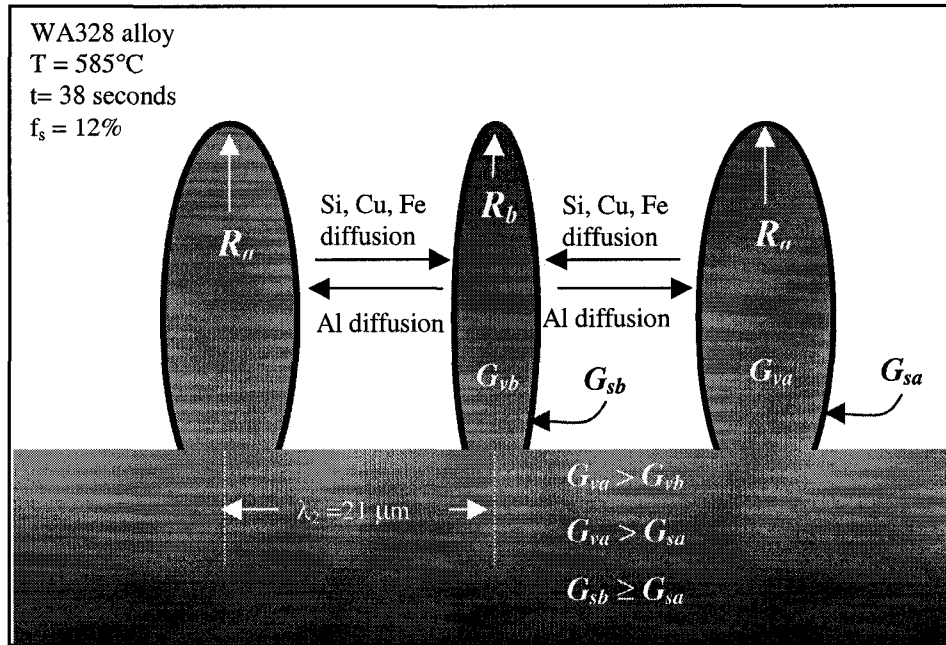


Figure 5.5a: The first quenched stage the dendrite size distribution results in dendrites with a radii of curvature at the tips. In the above case $R_a > R_b$. This drives the diffusion paths of solute elements (Si, Cu and Fe) along the diffusion paths indicated, while the solvent element (Al) diffuses in the reverse direction.

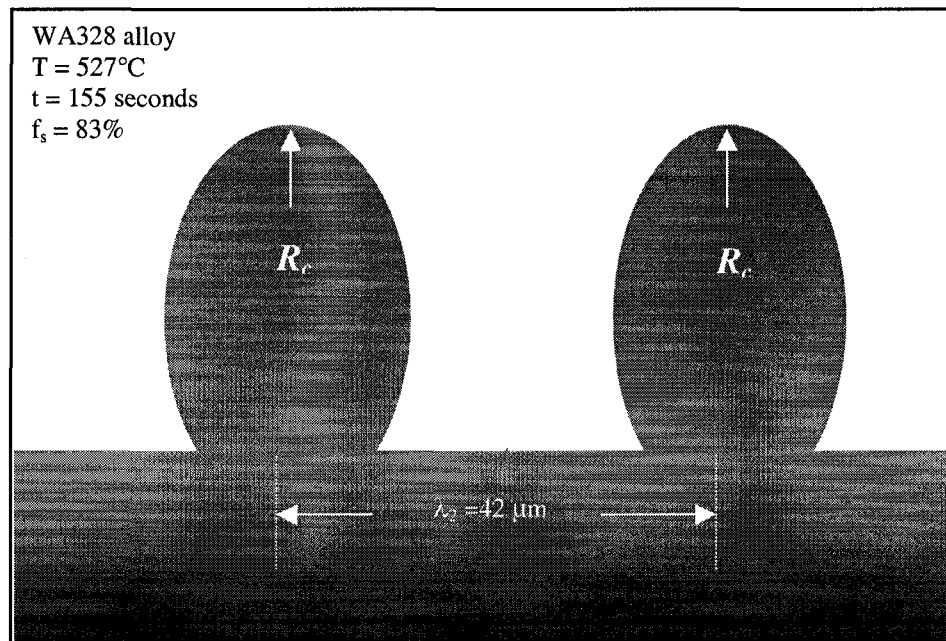
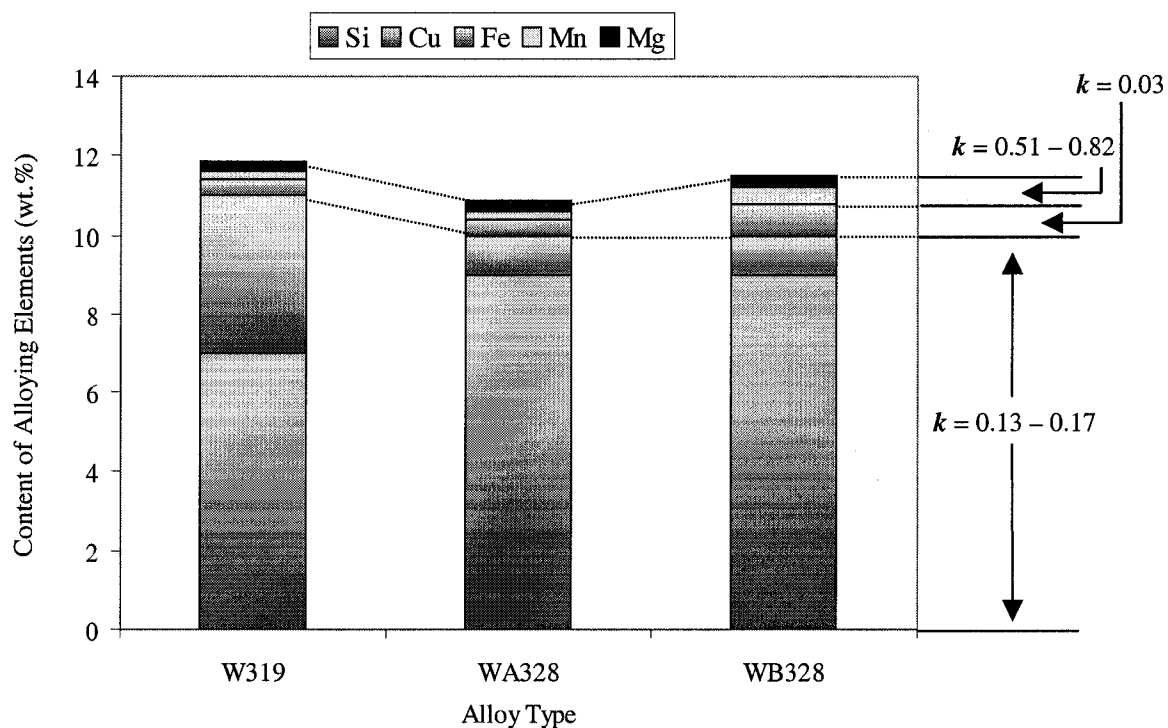


Figure 5.5b: At the end of solidification for the WA328 alloy the dendrites were free to ripen (no quenching). In other words thinner dendrites have dissolved at the expense of the larger dendrites. The cells are now larger yielding a radius of curvature of R_c , which is larger than R_a and R_b seen in Figure 5.5a.

Table 5.5: The calculated equilibrium partition coefficient, k , and the slope of the liquidus line for Si, Cu, Fe, Mg and Mn.

Element	k	M ($^{\circ}\text{C}/\text{wt.}\%$)
Si	0.13	-6.6
Cu	0.17	-3.43
Fe	0.03	-2.96
Mg	0.51	-6.2
Zn	0.88	-2.9
Ni	0.007	-3.3
Cr	2.0	3.5
Mn	0.82	-1.21

**Figure 5.5c:** Solute content in the W319, the WA328, and the WB328 alloys.

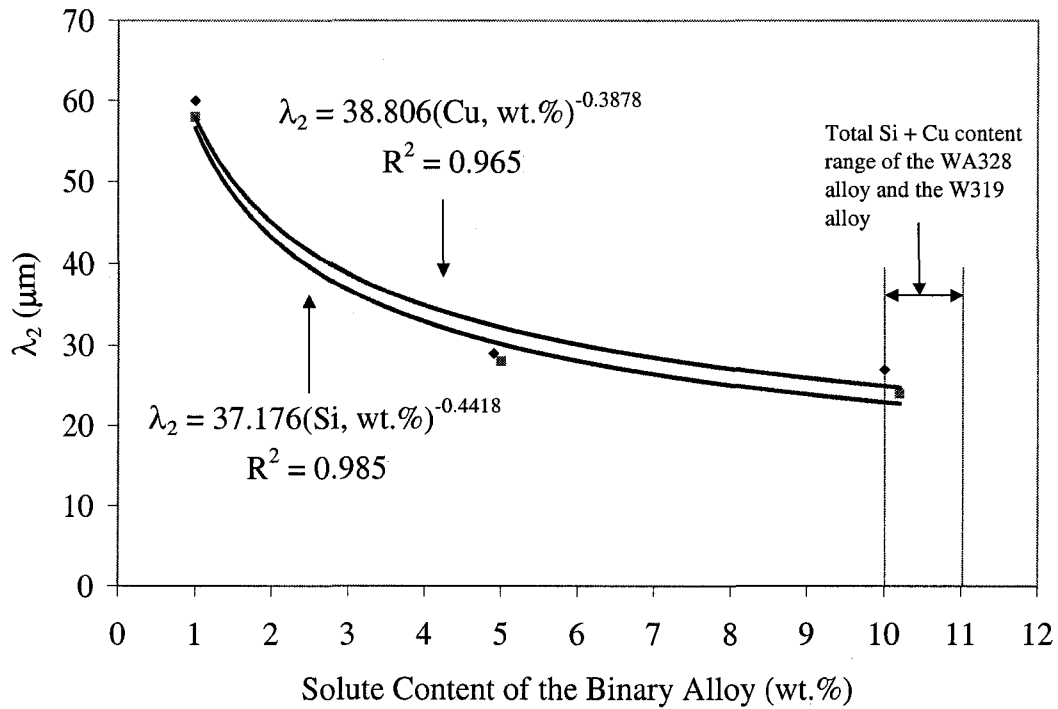


Figure 5.5d: The change in λ_2 due to the content of an Al binary alloy with either Si or Cu. The above graph is reproduced from Shivkumar et al [107]. The best fitted curve along with goodness of fit was not included in the referenced work.

5.6 Volume Fraction of Dendrites in the WA328 and W319 Alloys

Section 5.5 discussed why the values of λ_2 and DCSz were similar between the W319 alloy and the WA328 alloy for the same given solidification time. However the temperature range and duration of the liquidus profile for the WA328 alloy is smaller than the W319 alloy. It would be logical to assume that the partitioned parameter events ($\Delta T^{\alpha DEN}_{SRAN}$, & $\Delta t^{\alpha DEN}_{SRAN}$) taken from the cooling curves would indicate that the volume fraction of the dendrites is larger in the W319 alloy than for the WA328 alloy. In fact the calculated value of $af_s^{\alpha DEN}$ for the W319 alloy is almost twice that for the WA328 Cu alloy (see Figure 5.2b).

Thus it becomes apparent that additional analysis of the volume fraction of α -Al dendrites is needed to confirm the relevance of the apparent fraction calculation $af_s^{\alpha DEN}$. Three different methods to assess the volume of the α -Al dendrites for the two alloys were used. They are:

- 1) Through binary phase diagrams the method of the lever rule was used to calculate what weight fraction of primary dendritic phase should exist for a binary Al-7wt.%Si alloy and a Al-9wt.%Si alloy [79, 80]. Knowing the density (of α -Al and the Al-Si eutectic), and the calculated weight fractions, the corresponding volume of both phases was determined. Performing the lever rule calculation at the event of the Al-Si nucleation ($T^{\text{Al-Si}}_{E,NUC}$) as shown in Figure 5.6a provided a reliable but simplified assessment of the quantity of primary dendrites. The point where the lever rule would be calculated in Figure 5.6a also corresponds to the quenched event at $T^{\text{Al-Si}}_{E,NUC}$ (*end temperature for the partitioned thermal analysis and fraction solid events which quantify the amount of α -Al*

primary dendrites: $\Delta T_{SRAN}^{\alpha DEN}$, $\Delta t_{SRAN}^{\alpha DEN}$ & $af_s^{\alpha DEN}$). The results are shown in Figure 5.6b.

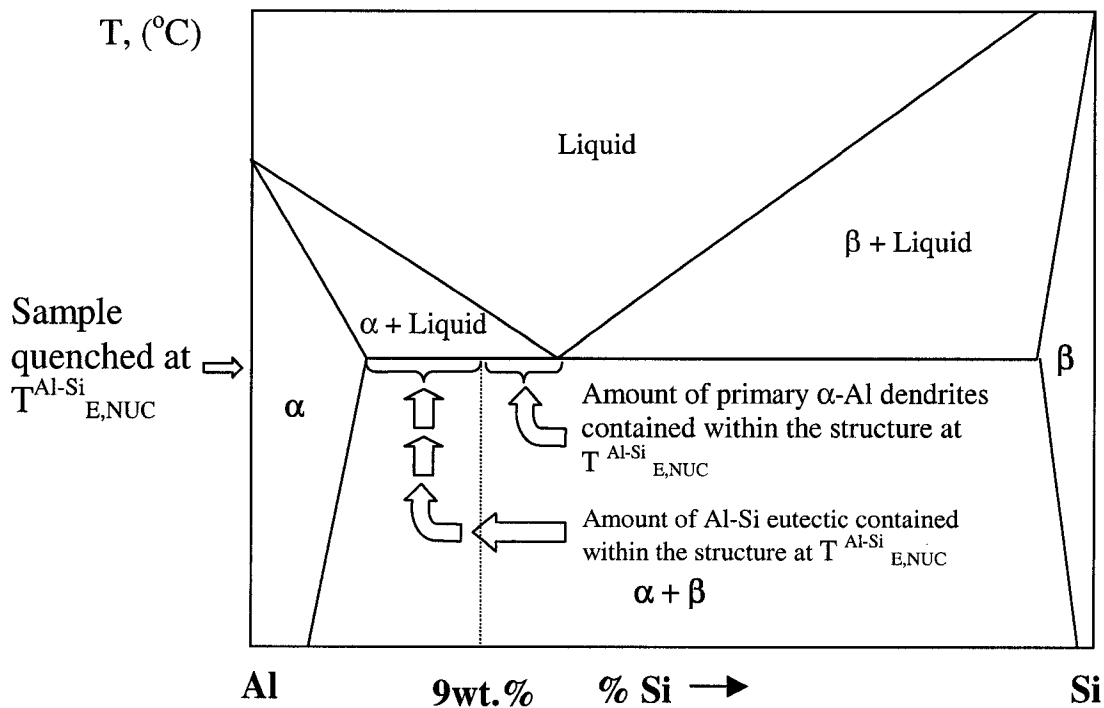


Figure 5.6a: The lever rule is a basic method to quantify the relative amounts of the primary α -Al phase and the Al-Si eutectic phase if the initial alloy composition is known. The values are shown in Figure 5.6b.

- 2) The alloy composition can be used to calculate the Silicon Equivalent (Si_{EQ}) of the alloy. The Si_{EQ} can determine the effect of all alloying elements on a pseudo-type binary diagram. Thus the method outlined in 1) can then be recalculated. The results are shown in Figure 5.6b.
- 3) Taking a sample quenched at $T_{E,NUC}^{Al-Si}$ and measuring it via IA methods the dendrite cross-sectioned area (AFSP(α -Al)) should indicate the difference in the amount of dendrites in the WA328 and W319 alloys. A large value for a surface area of a sectioned dendrite would surely correspond to a larger volume fraction of α -Al primary dendrites found in the structure [108, 109]. Thus, a relative measurement to the surface area of α -Al primary dendrites can correspond to the value partition fraction solid parameter $af_s^{\alpha DEN}$. The results of AFSP(α -Al) are shown in Figure 5.6b.

All three methodologies, lever rule calculation, lever rule calculation with the Si_{EQ} calculation, and IA measurement, are compared to the calculated $af_s^{\alpha DEN}$ value from the partitioned fraction solid method, as shown in Figure 5.6b. From Figure 5.6b it would appear that regardless of the method used to assess the volume fraction of primary α -Al dendrites the W319 alloy will have the largest quantity of this phase when compared to the WA328 alloy. The significance of this relatively basic observation can be illustrated in the LOM micrographs shown in Figures 5.6c and 5.6d.

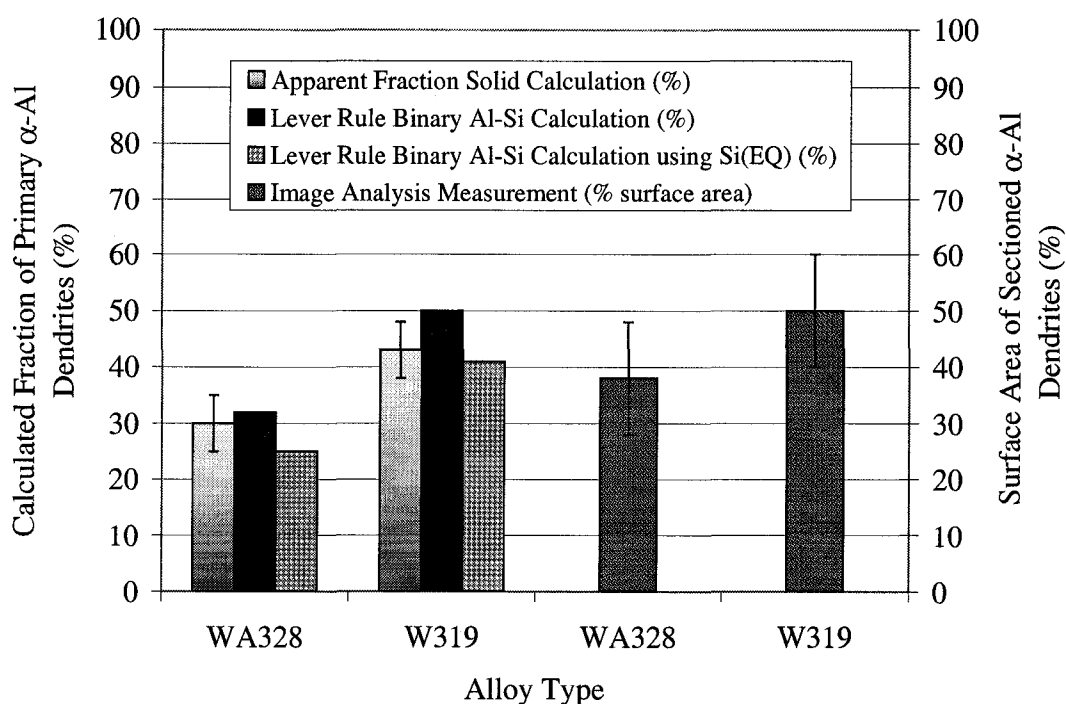


Figure 5.6b: Summary of the four types of measurements or calculations used to assess the fractional amount of primary α -Al dendrites.

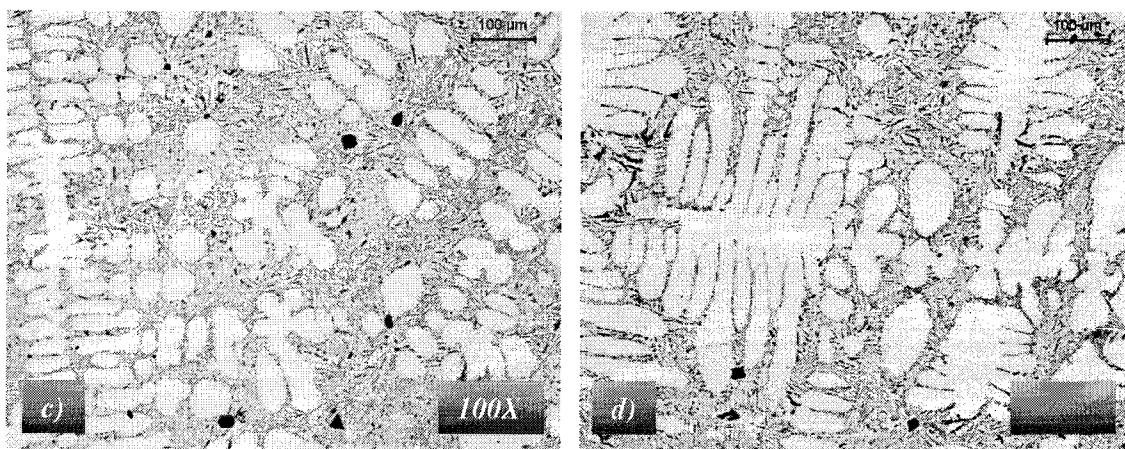


Figure 5.6c: The quenched structure at $T_{E, NUC}^{Al-Si}$ for the WA328 alloy and **d)** the W319 alloy. The area of the sectioned dendrites was measured using IA and the results are reflected in Figure 5.6b.

Dendrites contract volumetrically by a larger amount (volumetric contraction by 7.14% [14, 59]) than any other phase in both alloys. Since no difference in dimension for DCSz or λ_2 exists they can be ruled out as a dominant influence on localized interdendritic feeding occurring in a greater or lesser amount in either the W319 or WA328 alloys. If differences in DCSz or λ_2 existed between the W319 alloy and the WA328 alloy there would also be an effect on the impairment of liquid circulation during mushy zone solidification. The consequence of this finding means that it is justified to argue that the WA328 alloy will exert less hydrostatic stress on the liquid than will the W319 alloy due strictly to the difference in the volume of α -Al dendrites. This is illustrated schematically in Figures 5.6e for the WA328 and W319 alloys. The values of λ_2 , DCSz and HV25g/15s are listed for the two alloys to indicate that the dendrites condition is essentially the same at $T_{E,NUC}^{Al-Si}$.

Figure 5.6f shows the Gas-Shrinkage Map and outlines the importance the hydrostatic stress plays on nucleating pores within the interdendritic liquid. The basic concept of the Gas-Shrinkage Map was outlined in Chapter 2. However, in Figure 5.6f the Gas-Shrinkage Map has labeled volume fraction of the α -Al dendrites ($af_s^{\alpha DEN}$) for the W319 and WA328 alloys. The larger volume fraction of dendrites will most likely increase the hydrostatic stress encountered during solidification.

The level of hydrogen solubility could be a factor between the W319 and WA328 alloys. Should the solubility of hydrogen be, for example, substantially higher in the WA328 alloy than in the W319 alloy then the previous argument, that the hydrostatic stress contributes predominantly to the porosity difference between the two alloys would be flawed. The IRC

has published work concerning the influence of alloying in the solubility of dissolved hydrogen using the AISCAN Chemistry Correction CF(A), and Temperature Correction CF(T) factors [110]. The method of using the AISCAN Chemistry and Temperature Correction is also outlined in detail in the AISCAN User Manual [111]. Table 5.6 summarizes the calculated solubility of dissolved hydrogen in the W319 alloy and in the WA328 alloy. It can be seen in Table 5.6, by using the AISCAN corrections [111], that the hydrogen solubility is only 9% higher for the WA328 alloy. Thus, while the WA328 alloy may be able to dissolve slightly more hydrogen in the liquid state the assessment of the hydrostatic stress contribution to pore development, outlined in Figure 5.6f, is believed to be the predominant factor that reduces the level of gas and gas-shrinkage porosity during solidification.

Thus, referring back to the Gas-Shrinkage Map of Figure 5.6f it can be seen that if W319 has a higher hydrostatic stress then a larger span of heterogeneous nuclei (particles 1, 2 & 3) for pore nucleation can be activated. Conversely the WA328 alloy, using the very same argument, has a lower quantity of α -Al dendrites and thus incorporates a slightly smaller span of heterogeneous nuclei (particles 1 & 2 only) for pore nucleation.

Microscopic observations support these findings of this dissertation, along with the reported literature [48, 112]. Figures 5.6g and 5.6h show quenched structures of the W319 alloy at 555°C where evolving pores are seen. Despite these LOM micrographs being 2-D sections of the microstructure, the pores are flanked only by primary dendrites and quenched Al-Si eutectic liquid. The dendrites contract during mushy solidification resulting in hydrostatic

stress being exerted on the Al-Si liquid. These pores seen in Figures 5.6g and 5.6h result due to an attempt to locally relieve this hydrostatic stress that was successfully achieved by the nucleation and growth of these pores.

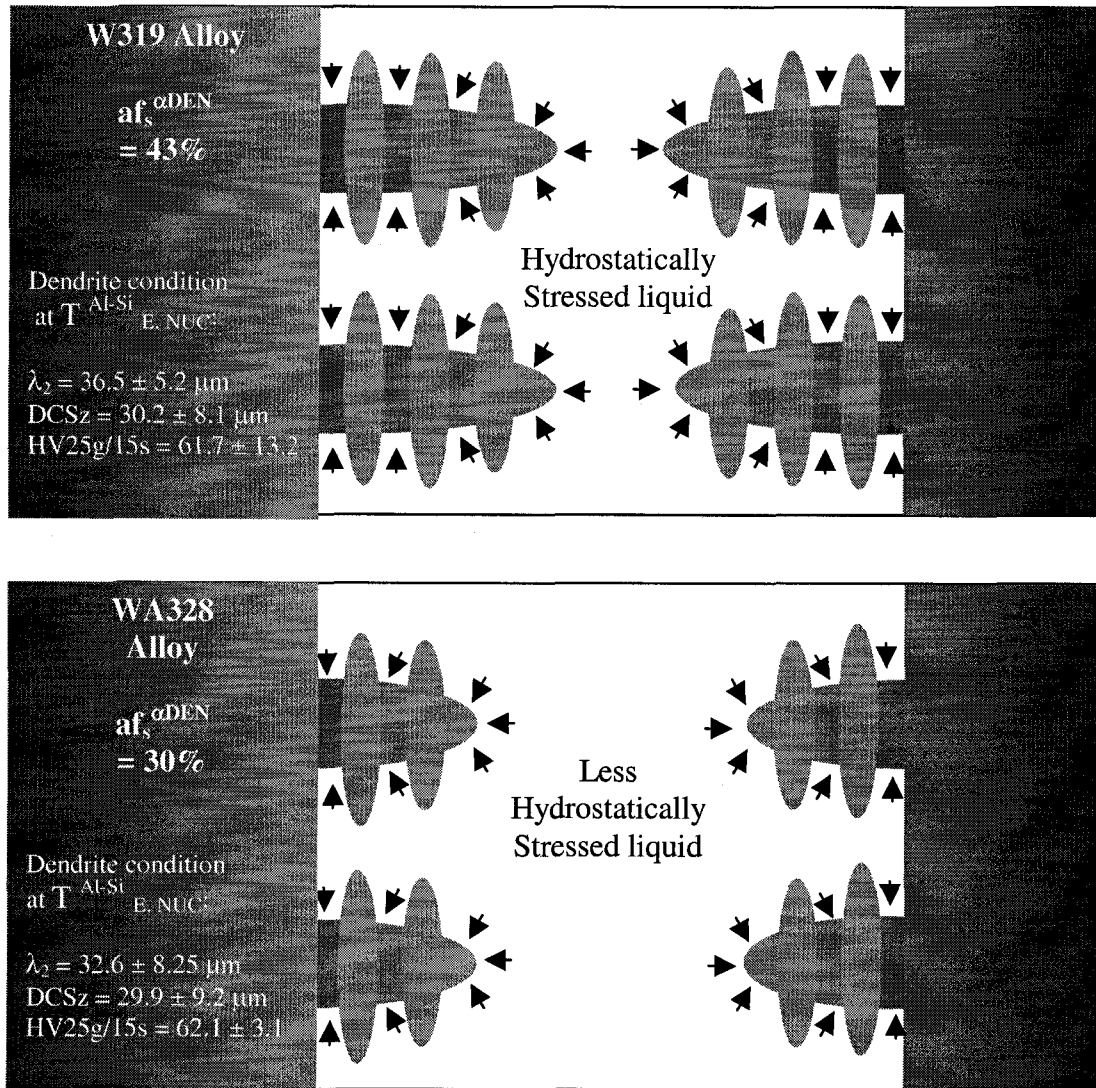
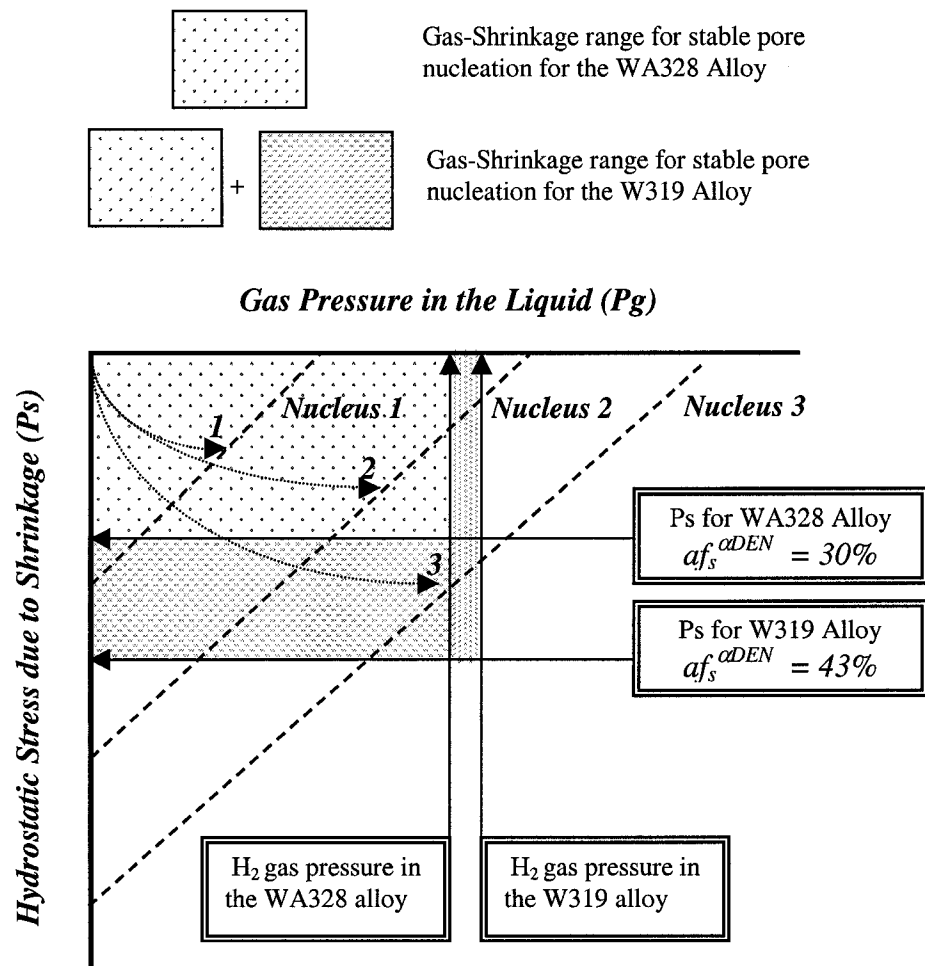


Figure 5.6e: Schematic of dendrites which experience volumetric contraction on cooling. The smaller the volume fraction of the dendrites, as in the WA328 alloy, the lower the hydrostatic stress that is exerted on the liquid, which consequently leads to a lowering of the driving force for pore nucleation.

Table 5.6: Hydrogen Solubility as calculated by the AISCAN algorithms and assuming a melt temperature of 760°C.

Alloy Type	AISCAN Correction [110, 111] $CF(A) = e^{-(0.0119Si\% + 0.0269Cu\% - 0.0170Mg\%)}$ $CF(T) = e^{-[6.531(T-700)/(T+273)]}$	Solubility of Hydrogen at a melt holding temperature of 760°C (cc of H_2 /100 Grams Al) $S = S_0CF(A)CF(T)$
W319 Alloy	$CF(A) = -0.1705$	0.9078
WA328 Alloy	$CF(A) = -0.1289$	0.9991

**Figure 5.6f:** The Gas-Shrinkage Map, which illustrates the combination of shrinkage stress, and internal gas pressure that can be relieved by heterogeneous nucleation of pores. If the WA328 has a smaller fraction of primary dendrites than the W319 alloy then the contribution of hydrostatic stress towards pore growth will be less.

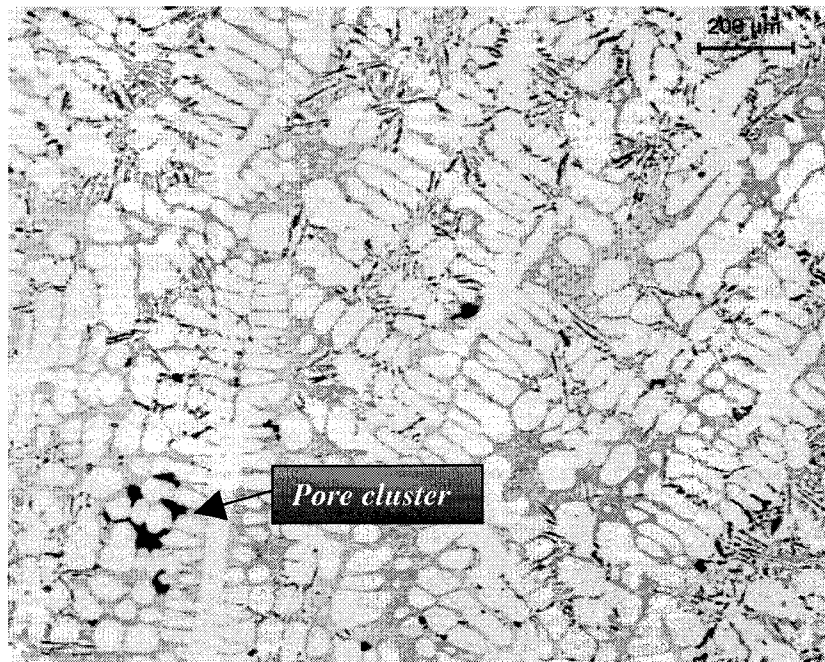


Figure 5.6g: Microstructure of the W319 alloy (quenched at 555°C) at 50X magnification.

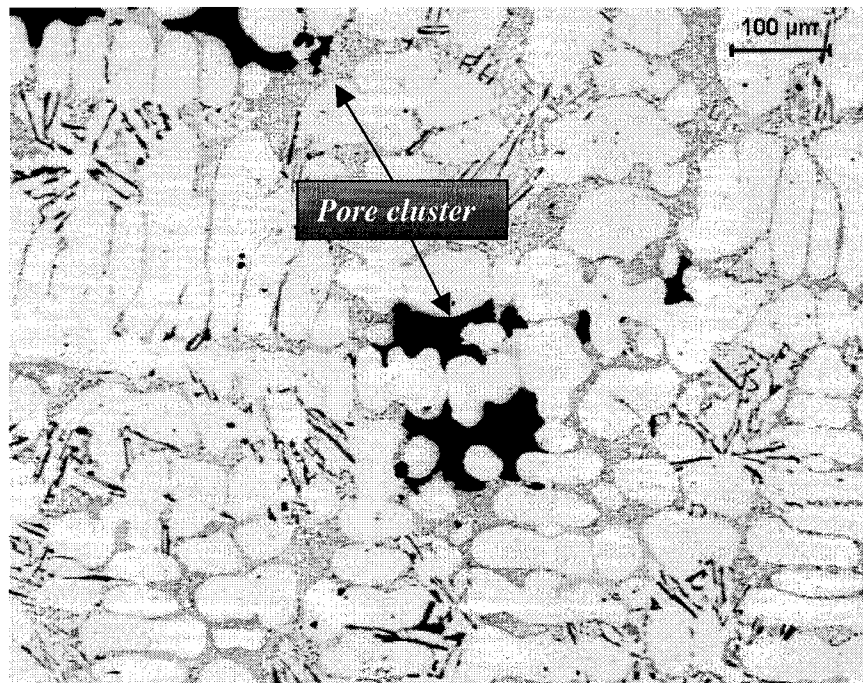


Figure 5.6h: Microstructure of the W319 alloy (quenched at 555°C) at 100X magnification.

5.7 Thermal Analysis for Assessing Shrinkage Pore Growth Mechanisms

While the effect of Si in pore growth mechanisms has been alluded to in Sections 5.4 and 5.5 the effect of Cu is less clear at this point. The WA328 alloy has one fourth the content of Cu than the W319 alloy does. Edwards et al. [59] investigated the effect of Cu on porosity and found that Cu liquid pools can be fed if the extent of the mushy zone is small. Shortening the mushy zone requires a steep temperature gradient, which in turn results in a high cooling rate. However, in slower cooling rate conditions this may not be the case. Cáceres et al. [60] indicated that under slower cooling rate conditions a threshold of 0.2wt. % Cu in a 356 alloy is required to facilitate any increase in pore nucleation and growth.

The cooling curves of the AITAS test samples composed of the wedge compositions were analyzed via partitioned parameters as outlined in Appendix A. An overall summary of the behaviour of Al alloyed with Si and Cu on $T^{\alpha\text{DEN}}_{\text{NUC}}$, $T^{\text{Al-Si}}_{\text{E,NUC}}$, and $T^{\text{Al-Fe-Mg-Si-Cu(one)}}_{\text{E,NUC}}$ are depicted in Figure 5.7a. As can be seen in the Figure 5.7a the value of $\Delta T^{\alpha\text{DEN}}_{\text{SRAN}}$ is consistently at 20°C (for 9wt.% alloys), and at 40°C (for 7wt.% alloys), regardless of the Cu content. In other words the content of Si controls the value of $\Delta T^{\alpha\text{DEN}}_{\text{SRAN}}$, while the content of Cu controls $T^{\alpha\text{DEN}}_{\text{NUC}}$ and $T^{\text{Al-Si}}_{\text{E,NUC}}$. However, the value of $\Delta T^{\text{Al-Si}}_{\text{SRAN}}$, for both 7wt.Si alloys and 9wt.%Si alloys, is similar for the given Cu content. If the Cu content increases from 1wt.% to 4wt.%, then $\Delta T^{\text{Al-Si}}_{\text{SRAN}}$ increases from approximately 40°C to 50°C.

Figure 5.7b shows the apparent fraction solid results of the primary dendritic solidification and the Al-Si eutectic solidification events. It would appear that Cu plays a negligible role in controlling the amount of the partitioned fraction solid of α -Al dendrites. The reduction of Si

from 9wt.% to 7wt% resulted in a decrease in $af_s^{\alpha_{DEN}}$ of 15% to 17% regardless of the Cu level.

The partitioned fraction solid parameter results for the Al-Si eutectic reaction (af_s^{Al-Si}) are shown in Figure 5.7b. As in the case of the α -Al primary dendritic fraction solid, Cu plays a minor role in the af_s^{Al-Si} when compared to the effect on the Si level. It is expected that higher Si levels would be positively correlated with the Al-Si volume fraction. It is interesting to note that the temperature range for the Al-Si eutectic reaction remained essentially the same for both high and low Si alloys, while the fraction solid analysis indicates that a different amount of Al-Si eutectic is present in both structures. This is due to the temperature range for the Al-Si eutectic structure formation being controlled by the Cu content, while the fraction solid amount is controlled by the Si content. These results are in agreement with the results found in Section 5.4.

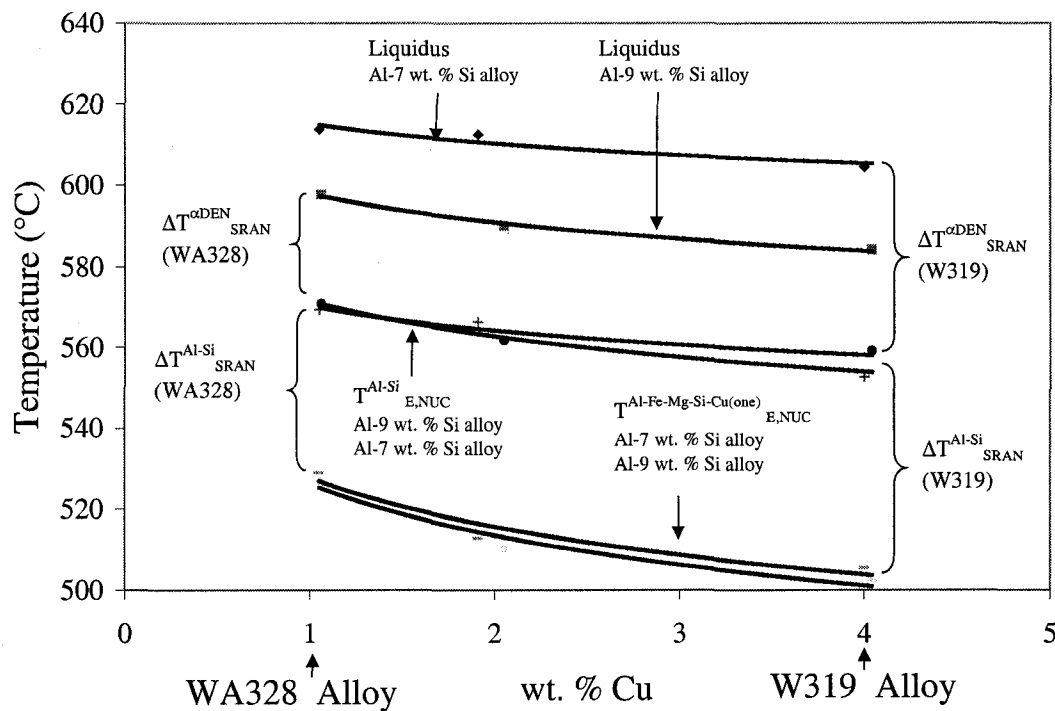


Figure 5.7a: The value of $\Delta T^{\alpha\text{DEN}}_{\text{SRAN}}$ and $\Delta T^{\text{Al-Si}}_{\text{SRAN}}$ for the Al-7 wt. % Si alloys, and the Al-9 wt. % Si alloys, having 1, 2 and 4 wt. % Cu. The standard deviation for each mean characteristic temperature point ($T^{\alpha\text{DEN}}_{\text{NUC}}$, $T^{\text{Al-Si}}_{\text{E,NUC}}$, and $T^{\text{Al-Fe-Mg-Si-Cu(one)}}_{\text{E,NUC}}$) is no higher than ± 3.7 °C. Each characteristic temperature is comprised of four repeats.

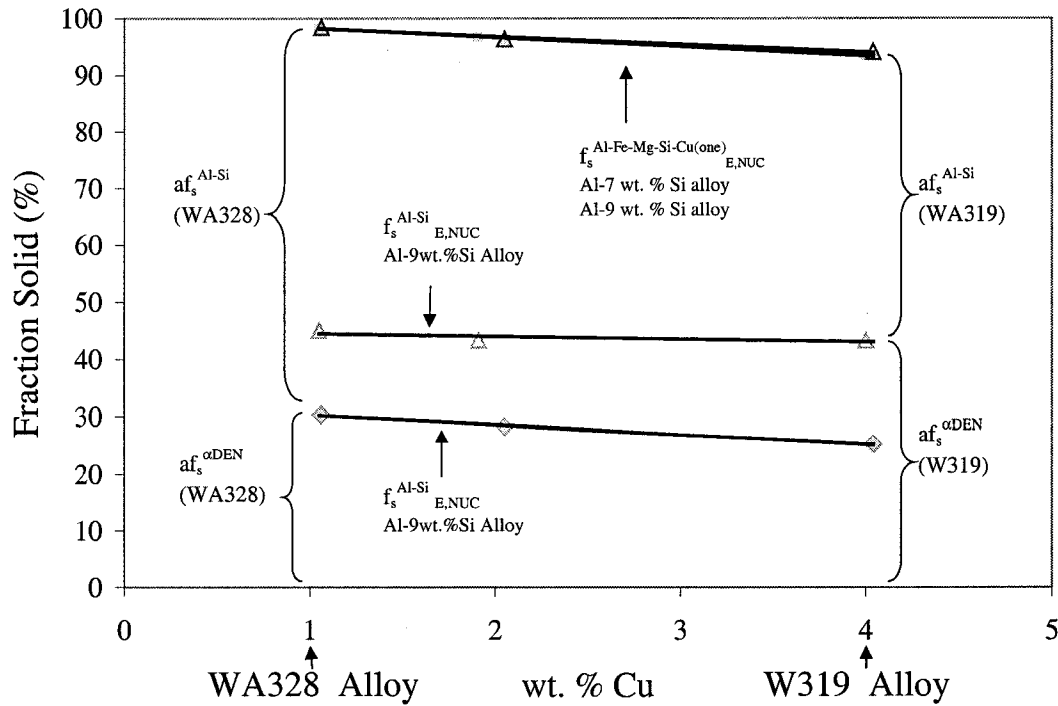


Figure 5.7b: The apparent fraction solid of the primary dendritic structure, $af_s^{\alpha DEN}$, and the apparent fraction solid of the Al-Si eutectic, af_s^{Al-Si} , for the Al-7 wt. % Si alloys and the Al-9 wt. % Si alloys having 1, 2 and 4 wt. % Cu. The standard deviation for each mean characteristic fraction solid point is no more than ± 2.3 %. Each characteristic fraction solid point is comprised of four repeats.

5.8 The Contribution of Cu to Pore Development in Al-Si-Cu Based Casting Alloys

In Section 5.7 it was shown that the level of Si plays a substantial role in the magnitude of the driving force for pore nucleation. However, the role of Cu is less clear since most of the pores which nucleate and expand do so during Al-Si eutectic solidification, prior to the advent of Cu-based phase solidification. The assessment of the cooling curves via the partitioned method in Section 5.8 is used to help determine the role of Cu in pore development.

5.8.1 The Role of Cu in Porosity Development in the As-Cast Wedges

Figures 5.8.1a and 5.8.1b indicate that lower Cu levels are associated with lower porosity in the as-cast structure of the samples. Cu is known to extend the Al-Si eutectic solidification range much more than the primary dendritic solidification range as seen in the thermal analysis results. This is already known from comparisons of the 356 and 319 alloy cooling curves [59, 60].

Cu is also known to increase the volumetric amount of shrinkage in the remaining pools of Cu rich liquid during solidification [59, 60]. Figures 5.8.1c and 5.8.1d (at the riser end, where Cu segregation is worst) show that the amount of Cu-based phases in the as-cast condition goes up approximately 10 times for a 3 wt.% increase in Cu, while Figures 5.8.1a and 5.8.1b show that the level of porosity increases by approximately 25% for the same increase in Cu. This lack of a proportionality shows that the percent area of Cu-based phases does not entirely cause pore nucleation or growth. Conversely, at the chilled end of the

wedge casting, the level of porosity for all of the alloys is virtually identical regardless of the increase in Cu-based phases. It is quite clear that the relationship between Cu and porosity is not a proportional one. Clearly the contribution of Cu to enhance pore growth is tied to the cooling rate. A high cooling rate minimizes the contribution of Cu to pore formation while a slow cooling rate enhances its contribution to the volume of shrinkage porosity.

In this work, and after careful scrutiny of the existing literature, it was observed that the higher Cu levels can result in more shrinkage porosity. An indication at what elevated level Cu may substantially contribute shrinkage type porosity in aluminum castings was undertaken by Cáceres et al. [60]. They indicated that the threshold level of Cu at which the volume fraction of porosity increases is about 0.2 wt. %. However, Cáceres and his co-workers did not perform thermal analysis to show that the nucleation temperature of the Cu rich phases considerably increases with a decrease in the Cu content and thereby increases the solidification range for Al-Si formation (*i.e. increasing the magnitude of ΔT^{Al-Si}_{SRAN}*). Also, Recall from Figure 5.2.2d that the cooling rate for the phases which grow after $T^{Al-Fe-Mg-Si-Cu(one)}_{E,NUC}$ increases by at least three times. The high cooling rate of the phases that include Cu would not permit large pores to form, as has been found in the literature [95]. This again supports the observation that increasing ΔT^{Al-Si}_{SRAN} increases the range which permits pore growth.

It is quite probable that in the presence of a temperature gradient the alloys with higher Cu will have Cu-rich liquid pools that can become enveloped by solid Al-Si eutectic and α -Al dendrites that significantly choke these Cu-rich liquid pools from the liquid feed.

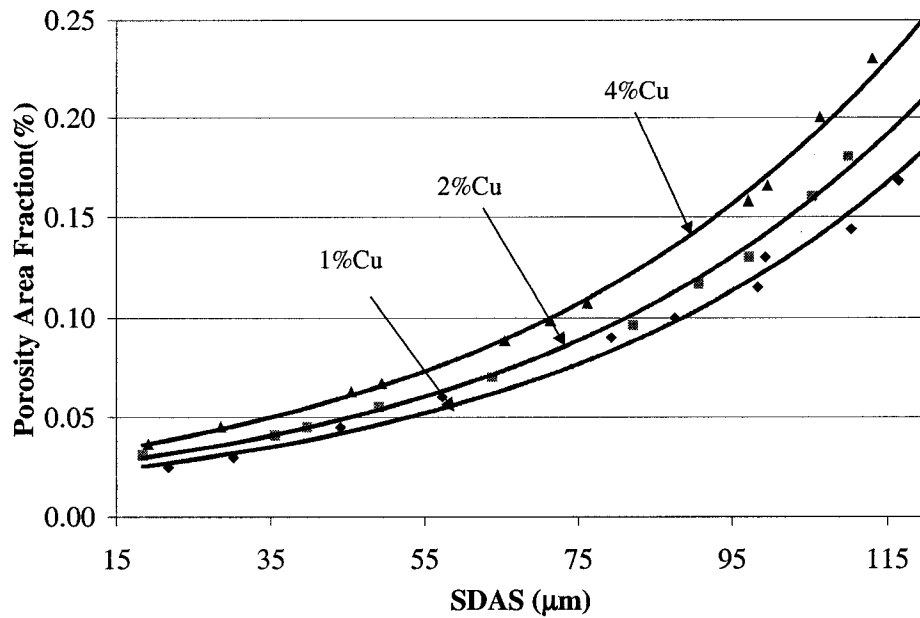


Figure 5.8.1a: Relationship between Porosity Area Fraction and SDAS for wedges with 7wt.%Si [19, 20].

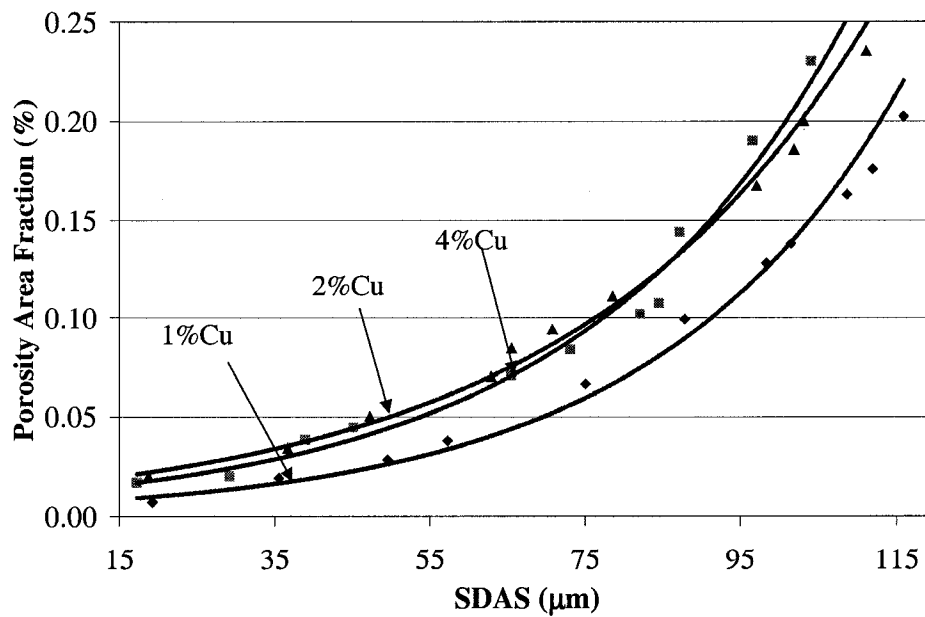


Figure 5.8.1b: Relationship between Porosity Area Fraction and SDAS for wedges with 9wt.%Si [19, 20].

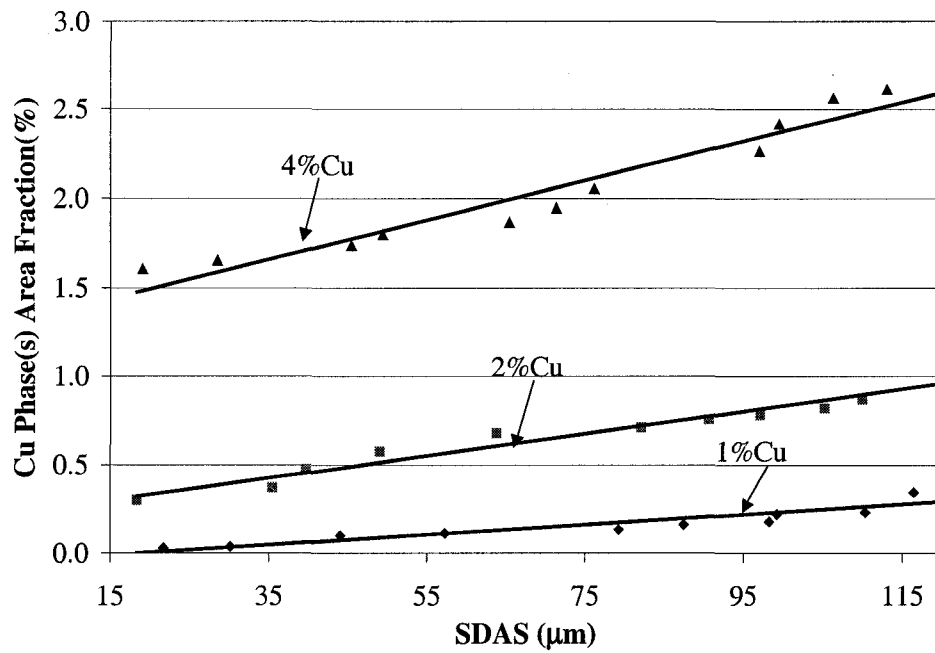


Figure 5.8.1c: Relationship between Cu based phase(s) Area Fraction and SDAS for wedges with 7wt%Si in the as-cast condition [19, 20].

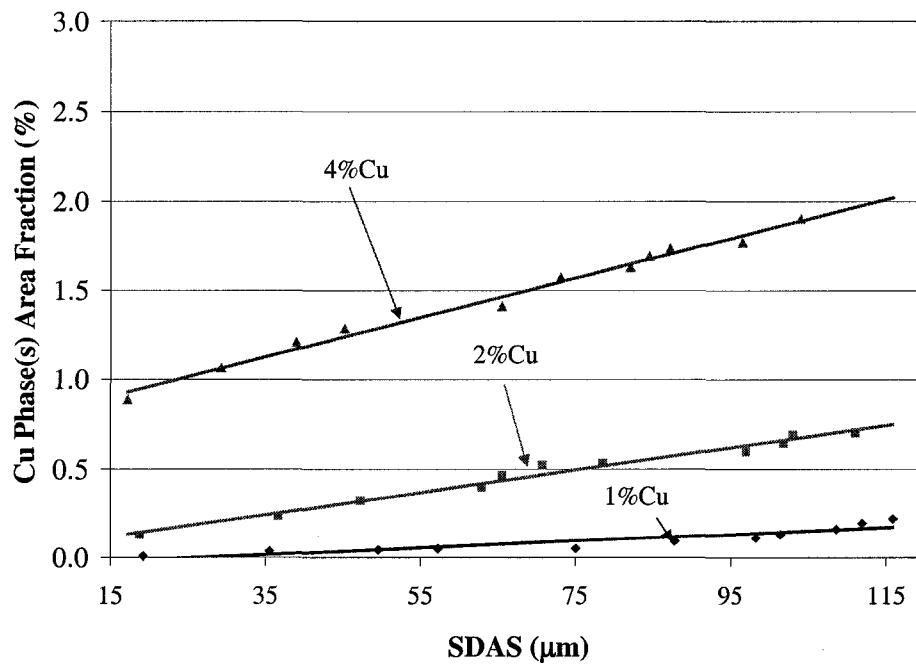


Figure 5.8.1d: Relationship between Cu based phase(s) Area Fraction and SDAS for wedges with 9wt%Si in the as-cast condition [19, 20].

5.9 The Effect of Chemistry and Cooling Rate on Mushy Zone Evolution as Determined via Partitioned Thermal Analysis/Fraction Solid Parameters

The effect of cooling rate on cast structure is well known within both the metallurgical research community and by the metal casting practitioners [2, 3, 14, 19-22, 78, 81, 85, 88, 96-98, 102-106]. Generally the most beneficial result of an increased cooling rate is the reduction of porosity and secondary phase refinement which occurs within the cast structure. The reasons for the reduction of porosity at increased cooling rates are the reduction in the driving force for pore nucleation and the reduced time for already nucleated pores to grow. However the changes in conditions by which pores grow due to the higher cooling rates are not fully understood. Ideally the condition of the interdendritic structure plays a prominent role in stable pore nucleation and growth as outlined by Campbell [14] and others [62-67].

A new schematic concept will be introduced in this dissertation concerning the effect that Cu and Si have on the evolving mushy zone. This will be done by using the partitioned parameters determined in Figures 5.7a and 5.7b in a schematic diagram of a mushy zone along a temperature gradient in a cross-section of a completely filled casting mould. Figure 5.9a is a schematic of the evolving dendritic structure and the subsequent Al-Si eutectic structure along a thermal gradient that would be present within a cast structure. The thermal gradient shown in Figure 5.9a is linear in this case only to provide simplicity to the proposed argument made within this dissertation. Typically thermal gradients may be parabolic in nature, but this will not change the argument proposed here.

Depicted in Figure 5.9a is the level of Si which reduces the overall solidification range of the alloy. It can be seen from Figure 5.9a that the Al-7wt.%Si-4wt.%Cu alloy has the longest solidification range ($T_{\text{NUC}}^{\alpha\text{DEN}} - T_{\text{E,NUC}}^{\text{Al-Fe-Mg-Si-Cu(one)}}$ = 92°C), and that the Al-9wt.%Si-4wt.%Cu alloy and Al-9wt.%Si-1wt.%Cu alloy would have the shortest ($T_{\text{NUC}}^{\alpha\text{DEN}} - T_{\text{E,NUC}}^{\text{Al-Fe-Mg-Si-Cu(one)}}$ = 71°C). The prevailing observation is that the shorter the solidification range, the shorter the feeding distance [2, 14, 47, 68, 72, 104, 106]. In Section 5.6 the lower volume fraction of dendrites in the WA328 plays an additional role in reducing porosity. Thus the lower level of porosity found in the WA328 alloy is due to a combination of the reduced driving force for pore nucleation, plus the enhanced ability to deliver liquid feed to an interdendritic region which is hydrostatically stressed.

There is a third factor which may help reduce the level of porosity found in the WA328 alloy. The alloy having the smallest value of $\Delta T_{\text{SRAN}}^{\text{Al-Si}}$ is the same alloy having the smallest level of porosity for the wedge castings. The smallest value of $\Delta T_{\text{SRAN}}^{\text{Al-Si}}$, viewed in the context of the temperature gradient of Figure 5.9a, indicates that pores do not have a chance to grow and expand to the same extent as the pores in alloys having a larger value of $\Delta T_{\text{SRAN}}^{\text{Al-Si}}$. Additionally, in the context of the temperature gradient as seen in Figure 5.9a, one is able to get a better view of the role that elevated Cu content has in contributing to stable pore growth. Higher Cu levels extend the end temperature $T_{\text{E,NUC}}^{\text{Al-Fe-Mg-Si-Cu(one)}}$ of the partitioned parameter $\Delta T_{\text{SRAN}}^{\text{Al-Si}}$. The direct role Cu based phase have on pore nucleation is less clear at this point. Figure 5.9a is labeled at the top of the cooling rate of each stage of solidification (taken from Figure 5.2.2d). The stage at which Cu based phases begin to grow is when the cooling rate becomes very high. This is not reflected within the schematic seen in Figure

5.9a. However, if pores grew after $T_{E,NUC}^{Al-Fe-Mg-Si-Cu(once)}$ the higher cooling rate would deter any substantial pore growth. The role Cu plays in pore development most likely increases the feeding distance of the Al-Si eutectic stage as seen in Figure 5.9a.

Finally, taking the particular constructs of Figures 5.7a into consideration it can be seen how the use of the partitioned thermal analysis parameters can generate the snap shot of the evolving mushy zone in a simple geometric cast section. This is shown in Figure 5.9b where the right side is the Al-7wt.%Si-4wt.% alloy (W319 alloy), and the left side is the Al-9wt.%Si-1wt.%Cu alloy (WA328 alloy). The temperature gradient seen in Figure 5.9b is considered symmetrical for both sides having the different alloys. It is assumed that factors such as the higher quantity of latent heat, due to the higher Si content in the Al-9wt.%Si-1wt.%Cu alloy, had a minimal effect so that simplicity could be used for the proposed argument. The values determined for the partitioned parameters from the cooling curves and fraction solid curves are listed at the bottom of Figure 5.9b. It can be seen that the mushy zone for the Al-7wt.%Si-4wt.%Cu alloy was developed to the point where liquid feeding channels have closed off and subsequent feeding must occur via interdendritic feeding. This is due to the large magnitudes of both $af_s^{\alpha DEN}$ and $\Delta T^{\alpha DEN}$ for the 7wt.% containing alloys. This would also possibly imply that the delay in the relief of hydrostatic stress would also occur and allow more nucleants to actively nucleate pores (see Figure 5.6f). The Al-9wt.%Si-1wt.%Cu alloy has liquid feed channels which are non-existent in the Al-7wt.%Si-4wt.%Cu alloy. In addition to the previous argument the benefits of reducing the magnitude of the partitioned parameter ΔT_{SRAN}^{Al-Si} which is the case for the Al-9wt.%Si-1wt.%Cu alloy, also helps to reduce the propensity for stable pore nucleation and growth.

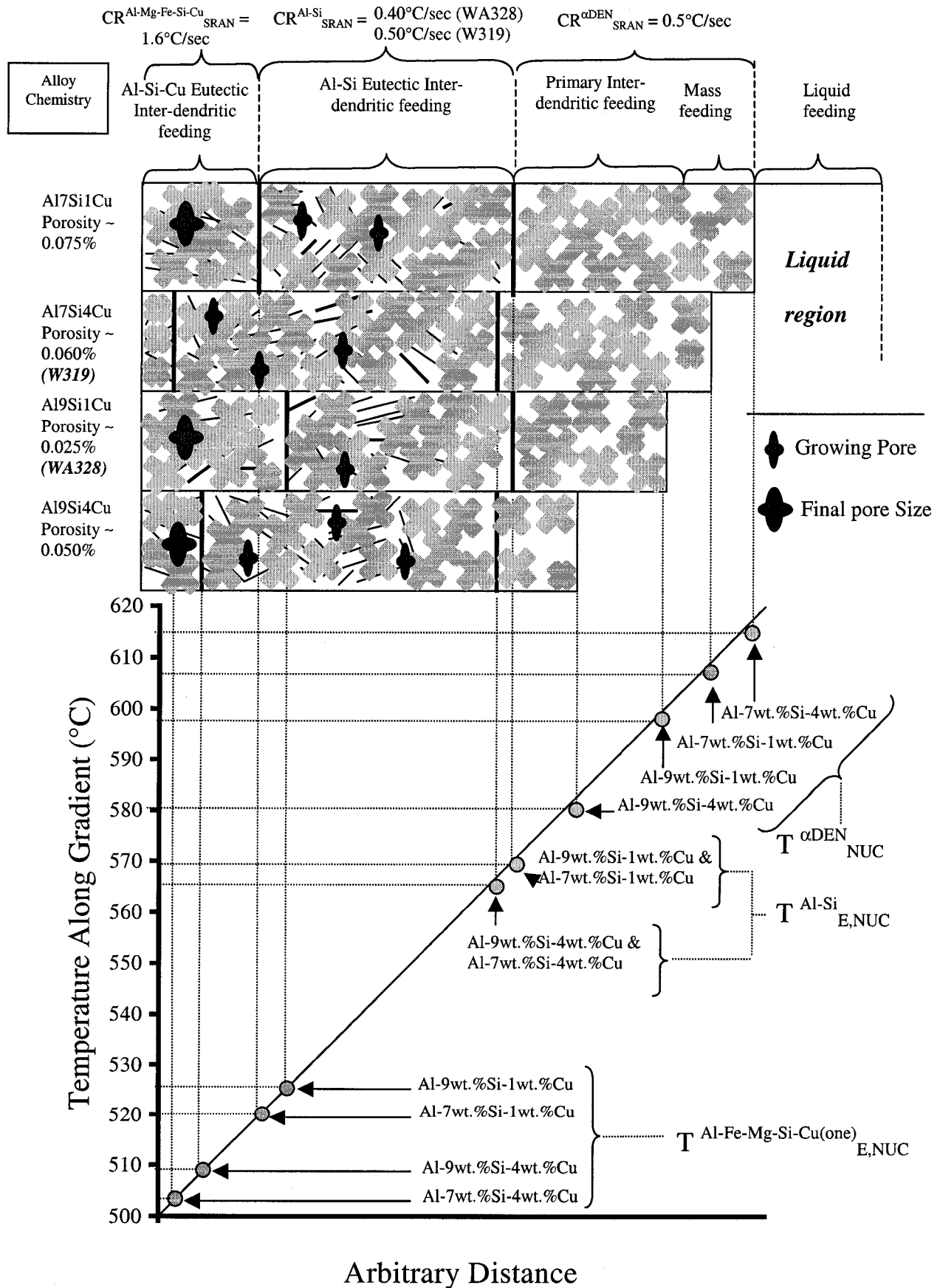


Figure 5.9a: Labelling of partitioned thermal analysis parameters along a temperature gradient.

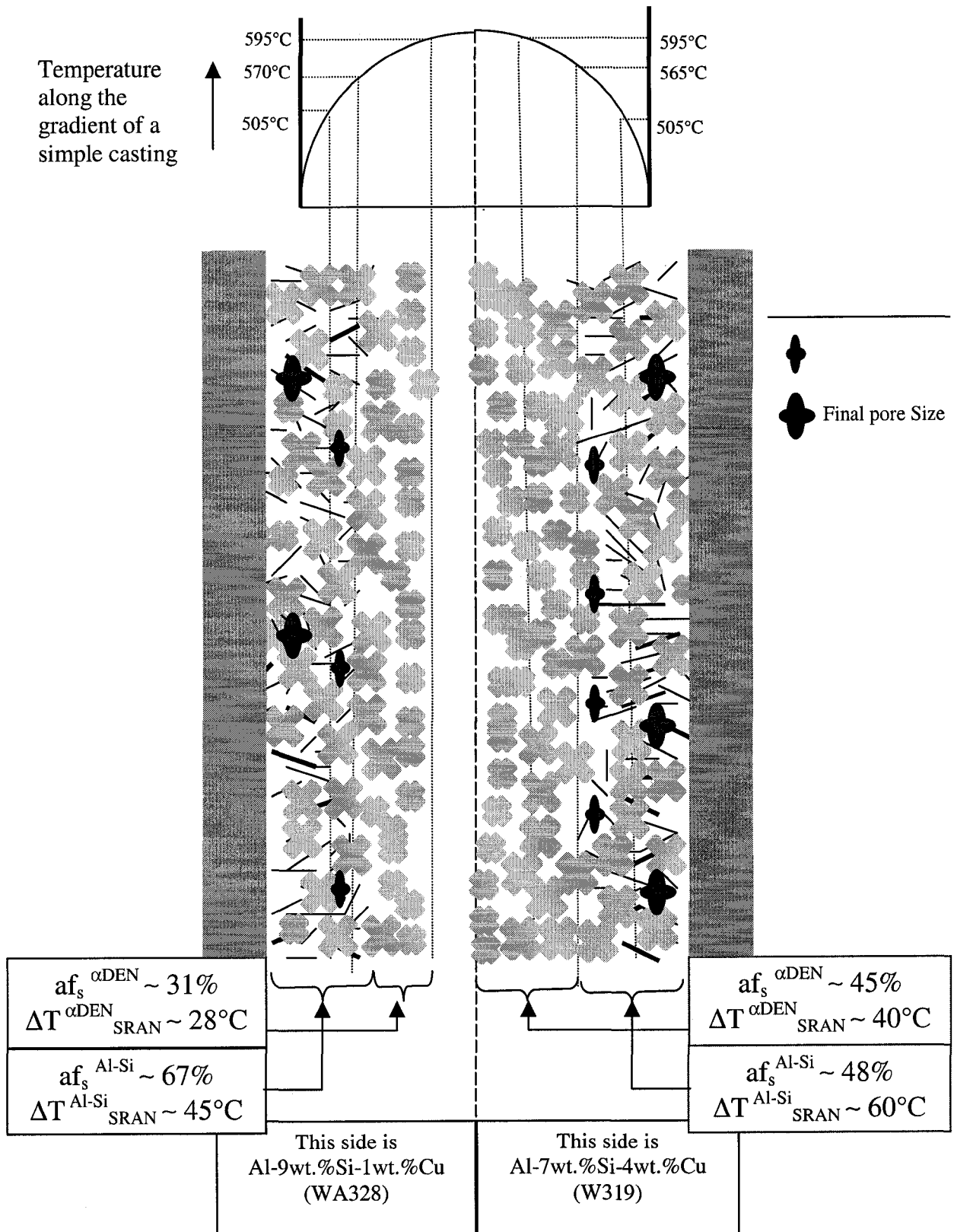


Figure 5.9b: The cross-section of a simple cast section where one side is the Al-9wt.%Si-1wt.%Cu alloy (WA328) and the other side is the Al-7wt.%Si-4wt.%Cu alloy (W319).

Chapter Six

Integrity & Durability of the V8 Engine Block Cast from the WA328 & WB328 Alloys

6.0 Preliminary Discussion

Chapter Six discusses the assessment of the W319 alloy, the WA328 alloy, and the WB328 alloy's ability to be cast as a suitable V8 engine block using the Cosworth Precision Sand Casting Process (CPSP). Suitability here will imply that the WA328 and WB328 alloys are compliant with the Ford Engineering Material Specification WSE-M2A151-A3 standard [17]. It should be pointed out that High Cycle Fatigue (HCF) analysis was performed on the WA328 alloy but not on the WB328 alloy due to time constraints.

6.1 Assessment of Porosity of the V8 Engine Block Bulkhead Sections

X-ray radiographic and metallographic methods of analysis were employed to assess shrinkage porosity of all V8 engine block bulkheads. Radiographic results are presented since they were used as a front line method at WAP for assessing bulkhead soundness. The metallographic analysis of the bulkhead sections A, B, C, D and E was used since the size and distribution of fine pores are usually not discernable on X-ray radiographs.

6.1.1 Radiographic Examination of the WA328 & WB328 Alloys used to cast in the V8 Engine Block

The X-ray radiographic examination of the V8 engine block was completed by sectioning the casting into 13 slices as indicated in *Figure 4.0, Chapter Four*. The results of the radiographic analysis of four V8 engine blocks cast from the WA328 and WB328 alloys are shown in Table 6.0. The engine block was sliced in this fashion so that clear radiographic images of the bulkhead sections could be obtained. It should be pointed out that no indication of detectable porosity was found for sections 5, 8 and 11 of the engine block.

Sections 1, 2, 3, 4, 6, 9, 10, 12 and 13 of the engine block examined using radiography indicate that a low level of porosity was found (i.e. P1, G1, G2 and S1). Section 7 (associated with bulkhead C) shows signs of S3 to S4 level shrinkage porosity. This is a known trouble spot in the V8 engine block castings and is due to cast geometry, not cast chemistry. This assessment was made since the S3 and S4 category of shrinkage porosity was in the subsurface, and in the vicinity of the Hone Clearance Window (HCW). The origin of the shrinkage porosity is believed to be a combination of feeding problems, due to the relatively thin section of bulkhead required to feed the affected area, and gaseous binder evolution since the shrinkage is in the subsurface region.

At the time of the writing of this dissertation a separate investigation was under way at WAP to assess the benefits of closing the HCW on the level of shrinkage porosity at this problem spot on bulkhead C. It was found that the level of porosity dropped from $1.01 \pm 0.2\%$ (open HCW) to $0.67 \pm 0.18\%$ (closed HCW) [113]. This drops the radiographic shrinkage rating

from an S3 or S4 to an S2 rating. However, there is a performance deficit encountered with V8 engine blocks having closed HCWs. Machining out the HCWs after the cast operation is cost prohibitive.

Table 6.0: The radiographic results for the V8 engine block cast in the WA328 alloy, and in the WB328 alloy. The casting x-ray is identified and the date on which radiographic examination was performed is also indicated. Refer to *Figure 4.0, Chapter Four*, for the layout of where radiographic sections were taken on the V8 engine block.

Cast i.d. (X-ray date)	Section of the V8 Engine Block												
	1	2	3	4	5	6	7	8	9	10	11	12	13
A1 (21/01/02)	P1	P1 G1	G1 S2	P1 G1 S1			P1 S4			P1 S1 S3		P1	P1
A2 (21/01/02)	P1 G1	P1 G1	S2 G2	P1 G1 S1		G1	P1 S4			P1 S1		P1	P1
A3 (29/01/02)	P1 G1 G2	G1	P1 G1 G2	S1			S3			S1		P1	P1
A35 (05/04/02)	P1 G1			P1 G1			P1 G1 S4		P1	P1 S1		P1	P1

X-Ray Radiograph Indication Levels

G: Gas levels 1 through 7 (*Beyond 4 Critical*)

P: Porosity levels 1 through 7 (*Beyond 4 Critical*)

S: Shrinkage levels 1 through 7 (*Beyond 4 Critical*)

Note:

G signifies pores which are oval to circular in shape and originate from either gas pore (H_2), which nucleated and grew fairly early on during solidification or is the result of a pocket of air, which became encapsulated by an oxide skin during turbulent filling.

P signifies highly dispersed porosity, which results from the retarded feeding condition during solidification.

S signifies localized feeding issues, which may have resulted from a hot spot condition or a latent heat generated hot spot [103].

6.1.2 Results of Porosity Analysis of the V8 Engine Block

Figure 6.1.2a shows the riser and adjoining bulkhead. The dashed angled lines seen in Figure 6.1.2a mark the region where the metallographic determination of porosity was made. This will be important for subsequent analysis. In addition to the porosity assessment the volume of the riser sink and sink asymmetry were evaluated.

Results of mean area fraction porosity (%) found in the left and right sides of all metallographic sections of the bulkheads for the WA328 alloy, the WB328 alloy, the W319 alloy, W319 alloy with Tibor (Al-5Ti-1B), and the W319 alloy with a Tibor/Sr modifier (Al-5Ti-1B-10Sr) are presented together via a bar graph in Figure 6.2.1b. Bar graphs of the mean pore diameter and the maximum pore size (*longest length of a single shrinkage pore*) are shown in Figures 6.1.2c and 6.1.2d, respectively. The standard deviation for the mean area fraction porosity and mean pore diameter are presented in Appendix E.

There are several trends found in Figures 6.1.2b, 6.1.2c and 6.1.2d that need to be addressed. The main feature is the effect of alloy chemistry, both macro and micro alloying elements, on the mean percentage of porosity, mean pore diameter and largest pore found on all five bulkheads. The mean area fraction porosity was the highest in bulkheads containing the W319 alloy having the Al-5Ti-1B-10Sr master alloy, and dropped for the W319 alloy having the Al-5Ti-1B master alloy, and was even lower for the W319 alloy having no in-mould master alloy. The lowest porosity was seen in Figures 6.1.2b, 6.1.2c and 6.1.2d, for the V8 engine blocks containing either the WA328 alloy or the WB328 alloy. In fact, Figure 6.1.2d shows that the V8 engine blocks cast in the WA328 and WB328 alloys are the only engine

blocks where all bulkheads contain the maximum diameter pores and are well within the 750 μm limit as outlined in Ford Engineering Material Specification WSE-M2A151-A3.

In Figures 6.1.2b, 6.1.2c and 6.2.1d the porosity does increase when in-mould master alloying is involved and an explanation is warranted. The Al-5Ti-1B, and the Al-5Ti-1B-10Sr master alloys will introduce particles such as Al_3Ti , AlB_2 and Sr based particles [2-6, 16, 33, 44, 47, 55, 56, 112]. Coupled with the slow cooling rate of the bulkhead (0.18-0.22°C/sec, see Appendix C), these particles can nucleate and grow pores. Without the Al-5Ti-1B, and Al-5Ti-1B-10Sr master alloys, a reduction in Al_3Ti and AlB_2 and Sr based particles exists, consequently reducing the severity of the porosity found.

Another very important observation is that the porosity seems to be higher on the left side of the bulkhead than on the right side for most alloy conditions investigated within this dissertation. The reason for the apparent higher propensity for pore formation on the left side of the bulkhead is due to the fact that the riser sink volume is skewed towards the right side. Observations made for all sectioned V8 engine block risers, as seen in Figure 6.1.2e, for the W319 alloy and the WA328 alloy, revealed that this asymmetry is skewed towards the right side, and is found in risers B, C, D and E. Riser A fails to show such asymmetry. This indicates that feed metal was drained on the right side of the riser and consequently fed the right side of the bulkhead more than the left side. This clearly resulted in a sounder bulkhead on the right side.

The amount of porosity found is dependent on the amount of liquid feed possible from the adjoining riser. Figure 6.1.2f shows a bar graph reflecting the magnitude of the riser sink

volume of all risers (of the V8 engine blocks) cast with the specified alloy, and its conditions as seen in Figures 6.1.2b, 6.1.2c, and 6.1.2d. The risers associated with the engine blocks having grain refiner yielded the largest volume of riser sink, while the castings which include Sr yielded the smallest volume of riser sink. Another important observation was that the magnitude of volume sink for each riser was essentially the same for both the non-grain refined W319 alloy, and the WA328 alloy. This minimal difference in the riser volume sink occurred despite the fact that the bulkhead porosity was lower for the WA328 alloy, than for the W319 alloy as seen in Figure 6.1.2b, 6.1.2c and 6.1.2d. This observation strongly reflects the fact that the riser was not optimally designed. This is particularly true for riser D, which essentially shows no real change for any of the investigated alloys and master alloying conditions.

There is one more important observation found in Figure 6.1.2b. Figure 6.1.2g shows a schematic of the bulkhead section with the adjoining riser. The arrows indicate the direction the liquid feed must traverse in order to compensate for solidification within the bulkhead section. The porosity difference (*Percent Porosity on the Left Side of the Bulkhead – Percent Porosity on the Right Side of the Bulkhead: ΔPP*) can be seen in Figure 6.1.2h.

The method of illustrating the value of porosity in Figure 6.1.2h is important because it shows that the right side of the bulkhead indicates only a minimal improvement for the WA328 alloy and for the WB328 alloy. This is due to the right side being well fed. However, the left side of the bulkhead is poorly fed due to the riser condition, and shows a smaller disparity in porosity difference between the left and the right side of the WA328 alloy, and

the WB328 alloy bulkheads when compared to the W319 alloy bulkheads. This implies that the WA328 and WB328 alloys were able to considerably compensate for the feeding difficulties on the left side of the bulkhead. The reason for this is presumably due to the differing volume fractions of the α -Al dendrites, the Al-Si eutectic and the lower Cu content in the WA328 and WB328 alloys in comparison to the W319 alloy. The role of these three factors towards pore nucleation and growth kinetics was discussed in *Sections 5.4, 5.5, 5.6 and 5.7 of Chapter Five*.

All complex shaped castings are prone to hot spots, which result in anomalously higher porosity in that hot spot area [2, 3, 14, 103, 104]. The WA328 and WB328 alloys appear to not only reduce porosity as a whole, but also to reduce the severity of problem areas (i.e. left side of the bulkhead) compared to the W319 alloy.

Nonetheless, the observed results in Figure 6.1.2h complement further the results referenced in Figures 5.8.1a and 5.8.1b [19, 20], which show that the Al-9wt.%Si-1wt.%Cu alloy (synthetic version of the WA328 alloy) had lower porosity than the Al-7wt.%Si-4wt.%Cu alloy (synthetic version of the W319 alloy). The wedge casting represents directional solidification while the V8 engine block does not.

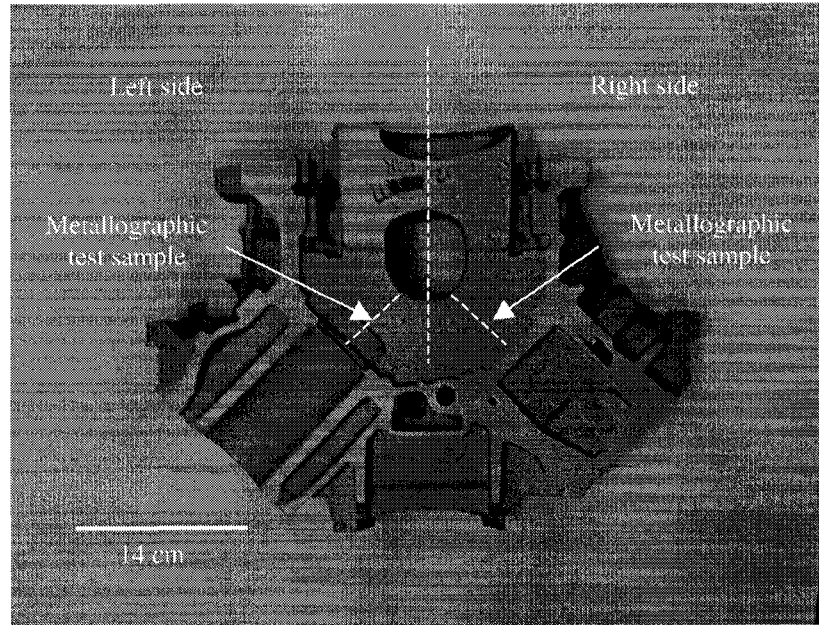


Figure 6.1.2a: Bulkhead E with adjoining riser. Note the asymmetry of the riser sink towards the right side of the bulkhead. This implies that the right side of the bulkhead drew more liquid feed than the left side. The dashed line delineates the boundaries between the left and the right bulkheads and the risers.

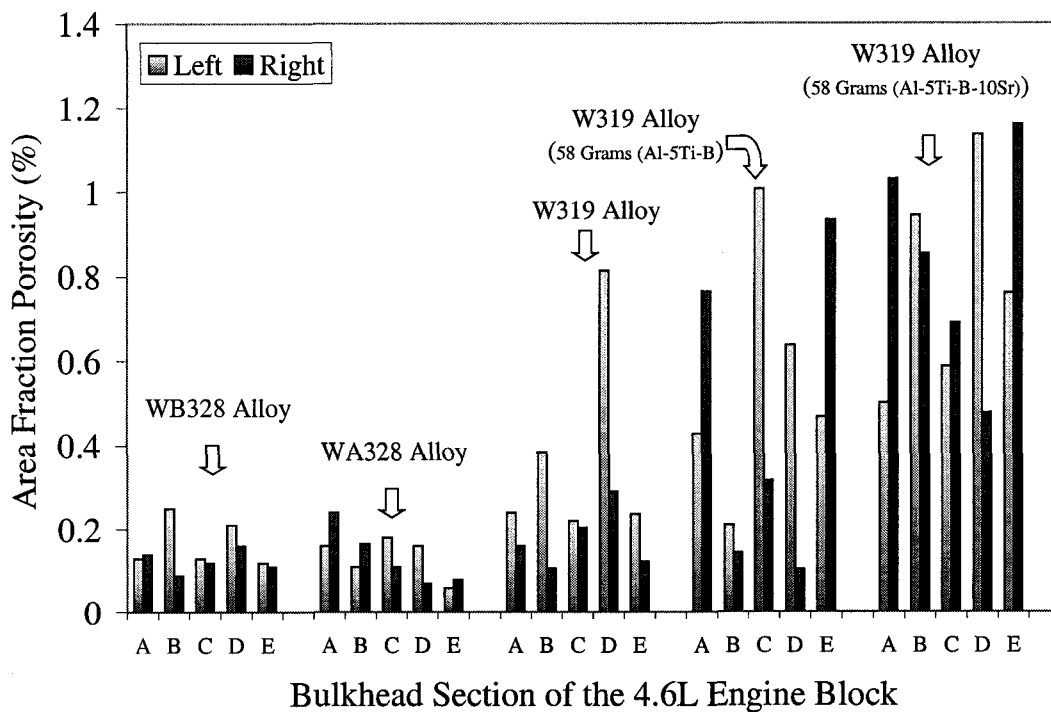


Figure 6.1.2b The level of mean area fraction porosity found on both the right, and the left side of each bulkhead of the V8 engine block cast under the listed conditions.

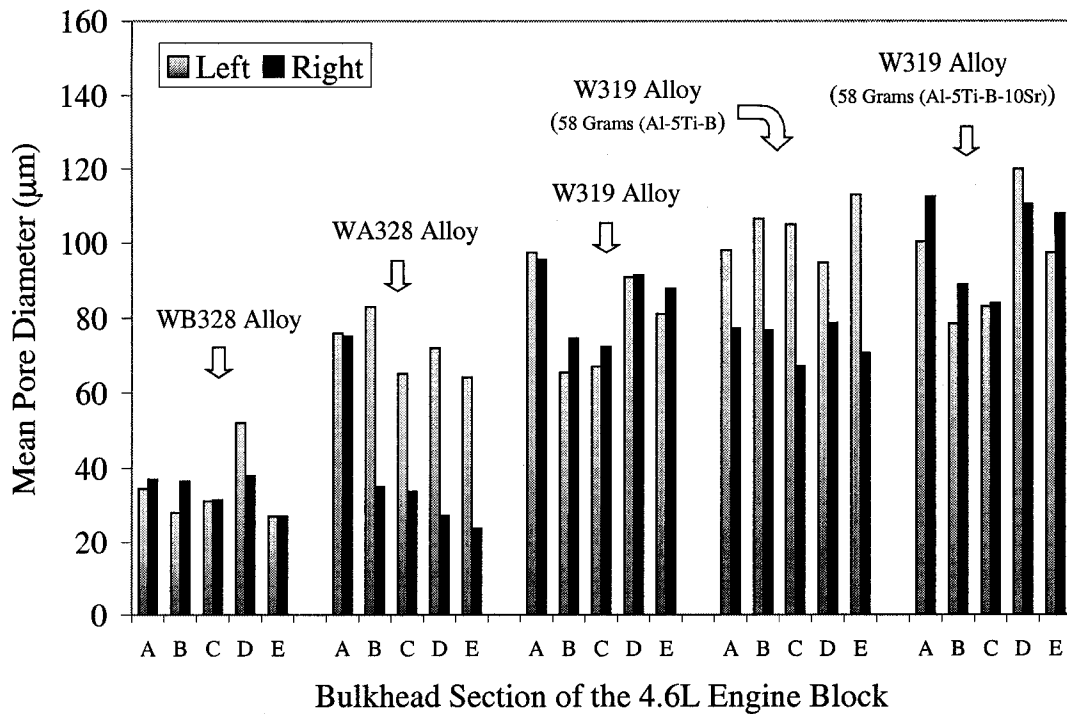


Figure 6.1.2c: Summary of the Mean Pore Diameter found in Bulkheads A through E of the V8 engine block.

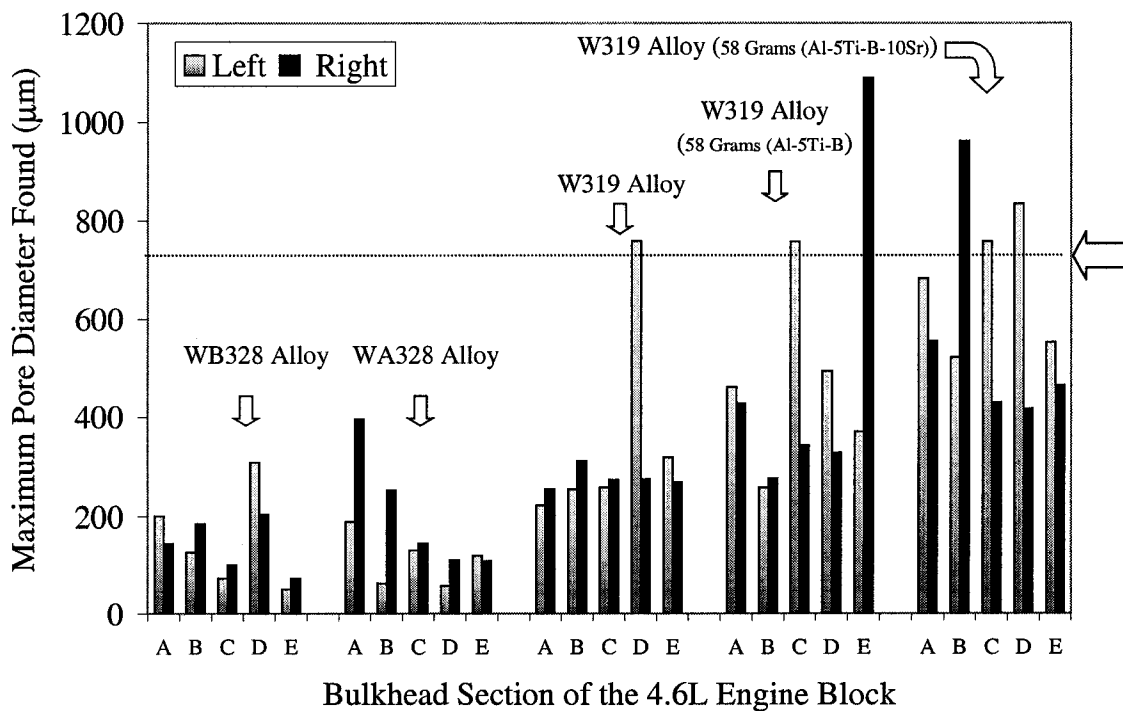


Figure 6.1.2d: Summary of the Maximum Pore Diameter Found in Bulkheads A through E of the V8 engine block. The dashed line with an arrow on the right side represents the maximum pore diameter allowable under the WSE-M2A151-A3 specification.

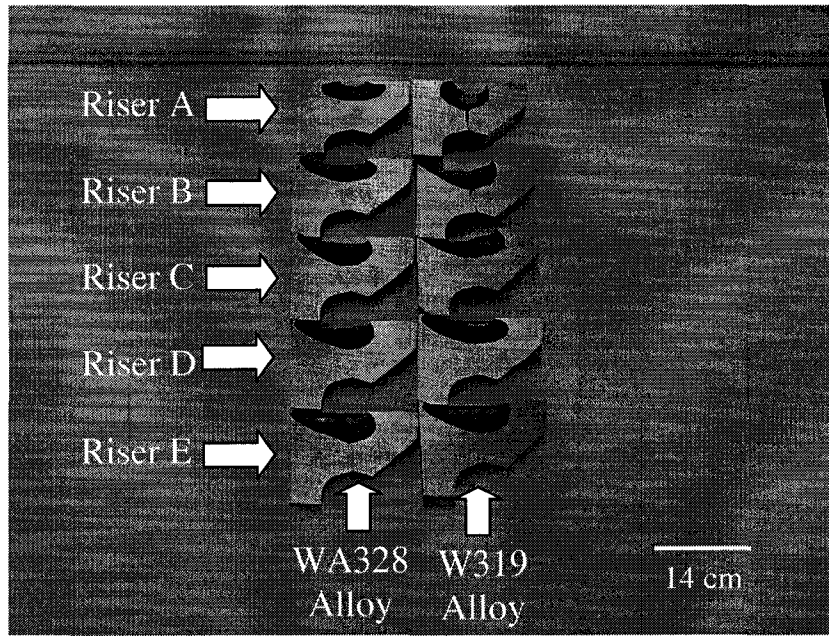


Figure 6.1.2e: The sectioned risers of both the W319 alloy and the WA328 alloy in the non-grain refined condition. The asymmetry of the riser volume sink, seen in risers B, C, D, E, is present irrespective of alloy chemistry.

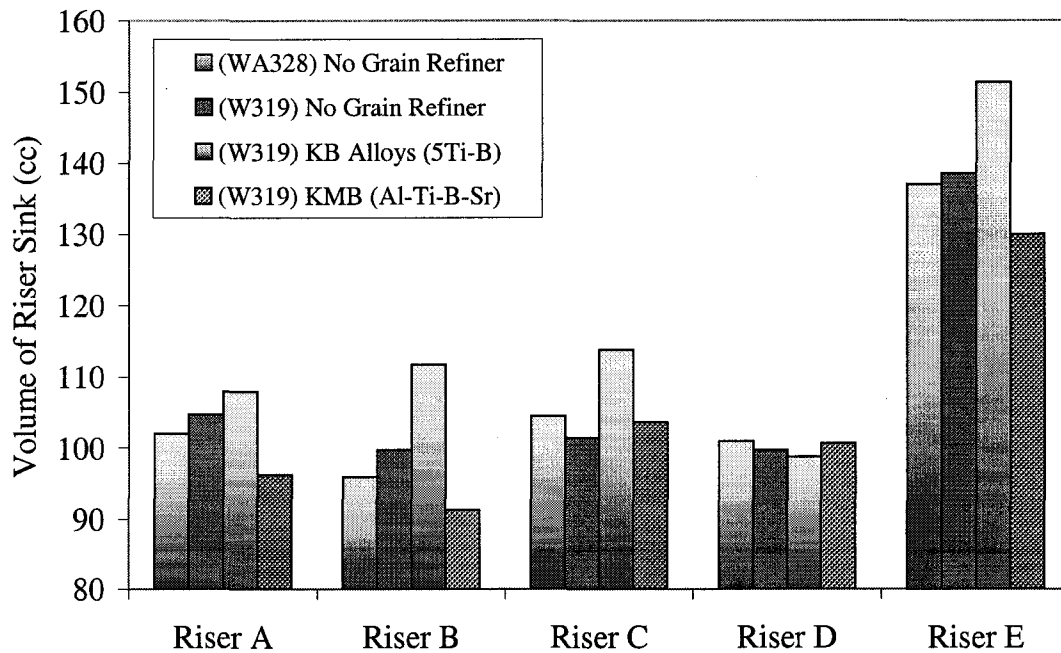


Figure 6.1.2f: The volume of riser sink data for both the WA328 and W319 alloys.

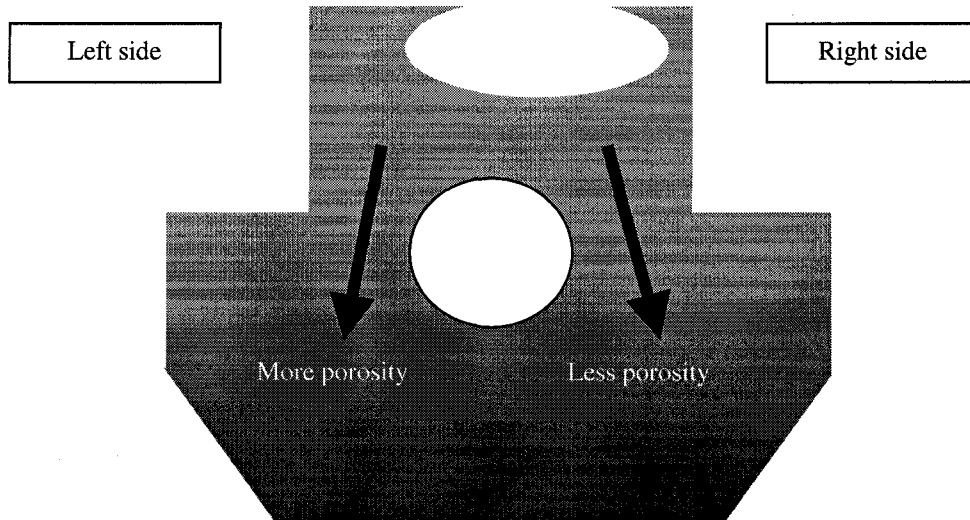


Figure 6.1.2g: A schematic vertical cross-section (as shown in the picture of Figure 6.1.2a) showing the configuration between the riser and bulkheads B, C and D. Bulkhead B is the critical bulkhead requiring maximum soundness for the running engine operation. Risers B, C, D, and E contain the asymmetrical nature of the sink. The arrows represent the feed paths that would occur around the crankshaft passage way.

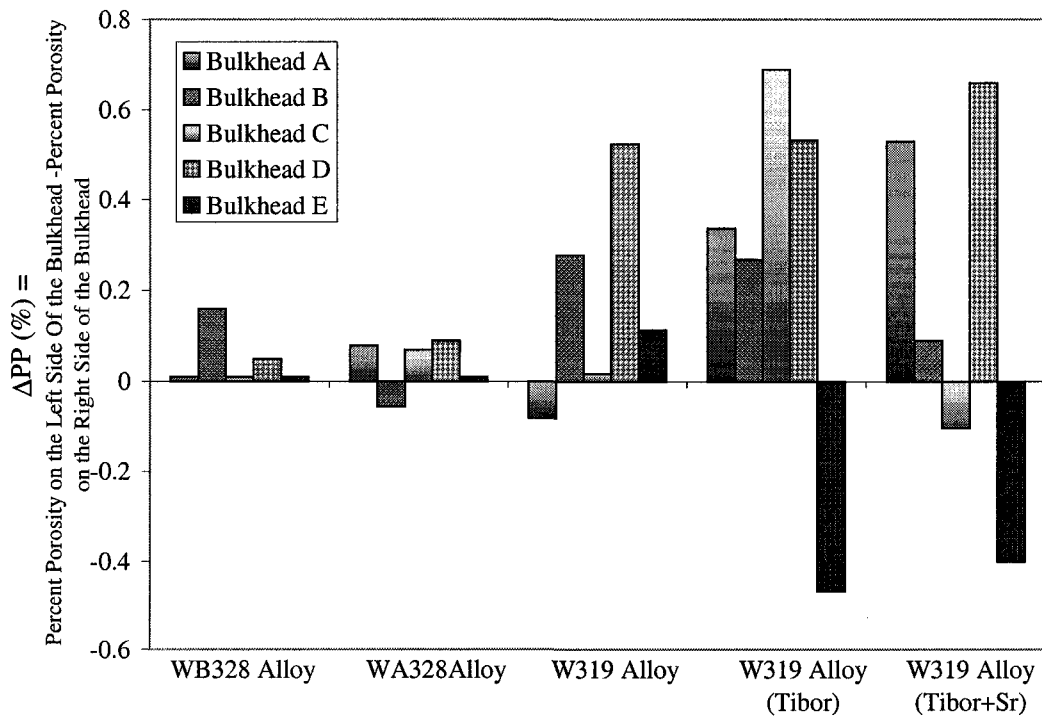


Figure 6.1.2h: The difference in mean area fraction percent porosity found on the left side versus the right side of each bulkhead section for the five alloy conditions investigated.

6.1.3 The Effect of Distribution of Bulkhead Porosity on Fatigue Performance

The asymmetry of the volume sink of the riser could affect the ultimate value of the sustainable mean High Cycle Fatigue (HCF) stress of the bulkhead section of the V8 engine block. The level of porosity affects the number of cycles, and the level of the mean alternating stress that can be sustained by an excised test sample [14, 18, 21-28, 75-78, 81]. An example is the staircase study performed by Climax Research Services (CRS) on the V8 engine block with residual Sr and in-mould grain refiner [113, 114]. It was found that out of 36 fatigue test specimens, 20 were run-outs and 16 failed. Of the 20 run-outs only 9 were from the left side of the bulkhead, and 11 were from the right side of the bulkhead. However, of the 16 samples which failed 10 were from the left side of the bulkhead and only 6 were from the right side of the bulkhead. It would appear that the fatigue test specimens cut from the left side of the bulkhead, which has a higher level of porosity, have a higher propensity for failing than the test samples taken from the right side of the bulkhead.

It would appear that in order to produce accurate upper bounds for the measured mean HCF stress sustained only fatigue test specimens excised from the left side of the bulkhead be analyzed. Probably the mean HCF stress that would result from a completed staircase test would be lower than if both left and right excised fatigue samples were used.

The question arises whether testing of the new WA328 alloy should be performed on the fatigue test samples from the left side of the bulkhead so that the accurate lower bounds of V8 engine block durability could be made. The problem with performing a staircase fatigue test on the WA328 alloy based only on the fatigue test samples taken from the left side of the

bulkhead is that a comparable result to the previous work done by CRS on the V8 engine block cast in the W319 alloy with Sr [114] and with residual Sr and Tibor [18] could not be made.

6.2 The Value of Secondary Dendrite Arm Spacing (λ_2) found in the V8 Engine Block

In-situ thermal analysis was performed on bulkhead E of the V8 engine block using the W319 alloy. The calculated cooling rate $\approx (T_{\text{NUC}}^{\alpha\text{DEN}} - T_{\text{SOL}})/(t_{\text{NUC}}^{\alpha\text{DEN}} - t_{\text{SOL}})$ measured from the bulkhead section is shown in Figure 6.2a, while the layout of the thermocouple array (shown as white dots) is shown in Figure 6.2b. Appendix C explains in detail how the in-situ thermal analysis was carried out. The value of λ_2 found with thermocouple locations 5, 7, 9 and 10 is also shown in Figure 6.2b. The Ford Engineering Material Specification WSE-M2A151-A3 requires that the average value of λ_2 should be 50 μm in critical areas while no area shall have an average value of λ_2 which exceeds 60 μm [17].

As seen in Figure 6.2b both λ_2 measured in the production W319 alloy and the WA328 alloy exceed the maximum level of 50 μm specified by WSE-M2A151-A3. Actually, due to the prolonged solidification time (~ 500 seconds) both the W319 alloy and the WA328 alloy yield similar values for λ_2 .

The values for λ_2 measured from the bulkhead do not show any asymmetry in the left and right sides of the bulkhead as with porosity (see Section 6.1.2). This is due to the fact that λ_2 is controlled by solidification time, while porosity is controlled by solidification time and also the access to a suitable source of liquid feed.

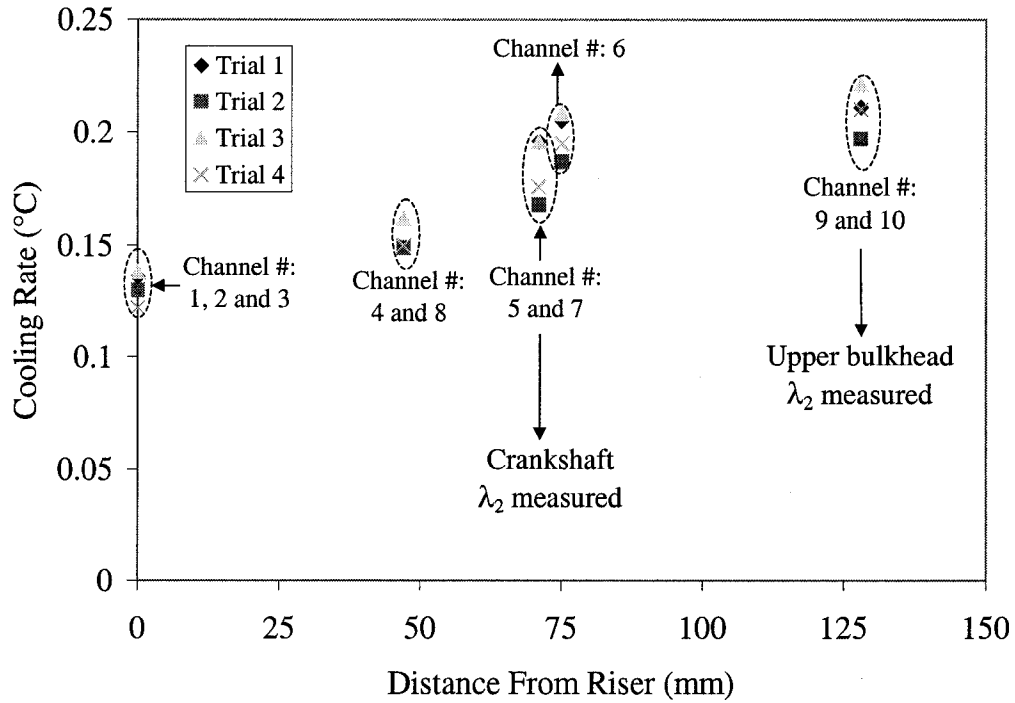


Figure 6.2a: The total cooling rate ($\approx (T_{\text{NUC}}^{\alpha\text{DEN}} - T_{\text{SOL}})/(t_{\text{NUC}}^{\alpha\text{DEN}} - t_{\text{SOL}})$) as recorded by each thermocouple as a function of the distance from the riser thermocouple. Repeated four times.

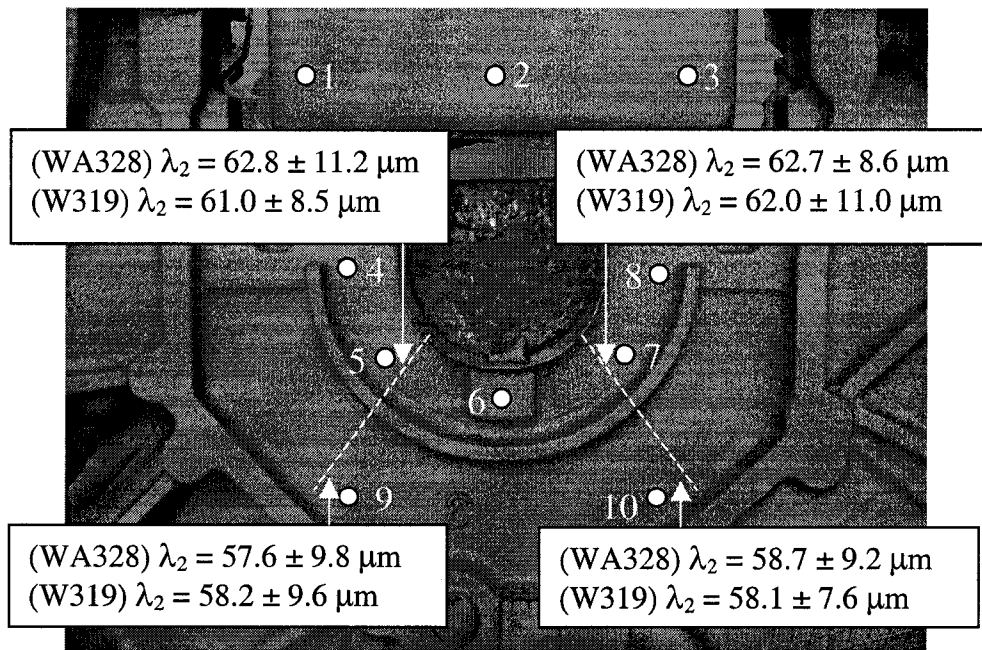


Figure 6.2b: The layout of the in-situ thermal analysis method used for the V8 engine block (bulkhead E) and the locations where λ_2 was measured.

6.3 Results of Monotonic Mechanical Testing of the W319 Alloy & the WA328 Alloy

A total of 20 tensile tests were conducted for the W319 and WA328 alloys. The results of the yield stress (0.2% offset), ultimate tensile stress, modulus of elasticity, and elastic and total elongation are shown in Table 6.1. The Vickers Microhardness results were determined for the same samples used to acquire the porosity data for the W319, WA328 and WB328 alloys and are shown in Table 6.2. Brinell Hardness was measured on the grip ends of fatigue test samples cut from the left side of the bulkhead, and the results are shown in Table 6.3.

From Tables 6.1 and 6.2 the elastic monotonic properties and matrix microhardness are fairly close to the W319 alloy and the WA328 alloy. However, the ultimate tensile stress is high for the W319 alloy. It is known that λ_2 measurements, as seen in Figure 6.2b, are similar for the W319 alloy and for the WA328 alloy, but that the volume fraction of the α -Al dendrites is larger in the W319 alloy (i.e. $af_s^{\alpha DEN} \approx 30\%$ for the WA328 alloy, and 43% for the W319 alloy). Following yielding, the structure of the alloy is known to plastically deform via the movement of slip bands within the α -Al matrix and eventually these slip bands come in contact with a discontinuous interface of the α -Al matrix. These interfaces are:

- 1) Si platelet/ α -Al matrix interface, (poor cohesion [22, 23, 95, 81, 117, 118, 120]).
- 2) Al_5FeSi / α -Al matrix interface, (poor cohesion [31-39, 55, 95, 104, 117, 118]).
- 3) $Al_{15}(Fe,Mn,Cr)_3Si_2$ / α -Al matrix interface, (better cohesion [22, 23, 96, 81, 117]).
- 4) Mg_2Si script phase/ α -Al matrix interface, (better cohesion [119]).
- 5) Juncture between the α -Al matrix and a shrinkage pore [21-23, 26, 28, 81-85, 119].

Other phases, such as the Al_2Cu phase, have either dissolved or partially dissolved in response to the applied heat treatment (see Section 5.1).

The higher ultimate tensile stress of the W319 alloy could be due to its larger volume fraction of the α -Al dendrites. Since similar values of microhardness and monotonic elastic properties (for the W319, and the WA328 alloys) exist, slip planes would have similar mobility in the α -Al dendrites of both alloys. However, the slip bands in the W319 alloy have longer distances to traverse before encountering any of the 5 previously mentioned discontinuous interfaces. As multiple decohesions at phase interfaces occur, a reduction in the load bearing cross-sectional area of the tensile test sample results in the full rupture of the test sample.

Boileau [81] used the same monotonic test sample dimensions as were used in this dissertation. The values obtained here compare very well to the observed monotonic results found for the test samples excised from Boileau's W319 alloy cast in a V8 engine block (containing 70 ppm Sr), and having a λ_2 of approximately 60 μm . The yield stress was 215 MPa, with an elastic elongation of 0.3%. The ultimate tensile stress measured was lower in Boileau's dissertation and found to be 221 MPa, due to the higher level of porosity measured from the test sample cross-section (0.56 ± 1.03 %, *mean pore diameter of 35 ± 37 μm , and largest pore diameter of 217 μm*).

A point needs to be made concerning the Brinell Hardness measured on the fatigue test bar grip ends cut from bulkhead C. The Ford Engineering Material Specification WSE-M2A151-A3 requires that the Brinell Hardness be no lower than 85. As seen in Table 6.3 the

requirement is not only met but exceeded. While Table 6.2 indicates that the α -Al dendritic matrix is slightly softer for the WA328, and WB328 alloys, than for the W319 alloy, the difference in Brinell Hardness of the WA328 and WB328 alloys compared to the W319 alloy is not apparent. This is most likely due to the higher volume fraction of the brittle Si phases in the WA328 and WB328 alloys.

Table 6.1: Summary of monotonic test results from the V8 engine block cast from the W319 and WA328 alloys after heat treatment.

Alloy	λ_2 (μm)	Tensile Strength (MPa)		Elongation (%)		Modulus of Elasticity (GPa)
		0.2% Yield	Ultimate	Elastic	Total	
W319 (In-mould Al-5Ti-1B) (10 samples)	58 to 62	225 ± 19	270 ± 9	0.47 ± 0.03	1.2 ± 0.2	78 ± 12
WA328 (10 samples)	58 to 62	232 ± 9	236 ± 10	0.48 ± 0.02	0.8 ± 0.2	81 ± 8.5
W319 ~ 70 ppm Sr (6 samples) [81]	60	215 ± 6	215 ± 9	0.30 ± 0.00	0.5 ± 0.1	74 ± 4.0

Table 6.2: Vickers Microhardness (HV25g/15s) from the left side of the bulkhead of the V8 engine block cast in the W319, WA328 and the WB328 alloys after heat treatment.

Alloy	Bulkhead A	Bulkhead B	Bulkhead C	Bulkhead D	Bulkhead E
W319 (In-mould Al-5Ti-1B)	105.1 ± 4.7	107.5 ± 5.2	98.3 ± 5.1	103.5 ± 3.8	96.2 ± 6.4
WA328	91.1 ± 6.0	86.6 ± 5.3	81.6 ± 4.7	88.4 ± 7.4	92.2 ± 2.7
WB328	95.2 ± 4.8	82.8 ± 9.1	84.8 ± 7.4	87.2 ± 2.0	91.4 ± 7.3

Table 6.3: Brinell Hardness (HB500Kg/15s) measured on fatigue test bars excised from the left side of bulkhead C of the V8 engine block after heat treatment.

Alloy	Bulkhead C
W319 (In-mould Al-5Ti-1B)	101.2 ± 4.76
WA328	100.0 ± 5.78
WB328	105.0 ± 5.52

6.4 High Cycle Fatigue Results

6.4.1 Summary of the Staircase Results

The Ford Engineering Material Specification WSE-M2A151-A3 requires the mean HCF stress to be 65 MPa [17], which is not achieved with the current production or the past production of the V8 engine blocks. Figure 6.4.1a shows the results of the HCF staircase data for the W319 alloy (~ 70 ppm Sr added in-furnace [114]), W319 alloy with in-mould Al-5Ti-1B grain refiner, and the WA328 alloy. Table 6.4 summarizes the mean HCF results along with the standard deviation for the three conditions seen in Figure 6.4.1a.

Also listed in the summary in Table 6.4 are the mean HCF results of the V8 engine block cast with a chill in accordance with the Ford Engineering Material Specification WSE-M2A151-A4 [17]. The Ford Engineering Materials Specification WSE-M2A151-A4 requires a mean alternating stress of 85 MPa which is achieved through the use of a chill running along the crankshaft bearing from bulkhead A through E. However, the production of the V8 engine block produced made with a chill achieves a mean HCF stress of 65 MPa. At the time of writing of this dissertation the actual staircase results for the chilled V8 engine block were not available, only the mean HCF stress was given through personal communication [121].

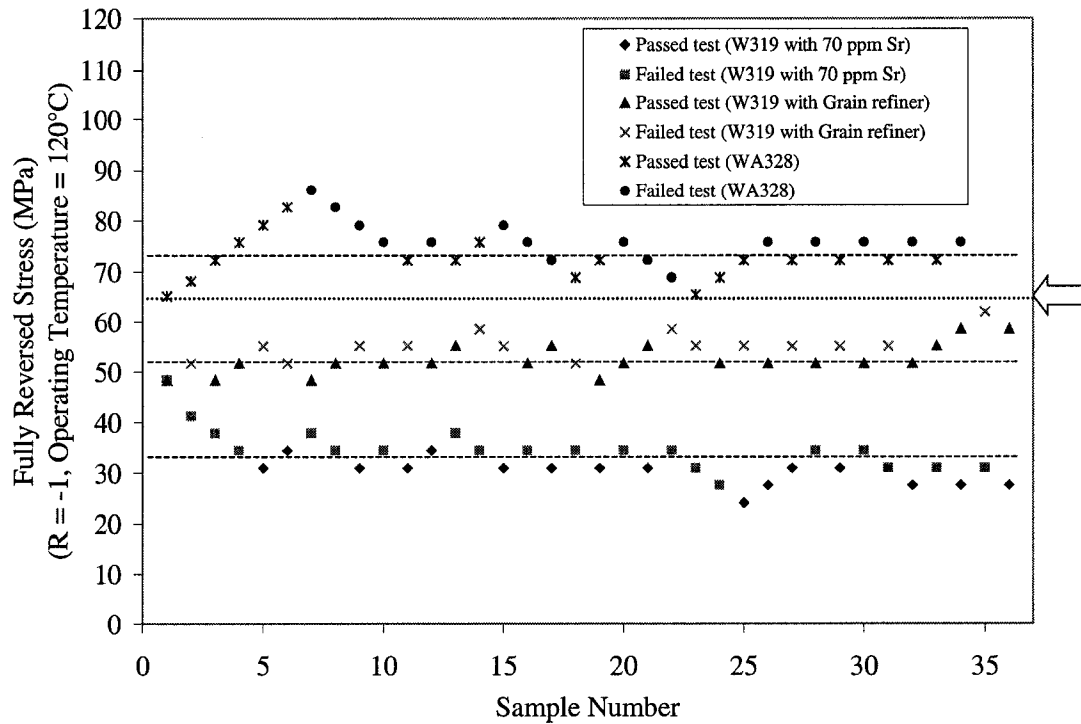


Figure 6.4.1a: The fatigue staircase results of the bulkhead sections taken from the W319 alloy [18, 114] and the WA328 alloy all cast from the V8 engine block. The arrow signifies the mean HCF stress required for the WSE-M2A151-A3 specification.

Table 6.4: Summary of the mean HCF stress found for the investigated bulkhead conditions along with the Ford Engineering Material Specification [17].

<i>Alloy</i>	<i>Number of Test Samples/Number of Run-outs</i>	<i>Mean HCF Stress (MPa)</i>
W319-T7 [119] (In-furnace 70 ppm Sr)	36/16	31.5 ± 2.6
W319-T7 [18] (In-mould Al-5Ti-1B)	36/20	52.0 ± 3.0
*W319-T7 [120] (Chill, In-mould Al-5Ti-1B)		65 ± ?
WA328-T6	33/18	76 ± 4.5
WSE-M2A151-A3 [17]	-	65 Required
WSE-M2A151-A4 [17]	-	85 Required

**Note: The number of test samples/Number of Runouts and the standard deviation for the chill condition is not released.*

6.4.2 Analysis of the Fatigue Fracture Surfaces

Figures 6.4.2a to 6.4.2f show at a low magnification (20X) the Scanning Electron Microscope/Secondary Electron (SEM/SE) micrographs of the fracture surface of 6 different test samples which failed prior to achieving 10^7 cycles. The white arched line represents the transition between what is known to be slow fatigue growth and fast crack growth (tensile overload) leading to full rupture. Typically, as seen in Figures 6.4.2a, b, c, e and f, fatigue crack nucleation appears to originate from a single source which is a subsurface pore or exposed pore. One of the six samples analyzed, seen in Figure 6.4.2d, appears to have multiple nucleation sites which all grow as fatigue cracks and eventually coalesce to make a larger crack. This is why the slow fatigue fracture surface for the fatigue test sample, seen in Figure 6.4.2d, is not shell shaped. Boileau [81] used the same fatigue test sample dimension as was used in this dissertation, and made the same observation of multiple nucleation sites on a limited number of test samples. One of the six fractures, as seen in Figure 6.4.2e, shows damage which occurred when the two sides of the fractured test sample collided one or more times before the servohydraulics of the Instron 8801 system shut down automatically.

The fatigue test sample fracture surfaces, as seen in Figure 6.4.2c (sample# 13) are shown in more detail at a higher magnification in SEM/SE micrographs (Figures 6.4.2g through to 6.4.2j). Figure 6.4.2g shows the whole fracture surface, and the dashed boxes are the SEM/SE micrographs taken at higher magnifications. Figure 6.4.2h shows that a pore was the origin of the crack and that this pore was approximately 5 μm away from the polished surface of the test sample. The regions surrounding the initiating pore are relatively smooth and reveal the presence of striations. Figure 6.4.2h shows the dashed box of a region at a higher

magnification in Figure 6.4.2j. Figure 6.4.2j reveals a possible striation region and an oxide, both labeled. Figure 6.4.2j shows the region past the transition line where the crack growth was instant. Evidence of ductile rupture and fractured brittle Si phases can be seen.

The fatigue test sample fracture surfaces seen in the SEM/SE micrograph in Figure 6.4.2b (sample# 8) are shown in more detail at a higher magnification in SEM/SE micrographs of Figures 6.4.2k through to 6.4.2p. Figure 6.4.2k shows the whole fracture surface and the dashed boxes are images taken at higher magnifications. Figure 6.4.2l shows the extent of possible connected porosity which can occur in as-cast structures. It is not known if the two pores are really connected. Figure 6.4.2m shows the extent of the pore seen in Figure 6.4.2l, and it appears to be exposed to the surface of the fatigue test sample. Figure 6.4.2n shows the other pore which is between the pore, as seen in Figure 6.4.2m, and the transition line that appears to be quite large, spanning almost 100 μm . The dashed box in 6.4.2m seen in Figure 6.4.2o reveals striations which appear to have a spacing of approximately 5 μm . Figure 6.4.2p shows the region past the transition line where ductile rupture and fractured brittle Si particles are seen.

The fatigue test sample fracture surfaces as seen in the SEM/SE micrograph of Figure 6.4.2f (sample# 24) are outlined in more detail at a higher magnification in the SEM/SE micrographs in Figures 6.4.2q through 6.4.2u. The dashed boxes in Figure 6.4.2q are seen at higher magnifications in Figures 6.4.2r and 6.4.2u. Figure 6.4.2r shows a shrinkage pore which was approximately 20 μm from the test sample surface. The dashed box seen in Figure 6.4.2r is seen at 250X magnification in Figure 6.4.2s. The striations are spaced approximately

5 to 7 μm apart. Figure 6.4.2t (taken adjacent to the region seen in Figure 6.4.2r) shows Si platelets (confirmed in Back Scattered Electron (BSE) mode using Energy Dispersive X-Ray (EDX)) which do not show the striations as seen in the adjacent $\alpha\text{-Al}$ matrix. Si platelets are very brittle and as a consequence have a tendency to cleave, not deform gradually through the formation of striations. Figure 6.4.2u shows the fast fracture region just past the transition line as seen in Figures 6.4.2p and 6.4.2i.

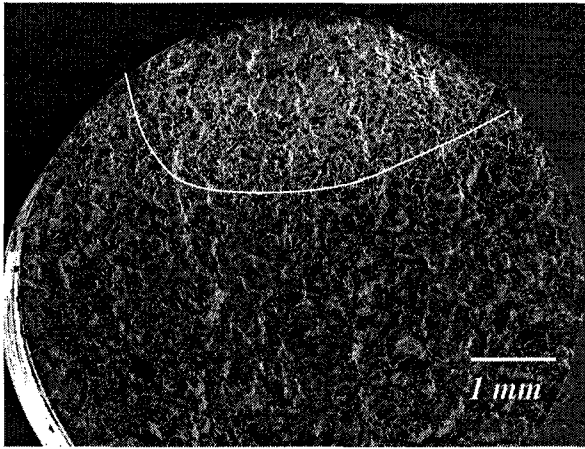


Figure 6.4.2a: (SEM/SE) micrograph of Sample # 3 which failed at a stress of 75.8 MPa & had a life of 2,108,933 cycles.

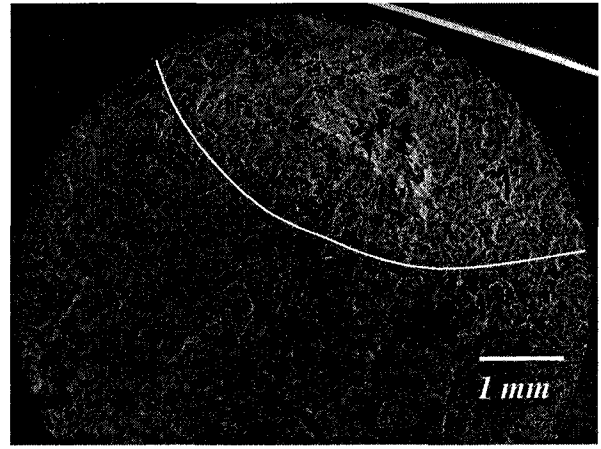


Figure 6.4.2b: (SEM/SE) micrograph of Sample # 8 which failed at a stress of 75.8 MPa & had a life of 4,933,391 cycles.

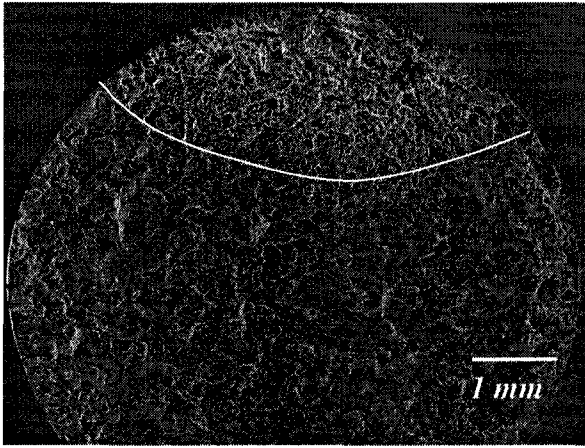


Figure 6.4.2c: (SEM/SE) micrograph of Sample # 13 which failed at a stress of 79.2 MPa & had a life of 385,668 cycles.

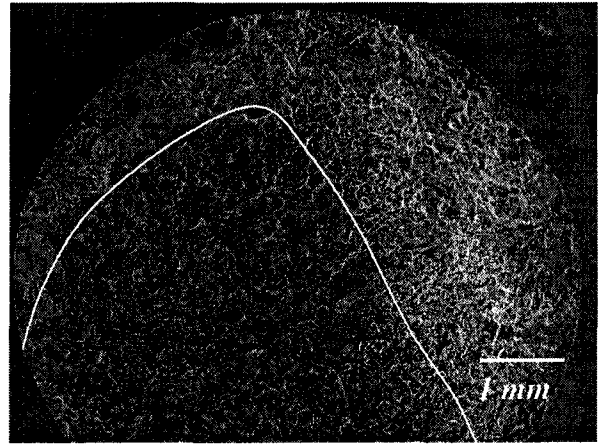


Figure 6.4.2d: (SEM/SE) micrograph of Sample # 11 which failed at a stress of 75.8 MPa & had a life of 6,996,681 cycles.

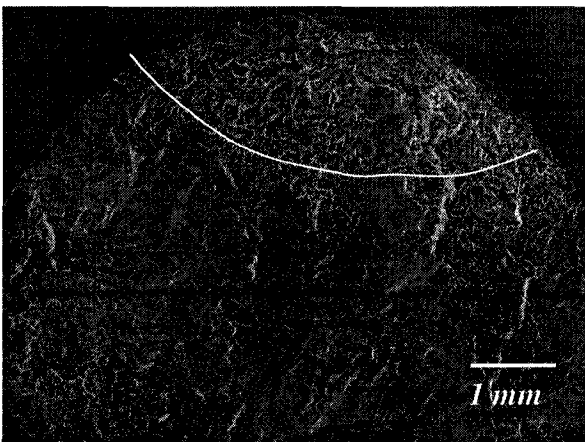


Figure 6.4.2e: (SEM/SE) micrograph of Sample # 22 which failed at a stress of 79.1 MPa & had a life of 4,391,998 cycles.

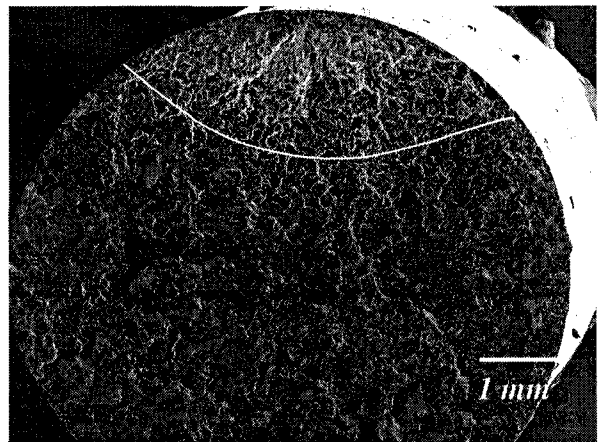


Figure 6.4.2f: (SEM/SE) micrograph of Sample # 24 which failed at a stress of 75.8 MPa & had a life of 789,774 cycles.

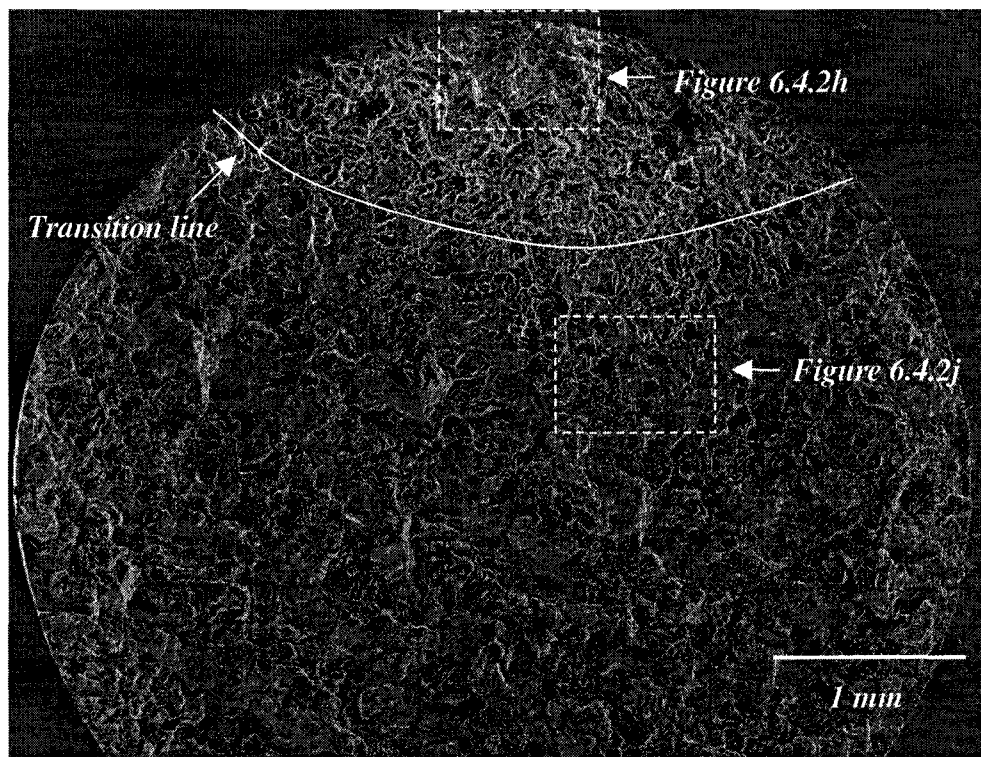


Figure 6.4.2g: (SEM/SE) micrograph taken from the fatigue test sample (sample # 13) fracture surface. The stress was at 79.2 MPa with a life of 385,668 cycles. The dashed boxes are shown at a higher magnification in Figures 6.4.2h and 6.4.2i.

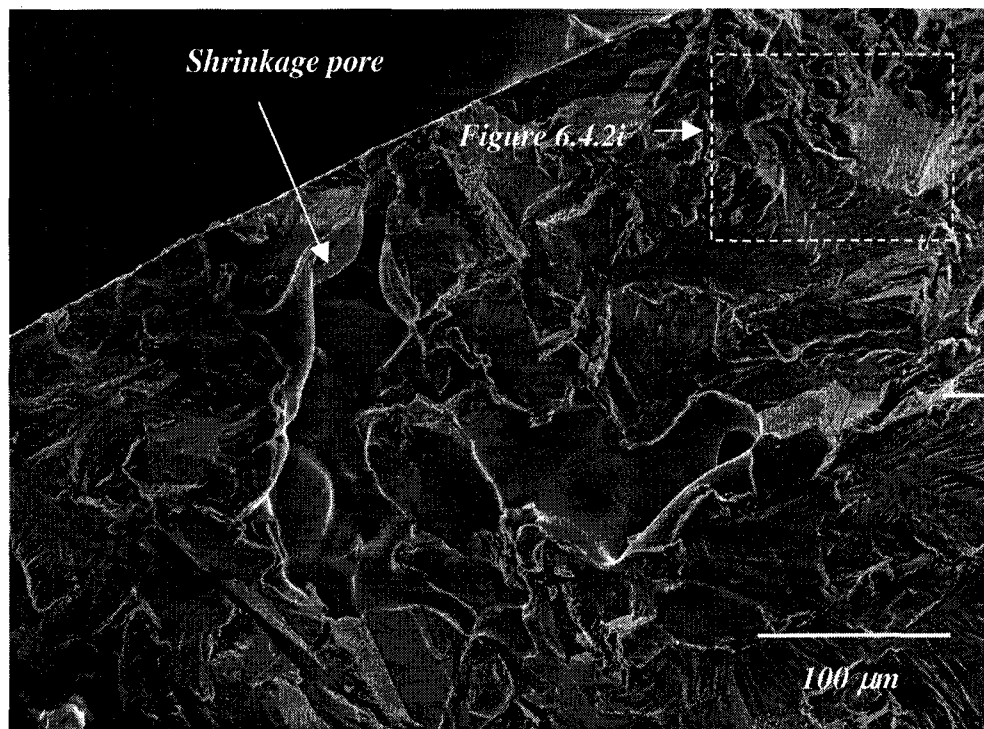


Figure 6.4.2h: (SEM/SE) micrograph showing subsurface pores located within the fractured region. The dashed region is shown in Figure 6.4.2j.

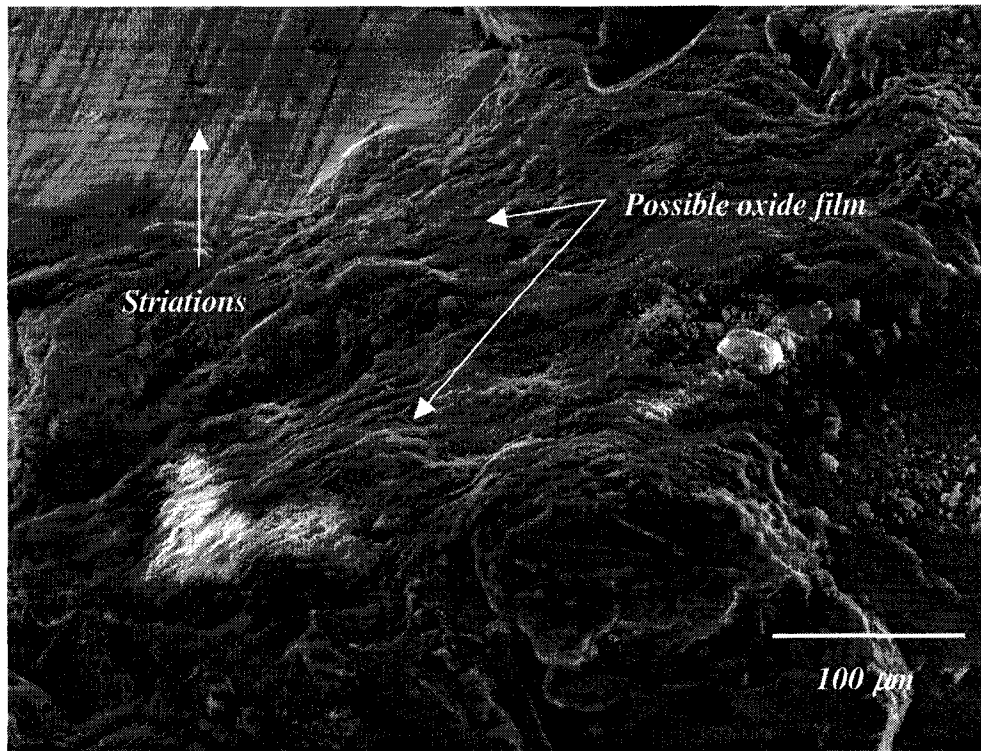


Figure 6.4.2i: (SEM/SE) micrograph showing striations and a possible oxide film within the fatigue fractured region.

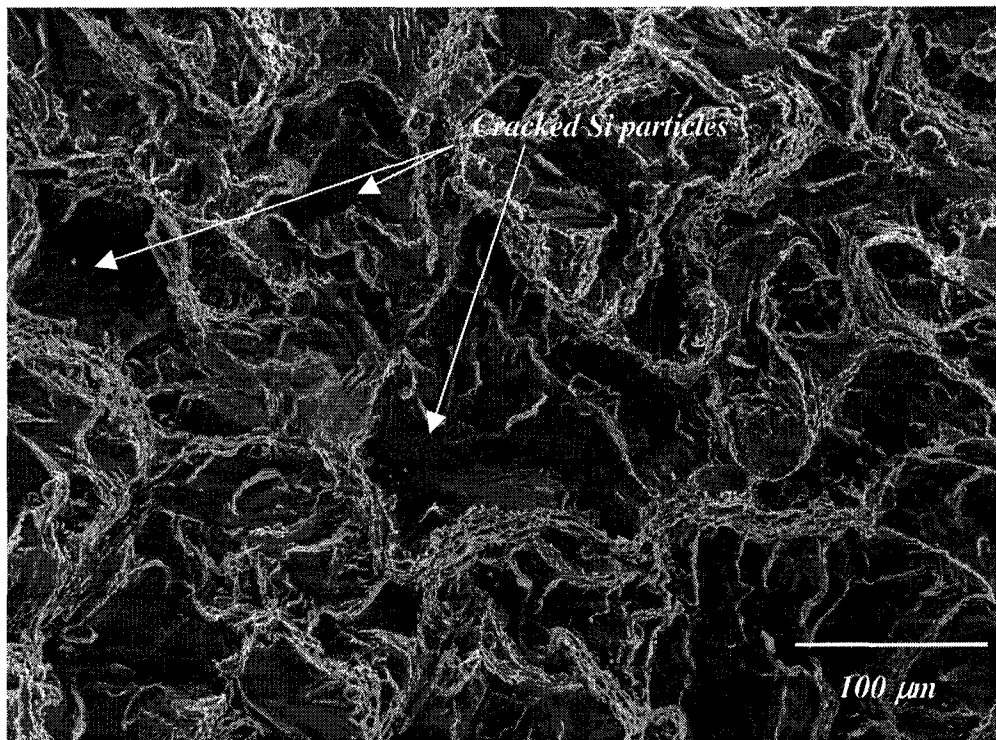


Figure 6.4.2j: (SEM/SE) micrograph showing the fast fracture (*tensile overload*) region just adjacent to the transition line as seen in Figure 6.4.2g.

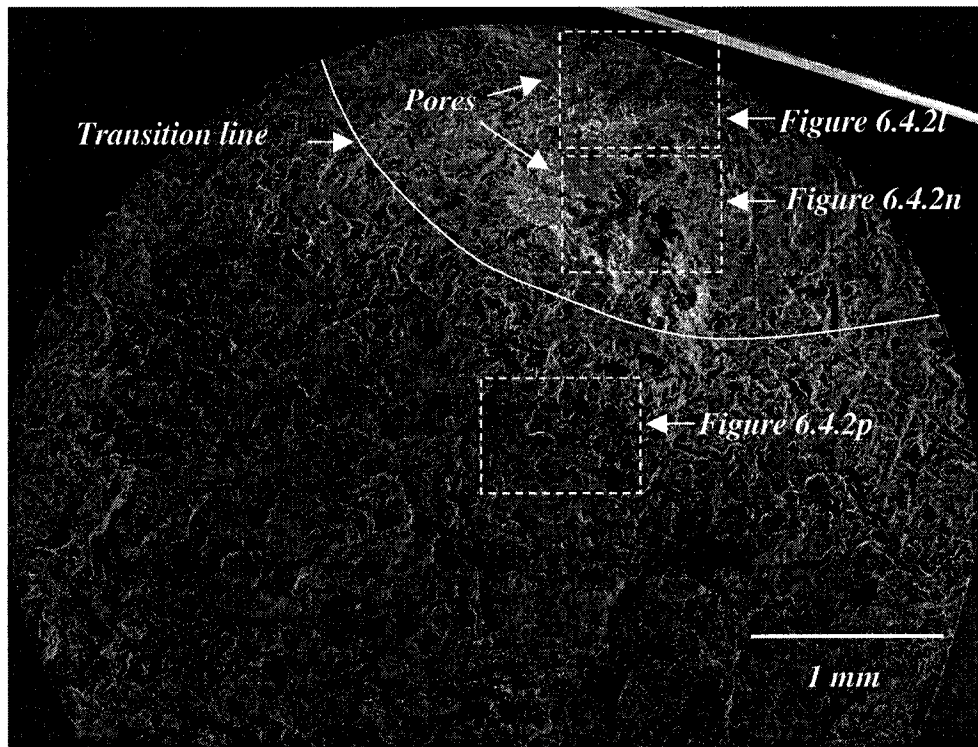


Figure 6.4.2k: (SEM/SE) micrograph taken from the fatigue test sample (sample # 8) fracture surface. The stress was at 75.8 MPa & had a life of 4,933,391 cycles. The dashed boxes are shown at a higher magnification in Figures 6.4.2l, 6.4.2n and 6.4.2p.

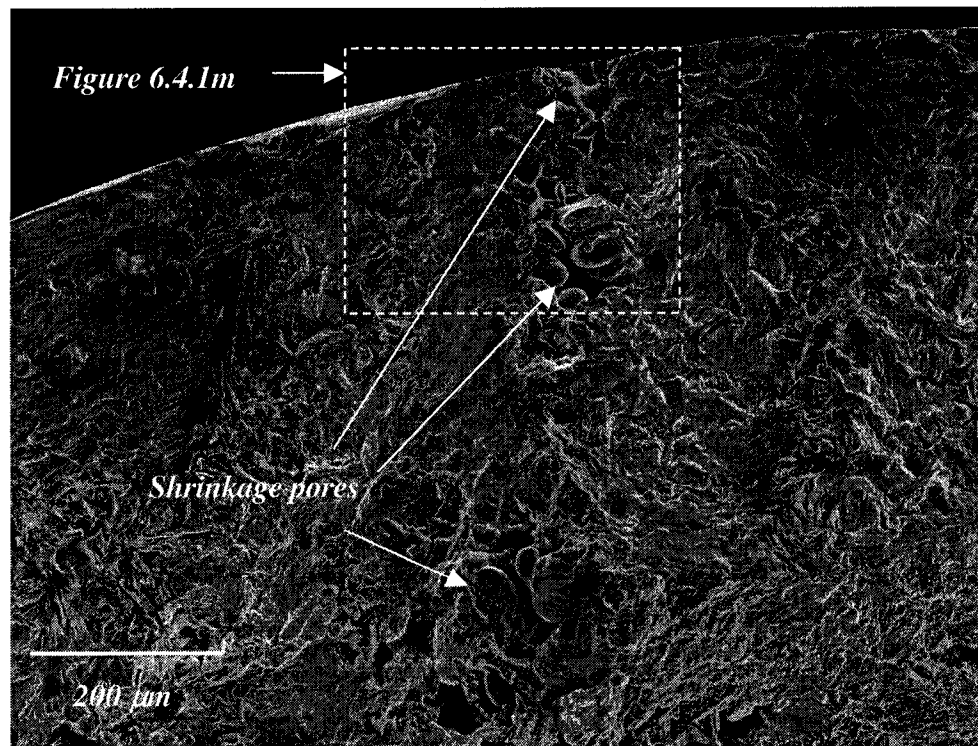


Figure 6.4.2l: (SEM/SE) micrograph showing subsurface pores located within the fatigue fractured region.

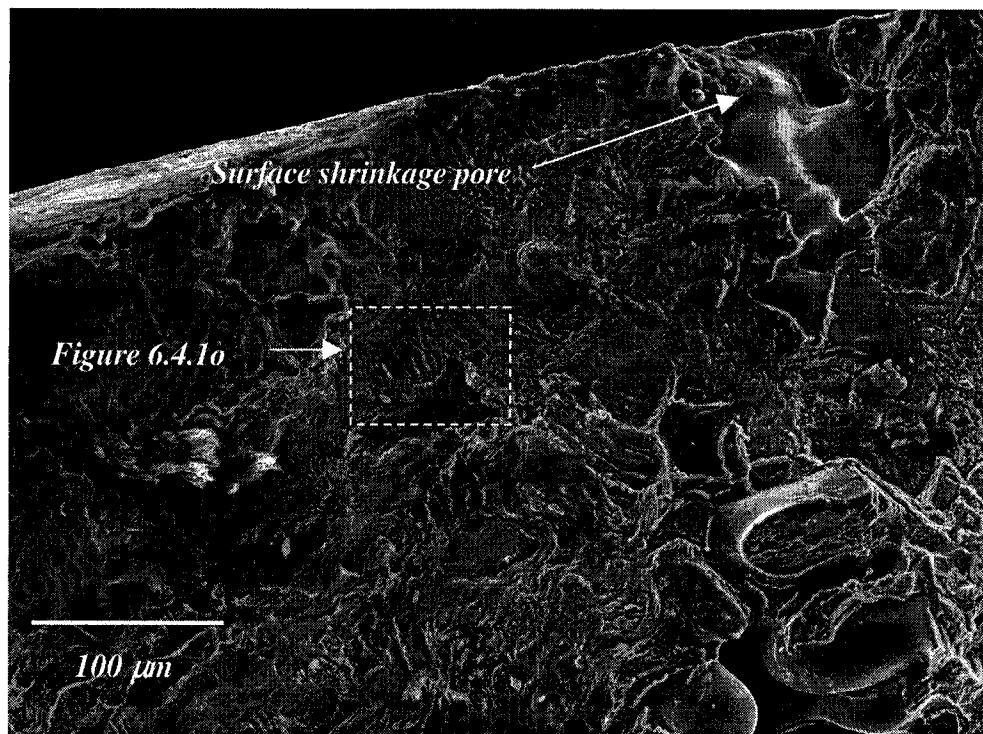


Figure 6.4.2m: (SEM/SE) micrograph showing subsurface pores located within the fractured region. The dashed region is shown in Figure 6.4.1o.

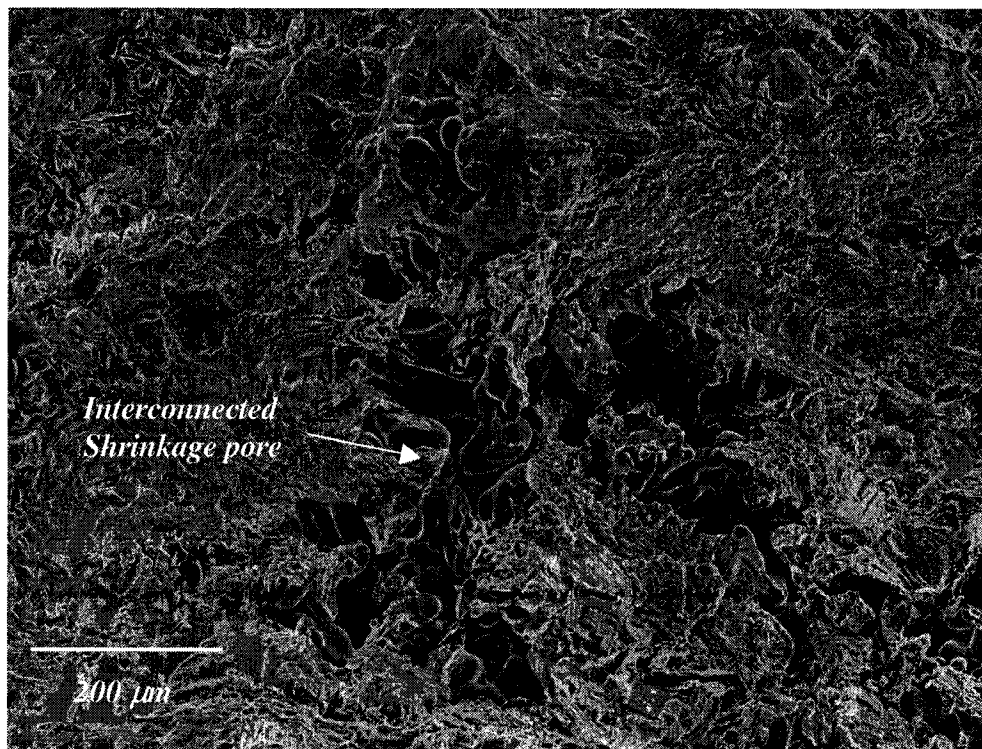


Figure 6.4.2n: (SEM/SE) micrograph showing shrinkage pore located within the fatigue fractured region approximately 1mm from the surface and possibly connected to the surface pore as seen in Figures 6.4.11 & 6.4.1m.

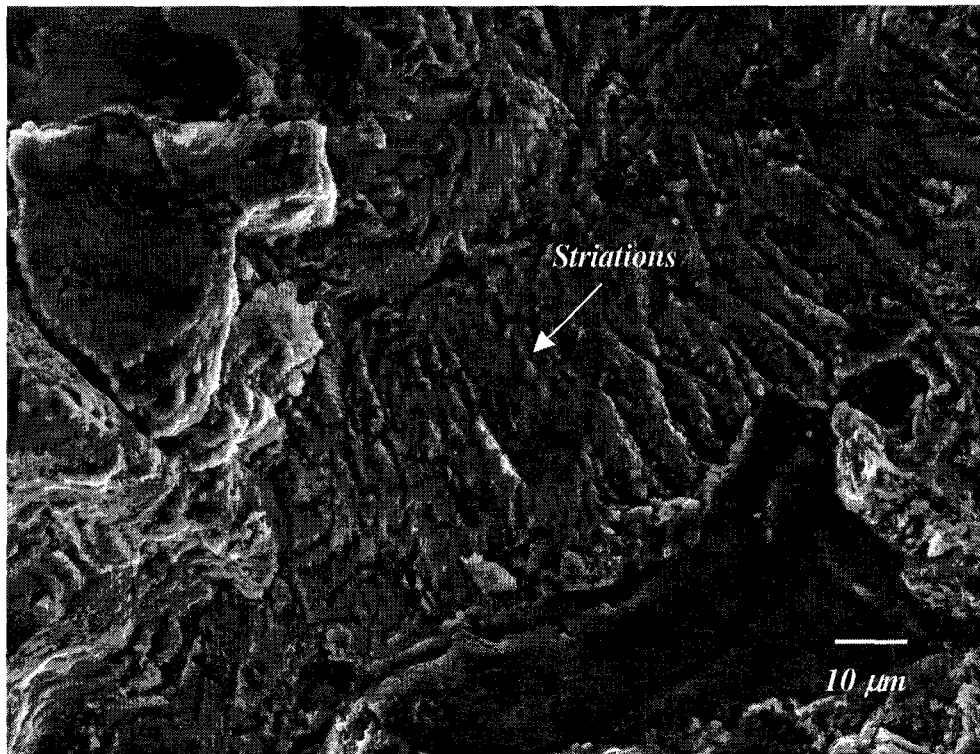


Figure 6.4.2o: (SEM/SE) micrograph showing striations ($\sim 5 \mu\text{m}$ spacing) within the fatigue fractured region.

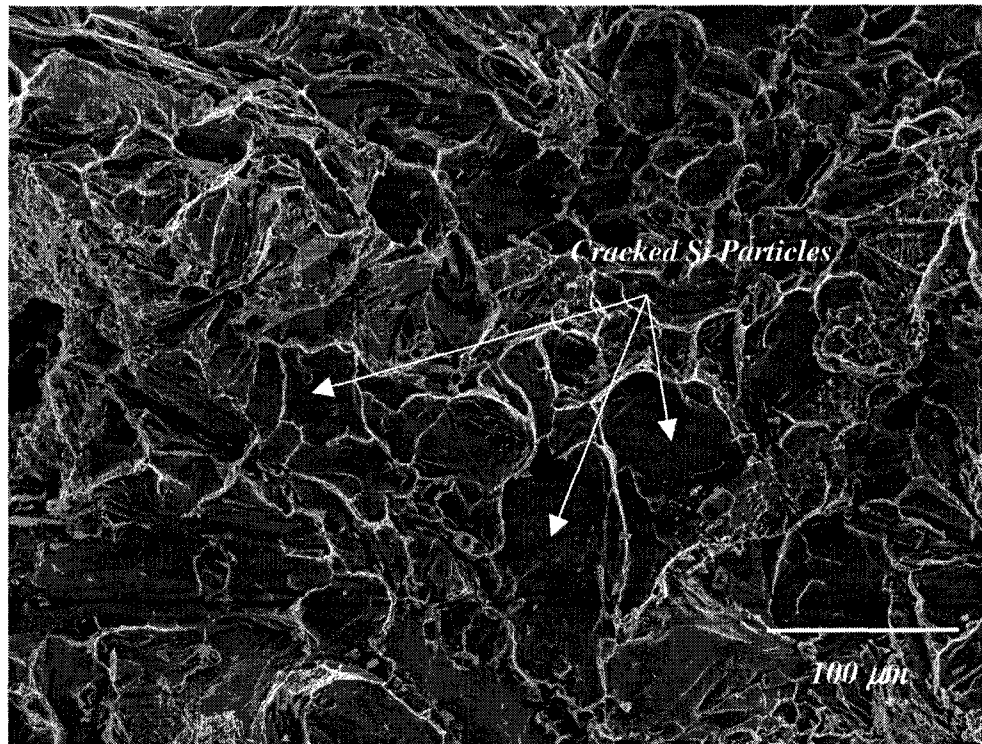


Figure 6.4.2p: (SEM/SE) micrograph showing the fast fracture (Tensile overload) region just adjacent to the transition line.

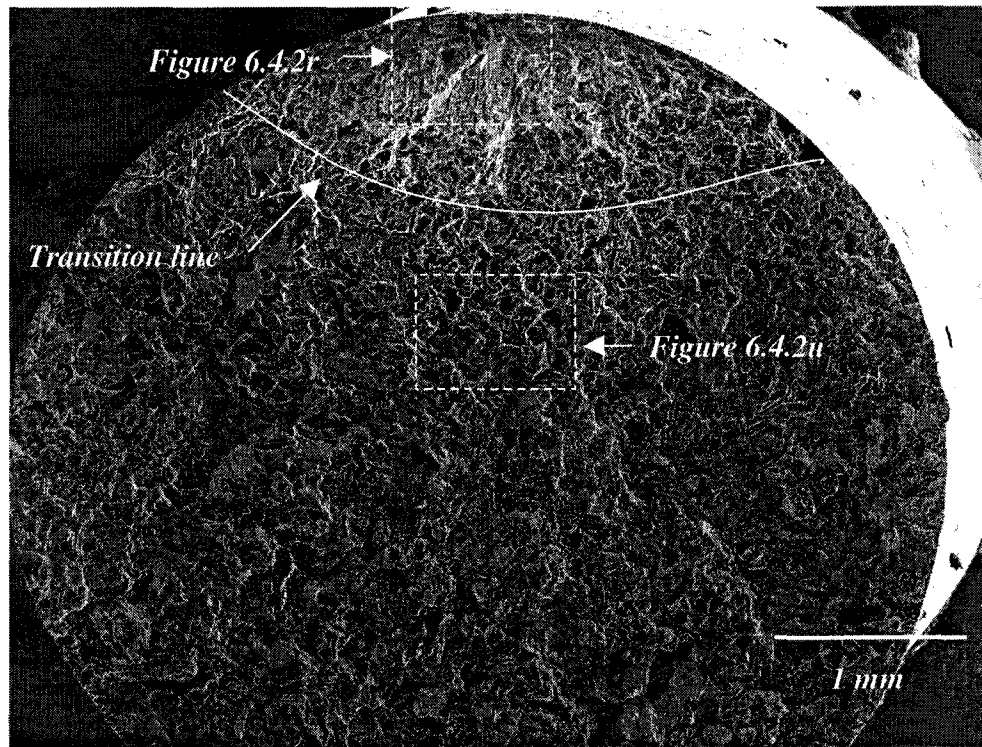


Figure 6.4.2q: (SEM/SE) micrograph taken from the fatigue test sample (sample # 24) fracture surface. The stress was at 79.2 MPa with a life of 385,668 cycles. The dashed boxes are shown at a higher magnification in Figures 6.4.2r and 6.4.2u.

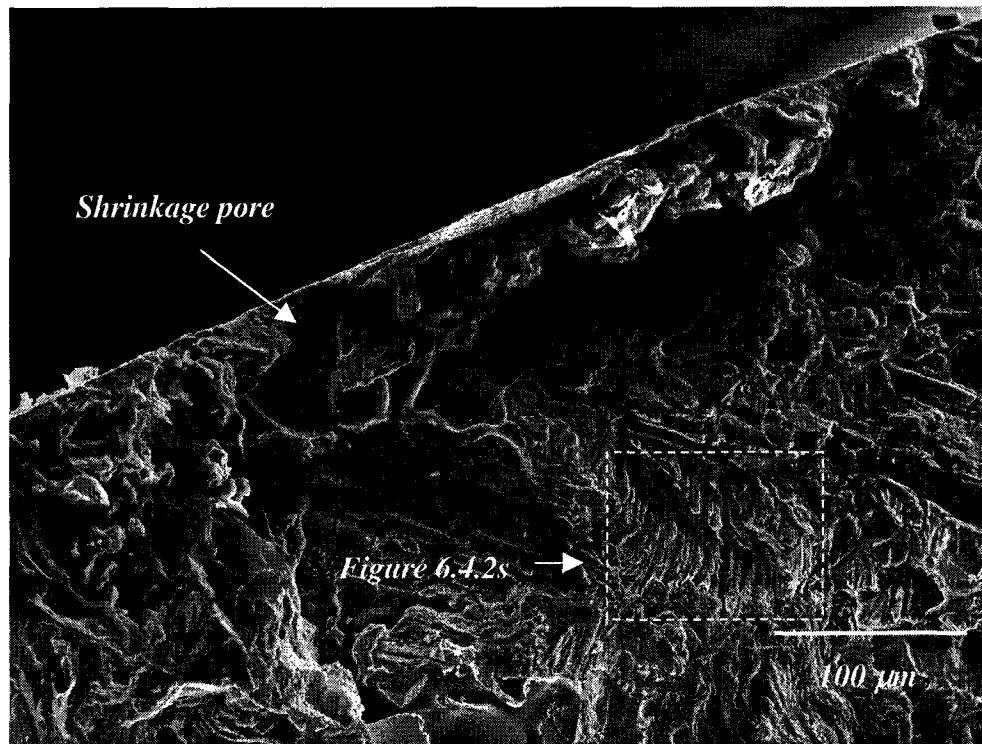


Figure 6.4.2r: (SEM/SE) micrograph showing subsurface pores located within the fatigue fractured region.

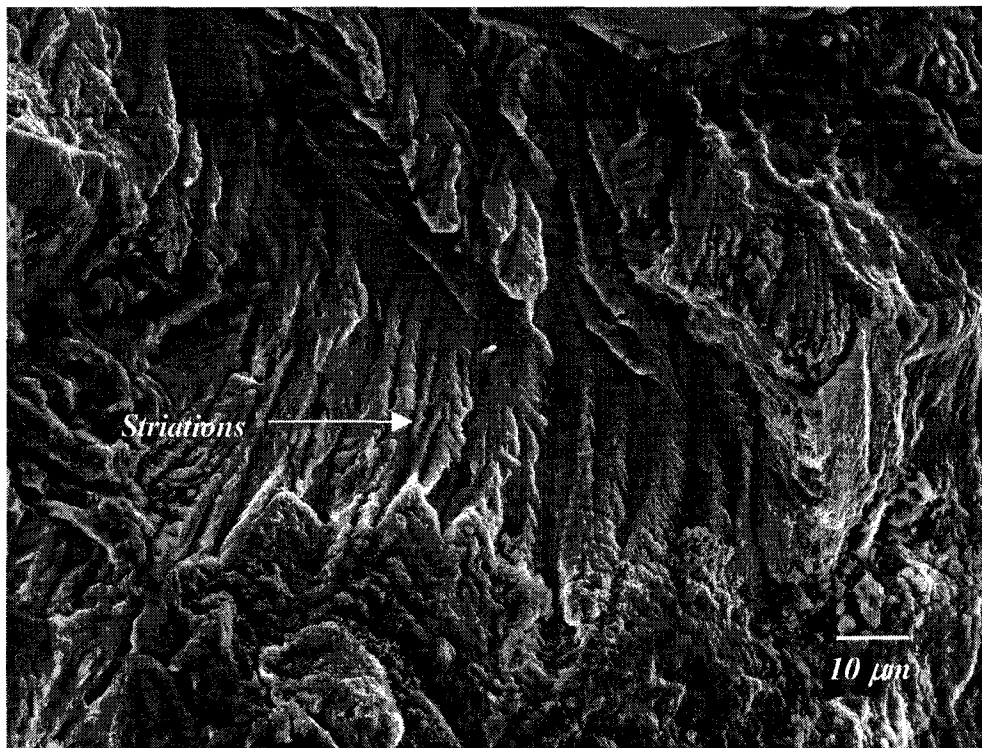


Figure 6.4.2s: (SEM/SE) micrograph showing striations (~ 3-5 μm spacing) within the fatigue fractured region.

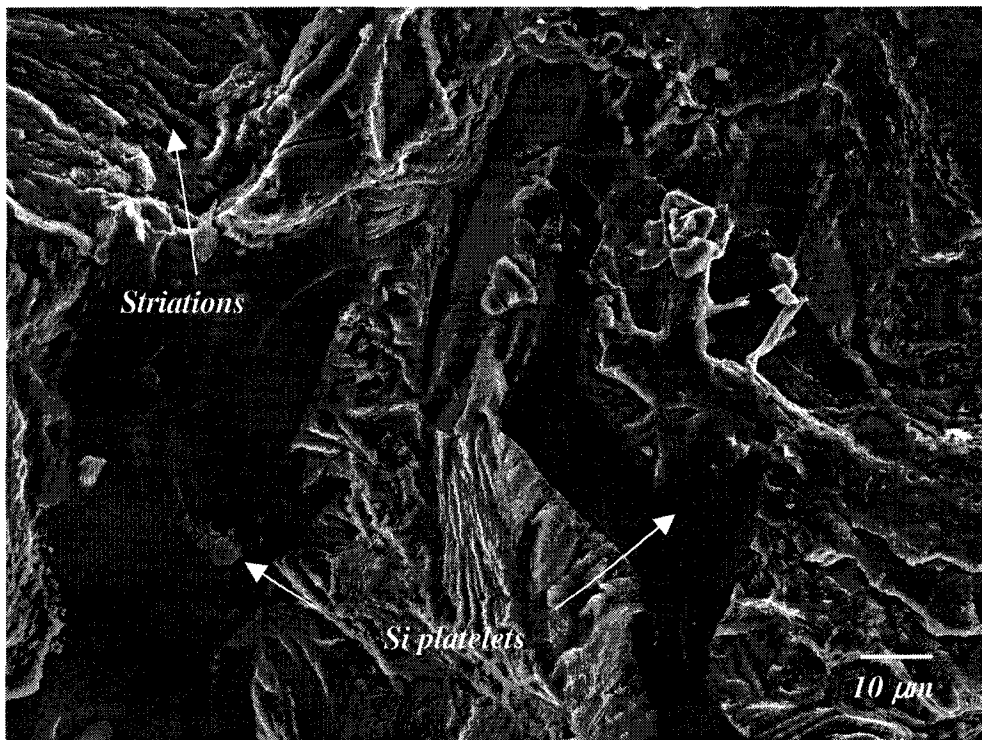


Figure 6.4.2t: (SEM/SE) micrograph showing Si platelets within the fatigue fractured region. Also seen in the micrograph are striations measuring approximately 5 μm.

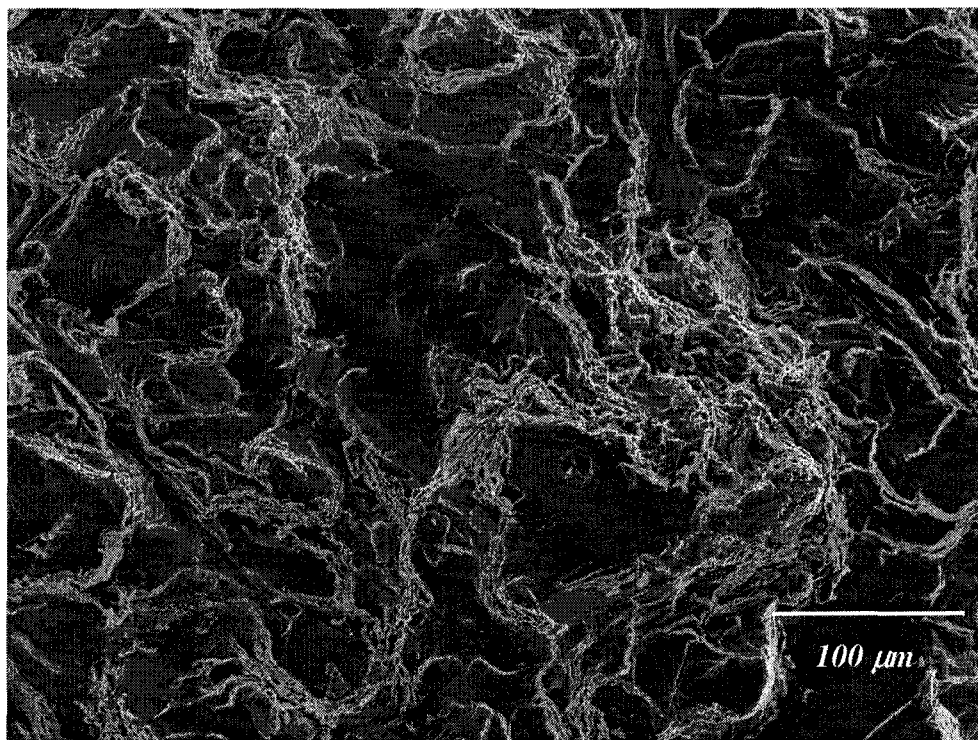


Figure 6.4.2u: (SEM/SE) micrograph showing the fast fracture (tensile overload) region just adjacent to the transition line seen in Figure 6.4.2q.

6.4.3 Relationship between Thermal Analysis & HCF Performance of the V8 Engine Block

Figures 6.4.2a through 6.4.2f indicate that the porosity near the polished surface of the test sample was the initiator of fatigue cracks. This observation agrees with numerous sources that stipulate the porosity to be the single largest contributor to the initiation of fatigue cracks in Al-Si-Cu casting alloys [18-28, 75-78, 81-85]. If the area fraction of pores or the maximum pore diameter were to go down the value of the mean HCF stress would increase.

Figure 6.4.3a shows the plot of the mean HCF stress found for the three conditions, as observed in Figure 6.4.1a, versus the mean area fraction of porosity. Figure 6.4.3b shows the plot of the mean HCF stress versus the mean maximum pore diameter. In both figures the mean area fraction, and the mean maximum pore size found are from bulkheads B, C, and D (the same bulkhead from which the fatigue test samples were cut). As seen in Figure 6.4.3a the higher the mean area fraction of pores, or in Figure 6.4.3b the larger the maximum pore size, the lower the mean HCF stress. The observations in Figure 6.4.3a and 6.4.3b are in agreement with the general observations reported by Boileau et al. [21, 81], Gall et al. [23], Caton et al. [22], Major [83], Zhang et al. [84], and Cooper et al. [85].

Figure 6.4.3c shows the partitioned temperature parameters $\Delta T^{\alpha\text{DEN}}_{\text{SRAN}}$, $\Delta T^{\text{Al-Si}}_{\text{SRAN}}$ and $\Delta T^{\text{Al-Fe-Mg-Si-Cu}}_{\text{SRAN}}$ measured for the Enviro-ALTAS test samples cast using the same sample chemistries that generated the mean HCF data. Figure 6.4.3d shows the corresponding partitioned fraction solid parameters $af^{\alpha\text{DEN}}$, $af^{\text{Al-Si}}$ and $af^{\text{Al-Fe-Mg-Si-Cu}}$ for each of the aforementioned alloy conditions. In Section 5.6 the volume fraction of the α -Al dendrites

($af^{\alpha\text{DEN}}$) phase partially contributes to the hydrostatic conditions which lead to stable pore nucleation and growth. The lower the volume fraction of α -Al dendrites (which contracts by 7% [59, 116]), and the larger the volume fraction of the Al-Si eutectic (which contracts by 3% [59]), the lower the severity of the pore growth. Having a lower volume fraction of dendrites and a higher volume fraction of the Al-Si eutectic reduces the number of oxides or other particles that can become active in pore nucleation (see Figure 5.6f, Chapter Five). This reduction in porosity invariably increases the mean stress at HCF.

The reason for the significant reduction in mean HCF stress for the Sr containing W319 alloy is due to the increase in porosity as shown in Figure 6.1.2b. However, this is not realized as readily from the partitioned temperature parameters or the partitioned fraction solid parameters, as is the case with the comparison between the W319 alloy, and the WA328 alloy. This observation points out the fundamental limitation of using thermal analysis for the assessment of pore nucleation kinetics and growth. The addition of Sr (In-mould or In-furnace) may add foreign particles, which would reduce the necessary driving force for pore nucleation [14, 15, 47, 55-58, 62, 73]. However, the increase in Sr based particles will not necessarily change the value of any temperature or fraction solid partitioned parameter.

Figure 6.4.3e shows a modified Gas-Shrinkage Map. In Figure 5.7f the value of $af_s^{\alpha\text{DEN}}$ for the W319 alloy containing 70 ppm Sr is included. Also included is the Sr based inclusions (labeled as Sr based nuclei 4 & 5), which were introduced into the melt during processing with a Sr containing master alloy. Figure 6.4.3e illustrates that while the Ps - Pg range for stable pore nucleation has not changed considerably in the W319 alloy, the density of the

particles which can nucleate pores has. Essentially the WA328 alloy (containing no master alloy) is able to nucleate pores from particles 1 and 2, the W319 alloy is able to nucleate pores from particles 1, 2 and 3 and the W319 alloy containing Sr can nucleate pores from particles 1, 2, 3, 4 and 5.

The addition of the Al-5Ti-1B grain refiner does not produce any detectable change on temperature or fraction solid partitioned parameters. The addition of a grain refiner has also added particles to the melt which has added more porosity, just as Sr additions add particles to the W319 alloy that also adds pores. This is illustrated in Figure 6.4.3f.

The role of Cu associated porosity is not a direct one and this was indicated in Section 5.9, Chapter Five. The value of the $af^{Al-Fe-Mg-Si-Cu}$ is not only small but the cooling rate for this phase, $CR^{Al-Fe-Mg-Si-Cu}_{SRAN}$, is very high. This is the reason why the phases associated with $af^{Al-Fe-Mg-Si-Cu}$ are very fine (see Section 5.1). A fine structure contributes less to crack growth and propagation [19, 21, 75, 76]. Cu will however extend the solidification range of the Al-Si eutectic reaction (ΔT^{Al-Si}_{SRAN}), which will in turn sustain the range in which the interdendritic liquid becomes hydrostatically stressed thereby activating pore nucleation. As indicated in Section 5.8.1 and confirmed through the work of Edwards et al. [59] Cu does not account for all of the observed porosity found in the cast structures of Al-Si-Cu alloys. Thus the solidification contraction of the Cu-based phases cannot be simply assumed to produce an increase in porosity.

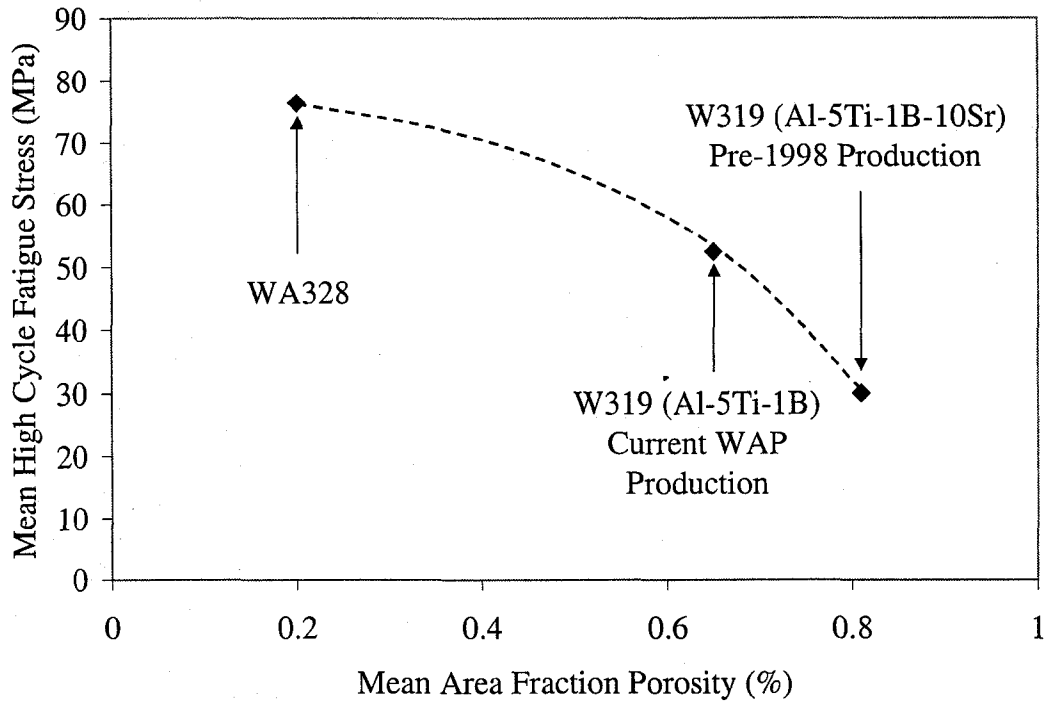


Figure 6.4.3a: The Mean Area Fraction Porosity of the five bulkhead sections plotted against the mean HCF for the three conditions shown in Figure 6.4.1a.

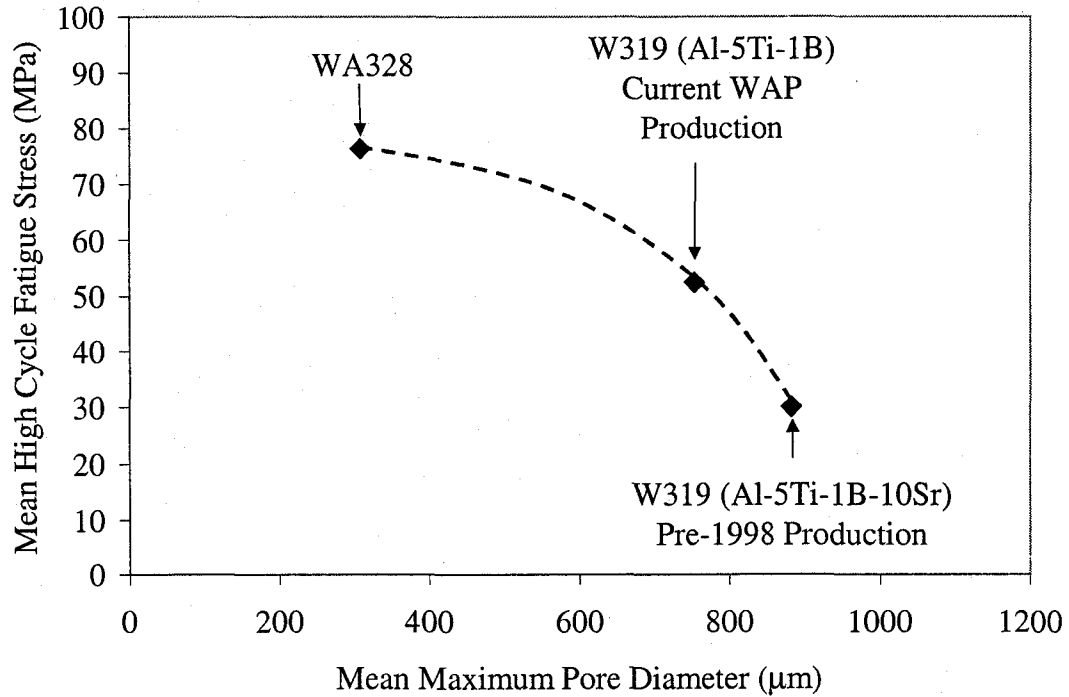


Figure 6.4.3b: The Maximum Pore Diameter of the five bulkhead sections plotted against the mean HCF for the three conditions shown in Figure 6.4.1a.

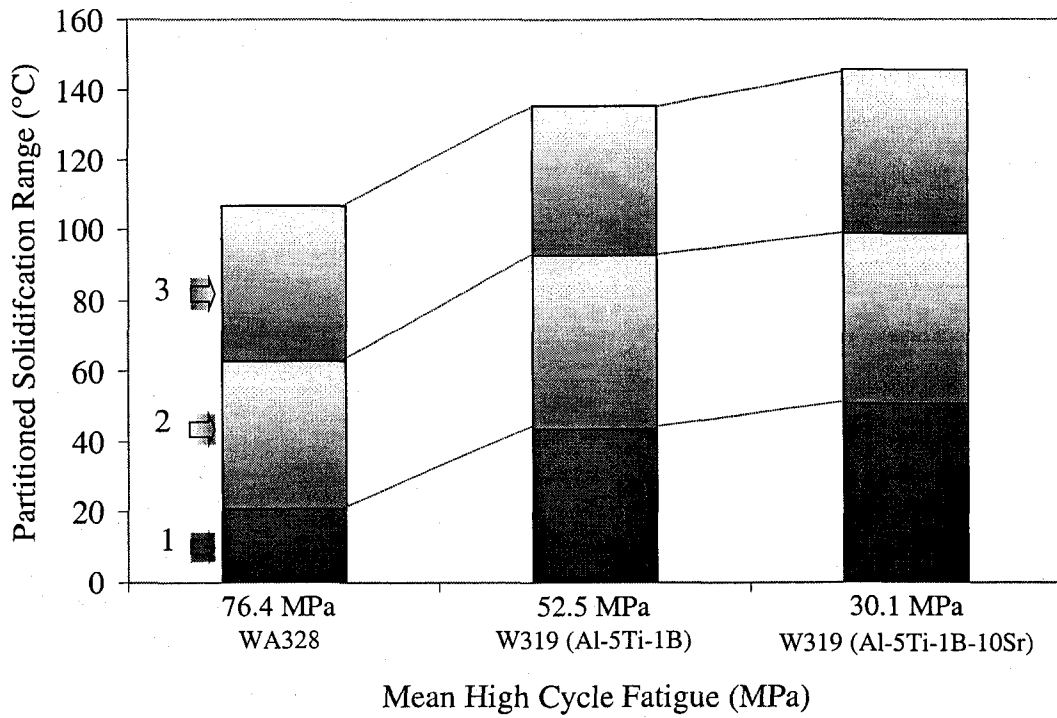


Figure 6.4.3c: Summary of the relationship between HCF and the value of the temperature partitioned parameters. 1) $\Delta T^{\alpha_{DEN}}_{SRAN}$, 2) ΔT^{Al-Si}_{SRAN} & 3) $\Delta T^{Al-Fe-Mg-Si-Cu}_{SRAN}$.

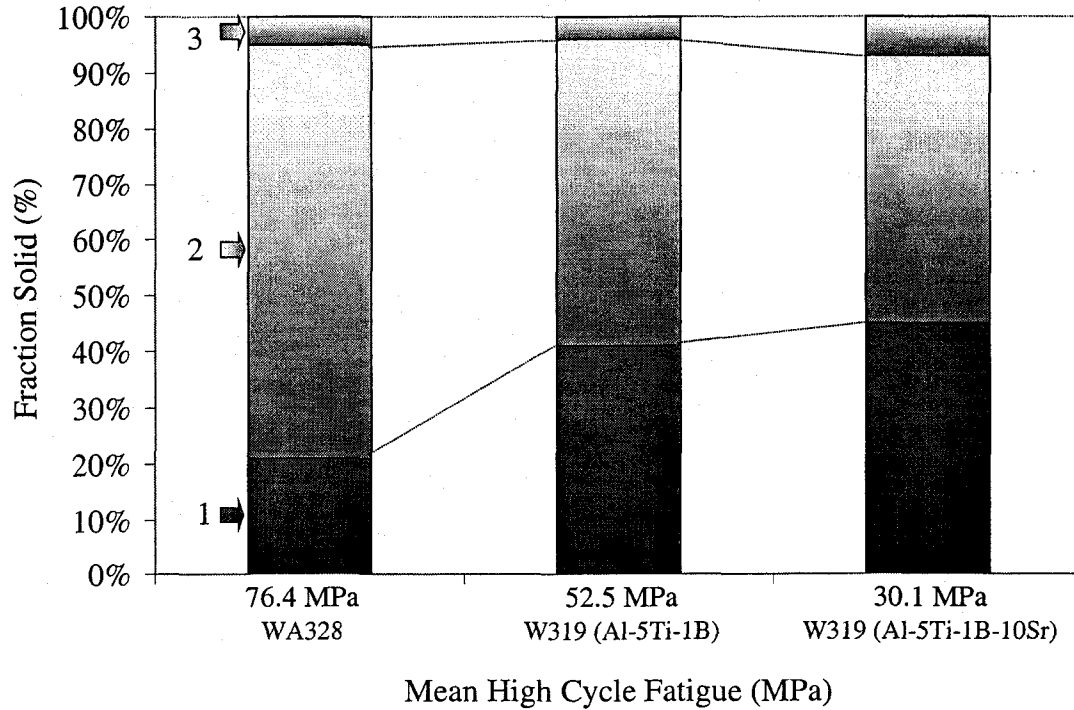


Figure 6.4.3d: Summary of the relationship between HCF and the value of the partitioned fraction solid parameters. 1) $af^{\alpha_{DEN}}$, 2) af^{Al-Si} & 3) $af^{Al-Fe-Mg-Si-Cu}$.

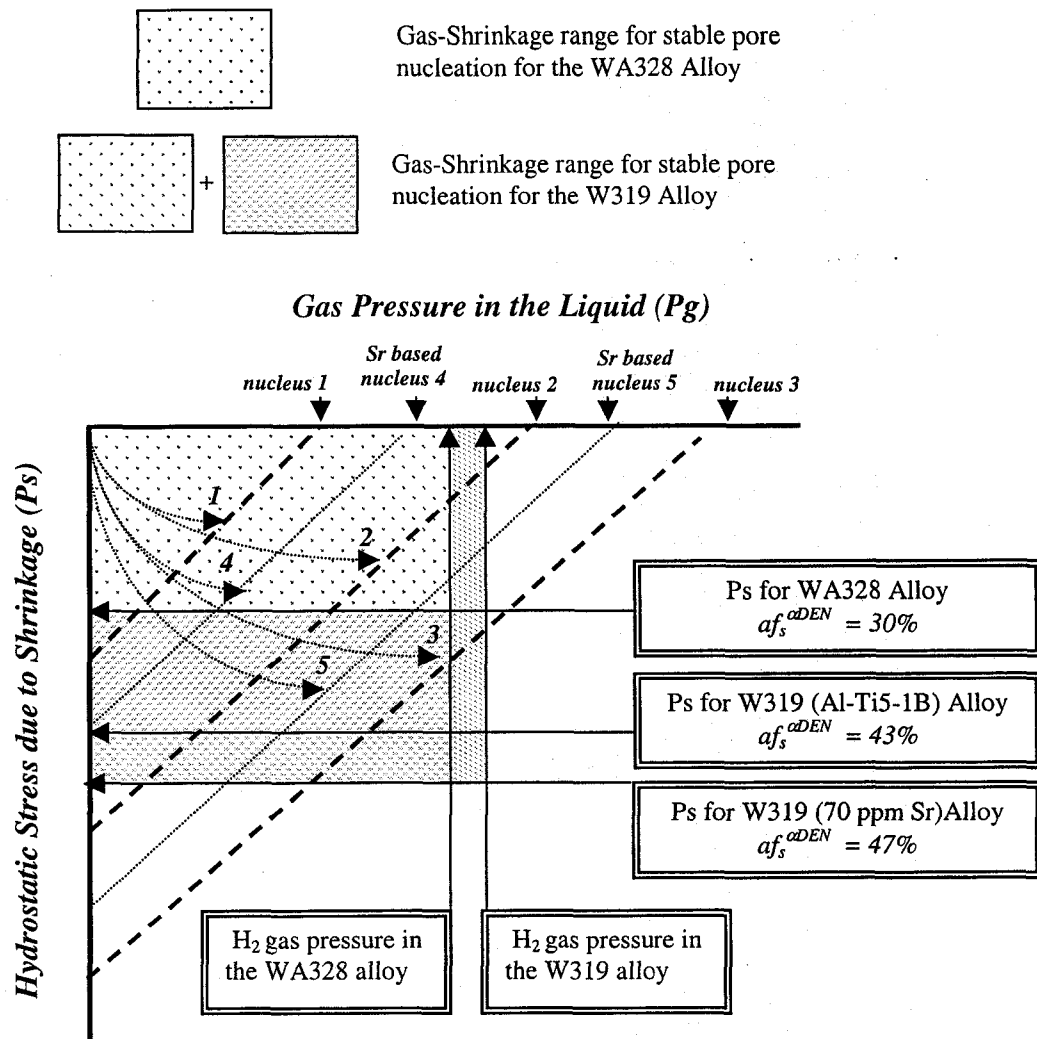


Figure 6.4.3e: The Gas-Shrinkage Map, modified from Figure 5.7f showing the effect of adding a master alloy, which in turn adds more Sr-based inclusions suitable to nucleate pores during solidification.

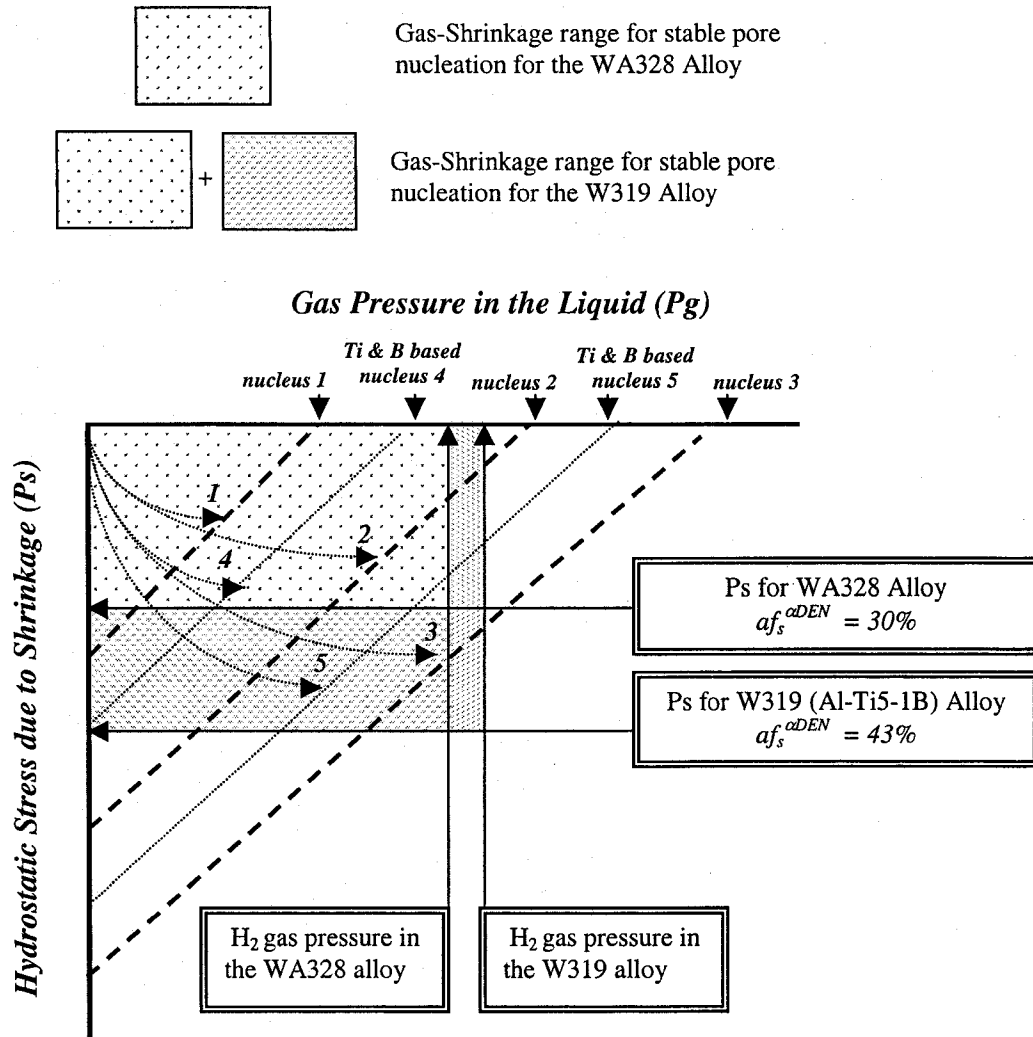


Figure 6.4.3f: The Gas-Shrinkage Map, modified from Figure 5.7f showing the effect of adding a master alloy, which in turn adds more Ti and/or B based inclusions suitable to nucleate pores during solidification.

6.5 Hot Tearing Susceptibility of the WA328 Alloy

Hot tearing susceptibility is a casting defect which occurs when a tear like defect manifests itself in a high fraction solid. In other words decohesion along the grain boundaries occurs just prior to complete solidification of the casting.

Hot tears are a cast part defect which requires corrective action. The risers studied in this dissertation (chemistries as outlined in Section 6.2) require no corrective action since they are a non-yielding component of the casting. They are however a part of the casting which experience a high degree of thermal stress and thus facilitate a higher driving force for hot tear nucleation. Thus, as investigated by Sadayappan et al. [122], the risers can be a useful tool in gauging hot tearing susceptibility.

The side view of risers B, C and D is shown in Figure 6.5a and reveals the condition of the side hot tears. In almost all cases hot tears were present along the sides of the 36 sets of V8 risers made with the W319 alloy. In all 43 cases in which V8 engine blocks were cast in the WA328 alloy no hot tears were present.

A second location where hot tearing was present for the W319 alloy casting but not for the WA328 alloy casting was on the archway of risers A, B, C and D in the W319 alloy. This is seen in Figure 6.5a for risers A and B. Hot tears along the side of the WA328 alloy risers, as seen in Figure 6.5a were present in all cases. However, they were not found in the archway of risers A, B, C and D. The cases in which hot tears were formed in the archway of these particular risers were relatively rare. In fact only 13 of the 215 risers (the number analyzed

for all 43 sets of V8 risers) had hot tears severe enough to be found in the archway. Observed once again in Figure 6.1.2e (section 6.1.2), the sectioned W319 alloy casting risers revealed these hot tears in the arched regions. This is the worst case situation where hot tears in the archway extend all the way to the sink itself. The hot tears seen in Figure 6.1.2e most likely nucleated in the sink and transected to the arch since the width of the hot tear seems larger in the sink than in the arch.

The hot tear would have transected to the arch since the arch has a high radius of curvature. This is analogous to the case where sharp corners of a casting reveal hot tears due to imposed thermal stress and can be corrected by replacement with fillets [3, 14]. The sides having the hot tears as seen in Figure 6.5a, are on the opposite side of the cut plane seen in Figure 6.1.2e.

The metallurgical analysis performed in *Chapter Five* yields some insight as to why the W319 alloy has a higher susceptibility to hot tear formation than the WA328 alloy. The presence of hot tears on the sides of the V8 risers B, C, and D, and in the less frequent case of hot tears in the archway of risers A, B, C, and D (cast in the W319 alloy) indicates that a high level of stress occurred during the later stages of solidification. The rectangular shaped riser of the V8 engine block, having edges which cool faster than the interior regions, permits the riser to sink by producing a roughly spherical or tear drop volume morphology as seen in Figure 6.1.2e. This results in a tall rim like shape on the top portion of the V8 riser, as seen in Figure 6.5b, which would be amenable to high stresses during the latter stages of

solidification. This high stress apparently produced a high enough driving force for nucleating tears.

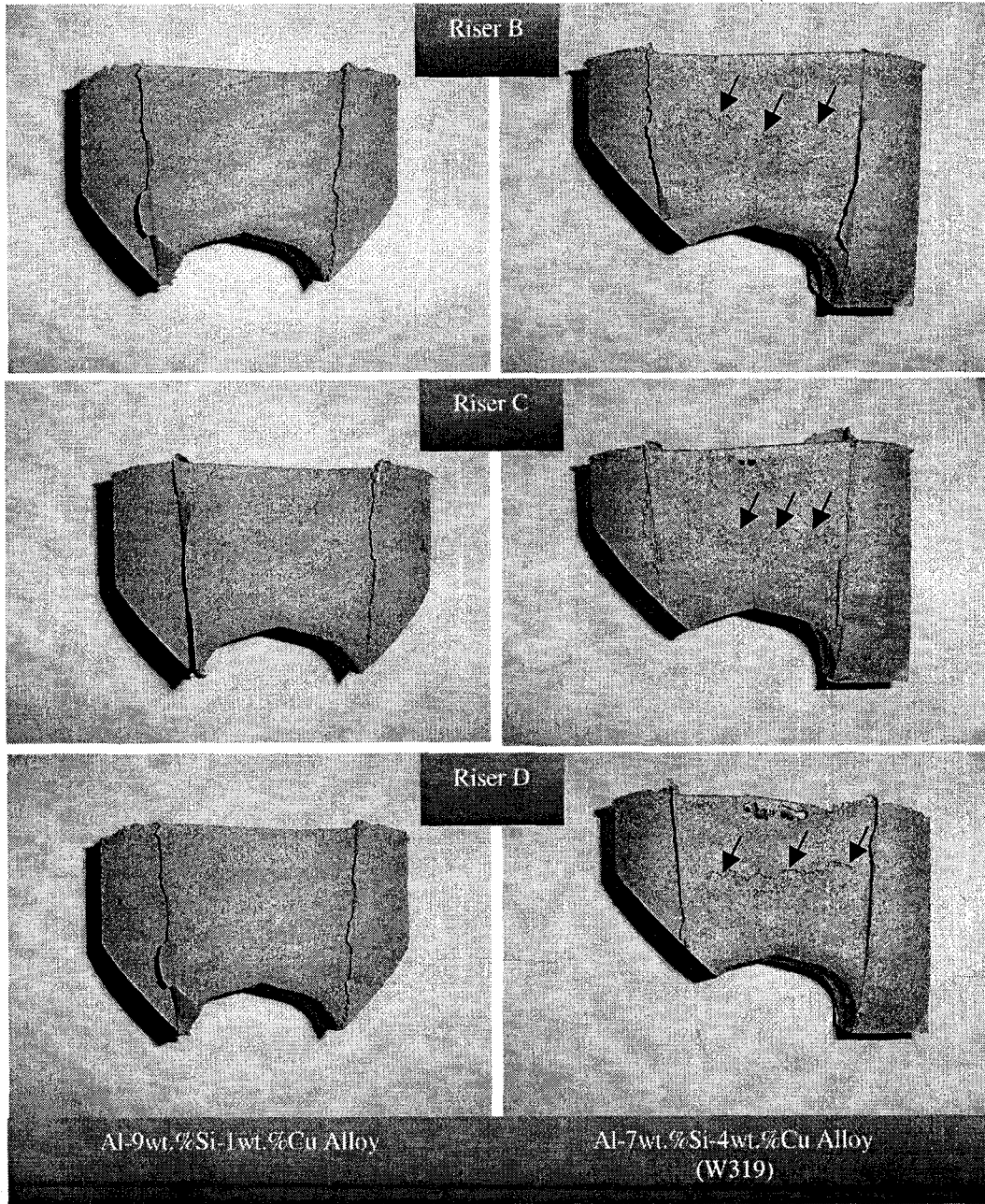


Figure 6.5a: The side view of risers B, C and D from the V8 engine block cast in the Al-9wt.%Si-1wt.%Cu alloy and the production W319 alloy. The hot tears were only evident in the W319 alloy and are indicated by arrows in the above pictures.

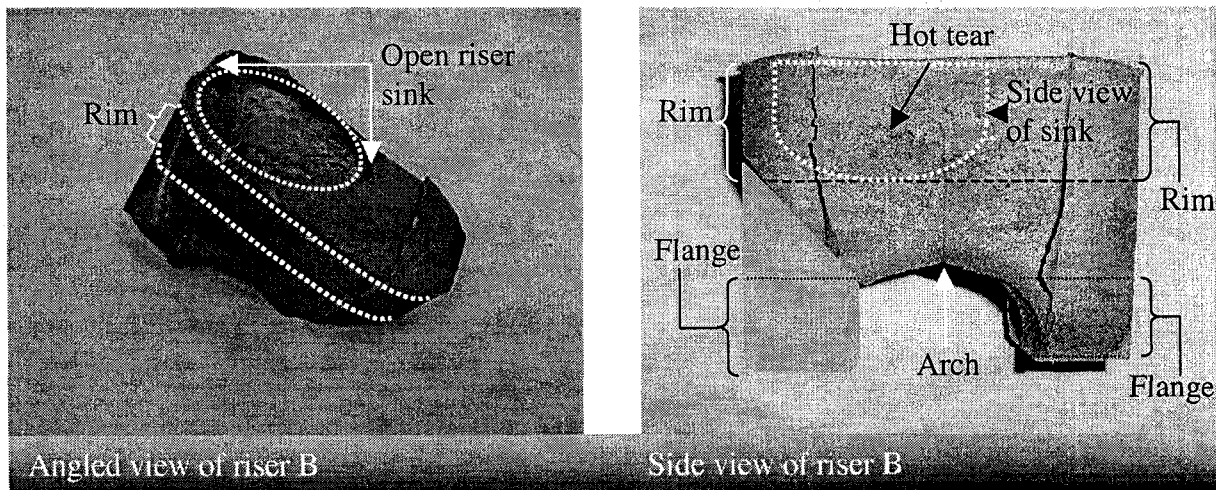


Figure 6.5b: Pictograph of an angle view and side view of riser B from a W319 V8 engine block illustrating the rim, flanging, arch and riser sink.

The addition of grain refiners to the V8 engine blocks cast using the W319 alloy did not show any observable reduction in the occurrence of hot tears. The master alloys used for this comparison were the Al-3Ti-1B and Al-1.7Ti-1.4B grain refiners from KB Alloys (Kentucky), the Al-5Ti-1B-10Sr modifier/grain refiner from KBM Affillips (Netherlands), and the Al-5Ti-1B and Al-8B from Metallurg (Brazil).

Given the similarity of volume sink magnitude for both alloys (seen in Figure 6.2.1f), one can also conclude that the intrinsic driving force conditions for hot tearing in the WA328 alloy is greatly inferior than for the W319 alloy (w/o grain refiner). This observation is based on the fact that all risers in the V8 engine block casting had no hot tears as found in the risers cast with the WA328 alloy. Thus a comparison of the two alloys, W319 (w/o grain refiner) and the WA328, for the same riser design (V8) illustrates the triggering effect of cast chemistry on the driving force for hot tear nucleation.

Hot tearing is a cast defect phenomena which occurs towards the later stages of cast solidification ($f_s \sim 95\%$ [14, 122]). The essential driving force for hot tear nucleation and growth stems from the fact that solidification contraction at angled regions of a casting can pull grain boundaries apart. In Section 5.7 it was alluded that the α -Al dendrites contract by 7% in volume, and the Al-Si eutectic contracts by 3% in volume. The WA328 alloy has approximately 50% less volume fraction of α -Al dendrites (based on $af_s^{\alpha\text{DEN}}$ calculation), and almost 25% more volume fraction of Al-Si eutectic structure (based on $af_s^{\text{Al-Si}}$ calculation). Thus we can assert that a greater stress is exerted at the grain boundary of the W319 alloy which is less than that for the WA328 alloy for the same given riser shape and the same magnitude of riser sink. See *Sections 5.6 and 5.7, Chapter Five*, for some important observations which could hypothetically explain the results outlined in Figure 6.5a.

Chapter Seven

Conclusions & Future Work

7.0 Conclusions

The main objective of this doctoral dissertation was to establish suitability, for engine block applications, the WA328 and WB328 alloys. The WA328 and WB328 alloys are less costly, and the WA328 alloy has a better fatigue strength than the existing W319 alloy. Conclusions will be broken down into 1: the Metallurgical Conclusions (Section 7.0.1) and 2: Casting Performance using the WA328 & WB328 Alloys (Section 7.0.2).

7.0.1 Metallurgical Conclusions

The principal metallurgical (previously unreported) findings of this work concerning the metallurgical characteristics of the WA328, WB328 and W319 alloys are:

- 1) The reduction in porosity seen in the bulkheads cast with the WA328 and WB328 alloys, compared to the same bulkheads cast with the W319 alloy. Three metallurgical observations were found to contribute to this reduction in porosity for the WA328 & WB328 alloys. They are:
 - a) The WA328 and WB328 alloys were shown to have a smaller volume fraction of α -

Al dendrites compared to the W319 alloy (difference in $af_s^{\alpha\text{DEN}}$ of 13%). In addition, the WA328 & WB328 alloys have a larger volume fraction of the Al-Si eutectic than for the W319 alloy (difference in $af_s^{\text{Al-Si}}$ of 17%). A smaller volume fraction of α -Al dendrites and a larger volume fraction of Al-Si eutectic favours a lower propensity towards pore nucleation and growth. To complement this result the Gas-Shrinkage Map was constructed to help illustrate the significance of how the volume of α -Al dendrites and Al-Si eutectic affects interdendritic hydrostatic stress development.

- b) The lower Cu content of the WA328 and WB328 alloys, compared with the W319 alloy, contributes to the further reduction in porosity by reducing the solidification range of the interdendritic regions during Al-Si eutectic growth ($\Delta T^{\text{Al-Si}}_{\text{SRAN}}$ by 15°C, see Figures 5.7a, 5.8.1a & 5.8.1b). In other words increasing $\Delta T^{\text{Al-Si}}_{\text{SRAN}}$ may extend the range needed for the expansion of growing pores and increase the hydrostatic stress during the later stages of Al-Si eutectic growth.
 - c) An additional method of assessing the propensity for pore formation of the alloys investigated in this dissertation was illustrated by plotting the cooling curve characteristic temperature data along an arbitrary temperature gradient (see Figures 5.9a and 5.9b). This method indicates the dominance the chemical composition has on controlling the feeding distances of a cast section. Reducing feeding distances enhance fluid flow to interdendritic regions under a growing hydrostatic stress.
- 2) Through partitioning the cooling rate for the W319 alloy, the WA328 alloy, and the

WB328 alloy for the solidification ranges of $\Delta T_{\text{SRAN}}^{\alpha\text{DEN}}$, $\Delta T_{\text{SRAN}}^{\text{Al-Si}}$ and $\Delta T_{\text{SRAN}}^{\text{Al-Fe-Mg-Si-Cu}}$, it was found that the cooling rate changes during each of these stages of solidification. The value of the cooling rate for the α -Al dendrites ($\text{CR}_{\text{SRAN}}^{\alpha\text{DEN}} \sim 0.38^\circ\text{C/sec}$), and for the Al-Si eutectic ($\text{CR}_{\text{SRAN}}^{\text{Al-Si}} \sim 0.50^\circ\text{C/sec}$) in all three alloys are similar. However, the cooling rate for the last pockets of liquid that solidifies in all three alloys increased by at least three times for all three alloys ($\text{CR}_{\text{SRAN}}^{\text{Al-Fe-Mg-Si-Cu}} \sim 1.4 - 1.7^\circ\text{C/sec}$). This presumably is the reason why the phases which grow at temperatures at or below $T_{\text{SRAN}}^{\text{Al-Fe-Mg-Si-Cu(one)}}$ exhibit a relatively fine microstructure. This observation was alluded to but not quantified by Mulazimoglu et al. [95].

- 3) Increasing the Fe content by 0.4wt.% in the WA328 alloy, to make the WB328 alloy, does not provide enhanced pore nucleation or pore growth kinetics. The $\text{Al}_{15}(\text{Fe,Mn,Cr})_3\text{Si}_2$ phase, which grows during the main Al-Si reaction, does not adversely retard interdendritic fluid flow in the way that Fe-based reactions involving the Al_5FeSi phase have been reported to do [31, 33, 37].
- 4) The growth of the $\text{Al}_{15}(\text{Fe,Mn,Cr})_3\text{Si}_2$ script phase forms through a binary-type eutectic reaction with Al. It has been reported [2, 67, 87, 88] that the $\text{Al}_{15}(\text{Fe,Mn,Cr})_3\text{Si}_2$ script forms through the tertiary eutectic with Al and Si. However, the reported literature [2, 67, 87, 88] did not use the method of quenching to verify the growth mechanism of the $\text{Al}_{15}(\text{Fe,Mn,Cr})_3\text{Si}_2$ script phase.
- 5) While the WA328 alloy has a smaller volume fraction of α -Al dendrites ($\text{af}_s^{\alpha\text{DEN}}$) when

compared to the W319 alloy (Conclusion 1), the kinetics of dendrite coarsening, as measured by the Secondary Dendrite Arm Spacing (λ_2), and the Dendrite Cell Size (DCSz) appears to be the same for both alloys during solidification. This is primarily due to the fact that Si and Cu have similar tendencies to segregate ($k = 0.13 - 0.17$), and that the total content of Si and Cu together is between 10 and 11 wt.% for the WA328 and W319 alloys. This observation was confirmed through the measurement of λ_2 in the V8 engine block bulkhead structure cast in the W319 and WA328 alloy (see Figure 6.2b).

- 6) The value of the λ_2 was found to have the same change in dimension as the Dendrite Cell Size (DCSz) for the W319, the WA328 and WB328 alloys (see Figure 5.4a). In other words both λ_2 and DCSz coarsen exponentially (at_f^n) where the value of a is 9.54 and 9.88, and the exponential n is 0.31 and 0.27 respectively for the measurement of λ_2 and DCSz. λ_2 is the normal method to indirectly assess dendrite coarsening while DCSz directly assesses dendrite coarsening.

- 7) Polyhedral phases of Si were observed in the cast structure of the W319 and the WA328 alloys quenched at the point of nucleation for the Al-Si eutectic ($T_{E,NUC}^{Al-Si}$). Polyhedral Si was not observed in the cast structures of test samples that were quenched before Al-Si nucleation (higher than $T_{E,NUC}^{Al-Si}$) or after Al-Si nucleation (lower than $T_{E,NUC}^{Al-Si}$). At $T_{E,NUC}^{Al-Si}$ the interdendritic liquid regions became enriched in Si, which, when quenched, are forced to form polyhedral Si as opposed to platelet Si (platelet Si needs more time for diffusion to establish the coupled growth process of the Al + Si polyphase interface). The non-equilibrium nucleation kinetics of the polyhedral Si was graphically explained

through the use of the skewed couple zone on the binary Al-Si phase diagram (see Figure 5.3.3a).

- 8) The WA328 and WB328 alloys were found to have the following sequence of phase reactions that span the entire range of the UMSA test samples solidification:

- a) $L \Rightarrow \alpha\text{-Al dendrites, also the Liquidus (591}^{\circ}\text{C for the WA328 Alloy, 593}^{\circ}\text{C for the WB328 Alloy)}$
- b) $L \Rightarrow \text{Al} + \text{Si (Eutectic) (571}^{\circ}\text{C)}$
- c) $L \Rightarrow \text{Al} + \text{Al}_{15}(\text{Fe, Cr, Mn})_3\text{Si}_2 \text{ (between 571}^{\circ}\text{C and the solidus (} \sim 480^{\circ}\text{))}$
- d) $L \Rightarrow \text{Al} + \text{Si} + \text{Mg}_2\text{Si} + \text{Al}_5\text{FeSi (527}^{\circ}\text{C for WA328 Alloy, 530}^{\circ}\text{C for the WB328 Alloy)}$
- e) $L \Rightarrow \text{Al} + \text{Si} + \text{Al}_2\text{Cu} + \text{Al}_5\text{FeSi} + \text{Al-Ni-Cu} + \text{Al-Ni-Fe} + \text{Pb particles (500}^{\circ}\text{C)}$
- f) $\text{Solidus (480}^{\circ}\text{C)}$

- 9) Using the UMSA apparatus it was found that the reduced Cu content of the WA328 and WB328 alloys decreases the liquidus as measured by the cooling curve by 10°C , and elevates the solidus as measured from the heating curve by 6°C . These cooling/heating curve results has a practical importance in the processing (*liquid metal holding temperatures and heat treat solution temperatures respectively*) of the WA328 and WB328 alloys.

7.0.2 Casting Performance using the WA328 & WB328 Alloys

This dissertation investigated the WA328 and the WB328 alloys suitability as a castable material. The WA328 and the WB328 alloys were cast into the V8 engine block mould and evaluated in terms of their compliance to the Ford Engineering Material Specification WSE-M2A151-A3. The findings are as follows:

- 1) The bulkhead sections of the V8 engine block cast in the WA328 and WB328 alloys showed a reduction in porosity (Area Fraction (by 70%), Mean Pore Diameter and Maximum Pore Size Found) when compared to the W319 alloy.
- 2) If grain refiner (Al-5Ti-1B) or Sr with grain refiner (Al-5Ti-1B-10Sr) is used, the porosity increases by nearly 50% in the V8 engine block bulkhead section over the non-master alloy condition. This porosity increase is presumably due to the combined effects of both slow cooling rate of the bulkhead section ($0.18^{\circ}\text{C}/\text{sec}$ to $0.22^{\circ}\text{C}/\text{sec}$) and the increase in particles having a pore nucleation potential (introduced via the in-mould master alloy). The V8 engine blocks cast with the W319 alloy having either the Al-5Ti-1B, or the Al-5Ti-1B-10Sr in-mould master alloys both had incidents where the maximum pore diameter found exceeded the $750\text{ }\mu\text{m}$ allowed by the WSE-M2A151-A3 specification.
- 3) The WA328 and WB328 alloys can improve the soundness of the cast component regions, which are prone to anomalously higher levels of porosity (i.e. hot spot region, or regions which suffer from inadequate feeding). This was the case with the improved

soundness of the V8 engine block's right side bulkhead section cast from the WA328 and WB328 alloys (see Figure 6.1.2h).

- 4) The staircase method for HCF analysis was used, and it was found that the WA328 cast alloy had a mean HCF strength of 76 ± 4.1 MPa, which is higher than the case for the V8 engine block with a chill (65 MPa), the V8 engine block in W319 alloy with in-mould grain refiner (53.8 ± 3.5 MPa), and the V8 engine block cast in the W319 alloy with 70 ppm Sr added in-furnace (31.5 ± 2.7 MPa). The Ford Engineering Material Specification WSE-M2A151-A3 requires that a non-chilled V8 engine block achieve 65 MPa for a mean HCF strength.
- 5) The mean HCF stress was related to the partitioned temperature parameters (Figure 6.4.3c) and the partitioned fraction solid parameters (Figure 6.4.3d). The lower value of $af_s^{\alpha DEN}$, larger value for af_s^{Al-Si} and a shorter solidification range (i.e. $\Delta T^{\alpha DEN}_{SRAN} + \Delta T^{Al-Si}_{SRAN}$) lead to a lower propensity for porosity formation and thus a higher mean HCF stress.
- 6) The elastic monotonic properties of the WA328 cast alloy and the W319 cast alloy are all essentially similar, while the plastic monotonic properties are superior for the W319 cast alloy. The similarity in elastic monotonic properties is due to the similarity of the α -Al dendrite condition (despite different heat treatments) while the difference in plastic properties is due to the increase in the volume fraction of the α -Al dendrite structure of the W319 castings.

- 7) The Vickers Microhardness of the dendritic matrix was slightly lower (by 15%) in the WA328 and the WB328 cast alloys when compared to the W319 alloy. However, the Brinell Hardness was essentially similar for all three cast alloys. The α -Al dendritic matrix was most likely softer in the WA328 and WB328 castings due to the reduced Cu content, the reduced heat treatment duration, or a combination of both. The increase in the volume of the Si phase in the WA328 and WB328 alloys likely compensated for the softer matrix, bringing the value of Brinell Hardness close to that of the W319 cast alloy.

- 8) The WA328 cast alloy had a lower susceptibility to hot tearing compared to the W319 alloy. This is most likely due to the considerable lower amount of volume contraction (since the W319 alloy has more α -Al dendrites), and the shorter freezing range (reduction of about 30°C).

7.1 Future Work

There are several other aspects of the WA328 alloy and the WB328 alloy that need to be investigated in order to optimize the alloys' casting and property characteristics.

- 1) Assessment of the mean HCF stress of the WB328 alloy needs to be completed. This alloy essentially has the same low level of porosity found in the WA328 alloy and thus should have similar HCF characteristics to the WA328 alloy. The WB328 alloy has a lower ingot cost than the WA328 alloy.
- 2) Machinability of the WB328 alloy should be investigated because machining operations can substantially raise the cost of the final cast product. The investigation of the machinability of the WA328 alloy cast in a Machinability Test Block (MTB) casting has already been undertaken. The WA328 MTB casting was poured from the same melting furnace that was used to cast the V8 engine blocks A1 through to A21 in this dissertation.
- 3) Optimization of the heat treatment for the WA328 and WB328 alloys is needed. As described in Chapter Five, the Mg_2Si phases do not dissolve during the solution treatment used in this dissertation ($505^{\circ}C$ for four hours). A method to achieve complete dissolution would be to implement a two-step solution treatment where a lower solution temperature (step one) would dissolve the Al_2Cu phase, then a higher solution temperature (step two) would dissolve the Mg_2Si phase. It is not known if the Al-Ni-Fe and Al-Ni-Cu phases would fully dissolve with the two-step solution treatment method.

- 4) Corrosion tests as outlined in the ASTM B557 standard should be used to assess the corrosion resistance of the WA328 and the WB328 cast alloys. It is speculated that due to the lower Cu content of the cast alloys, that the corrosion rates should be lower than for the W319 cast alloy.
- 5) Dynamometer testing of an assembled V8 engine block, using the WA328 alloy as the cast block material, is needed to further validate the this alloys' superior durability. Both the shape of the casting and the possibility that machined threads (i.e. M8 and M10) could expose pores that can ultimately contribute to fatigue failure, in addition to what is encountered with axial fatigue test samples.

References

- 1) G. F. Bourcier, J. Dickinson, J. Tessandori & D. Schiffer, Aluminum Recycling Casebook, *The Aluminum Association Inc.*, pp. 56, 1985.
- 2) J. E. Gruzleski & B. M. Closset, The Treatment of Liquid Aluminum-Silicon Alloys, *American Foundry Society, Inc.*, 1990, 256pp, 1990.
- 3) Aluminum Casting Technology, Revised by J. L. Jorstad, W. M. Rasmussen, Edited by D. L. Zalensas, 2nd Ed., *American Foundry Society, Inc.*, 201pp, 1993.
- 4) Q. S. Hamed, M. Dogan & R. Elliot, "The Dependence of Secondary Dendrite Arm Spacing on Solidification Conditions of Al-7Si-0.5Mg Alloys Treated with TiBAl and TiBAl/Sr Additions", *Cast Metals*, Vol. 6, Number 6, pp.47-53, 1993.
- 5) F. Paray & J. E. Gruzleski, "Microstructural-Mechanical Property Relationships in a 356 Alloy, Part 1: Microstructure" *Cast Metals*, Vol. 7, Number 3, pp. 29-40, 1994.
- 6) F. Paray & J. E. Gruzleski, "Microstructural-Mechanical Property Relationships in a 356 Alloy, Part 2: Mechanical Properties" *Cast Metals*, Vol. 7, Number 3, pp. 153-163, 1994.
- 7) M. B. Djurdjevic, J. H. Sokolowski and T. J. Stockwell, "Control of the Aluminum-Silicon Alloy Solidification Process Using Thermal Analysis", *Journal of Metallurgy*, Vol. 4, pp. 237-248, 1998.
- 8) M. Djurdjevic, T. Stockwell and J. H. Sokolowski, "The Effect of Strontium on the Microstructure of Aluminum-Silicon and Aluminum-Copper Eutectics in the

- 319 Alloy”, *International Journal of Cast Metals Research*, Vol. 12, pp. 67-73, 1997.
- 9) M. Djurdjevic, J. H. Sokolowski and H. Jiang, “On-Line Prediction of the Aluminum-Silicon Eutectic Modification Level Using Thermal Analysis”, *Materials Characterization*, Vol. 45, pp. 31-38, 2000.
 - 10) F. Paray & J. E. Gruzleski, “Factors to Consider in Modification”, *AFS Transactions*, Vol. 102, pp. 833-842, 1994.
 - 11) L. Backerud, G. Chai, J. Tamminen, “Solidification Characteristics of Aluminum Alloys” Vol. 2, Foundry Alloys, *AFS/Skanaluminum*, pp.255, 1990.
 - 12) F. Paray & J. E. Gruzleski, “Modification-A Parameter to Consider in the Heat Treatment of Al-Si Alloys”, *Cast Metals*, Vol. 5, Number 5, pp.187-197, 1993.
 - 13) J. Campbell, 10 Rules for Good Castings, *Modern Castings*, pp. 36-39, April, 1997.
 - 14) J. Campbell, *Castings*, Butterworth Heinemann, pp. 234, 1997.
 - 15) E. L. Rooy, “Mechanisms of Porosity Formation in Aluminum”, *Modern Casting*, pp. 34-36, Sept. 1992.
 - 16) P. S. Mohanty, F. H. Samuel, J. E. Gruzleski, “Experimental Study on Pore Nucleation by Inclusions in Aluminum Castings”, *AFS Transactions*, Vol. 105, pp. 555-564, 1995.
 - 17) Ford Motor Company Engineering Material Specification *WSE-M2A151-A2/A3/A4*, Revised by R. Thomas, 2002.

- 18) D. Rose, "Staircase Axial Fatigue Testing of Specimens from Main Bearing Saddles of 4.6L FWD Cylinder Block Castings with Residual Sr and Ti-B Additions", *Climax Research Services Report*, S-8413, June 9, 1999.
- 19) Q. Ren, "Optimization of the 3xx.x Aluminum Alloy Microstructures and Mechanical Properties for the Next Generation of Durable Engine Block", M.A.Sc. Thesis, *University of Windsor*, 2000.
- 20) R. Mackay, Q. Ren, J. H. Sokolowski and R. Hasenbusch, "Effect of Cu and Si on the Microstructural Properties in the 3xx.x Alloy Series", *NSERC/Ford-Nemak/University of Windsor Industrial Research Chair in Light Metals Casting Technology Confidential Report*, August, 2001.
- 21) J. M. Boileau, J. W. Zindel, & J. E. Allison, "The Effect of Solidification Time on The Mechanical Properties of A356-T6 Aluminum Alloys," SAE, Paper # 970019, SAE Warrendale, PA, 1997.
- 22) M. J. Caton, J. W. Jones, J. M. Boileau, & J. E. Allison, "The Effect of Solidification Rate on the Growth of Small Fatigue Cracks in a Cast 319-Type Aluminium Alloy", *Metallurgical & Materials Transactions A*, Vol. 30A, pp. 3055-3068, 1999.
- 23) K. Gall, N. Yang, M. Horstemeyer, D. L. McDowell, J. Fan, "The Debonding of Si Particles During the Fatigue of a Cast Al-Si Alloy", *Metallurgical & Materials Transactions A*, Vol. 30A, pp. 3079-3088, 1999.
- 24) G. E. Byczynski, "The Strength and Fatigue Performance of 319 Aluminum Alloy Castings", Ph.D. Dissertation, *University of Birmingham*, 2002.

- 25) C. E. Boyle, "Cast Aluminum Primary Aircraft Structure", Technical Report, Materials Laboratory, *Air Force Wright Aeronautical Laboratories*, pp. 641, August 1982.
- 26) N. R. Green, J. Campbell, "High Reliability Aluminum Alloy Castings", Presented at the 27th *ISATA Conference*, Aachen, Germany, (Oct-Nov 1994).
- 27) S. J. Mocarski, G. V. Scarich, K. C. Wu, "Effect of Hot Iso-static Pressure on Cast Aluminum Airframe Components", *AFS Transactions*, Vol. 99, pp. 77-81, 1991.
- 28) T. Reinhart, "Characterization of Alloy D357.0-T6", *Presented at AEROMAT*, Anaheim, California, USA, (June 1994).
- 29) D. P. Kanicki, "Changing Casting Demands Shape Ford's New Foundry", *Modern Casting*, pp.24-27, Sept. 1994.
- 30) J. H. Sokolowski, C. A. Kierkus, B. Brosnan and W. J. Evans, "Formation of Insoluble Ti (Al, Si)₃ Crystals in 356 Alloy Castings and Their Sedimentation in Foundry Equipment: Causes, Effects and Solutions", *AFS Transactions*, 2000, Vol. 21, 491-495.
- 31) Editor: J. R. Davis, " *ASM Specialty Handbook: Aluminum & Aluminum Alloys*", pp. 306, 1996.
- 32) P. N. Crepeau, "Effect of Iron in Al-Si Alloys: A Critical Review", *AFS Transactions*, Vol. 103, pp. 361-366, 1995.
- 33) G. Gustafsson, T. Thorvaldsson, & G. L. Dunlop, "The Influence of Fe and Cr on the Microstructure of Cast Al-Si-Mg Alloys", *Metallurgical Transactions A*, Vol. 17A, pp. 45-52, 1986.

- 34) G. K. Sigworth, S. Shivkumar, & D. Apelian, "The Influence of Molten Metal Processing on Mechanical Properties of Cast Al-Si-Mg Alloys", *AFS Transactions*, Vol. 98, pp. 811-823, 1989.
- 35) J. Gauthier, F. H. Samuel, "Tensile Properties and Fraction Behaviour of Solution Heat Treated 319.2 Al Automotive Alloy", *AFS Transactions*, Vol. 103, pp. 849-855, 1995.
- 36) G. Shabestari & J. E. Gruzleski, "Modification of Iron Intermetallics by Strontium in 413 Alloys", *AFS Transactions*, Vol. 103, pp. 285-293, 1995.
- 37) R. Mackay, "Quantification of Iron Content in Al-Si Alloys via Thermal Analysis", Masters Thesis, *McGill University*, 1995.
- 38) B. Xiufang, C. Guohua & M. Jiaji, "A Master Alloy for the Spheroidisation of Needle-From Iron Compounds in Aluminum Alloys" *Cast Metals*, Vol. 6, Number 3, pp. 159-161, 1993.
- 39) B. Xiufang, Z. Guohua, Z. Shengxu & M Jiaji, " The Spheroidisation of Needle-from Iron Compounds in an Al-Si Alloy", *Cast Metals*, Vol. 5, Number 1, pp.39-42, 1992.
- 40) J. Resch & E. Miguelucci, "The Effect of Increased Zinc Content on the Mechanical Properties of Aluminum 333.0", *AFS Transactions*, Vol. 94, pp. 17-20, 1986.
- 41) R. Mackay, and J. H. Sokolowski, "Investigation of Zn in an Al-Si Alloy", *40th Conference of Metallurgists (COM)*, Toronto, Ontario, August 26-29, 2001.
- 42) M. Djurdjevic, P. Gallo, W. Kasprzak, C. Kierkus, R. Mackay and J. H. Sokolowski, Contributors: R. Hasenbusch and W. MacKinnon (Ford CPDC),

- "The Hot Tearing and Cracking Problem in the Prototype CPDC 2.3L Engine Block Castings, 1st Progress Report", *NSERC/Ford-Nemak/University of Windsor Industrial Research Chair in Light Metals Casting Technology Confidential Report*, March 14, 2000.
- 43) J. Cho & C. R. Loper, "Limitation of Bismuth Residual in A356.2 Aluminum" *AFS Transactions*, Vol. 108, pp. 17-20, 2000.
- 44) L. Heusler, F. J. Feukus and M. O. Otte, "Alloy and Casting Process Optimisation for Engine Block Application", *AFS Transactions*, Vol. 109, pp. 215-223, 2001.
- 45) J. E. Gruzleski, "The Art and Science of Modification: 25 Years of Progress", *AFS Transactions*, Vol. 92, pp. 673-683, 1994.
- 46) M. Djurdjevic, W. Kasprzak, R. Mackay and J. H. Sokolowski, Contributors: P. Gallo and G. Pelayo, "The Effect of Pb and Sn on the Thermal Signature Behaviour of W319 Alloy Cooling Curves", *NSERC/Ford-Nemak/University of Windsor Industrial Research Chair in Light Metals Casting Technology Confidential Report*, February 9, 2001.
- 47) G. Pelayo, "Development of a Knowledge-Based System for the Control of 319-Al Melt Quality and Prediction of Casting Characteristics", M.A.Sc. Thesis, *University of Windsor*, 2001.
- 48) J. Taylor, D. Graham, M. Easton, "The Redistribution of Shrinkage Porosity in Eutectic Al-Si alloy by the Addition of Ti-B Grain Refiner", *AFS Castexpo 99*, St. Louis Missouri, March 1999.

- 49) W. Reif, "Melt Treatment Practice of Aluminum and Al-Alloys. Advanced Light Alloys and Composites", *NATO ASI Series. High Technology* - Vol. 59, pp. 191-200, 1994.
- 50) F.A Fasoyinu, D. Cousineau, P. Newcombe, T. Castles & M. Sahoo, "Grain Refinement of Aluminum Alloy 356.0 with Scandium, Zirconium, and a Combination of Titanium and Boron", *AFS Transactions*, Vol. 109, pp. 159-184, 2001.
- 51) M. Djurdjevic, J. H. Sokolowski, "Thermal Analysis as a Tool for Prediction of Hydrogen Solubility in the 319 Aluminum Alloy", *Proceedings of Sessions and Symposia sponsored by the Extraction and Processing Division (EPD) of TMS (The Minerals, Metals & Materials Society)*, 2002 TMS Annual Meeting, Seattle, Washington (USA), February 2002, 17-21, pp. 235-245.
- 52) M. B. Djurdjevic & J. H. Sokolowski, "Thermal Analysis as a Tool for Prediction of Hydrogen Solubility in the 319 Aluminum Alloy", *TMS 131st Annual International Meeting and Exhibition*, February 17-21, 2002, Seattle, Washington.
- 53) J. P. Anson & J.E. Gruzleski, "A Quantitative Evaluation of the Effect of Hydrogen Content on the Relative Amounts of Shrinkage and Gas Microporosity in a Cast Al-7% Si Foundry Alloy", *AFS Transactions*, Vol. 107, pp.456-467, 1999.
- 54) J.P. Anson, M. Stucky & J. Gruzleski, "Effect of Modification on the Growth of Microporosity during the Solidification of Aluminum-7%Silicon Foundry Alloy", *AFS Transactions*, Vol. 108, pp. 611-623, 2000.

-
- 55) R. Fuoco & E. Correa, "Characterization of Some Types of Oxide Inclusions in Aluminum Alloy Castings", *AFS Castexpo*, 1999.
- 56) W. LaOrchan, M. H. Mulazimoglu, X. G. Chen, & J. E. Gruzleski, "Quantified Reduced Pressure Test", *AFS Transactions*, Vol. 103, pp. 565-574, 1995.
- 57) P. N. Crepeau, "Molten Aluminum Contamination: Gas, Inclusions and Dross", *Molten Aluminum Processing*, AFS Special Meeting, Orlando, Florida, 1995.
- 58) D. Emadi, "Porosity Formation in Sr-Modified Al-Si Alloys", Ph.D. Thesis, *McGill University*, 1995.
- 59) G. A. Edwards, G. K. Sigworth, C. H. Cáceres, D. H. St. John, & J. Barresi, "Microporosity Formation in Al-Si-Cu-Mg Casting Alloys", *AFS Transactions*, Vol. 105, pp. 809-818, 1997.
- 60) C. H. Cáceres, M. B. Djurdjevic, T. J. Stockwell and J. H. Sokolowski, "Cast Al: The Effect of Cu Content on the Formation of Microporosity in Al-Si-Cu-Mg Casting Alloys", *Scripta Materialia*, Vol. 40 (5), pp. 631-637, 1999.
- 61) C. Dupuis, "An analysis of factors affecting the response of hydrogen determination techniques for aluminum alloys", *Light Metals*, pp. 1055-1067, 1992.
- 62) K. E. Tynelius, "A Parametric Study of The Evolution of Microporosity in Al-Si Foundry Alloys", Ph.D. Thesis, *Drexel University*, 1992.
- 63) A. K. Dahle, "Mushy Zone Properties and Castability of Aluminum Alloys", Ph.D. Thesis, *Norwegian University of Science and Technology*, 1996.
- 64) G. Chai, "Dendrite Coherency During Equiaxed Solidification in Aluminum Alloys", Ph.D. Thesis, *Stockholm University*, 1994.

-
- 65) N. L. M. Veldman, D. H. St. John, A. K. Dahle, L. Arnberg, "Dendrite Coherency Point: Determination and Significance", *Materials*, Vol. 15, pp. 20-22, 1996.
- 66) J. Tamminen, "Thermal Analysis for Investigation of Solidification Mechanisms in Metal Alloys", Ph.D. Thesis, Department of Structural Chemistry, Arrhenius Laboratory, *Stockholm University*, 1988.
- 67) L. Arnberg, L. Backerud and G. Chai, "Solidification characteristics of aluminum alloys", Volume 3: "Dendrite Coherency", *AFS/Skanaluminum*, pp. 247, 1996.
- 68) R. J. M. Kim, H. W. Kwon, & C. R. Loper, "Feeding Behavior of Modified and Unmodified Al-Si Alloys", *AFS Transactions*, Vol. 98, pp. 743-749, 1996.
- 69) H. Jiang, W. T. Kierkus and J. H. Sokolowski, "Determining Dendrite Coherency Point Characteristics of Al Alloys Using the Single-Thermocouple Technique", *AFS Transactions*, Vol. 107, pp. 169-172, 1999.
- 70) M. Djurdjevic, W. T. Kierkus, J. H. Sokolowski and W. Evans, "Detection of the Dendrite Coherency Point of the Al-3xx Series of Alloys Using the Single Sensor Thermal Analysis Technique", *40th Conference of Metallurgists (COM)*, Toronto, Ontario, August 26-29, 2001.
- 71) G. K. Sigworth, "Theoretical and Practical Aspects of the Modification of Al-Si Alloy", *AFS Transactions*, Vol. 90, pp. 7-16, 1983.
- 72) D. St. John, A. K. Dahle, M. A. Easton, J. E. C. Hutt & N. L. M. Veldman, "Solidification of Hypoeutectic Aluminum-Silicon Alloys", *Materials Form*, Vol. 23, pp. 137-152, 1999.
- 73) J. M. Kim, H. W. Kwon, & C. R. Loper, "Feeding Behavior of Modified and Unmodified Al-Si Alloys", *AFS Transactions*, Vol. 104, pp. 743-749, 1996.

-
- 74) H. Iwahori, H. Takamiya, K. Yonekura, Y. Yamamoto, and N. Nakamura, "Influence of Fe on Feedability of AC2B Alloy", *Imono*, Vol. 60, pp. 590-595, 1988.
- 75) R. Osborne & D. Penrod, "Design & Product Optimization for Cast Light Metals", USAMP-LMD 110 Project, *American Foundry Society Publication*, pp. 99, 2001.
- 76) M. Horstemeyer, D. McDowell & J. Fan, "From Atoms to Atoms, A New Design Paradigm Using Microstructure-Property Modelling", *Sandia National Laboratories Report* (SAND2000-8661), pp. 267, 2001.
- 77) J. G. Kaufman, "Properties of Aluminum Alloys, Tensile, Creep, and Fatigue Data at High & Low Temperatures", *ASM International Publications*, pp. 302, 1999
- 78) J. M. Boileau, P. C. Collins, and J. E. Allison, "The Effect of Solidification Time and Heat Treatment on Tensile and Fatigue Testing of a Cast 319 Aluminum Alloy," SAE, Paper # 980211, SAE Warrendale, PA, 1997.
- 79) W. Callister, "Materials Science & Engineering", *John Wiley & Sons Inc.*, pp.793, 1994.
- 80) R. W. Hertzberg, *Deformation and Fracture Mechanics of Engineering Materials*, *John Wiley & Sons Inc.*, pp. 786, 1996.
- 81) J. Boileau, "The Effect of Solidification Time on the Mechanical Properties of a Cast 319 Aluminum Alloy", Ph.D. Thesis, *Wayne State University*, May 2000.
- 82) T. Lee, J. F. Major, F. H. Samuel, "Fatigue Crack Growth and Fracture Behavior of Al-12Wt%Si-0.35Wt%Mg-(0-0.02)Wt%Sr Casting Alloys", *AFS Transactions*, Vol. 104, pp. 785-795, 1996.

-
- 83) J. F. Major, "Porosity Control and Fatigue Behaviour in A356-T61 Aluminum Alloy", *AFS Transactions*, Vol. 105, pp. 901-906, 1997.
- 84) B. Zhang, D. R. Poirier, & W. Chen, "Microstructural Effects on High Fatigue Crack Initiation in the A356.2 Casting Alloy". *Metallurgical & Materials Transactions A*, Vol. 30A, pp. 2659-2666, 1999.
- 85) M. J. Cooper, A. E. Neilson, "Casting Defects and the Fatigue Behaviour of an Aluminum Casting", *Fatigue and Fracture of Engineering Materials & Structures*, Vol. 13, pp. 213-227, 1990.
- 86) J. Goldstein, D. Newbury, P. Echlin, D. C. Joy, A. D. Roming, C. E. Lyman, C. Fiori & E. Lifshin, "Scanning Electron Microscopy & X-Ray Microanalysis", Plenum Press, pp. 820, 1992.
- 87) L. Bäckerud, E. Krol and T. Tamminen, "Solidification Characteristics of Aluminum Alloys", Volume 1: "Wrought Alloys", *AFS/Skanaluminum*, pp. 156, 1996.
- 88) M. H. Mulazimoglu, N. Tenekedjiev, B. M. Closset, J. E. Gruzleski, "Microstructure and Thermal Analysis of Strontium Treated Aluminum-Silicon Alloys", *American Foundry Society, Inc.*, pp.116, 1997.
- 89) M. Kasprzak, W. Kasprzak, W. T. Kierkus and J. H. Sokolowski, "Method and Apparatus for Universal Metallurgical Simulation and Analysis", Patent, PCT/CA02/01903, Canada, 2002.
- 90) R. Francis, W. T. Kierkus & J. H. Sokolowski, "Calibrations of the Thermocouples used for Thermal Analysis", *NSERC/Ford-Nemak/University of*

Windsor Industrial Research Chair in Light Metals Casting Technology Confidential Report, February 9, 2001.

- 91) M. Kasprzak, W. Kasprzak, C. A. Kierkus, W. T. Kierkus, J. H. Sokolowski and W. J. Evans, *The Structure and Matrix Microhardness of the 319 Aluminum Alloy After Isothermal Holding During the Solidification Process*, AFS Transactions, 15th Casting Congress, Dallas, USA, 2001.
- 92) M. Djurdjevic, W. Kasprzak, W. T. Kierkus, R. Mackay, A. Mitrasinovic and J. H. Sokolowski, "Thermal Analysis and Metallography of the Alcoa W319 Alloys (4J53 and B34055-2 Ingots)", *NSERC/Ford-Nemak/University of Windsor Industrial Research Chair in Light Metals Casting Technology Confidential Report*, May 1, 2003.
- 93) J. H. Sokolowski, X. C. Sun, D. O. Northwood, G. E. Byczynski, D. E. Penrod, R. Thomas and W. A. Esseltine, "The Removal of Copper-Phase Segregation and Subsequent Improvement in the Mechanical Properties of Casting 319 Aluminum Alloy by a Two-Step Heat Treatment.", *14th International Scientific Conference on Advanced Materials and Technologies*, Gliwice, Poland, published in the *Journal of Advanced Materials Processing Technology*, Vol. 53, Nos. 1-2, pp. 385-392, F. W. Travis ed., 1995.
- 94) J. H. Sokolowski and D. O. Northwood. "Improvement of the Mechanical Properties of a Cast 319 Aluminum Alloy Automotive Component using a 2-Step Solution Treatment", *Advances in Materials and Processing Technology*, Vol. 1, 81-88, *AMPT' 98 International Conference*, Kuala Lumpur, Malaysia, August, 1997.

-
- 95) M. H. Mulazimoglu, A. Zaluska, J. E. Gruzleski & F. Paray, "Electron Microscope Study of Al-Fe-Si Intermetallics in 6xxx.x Series Aluminum Alloys", *Metallurgical & Materials Transactions A*, Vol. 27A, pp. 929-936, 1996.
- 96) M. Djurdjevic, A. Mitrasinovic, J. H. Sokolowski & G. Byczynski, "Development of the Silicon Equivalent (Si_{EQ}) Algorithm and its Application for Calculation of the Characteristic Solidification Temperatures for the Multi-Component 3XX Series of Aluminum Alloys" *Submitted to the XV International Conference & Exposition for the Foundry Industry*, Monterrey, Mexico, October 2 to 4, 2003.
- 97) Ø. Nielsen & S. O. Olsen, "Assessment of Dendrite Morphology by Quenching from the Mushy State", *AFS Transactions*, Vol. 110, pp. 567-572, 2002.
- 98) J. W. Zindel, G. Goldewski & D. Donlon, "Microstructural Evolution of an 319 Alloy During Solidification", *Modeling of Casting, Welding & Advanced Solidification Processes VII*, TMS, San Diego, June 7-12, 1998.
- 99) W. Kurz, and D. J. Fisher, Fundamentals of Solidification, *Trans Tech Publications*, U.K.-USA, pp. 299, 1986.
- 100) M. C. Flemings, T. Z. Kattamis & B. P. Bardes, "Dendrite Arm Spacing in Aluminum Alloys", *AFS Transactions*, Vol. 99, pp. 501-506, 1991.
- 101) P. Kumar & J. L. Gaindhar, "DAS, Solidification Time and Mechanical Properties of Al-11%Si Alloy V-Processed Castings", *AFS Transactions*, Vol. 105, pp. 635-638, 1997.

-
- 102) T. Campanella, C. Charbon & M. Rappaz, "Microstructural Development in Copper-Based Alloys during Solidification", *7th European Conference on Advanced Materials and Processes, EUROMAT 2001*, Rimini, Italy, pp. 456-466, 2001.
- 103) P. N. Crepeau, W. T. Whited & M. E. Hoover, "Automatic Assessment of Dendrite Cell Spacing in Cast Aluminum Microstructures", *AFS Transactions*, Vol. 105, pp. 567-577, 1997.
- 104) J. E. Gruzleski, "Microstructure Development during Metalcasting", *American Foundrymen's Society, Inc.*, pp. 236, 2000
- 105) R. MacKay, M. Djurdjevic, J. H. Sokolowski and W. Evans, "Using the Method of an In-Situ Thermal Analysis Array in a Cast Section to Assess Riser Feeding Efficiency", accepted for the *TMS 131st Annual International Meeting and Exhibition*, Seattle, Washington, February 17-21, 2002.
- 106) R. MacKay, M. Djurdjevic and J. H. Sokolowski, "The Effect of Cooling Rate on the Fraction Solid of the Metallurgical Reactions in the 319 Alloy", *AFS Transactions*, Vol. 108, pp. 521-529, 2000.
- 107) S. Shivkumar, L. Wang, & B. Steenhof, "Relationship between Cast Chemistry & Cast Structure", *AFS Transactions*, Vol. 89, pp. 825-836, 1981.
- 108) M. Kiuchi, S. Sugiyama, "A New Method to Detect Solid Fractions of Mushy/Semi-Solid Metals & Alloys", *Annals of the CIRP*, Vol. 43, pp. 271-274, 1994.

-
- 109) A. M. de Figueredo, Y. Sumartha & M. C. Flemings, "Measurement and Calculation of Solid Fraction in Quenched Semi-solid Melts of Rheocast Aluminum Alloy A357" *Light Metals*, pp. 1,103-1,106, 1998.
- 110) H. Liu & J. H. Sokolowski, "Effects of Hydrogen on Aluminum and its Alloys", *NSERC/Ford/University of Windsor Industrial Research Chair in Light Metals Casting Technology*, June 2, 1997.
- 111) AISCAN Model F, Operating Manual, Version 1.3, February 1997.
- 112) L. Liu, A. M. Samuel, F. H. Samuel, H. W. Doty, and S. Valtierra, "Role of Strontium Oxide on Porosity Formation in Al-Si Casting Alloys, *AFS Transactions*, 2002, Vol. 104, pp. 561-577.
- 113) D. Cusinato, "DOE on the Grain Refiner and Closing the Hone Window Clearance of the 4.6L Engine Blocks" *Special Casting Run #374*, June 2002.
- 114) Rose, D., "Staircase Axial Fatigue Testing of Specimens from Main Bearing Saddles of 4.6L FWD Cylinder Block Castings", *Climax Research Services Report*, S-7609, July 29, 1998.
- 115) J. Chen, "The Effect of Novel Solution Treatment during the Solidification Process on the Structure and Mechanical Properties of the W319 Alloy", M.A.Sc. Thesis, University of Windsor, 2003
- 116) ASM Handbook Vol. 3: Alloy Phase Diagrams, The Materials Information Society, 1992.
- 117) H. de la Sablonniere and F. H. Samuel, "Solution Treatment of 319 Aluminum Alloy Containing ~ 0.50% Mg, Part 1 – Solidification and Tensile Properties", *Int. J. Cast Metals Res.*, 1996, Vol. 9, 195-211.

-
- 118) H. de la Sablonniere and F. H. Samuel, "Solution Treatment of 319 Aluminum Alloy Containing ~ 0.50% Mg, Part 2 – Microstructure and Fractography", *Int. J. Cast Metals Res.*, 1996, Vol. 9, 213-225.
- 119) Q. G. Wang, C. H. Cáceres, & J. H. Griffiths, "Transgranular and Intregranular Fracture in Al-Si-Mg Casting Alloys", 9th International Conference on Fracture in Sydney, April 1997.
- 120) J. Yao, G. Edwards, & D. Graham, "Precipitation and Age Hardening in Al-Si-Cu-Mg-Fe Casting Alloys", *Material Science Forum*, Vol. 217-222, pp. 777-782, (1996).
- 121) D. Cusinato, Personal Communication, 2003.
- 122) M. Sadayappan & M. Sahoo, "Influence of Alloying Elements and Melt Treatment on the Hot Tearing Resistance of Aluminum Alloy A210", 40th Conference of metallurgist (COM), Toronto, Ontario, pp. 455-466, August 26-29, 2001.
- 123) M. B. Djurdjevic, W. Kasprzak, C. A. Kierkus, W. T. Kierkus and J. H. Sokolowski, "Quantification of Cu Enriched Phases in Synthetic 3XX Aluminum Alloys Using Thermal Anaylsis", *AFS Transactions*, 2001, Vol. 103, pp. 455-467.

Appendix A

A.1 Introduction

This appendix will describe the interpretative methodology of the cooling curve and the fraction solid curve. This appendix will outline the method at which characteristic temperature and fraction solid points are determined through the use of algorithms. Once a characteristic temperature and characteristic fraction solid value are determined, then partitioned temperature and fraction solid parameters can be measured.

A.1.1 Characteristic Point Determination

Figures A.1a, A.1b and A.1c show the cooling curve and associated first derivative (dT/dt) for the primary α -Al dendritic phase, the Al-Si eutectic phase and the post eutectic (Fe, Mg, Si & Cu-rich) phases respectively. With each figure includes an associated table which lists the characteristic temperature, metallurgical name, algorithm method and the metallurgical definition. The common method (algorithm procedure) for characteristic temperature determination is the intersection of two sloping lines. This is done for $T^{\alpha\text{DEN}}_{\text{NUC}}$, $T^{\text{Al-Si}}_{\text{E,NUC}}$, $T^{\text{Al-Fe-Mg-Si-Cu(one)}}_{\text{E,NUC}}$, $T^{\text{Al-Fe-Mg-Si-Cu(two)}}_{\text{E,NUC}}$, $T^{\text{Al-Fe-Mg-Si-Cu(three)}}_{\text{E,NUC}}$ and T_{SOL} . Only $T^{\alpha\text{DEN}}_{\text{MIN}}$, $T^{\alpha\text{DEN}}_{\text{G}}$, $T^{\text{Al-Si}}_{\text{E,MIN}}$ and $T^{\text{Al-Si}}_{\text{E,G}}$ and is determined from the point at which the derivative curve intersects of the first derivative zero-line.

The aforementioned algorithms are implemented within the ALTAS software with the exception of $T_{E,NUC}^{Al-Fe-Mg-Si-Cu(two)}$, $T_{E,NUC}^{Al-Fe-Mg-Si-Cu(three)}$ which must be done manually since multiple peaks are not commonly seen on all cooling curves.

For the W319 alloy up to three distinct peaks associated with the Cu based reactions can be seen on the cooling curve. However in many cases a fourth peak can be seen which is convoluted with one of the original three peaks. Methods for Cu peak convolution have been addressed by the IRC [123]. Evidence of a convoluted peak is seen in Figure A.1c. However for both the WA328 and WB328 alloys, from what could be observed in Section 5.2.1, only two non-convoluted peaks (*presumed to be*) are seen. Thus the need for the Cu peak deconvolution is not necessary.

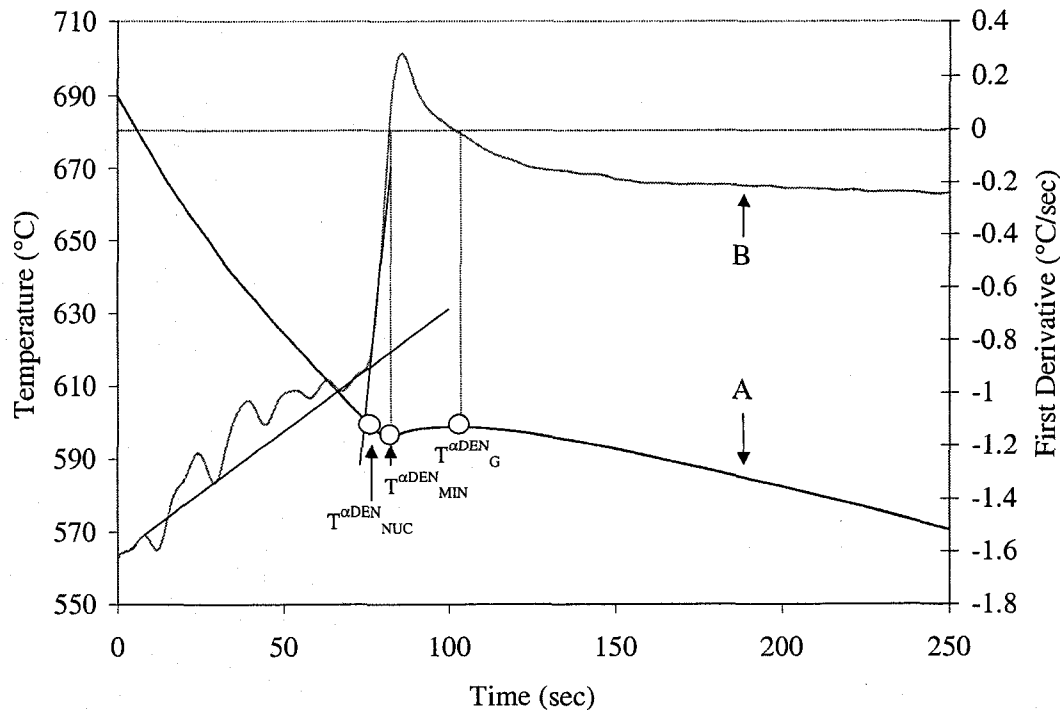


Figure A.1a: Method of determining $T^{\alpha\text{DEN}}_{\text{NUC}}$ (Liquidus), $T^{\alpha\text{DEN}}_{\text{MIN}}$ and $T^{\alpha\text{DEN}}_{\text{G}}$ from the first derivative curve. **A** is the cooling curve and **B** is the first derivative (dT/dt).

Table A.1a: Summary of the characteristic temperature points associated with primary α -Al dendrite nucleation and growth.

Symbol	Name	Detection Algorithm	Definition
$T^{\alpha\text{DEN}}_{\text{NUC}}$	α -Al dendrite nucleation temperature (Liquidus)	This corresponds to the intersection of two local sloped lines (labeled as 1 & 2) as seen in Figure A.1a.	This is the point at which primary α -Al dendrites begin to solidify from the melt.
$T^{\alpha\text{DEN}}_{\text{MIN}}$	α -Al dendrite undercooling temperature.	It is determined as the point at which the first derivative intersects the zero line ($dT/dt=0$). This is shown in Figure A.1a.	At this point, the nucleated dendrites have grown to such an extent that the latent heat liberated balances the heat extracted from the sample. After this point the temperature of the melt increases to the steady state growth temperature.
$T^{\alpha\text{DEN}}_{\text{G}}$	α -Al dendrite growth temperature (recalescence)	It corresponds to the second zero point on the first derivative curve following the start of nucleation ($dT/dt=0$). This is shown in Figure A.1a.	The maximum point of recalescence.

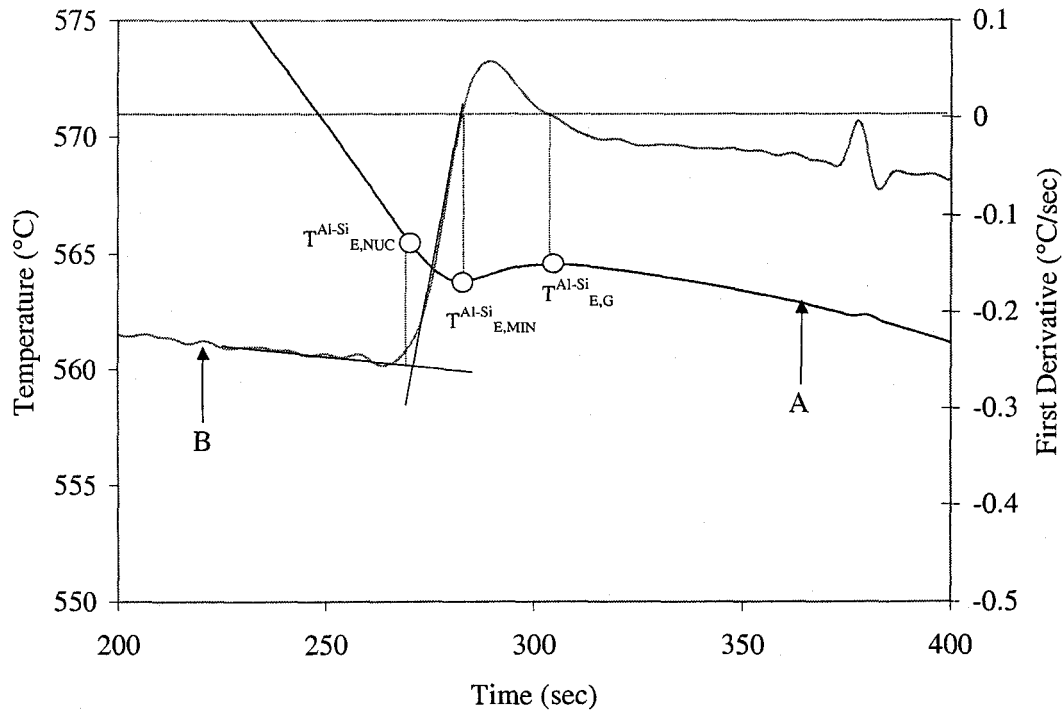


Figure A.1b: Method of determining $T_{Al-Si}^{E,NUC}$, $T_{Al-Si}^{E,MIN}$ and $T_{Al-Si}^{E,G}$ from the first derivative curve. **A** is the cooling curve and **B** is the first derivative (dT/dt).

Table A.1b: Summary of the characteristic temperature points associated with primary α -Al dendrite nucleation and growth.

Symbol	Name	Detection Algorithm	Definition
$T_{Al-Si}^{E,NUC}$	Al-Si eutectic nucleation temperature.	This corresponds to the intersection of two sloped lines (1 and 2).	This is the point at which primary Al-Si cells begin to solidify from the interdendritic melt
$T_{Al-Si}^{E,MIN}$	Al-Si minimum eutectic temperature	This point corresponds to a the first intersection of the zero line following the Al-Si nucleation temperature ($dT/dt=0$).	This temperature represents the first point at which the latent heat generated due to eutectic growth equals the heat loss from the test sample.
$T_{Al-Si}^{E,G}$	Al-Si eutectic growth temperature (sometimes referred to as the eutectic plateau temperature).	This point corresponds to the second zero intersection of the first derivative curve following the Al-Si nucleation temperature ($dT/dt=0$).	This point represents the temperature at which considerable eutectic growth occurs.

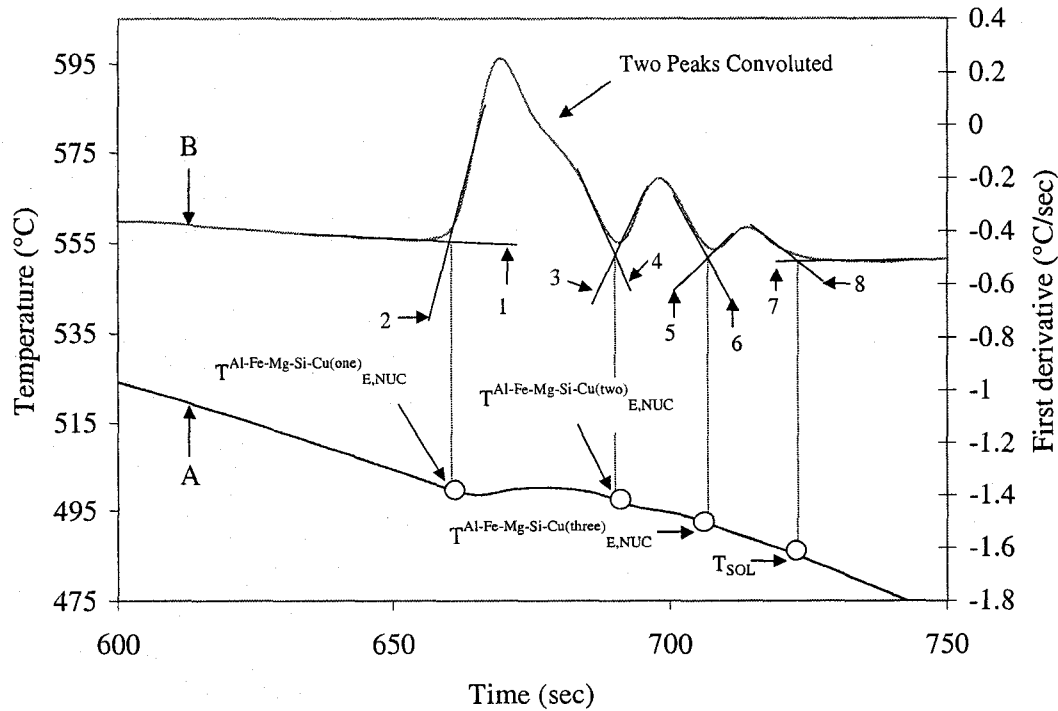


Figure A.1c: Method of determining $T_{\text{Al-Fe-Mg-Si-Cu(one)}_{\text{NUC}}}$, $T_{\text{Al-Fe-Mg-Si-Cu(two)}_{\text{NUC}}}$ and $T_{\text{Al-Fe-Mg-Si-Cu(three)}_{\text{NUC}}}$ from the first derivative curve. A is the cooling curve and B is the first derivative (dT/dt).

Table A.1c: Summary of the characteristic temperature points associated with the nucleation of the post eutectic type reactions.

Symbol	Name	Detection Algorithm	Definition
$T_{\text{Al-Mg-Fe-Si-Cu(one)}_{\text{E,NUC}}}$	First Cu rich phase nucleation.	This corresponds to the intersection of two local sloped lines (labeled as 1 & 2) as seen in Figure A.1c.	Temperature at which the first multi-phase nucleation occurs.
$T_{\text{Al-Mg-Fe-Si-Cu(two)}_{\text{E,NUC}}}$	second Cu rich based phase nucleation	This corresponds to the intersection of two local sloped lines (labeled as 3 & 4) as seen in Figure A.1c.	Temperature at which the second multi-phase nucleation occurs.
$T_{\text{Al-Mg-Fe-Si-Cu(three)}_{\text{E,NUC}}}$	Third Cu rich based phase nucleation	This corresponds to the intersection of two local sloped lines (labeled as 5 & 6) as seen in Figure A.1c.	Temperature at which the third multi-phase nucleation occurs. (Note: this third peak is not observed in the WA328 & WB328 alloy).
T_{SOL}	Solidus	This corresponds to the intersection of two local sloped lines (labeled as 7 & 8) as seen in Figure A.1c.	Temperature at which full solidification occurs.

A.1.2 ALTAS Partitioned Parameters Characterizing the Solidification Range Associated with Primary α -Al Dendritic Solidification

An example of the region where primary α -Al dendritic solidification occurs on the cooling curve and fraction solid plot (generated by the ALTAS software) is shown in Figure A.1.2a. The most commonly analyzed parameter during α -Al dendritic solidification is $af_s^{\alpha\text{DEN}}$ which was investigated in *Section 5.7, Chapter Five*. The temperature and time analogs to this parameter are $\Delta T^{\alpha\text{DEN}}_{\text{SRAN}}$ and $\Delta t^{\alpha\text{DEN}}_{\text{SRAN}}$, respectively.

A schematic of the thermal analysis test sample structure forming along with the actual temperature, time and fraction solid characteristic points that serve as the start and end of the primary interdendritic solidification process are given in Figures A.1.2b.

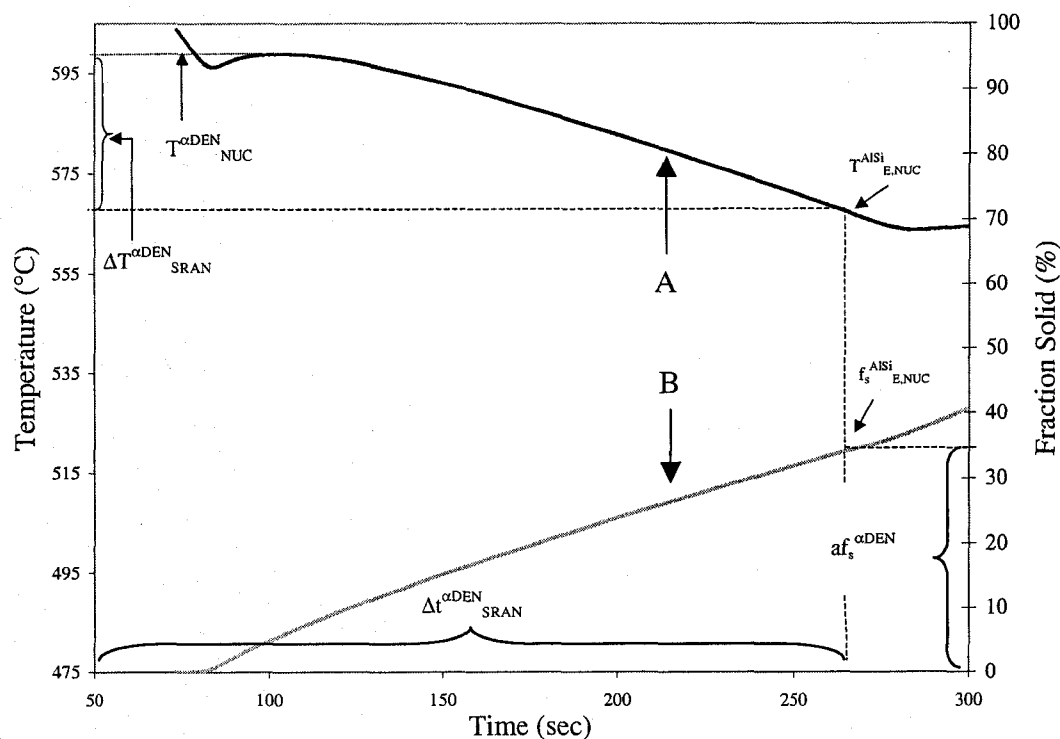


Figure A.1.2a: Cooling curve and calculated fraction solid curve between primary α -dendritic nucleation and the start of the Al-Si eutectic. **A** is the cooling curve and **B** is the first derivative (dT/dt).

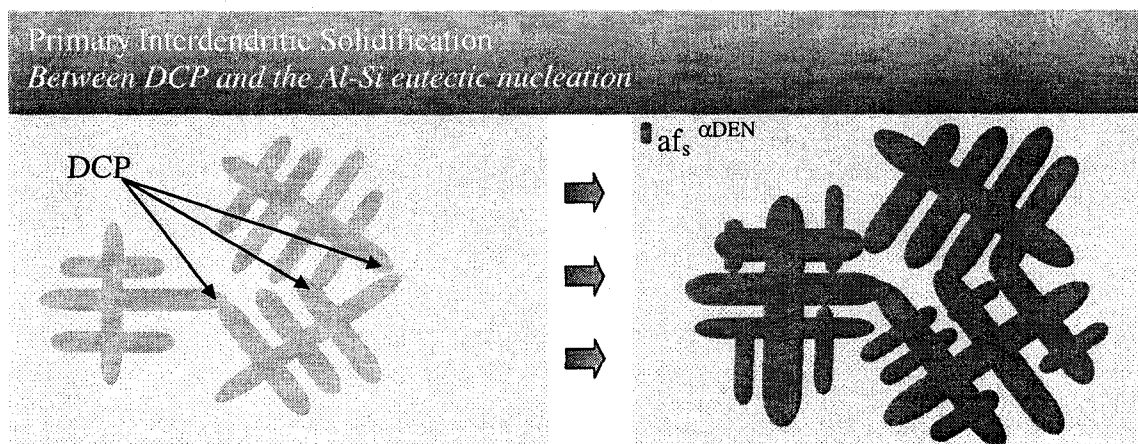


Figure A.1.2b: Schematic of the TA test sample structure during primary dendritic solidification. The temperature and time analogs are $\Delta T^{\alpha DEN}_{SRAN}$ and $\Delta t^{\alpha DEN}_{SRAN}$.

A.1.3 ALTAS Partitioned Parameters Characterizing the Solidification Range Associated with Al-Si Eutectic Solidification

Figure A.1.3a shows the calculated fraction solid at $f_s^{\text{Al-Si}}_{\text{E,NUC}}$, $f_s^{\text{Al-Si}}_{\text{E,MIN}}$, $f_s^{\text{Al-Si}}_{\text{E,G}}$ and $f_s^{\text{Al-Fe-Mg-Si-Cu(one)}}_{\text{E,NUC}}$ along with $T^{\text{Al-Si}}_{\text{E,MIN}}$, $T^{\text{Al-Si}}_{\text{E,NUC}}$, and $T^{\text{Al-Si}}_{\text{E,G}}$. These characteristic temperature and fraction solid points are associated with the undercooling (relative driving force) event for Al-Si nucleation and growth. The relative values of these characteristic points with respect to one another change in value in the presence of chemical modification [2, 3, 44, 54, 58, 64, 66, 82, 88, 124].

After $T^{\text{Al-Si}}_{\text{E,G}}$ the Al-Si eutectic is now stable and grows within the interdendritic regions of the thermal analysis test sample. During this time, the remaining liquid pools become progressively enriched with Cu, Fe, Mg Si and Fe until the first Al-Fe-Mg-Si-Cu based eutectic reaction nucleates.

The fraction solid that forms between $T^{\text{Al-Si}}_{\text{E,NUC}}$ and $T^{\text{Al-Fe-Mg-Si-Cu(one)}}_{\text{E,NUC}}$ reflects the relative or apparent fraction solid of the main Al-Si reaction that forms within the thermal analysis test sample. This is labeled as $af_s^{\text{Al-Si}}$ in Figure A.2c. The solidification temperature range for this thermal signature event is labeled as $\Delta T^{\text{Al-Si}}_{\text{SRAN}}$ and it's the time duration as $\Delta t^{\text{Al-Si}}_{\text{SRAN}}$. A schematic of the thermal analysis test sample structure forming along with the actual temperature, time and fraction solid characteristic points that serve as the start and end of the Al-Si eutectic solidification process is given in Figures A.1.3b.

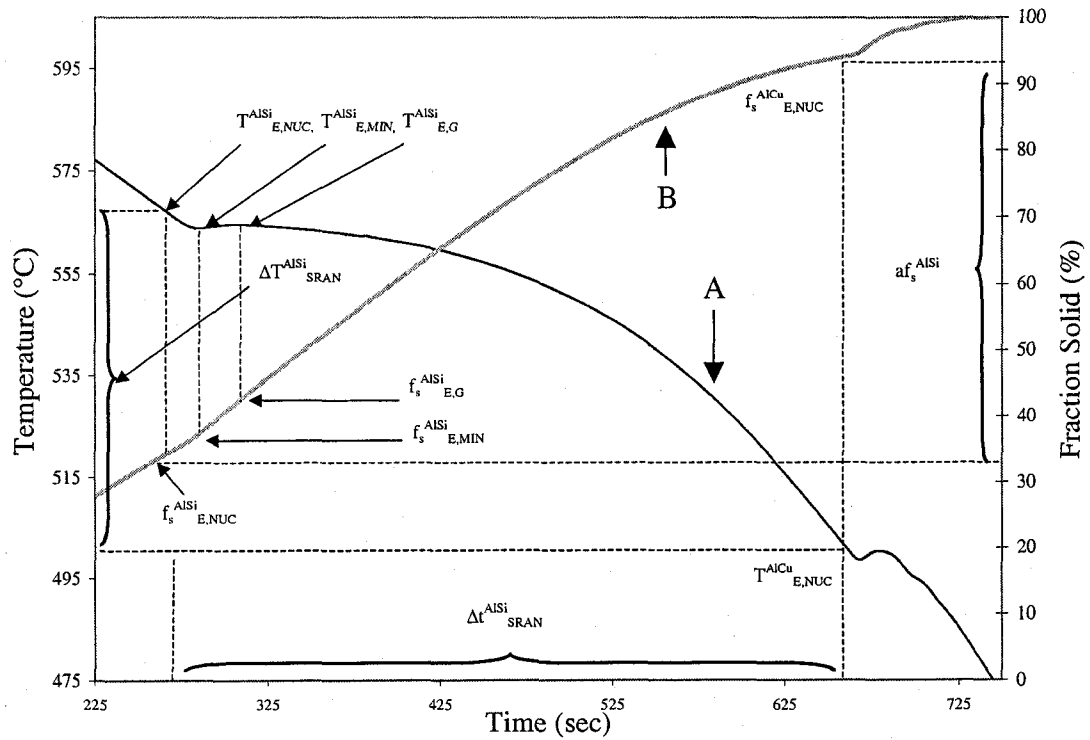


Figure A.1.3a: Cooling curve and calculated fraction solid curve between primary α -dendritic nucleation and the start of the Al-Si eutectic. A is the cooling curve and B is the calculated fraction solid.

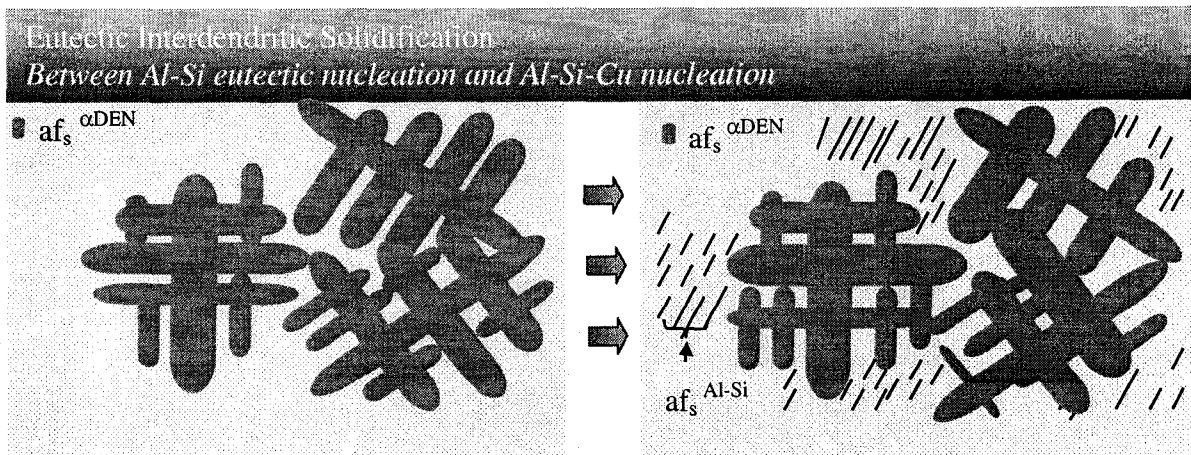


Figure A.1.3b: Schematic of the TA test sample structure during eutectic interdendritic solidification. The temperature and time analogs are ΔT_{SRAN}^{Al-Si} and Δt_{SRAN}^{Al-Si} .

A.1.4 ALTAS Partitioned Parameters Characterizing the Solidification Range Associated with the Cu Based Eutectic Reactions.

Typically by the time the post Al-Si eutectic phases have begun to nucleate at $T^{\text{Al-Fe-Mg-Si-Cu(one)}}_{\text{E,NUC}}$, $T^{\text{Al-Fe-Mg-Si-Cu(two)}}_{\text{E,NUC}}$ and $T^{\text{Al-Fe-Mg-Si-Cu(three)}}_{\text{E,NUC}}$ they have become rich in Fe, Mg, Si and Cu. As a result, depending on the actual concentration of Fe, Mg, Si and Cu rich pools between 1 and 4 distinct thermal signature events can be seen. Figure A.1.4a shows post Al-Si eutectic reaction thermal signature having three distinct anomalous events which are also evident on the calculated fraction solid curve. The derivative for this is shown in Figure A.1c.

Once the thermal analysis sample is totally solid (i.e. $f_{\text{SOL}} = 100\%$) the cooling curve and derivative curves have no further anomalous changes. The fraction solid that forms between $T^{\text{Al-Fe-Mg-Si-Cu(one)}}_{\text{E,NUC}}$ and T_{SOL} represents the fraction solid of post Al-Si eutectic phases in the structure. The solidification temperature range for this reaction is labeled as $\Delta T^{\text{Al-Fe-Mg-Si-Cu}}_{\text{SRAN}}$ and it's the time duration as $\Delta t^{\text{Al-Fe-Mg-Si-Cu}}_{\text{SRAN}}$. A schematic of the thermal analysis test sample structure forming and the actual temperature, time and fraction solid characteristic points that serve as the start and end of the post Al-Si eutectic solidification process is given in Figure A.1.4b.

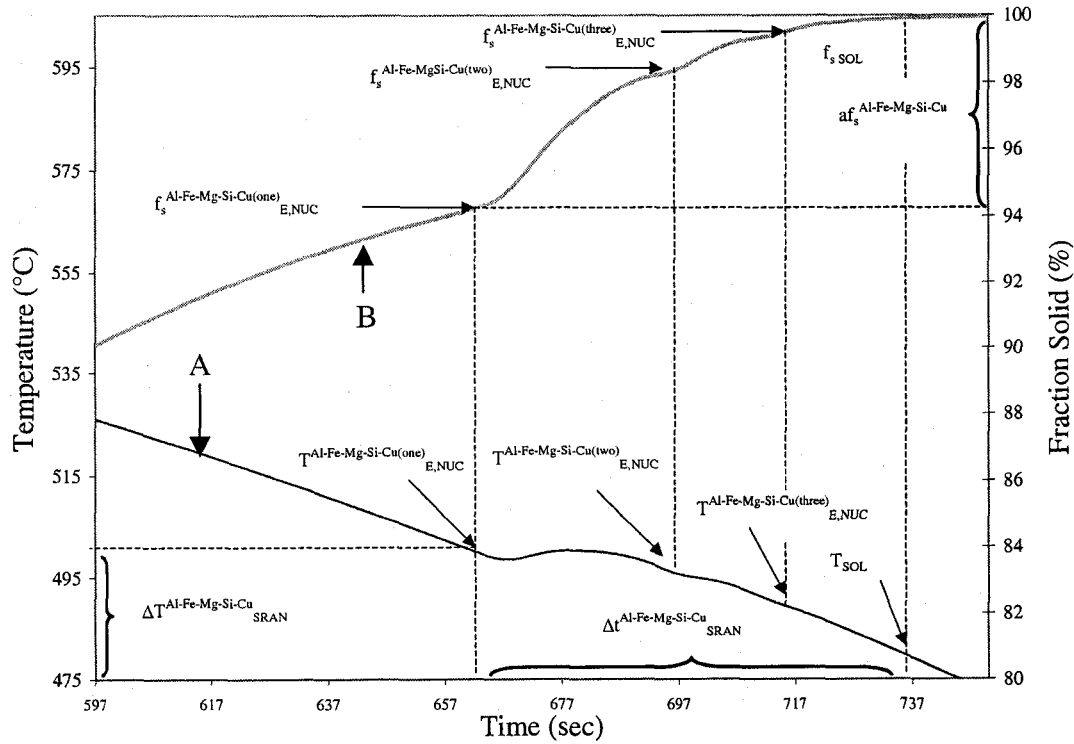


Figure A.1.4a: Cooling curve and calculated fraction solid curve between the start of the Al-Si-Cu eutectic and the solidus. **A** is the cooling curve and **B** is the calculated fraction solid.

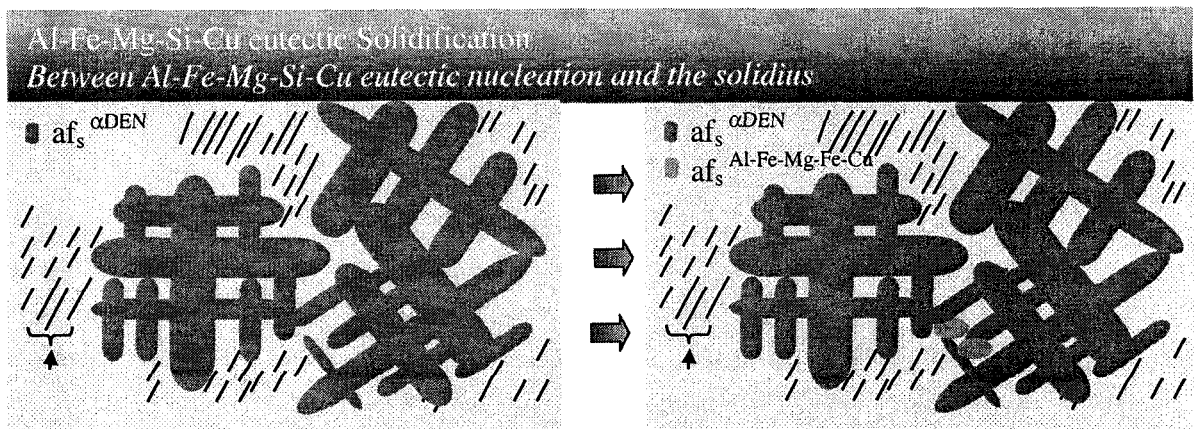


Figure A.1.4b: Schematic of the TA test sample structure during eutectic interdendritic solidification. The temperature and time analogs are $\Delta T^{\text{Al-Mg-Fe-Si-Cu}}_{\text{SRAN}}$ and $\Delta t^{\text{Al-Mg-Fe-Si-Cu}}_{\text{SRAN}}$.

A.1.5 ALTAS Partitioned Cooling Rate Calculation

Table A.1.5 list below the calculation used to determined the partitioned cooling rate for the primary α -Al dendritic growth, Al-Si eutectic growth & Al-Fe-Mg-Si-Cu eutectics.

Partitioned Event	Calculation
$CR^{\alpha\text{DEN}}_{\text{SRAN}}$	$(T^{\alpha\text{DEN}}_{\text{NUC}} - T^{\text{Al-Si}}_{\text{E,MIN}}) / (t^{\alpha\text{DEN}}_{\text{NUC}} - t^{\text{Al-Si}}_{\text{E,MIN}})$
$CR^{\text{Al-Si}}_{\text{SRAN}}$	$(T^{\text{Al-Fe-Mg-Si-Cu(one)}}_{\text{E,MIN}} - T^{\text{Al-Si}}_{\text{E,MIN}}) / (t^{\text{Al-Fe-Mg-Si-Cu(one)}}_{\text{E,MIN}} - t^{\text{Al-Si}}_{\text{E,MIN}})$
$CR^{\text{Al-Fe-Mg-Si-Cu}}_{\text{SRAN}}$	$(T^{\text{Al-Fe-Mg-Si-Cu(one)}}_{\text{E,MIN}} - T_{\text{SOL}}) / (t^{\text{Al-Fe-Mg-Si-Cu(one)}}_{\text{E,MIN}} - t_{\text{SOL}})$

Appendix B

B.1 Fraction Solid Determination

Fraction solid may be defined as the percentage of solid phase(s) that precipitate at any point in time between the liquidus and solidus temperatures in a solidifying melt. Accurate information concerning fraction solid is necessary to perform computer simulations of casting feedability and characterization of the solidification process as well as to make predictions concerning casting structure.

The literature presents a variety of methods for determining the fraction solid of casting alloys [14-25]. The most commonly used technique employs quantitative metallography using image analysis. An image analysis system can be used to measure the area fraction of phases formed prior to quenching in a set of melt specimens obtained between the liquidus and solidus temperatures. However methods that do not use thermal analysis are obviously not amenable to the rigors of the foundry production environment.

The baseline equation of a cooling curve represents an artificial curve in which no phase transformation has occurred (no release of latent heat of formation). This curve, once determined, could be subtracted from the actual dT/dt curve. This difference could then reflect the fraction solid that evolved during the solidification process of cast alloys. Fraction solid has been used in conjunction with cooling curves by many metal casting researchers, but a new method developed by Kierkus et al. [125] is an improvement upon existing fraction solid methods being used.

In the analysis of liquid metal feeding in the W319 alloy, or any other 3xx.x alloy, the use of an accurate fraction solid determination can be an important research tool and on-line quality control tool. The assessment of the fraction solid at some point during the solidification process can infer on how much has solidified and what fraction solid liquid metal must feed through to compensate for solidification shrinkage. Although the morphology of a partially solidified metal is not quantified by the fraction solid curve, it can infer on any changes in feeding modes based on either change in chemistry or cooling rate.

The solidification process of a thermal analysis test sample requires that the following assumptions outlined in the next few paragraphs need to be made.

The entire thermal system being considered (i.e. the alloy sample and the crucible) has a lumped thermal capacitance. In other words, the temperature within the system can be approximated by a spatially uniform, one dimensional model, at any instant during the cooling process. This assumption, which is typically valid for thermal analysis of aluminum alloys, requires the Biot modulus to be < 0.1 . The Biot modulus is defined as:

$$Bi = \frac{VU}{Ak} \quad (2)$$

Where:

V: Volume of the sample.

A: Surface area of the sample.

U: Overall heat transmission coefficient between the sample and its surroundings.

k: Thermal conductivity of the alloy.

During the solidification process, the product of density and specific heat (ρC) of an alloy must be temperature independent. This is very frequently the case for aluminum alloys in the temperature range between 800 and 400°C where ρC does not vary by more than +/- 0.7 percent of its average value. The heat balance equation for the assumptions given above can be written as:

$$V\rho C \frac{dT_c}{dt} = -UA(T_c - T_\infty) + \frac{dQ_L}{dt} \quad (3)$$

Where:

T_c The assumed uniform temperature within a sample (measured from the center thermocouple of the TA test sample).

ρ : Sample density.

C : Specific heat of the sample.

T_∞ : Ambient temperature.

Q_L : Latent heat generated due to phase transformation.

t : Time.

Equation (3) may be rewritten as follows:

$$\frac{dT_c}{dt} = \frac{1}{V\rho C} \left[\frac{dQ_L}{dt} - UA(T_c - T_\infty) \right] \quad (4)$$

Equation (4) represents the first derivative of a cooling curve, as a function of time. For the part of the cooling process when no phase transformation occurs, i.e.:

$$\begin{aligned} T &> T_L \text{ @ } t = t_L \quad \text{and} \\ T &< T_S \text{ @ } t = t_S \end{aligned}$$

This equation can be simplified to:

$$\frac{dT_{cz}}{dt} = \frac{1}{V\rho C}[-UA(T_{cz} - T_{\infty})] \quad (5)$$

Where the double subscript temperature $T_{cz}(t)$ represents the cooling curve of either liquid or solid metal and the left hand side of the equation denotes its first derivative, which is commonly called the “zero” or “base line” curve.

Under the assumption that V , ρC , A , T_{∞} are constants, the overall heat transmission coefficient can be assumed to be a function of T_{cz} only and can be expressed as follows:

$$\frac{dT_{cz}}{dT} = F(T_{cz}) \quad (6)$$

If the right hand side of this equation is expended into a Taylor series, this equation reads:

$$\frac{dT_{cz}}{dT} = \sum_{i=0}^n a_i(T_{cz})^i \quad (7)$$

Because the $T_{cz}(t)$ is recorded and $dT_{cz}(t)/dt$ can be easily calculated, the set of coefficients $\langle a_i \rangle$ can be obtained from a least squares fit of a polynomial of a selected order.

The aforementioned calculations were tested using many time traces of cooling curves. In general it was shown that it was always sufficient to use a polynomial not higher than $n = 3$ to assure a goodness of fit $R^2 > 0.99$. The results of the calculations done for $n = 3$ resulted in $R^2 = 0.9991$ and generated the following regression equation:

$$\frac{dT_{cz}}{dt} = -0.610363 - 0.448749 * 10^{-2} (T_c - 390) + 0.139216 * 10^{-4} (T_c - 390)^2 - 0.643171 * 10^{-7} (T_c - 390)^3 \quad (8)$$

Combining equations (4) and (5) results in:

$$\frac{dT_c}{dt} - \frac{dT_{cz}}{dt} = \frac{1}{V\rho C} \left[\frac{dQ_L}{dt} \right] \quad (9)$$

Integrating equation (9) between $T(t)$ and $T_s(t_s)$ results in:

$$\int_{t_L}^{t_s} \left[\frac{dT_c}{dt} - \frac{dT_{cz}}{dt} \right] dt = \frac{1}{V\rho C} [L] \quad (10)$$

Where

L : latent heat of solidification of a given alloy.

From the definition of heat generated due to phase transformation its derivative can be expressed as:

$$\frac{dQ_L}{dt} = L \frac{dfs}{dt} \quad (11)$$

Integrating equations (9) and (11) results in:

$$\int_{t_L}^t \left[\frac{dT_c}{dt} - \frac{dT_{cz}}{dt} \right] dt = \frac{1}{V\rho C} [Lfs]_{t_L}^t \quad (12)$$

Thus, by dividing equation (12) by (10) and because $fs(t_L) = 0$, one is able to deduce that:

$$fs(t) = \frac{\int_{t_L}^t \left[\frac{dT_c}{dt} - \frac{dT_{cz}}{dt} \right] dt}{\int_{t_L}^{t_s} \left[\frac{dT_c}{dt} - \frac{dT_{cz}}{dt} \right] dt} \quad (13)$$

This permits one to calculate the rate of change of solidification fraction in time (dfs/dt). Note: $fs(t)$ and $dfs(t)/dt$ are functions of time and measured solidifying alloy temperatures (T_c) only. The determination of the cooling curve $T_c(t)$ represents a necessary and sufficient condition to determine the solidification (fs , dfs/dt vs. time) history of the metal in any circumstances. No other information (for example V , A , ρ , C and k) regarding the thermal analysis test sample is required. The procedures described above, for calculating the base line, will be incorporated into the ALTAS software (developed and used by the IRC) for the estimation of fraction solid in the near future.

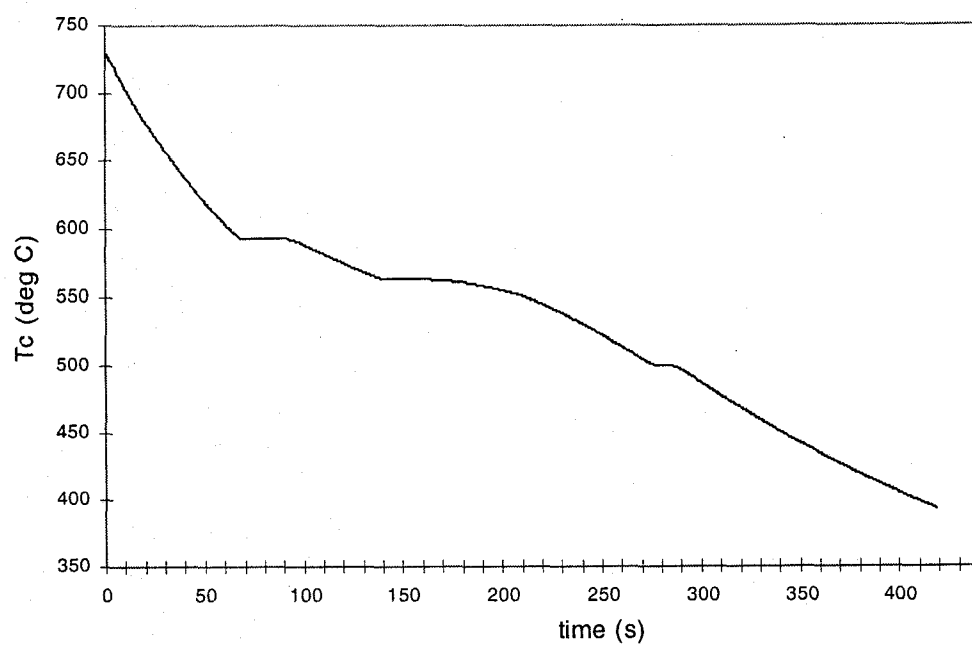


Figure 7: Cooling curve

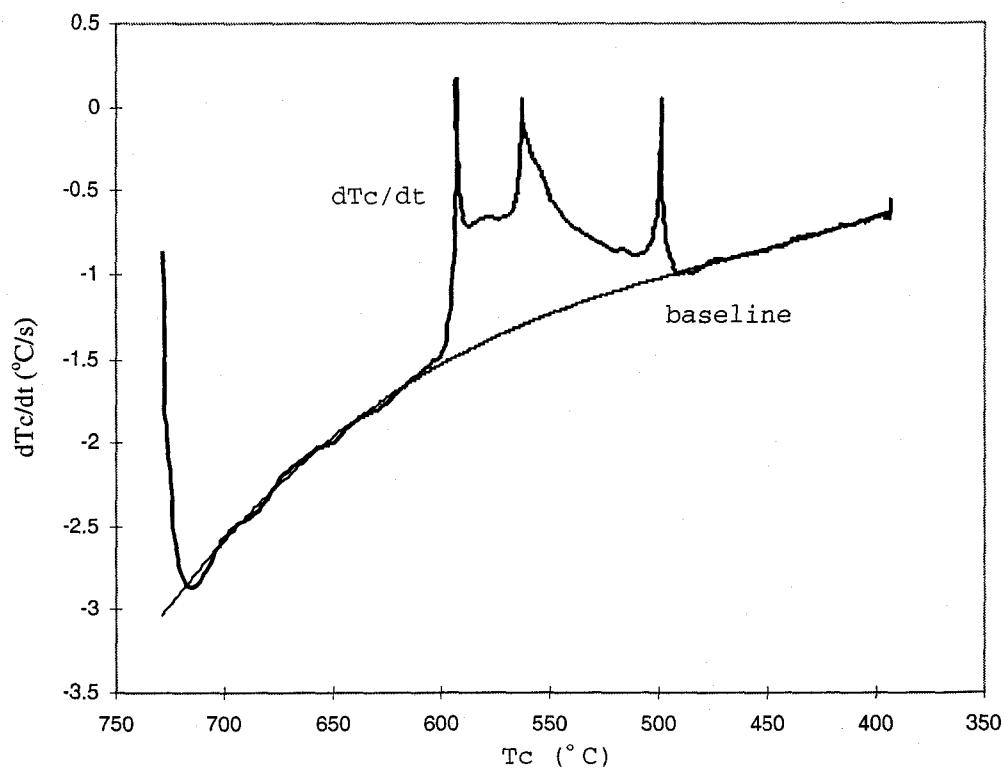


Figure 8: First derivative of sample temperature T_c and the calculated baseline curve as a function of solidification temperature.

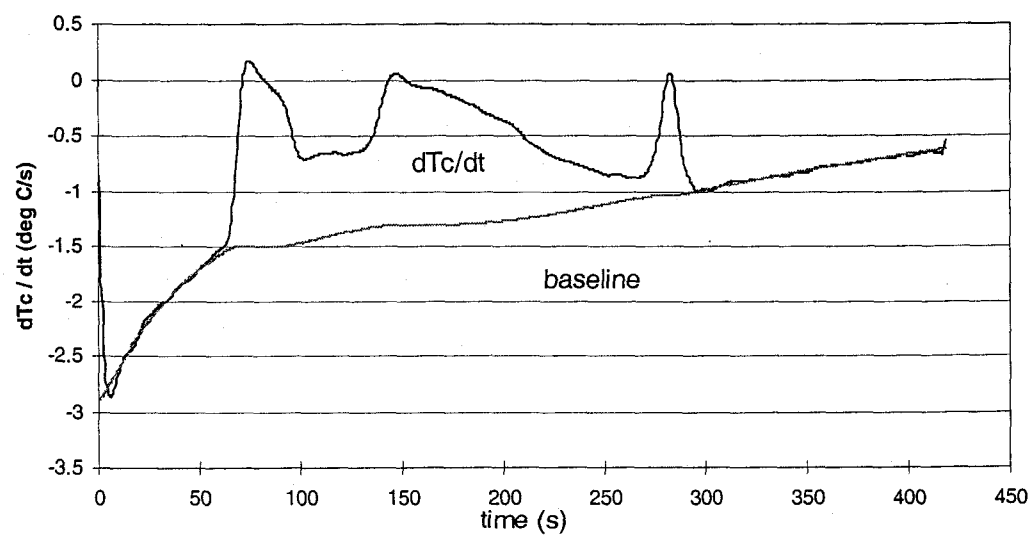


Figure 9: First derivative of sample temperature T_c and the calculated baseline curve as a function of solidification time.

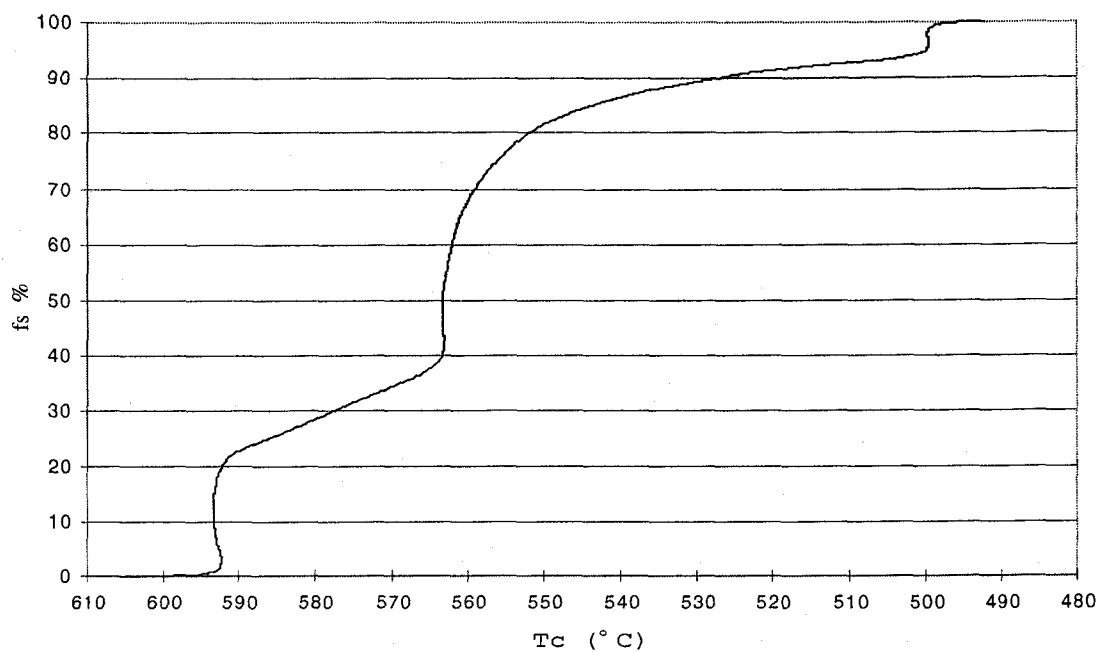


Figure 10: Fraction solid calculated as a function of temperature (T_c).

Appendix C

Experimental Method of the In-situ Thermal Analysis

C.1 Experimental Procedure

The thermocouple array number 1 to 10 (see Figure C.1) was designed to acquire temperature-time data from the riser, bulkhead, and regions adjacent to the bulkhead. The bulkhead (channels 4, 5, 6, 7 and 8) is situated in the region near the saddle bearing. Channels 9 and 10 are situated on the outer most regions of the bulkhead section, away from the saddle bearing. The risers are included in the thermocouple array (channels 1, 2 and 3) so that an assessment of their feeding capacity to the cast section could be made.

The engine block castings (a total of 6) were produced using the W319 alloy, in a 4000 lb capacity melting furnace at the Nema Engineering Center (NEC). The chemical composition of the alloy (W319) is given in Table C.1. The W319 alloy melt was treated with Al-5 wt. % Sr rods to reach an over-all Sr level in the melting furnace of about 73 ppm.

Once the metal enters the region containing the thermocouple array the data logger begins to record temperature-time data. The centre thermocouple (channel 2) where the first metal stream comes in contact with the thermocouple array initiates recording. Once the mould is filled (taking approximately 25 seconds) the mould roles over.

Figure C.2 represent an example of the cooling curve results of the whole array for the cast bulkhead and riser section. The characteristic temperature data acquired from the In-situ thermal analysis array, using the methods outlined Appendix A, are listed in Table C.2.

Channels 1, 2 and 3 which monitor the riser, have a longer time for complete solidification of the bulkhead section. Primary α -Al recalescence was absent in all cooling curves except for channels 1, 2 and 3. Heat transfer from the riser through the bulkhead likely smears out the effects of recalescence of the α -Al phase in cooling curves of the bulkhead section.

The effect of Al-Si eutectic recalescence is observable on the cooling curves of the riser (channels 1, 2 & 3) and bulkhead section (channels 5, 6, 7 & 9). Evidence of Al-Si eutectic recalescence on the cooling curves acquired from channels 4 and 8, which measure cooling curve data between the bulkhead and the riser, are absent. This is most likely due to the fact that heat transfers from the riser through the bulkhead.

It is from this cooling curve array that thermal gradient data and time for solidification of phase events (i.e. Al-Si eutectic) can be determined at any time during the solidification process. The solidification time data was used in this dissertation along with the measured Secondary Dendrite Arm Spacing (λ_2) from channels 4, 5, 7, 8, 9 and 10 (see Figure 6.2a, Chapter Six). Further analysis which was outside the scope of this

dissertation was presented in a publication presented at the TMS conferences in Seattle Washington by Mackay et al. [103].

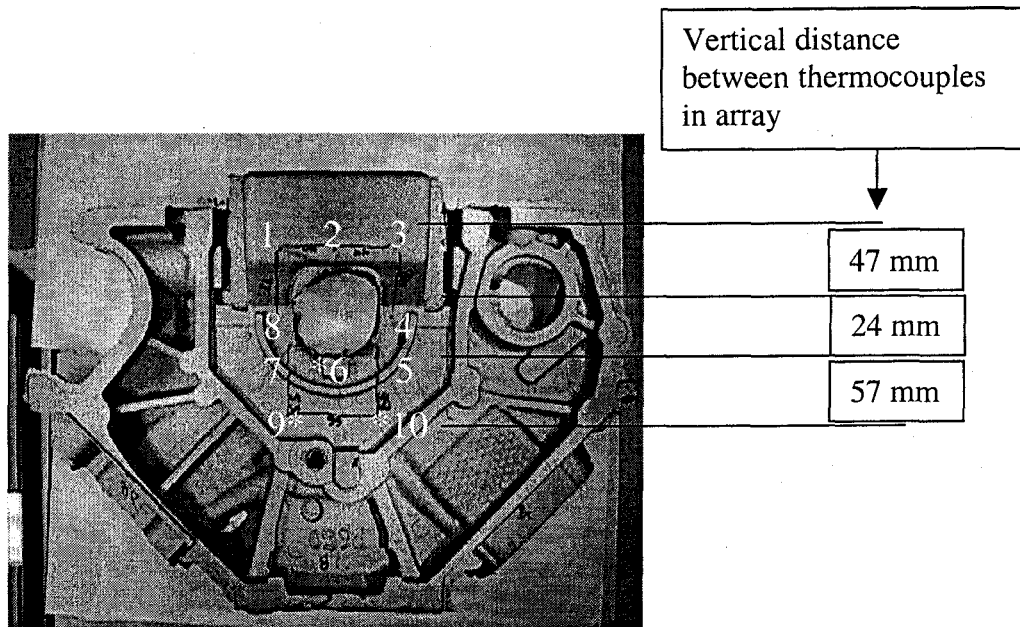


Figure C.1: Pictograph of the In-situ thermal analysis array in bulkhead E of the V8 engine block.

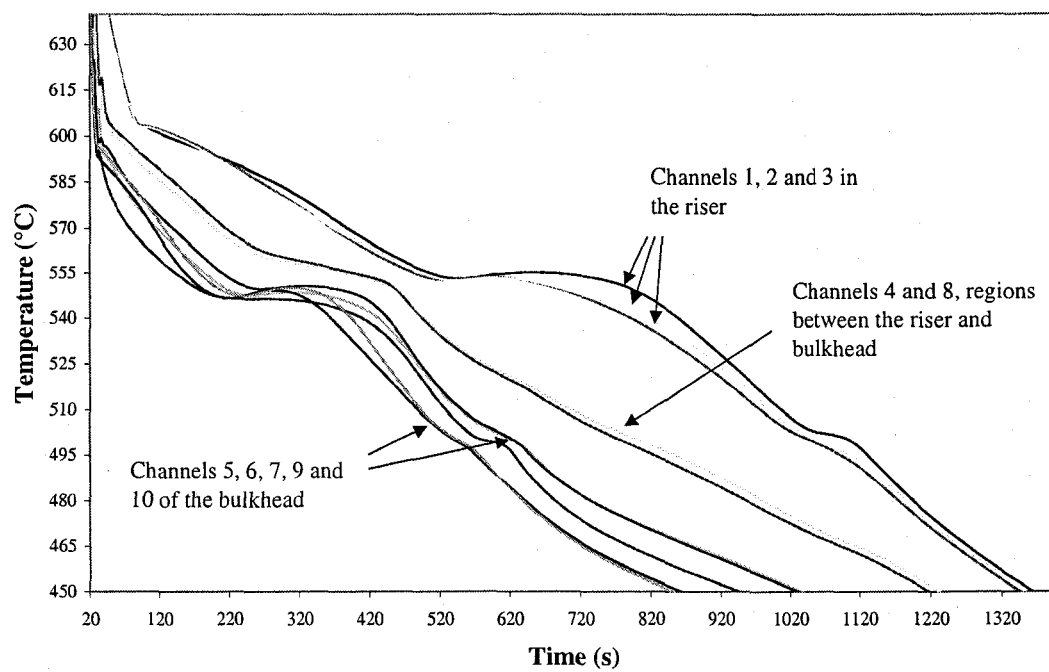


Figure C.2: Smoothed cooling curve data from the whole thermocouple array of the 4.6 L engine block.

Table C.1: Chemistry of V8 engine blocks cast with the embedded thermocouple array, (composition in wt. %)

	<i>Si</i>	<i>Cu</i>	<i>Fe</i>	<i>Mg</i>	<i>Zn</i>	<i>Ti</i>	<i>Ni</i>	<i>Cr</i>	<i>Sr</i>
May 12, 1999 <i>First three engine blocks cast</i>	7.12	3.41	0.33	0.28	0.15	0.10	0.02	0.02	0.0074
May 27, 1999 <i>Last three engine blocks cast</i>	7.11	3.43	0.30	0.30	0.16	0.11	0.01	0.02	0.0073

Table C.2: The results of the In-situ thermal analysis array of the V8 engine block. The values are the average of three repeats.

Channel	Max Temp (C°)	$T_{NUC}^{\alpha DEN}$ (C°)	$T_{E,NUC}^{Al-Si}$ (C°)	$T_{E,NUC}^{Al-Fe-Mg-Si-Cu}$ (C°)	$\Delta T_{SRAN}^{\alpha DEN}$ (C°)	ΔT_{SRAN}^{AlSi} (C°)
May 12, 1999						
1	708	600	551	510	50	40
2	727.8	603	553	510	50	43
3	711	603	550	510	53	40
4	710	601	<i>Not detectable due to thermal smearing</i>			
5	708	599	550	512	49	38
6	689	596	547	511	49	36
7	701	590	546	513	44	33
8	714	600	<i>Not detectable due to thermal smearing</i>			
9	685	589	546	509	43	37
10	685	600	550	510	50	40
May 27, 1999						
1	706	603	552	512	51	40
2	726	603	553	509	50	46
3	708	603	552	511	51	45
4	712	602	<i>Not detectable due to thermal smearing</i>			
5	704	595	547	514	48	31
6	650	596	547	516	49	37
7	704	600	549	514	51	35
8	712	601	<i>Not detectable due to thermal smearing</i>			
9	686	592	546	512	46	34
10	690	595	547	512	48	35

Appendix D

Table D.1: Composition (wt.%) of the WA328 and WB328 alloys during the production of test V8 engine block casting. * Indicates dates at which Enviro-ALTAS samples were collected. # indicates the date of which a V8 engine block was cast and then sectioned to produce UMSA test samples.

<i>Cast Date</i>	<i>Si</i>	<i>Cu</i>	<i>Fe</i>	<i>Mg</i>	<i>Mn</i>	<i>Zn</i>	<i>Ti</i>	<i>Sr</i>	<i>Ni</i>	<i>Al</i>
01/30/02	9.16	1.03	.341	.307	.151	.146	.075	<0.0005	.176	bal
01/31/02	9.07	1.02	.362	.303	.159	.146	.073	<0.0005	.174	bal
02/01/02	9.21	.997	.351	.302	.157	.143	.077	<0.0005	.178	bal
*02/05/02	9.19	1.03	.383	.284	.152	.147	.078	<0.0005	.184	bal
*02/06/02	8.92	1.09	.414	.323	.162	.146	.075	<0.0005	.202	bal
#02/07/02	9.23	1.01	.391	.311	.161	.143	.077	<0.0005	.192	bal
02/08/02	9.20	1.00	.362	.302	.159	.144	.078	<0.0005	.187	bal
*02/11/02	9.33	1.01	.363	.304	.159	.145	.077	<0.0005	.181	bal
*02/12/02	9.18	1.02	.372	.352	.161	.143	.077	<0.0005	.197	bal
*02/13/02	9.21	1.03	.375	.312	.160	.147	.077	<0.0005	.184	bal
02/14/02	9.18	1.02	.384	.312	.173	.148	.076	<0.0005	.185	bal
03/01/02	8.70	.996	.812	.293	.375	.143	.074	<0.0005	.185	bal
03/04/02	8.66	1.01	.823	.280	.388	.144	.074	<0.0005	.183	bal
03/05/02	8.71	.998	.842	.292	.384	.146	.074	<0.0005	.183	bal
*03/06/02	8.43	1.01	.833	.281	.388	.140	.074	<0.0005	.178	bal
#03/07/02	8.74	1.02	.812	.314	.354	.137	.075	<0.0005	.176	bal
03/11/02	8.83	1.06	.843	.313	.371	.141	.071	<0.0005	.174	bal
*03/18/02	8.81	1.07	.863	.312	.357	.139	.074	<0.0005	.166	bal
*03/19/02	8.57	1.02	.842	.321	.366	.133	.077	<0.0005	.168	bal

Appendix E

Porosity Results

Appendix E list in the mean porosity & mean pore diameter found in each of the left and right side of every bulkhead of the V8 engine block (see Figure 4.1 for the orientation of metallographic test samples).

Table E.1: The mean area fraction of porosity along with standard deviation

<i>Alloy and Master Alloy Conditions</i>	<i>Bulkhead Section</i>	<i>Left Side (%)</i>	<i>Right Side (%)</i>
WB328 Alloy	A	0.13 ± 0.08	0.14 ± 0.09
	B	0.25 ± 0.29	0.09 ± 0.05
	C	0.13 ± 0.07	0.12 ± 0.04
	D	0.21 ± 0.03	0.16 ± 0.05
	E	0.12 ± 0.08	0.11 ± 0.10
WB328 Alloy	A	0.16 ± 0.13	0.24 ± 0.15
	B	0.11 ± 0.05	0.16 ± 0.12
	C	0.18 ± 0.08	0.11 ± 0.09
	D	0.16 ± 0.12	0.07 ± 0.03
	E	0.06 ± 0.05	0.08 ± 0.05
W319 Alloy	A	0.24 ± 0.27	0.26 ± 0.16
	B	0.21 ± 0.38	0.27 ± 0.11
	C	1.08 ± 0.22	1.39 ± 0.20
	D	0.81 ± 0.60	0.46 ± 0.29
	E	0.24 ± 0.12	0.20 ± 0.12
W319 Alloy (Al-5Ti-1B)	A	0.73 ± 0.43	0.83 ± 0.76
	B	0.23 ± 0.21	0.22 ± 0.14
	C	1.51 ± 1.01	0.52 ± 0.32
	D	0.64 ± 0.49	0.19 ± 0.10
	E	0.47 ± 0.30	0.93 ± 0.40
W319 Alloy (Al-5Ti-1B-110Sr)	A	0.87 ± 0.50	1.18 ± 1.03
	B	0.94 ± 0.98	1.13 ± 0.85
	C	1.00 ± 0.59	1.01 ± 0.69
	D	1.78 ± 1.14	1.49 ± 0.48
	E	1.55 ± 0.76	1.35 ± 1.16

Table E.2: The mean pore diameter along with standard deviation

<i>Alloy and Master Alloy Conditions</i>	<i>Bulkhead Section</i>	<i>Left Side (μm)</i>	<i>Right Side (μm)</i>
WB328 Alloy	A	34.51 ± 27.3	37.3 ± 25.6
	B	28.33 ± 21.6	36.4 ± 30.2
	C	31.65 ± 19.6	31.4 ± 14.5
	D	52.32 ± 44.9	38.6 ± 30.2
	E	29.23 ± 15.2	27.1 ± 3.22
WB328 Alloy	A	75.80 ± 88.6	75.6 ± 95.3
	B	82.9 ± 66.5	35.3 ± 32.5
	C	65.7 ± 72.3	33.7 ± 22.1
	D	72.3 ± 55.2	27.1 ± 3.21
	E	64.2 ± 69.2	23.8 ± 10.2
W319 Alloy	A	75.8 ± 62.3	77.1 ± 17.2
	B	82.9 ± 36.6	76.6 ± 23.7
	C	65.7 ± 38.5	67.1 ± 31.2
	D	72.3 ± 45.2	78.6 ± 33.5
	E	64.2 ± 23.5	70.6 ± 33.5
W319 Alloy (Al-5Ti-1B)	A	98.1 ± 89.3	94.1 ± 74.1
	B	106.5 ± 96.2	75.5 ± 30.2
	C	105.3 ± 36.2	74.4 ± 35.2
	D	94.7 ± 45.2	72.4 ± 27.5
	E	113.1 ± 63.2	91.3 ± 52.8
W319 Alloy (Al-5Ti-1B-110Sr)	A	100.3 ± 99.2	112.8 ± 129.5
	B	78.5 ± 81.2	88.5 ± 135.6
	C	83.7 ± 62.3	88.9 ± 95.2
	D	119.9 ± 75.2	110.5 ± 94.5
	E	97.3 ± 85.2	108.5 ± 93.2

Appendix F

Enviro-ALTAS & UMSA Results

Table F.1: Results of characteristic temperatures and partitioned temperature parameters from the Enviro-ALTAS and the UMSA. The composition of the Enviro-ALTAS and the UMSA test samples is indicated in Appendix D.

Characteristic Temperature	WA328		WB328	
	Enviro-ALTAS	UMSA	Enviro-ALTAS	UMSA
$T_{\text{NUC}}^{\alpha, \text{DEN}} (^{\circ}\text{C})$	590.1 ± 1.6	590.3 ± 0.7	596.4 ± 2.0	592.2 ± 1.1
$T_{\text{E,NUC}}^{\text{Al-Si}} (^{\circ}\text{C})$	569.2 ± 2.2	571.6 ± 0.5	572.5 ± 4.1	571.3 ± 0.4
$T_{\text{E,NUC}}^{\text{Al-Fe-Mg-Si-Cu(one)}} (^{\circ}\text{C})$	525.3 ± 1.1	527.6 ± 2.1	533.6 ± 4.4	530.3 ± 0.8
$T_{\text{E,MIN}}^{\text{Al-Fe-Mg-Si-Cu(two)}} (^{\circ}\text{C})$	495.5 ± 6.2	499.4 ± 1.9	501.9 ± 5.7	498.2 ± 2.6
$T_{\text{SOL}} (^{\circ}\text{C})$	474.3 ± 6.0	460.3 ± 5.3	481.3 ± 1.2	465.2 ± 2.1
$\Delta T_{\text{SRAN}}^{\alpha, \text{DEN}} (^{\circ}\text{C})$	20.8 ± 1.9	18.2 ± 0.8	24.3 ± 3.7	21.3 ± 0.7
$\Delta T_{\text{SRAN}}^{\text{Al-Si}} (^{\circ}\text{C})$	43.7 ± 1.4	44.5 ± 2.9	39.2 ± 3.7	41.2 ± 1.9
$\Delta T_{\text{SRAN}}^{\text{Al-Fe-Mg-Si-Cu}} (^{\circ}\text{C})$	50.83 ± 6.5	66.8 ± 4.2	52.8 ± 2.5	65.0 ± 1.4

Table F.2: Results of Enviro-ALTAS and UMSA partitioned time, temperature parameters and cooling rate parameters.

Partitioned Parameter	WA328	WB328	W319
	UMSA	UMSA	UMSA
$\Delta t_{\text{SRAN}}^{\alpha, \text{DEN}} (\text{sec})$	35.8 ± 3.8	40.2 ± 0.8	65.2 ± 6.2
$\Delta t_{\text{SRAN}}^{\text{Al-Si}} (\text{sec})$	114.6 ± 14.2	101.6 ± 7.5	114.1 ± 14.2
$\Delta t_{\text{SRAN}}^{\text{Al-Fe-Mg-Si-Cu}} (\text{sec})$	66.8 ± 4.2	65.6 ± 1.4	54.2 ± 4.7
$\Delta T_{\text{SRAN}}^{\alpha, \text{DEN}} (^{\circ}\text{C})$	18.2 ± 0.8	21.3 ± 0.7	33.2 ± 5.0
$\Delta T_{\text{SRAN}}^{\text{Al-Si}} (^{\circ}\text{C})$	44.5 ± 2.9	41.2 ± 1.9	64.2 ± 6.2
$\Delta T_{\text{SRAN}}^{\text{Al-Fe-Mg-Si-Cu}} (^{\circ}\text{C})$	66.8 ± 4.2	65.0 ± 1.4	54.2 ± 4.7
$\text{CR}_{\text{SRAN}}^{\alpha, \text{DEN}} (^{\circ}\text{C}/\text{sec})$	0.51	0.52	0.50
$\text{CR}_{\text{SRAN}}^{\text{Al-Si}} (^{\circ}\text{C}/\text{sec})$	0.38	0.40	0.51
$\text{CR}_{\text{SRAN}}^{\text{Al-Fe-Mg-Si-Cu}} (^{\circ}\text{C}/\text{sec})$	1.6	1.7	1.4

Table F.3: Bulk partitioned thermal analysis data of UMSA test samples. As can be seen bulk parameters may give the impression that solidification conditions may be the same. The partitioned solidification range $\Delta T^{\alpha_{DEN}}_{SRAN} + \Delta T^{\alpha_{Si}}_{SRAN}$ is included since this is the solidification range in which porosity may grow.

<i>Bulk Parameter</i>	<i>Al-9wt.%Si- 1wt.%Cu</i>	<i>Al-9wt.%Si- 1wt.%Cu- 1wt.%Fe</i>	<i>W319</i>
Average Cooling Rate (°C/sec)	0.6832	0.7010	0.6612
Solidification Time Range (sec)	189.2 ± 16.36	180.5 ± 7.125	228.5 ± 17.23
Total Solidification Range (($\Delta T^{\alpha_{DEN}}_{SRAN} + \Delta T^{\alpha_{Si}}_{SRAN}$ + $\Delta T^{\alpha_{FeMgSiCu}}_{SRAN}$ (°C))	129.5 ± 5.552	127.5 ± 2.752	151.3 ± 6.652
Partitioned Solidification Range ($\Delta T^{\alpha_{DEN}}_{SRAN} +$ $\Delta T^{\alpha_{Si}}_{SRAN}$ (°C))	62.77 ± 4.210	62.55 ± 4.2	97.2 ± 2

Appendix G

4.6 L Engine Block & UMSA Mechanical Test Data

Table G.1: Summary of monotonic test results from the W319 and WA328 alloy. Test samples were excised from the bulkhead regions of the V8 engine Block. The results contained herein result from 10 test samples for each alloy.

<i>Alloy</i>	<i>Tensile Strength (MPa)</i>		<i>Elongation (%)</i>		<i>Modulus of Elasticity (GPa)</i>
	<i>0.2% Yield</i>	<i>Ultimate</i>	<i>Elastic</i>	<i>Total</i>	
W319	225 ± 19	270 ± 9	0.47 ± 0.03	1.2 ± 0.2	78 ± 12
WA328	232 ± 9	236 ± 10	0.48 ± 0.02	0.8 ± 0.2	81 ± 8.5

Table G.2: Vickers Microhardness from the left side of the Bulkhead for the W319 alloy, the WA328 alloy and the WB328 alloy. The results contained herein result from an average of 12 indentations.

<i>Alloy</i>	<i>Bulkhead A</i>	<i>Bulkhead B</i>	<i>Bulkhead C</i>	<i>Bulkhead D</i>	<i>Bulkhead E</i>
W319	105.1 ± 4.7	107.5 ± 5.2	98.3 ± 5.1	103.5 ± 3.8	96.2 ± 6.4
WA328	91.1 ± 6.0	86.6 ± 5.3	81.6 ± 4.7	88.4 ± 7.4	92.2 ± 2.7
WB328	95.2 ± 4.8	82.8 ± 9.1	84.8 ± 7.4	87.2 ± 2.0	91.4 ± 7.3

Table G.3: Vickers Microhardness from the quenched UMSA structures. The results contained herein result from an average of 12 indentations.

<i>Alloy</i>	<i>585°C</i>	<i>575°C</i>	<i>565°C/555°C</i>	<i>527°C</i>	<i>Full solidification</i>
W319	65.1 ± 5.2	61.7 ± 13.2	63.2 ± 3.7	-	68.2 ± 3.4
WA328	62.1 ± 4.4	59.1 ± 2.0	65.6 ± 2.0	58.4 ± 1.5	58.8 ± 6.0
WB328	60.5 ± 5.0	62.1 ± 3.1	58.4 ± 2.5	-	60.4 ± 5.2

Table G.4: Sample identification, run order, stress and end results of the test (run out or failure).

<i>Sample label</i>	<i>Sample Location</i>	<i>Date sample tested (Run order)</i>	<i>Stress (MPa)</i>	<i>Cycle failed or Run out</i>
1	A9-B-L	1	65.6	Run out
2	A21-C-R	2	68.9	Run out
3	A11-B-L	26	75.8	2,108,933 Cycles
4	A9-C-L	28	75.8	1,019,923 Cycles
5	A11-B-R	3	72.3	Run out
6	A9-D-L	23	65.6	Run out
7	A17-D-L	6	82.7	Run out
8	A18-D-L	20	75.8	4,933,391 Cycles
9	A11-C-L	12	75.8	1,233,445 Cycles
10	A17-C-L	11	72.3	Run out
11	A10-D-L	10	75.8	6,996,681 Cycles
12	A21-B2-R	19	72.5	Run out
13	A21-D-R	9	79.2	385, 668 Cycles
14	A17-D-R	5	79.2	Run out
15	A10-D-R	8	82.7	3,525,611 Cycles
16	A10-C-R	7	86.1	4,461,365 Cycles
17	A18-D-R	14	75.8	Run out
18	A9-D-R	13	72.5	Run out
19	A21-D-R	22	68.9	1,212,443 Cycles
20	A9-B-R	18	68.9	Run out
21	A21-C-R	27	72.5	Run out
22	A10-B-R	15	79.2	4,391,998 Cycles
23	A17-B-R	34	75.8	Run out
24	A18-C-R	30	75.8	789,774 Cycles
25	A11-C-R	17	72.5	Run out
26	A12-A-R	26	75.8	3,391,567 Cycles
27	A12-A-L	21	72.5	5,678,786 Cycles
28	A19-A-L	24	68.9	Run out
29	A12-A-R	31	72.5	Run out
30	A12-A-L	29	72.3	Surface Pore
31	A12-E-R	25	72.3	Run out
32	A21-B-L	32	75.8	1,455,391 Cycles
33	A17-C-R	33	72.3	Run out
34	A9-B-L	4	75.8	Run out

Appendix H

Summary of Riser Sink Evaluation

Table H.1: Summary of the mean volume of the riser sink along with standard deviation.

<i>Alloy and Master Alloy Conditions</i>	<i>Riser</i>	<i>Volume of Riser Sink (cm³)</i>
WA328	A	102.00 ± 0.10
	B	96.00 ± 0.10
	C	104.50 ± 0.11
	D	101.00 ± 0.10
	E	137.00 ± 0.41
W319	A	104.75 ± 0.11
	B	99.75 ± 0.13
	C	101.50 ± 0.14
	D	99.75 ± 0.13
	E	138.50 ± 0.14
W319 (Al-5Ti-1B)	A	107.94 ± 0.11
	B	111.75 ± 0.14
	C	113.81 ± 0.14
	D	98.81 ± 0.14
	E	151.38 ± 0.15
W319 (Al-5Ti-1B-10Sr)	A	96.33 ± 0.10
	B	91.33 ± 0.12
	C	103.67 ± 0.14
	D	100.67 ± 0.13
	E	130.12 ± 0.13

VITA AUCTORIS

Name: Robert Ian Mackay

Place of Birth: Montreal, Quebec, Canada

Year of Birth: December 3, 1969

Education:

West Kent Elementary School, Charlottetown, P.E.I. (1975-1982)

Queen Charlotte Junior High School, Charlottetown, P.E.I. (1982-1985)

Charlottetown Rural High School, Charlottetown, P.E.I. (1985-1988)

University of Prince Edward Island, Charlottetown, P.E.I., B.Sc., (Physics) (1988-1992)

Memorial University of Newfoundland, St. John's, Newfoundland, M.Sc., (Geophysics) (1992-1994)

McGill University, Montreal, Quebec, M.Eng. (Metallurgical Engineering), 1995-1997